Continuum Limit Of Lattice Gas Fluid Dynamics

by

Christopher M. Teixeira

B.A.Sc., Engineering Science
University of Toronto
(1988)

Submitted to the Department of Nuclear Engineering
in partial fulfillment of the requirements for the degree of

Doctor of Philosophy

at the

MASSACHUSETTS INSTITUTE OF TECHNOLOGY

September 1992

Signature of Author .....
Department of Nuclear Engineering
August 14, 1992

Certified by .....
Kim Molvig
Professor, Nuclear Engineering Department
Thesis Supervisor

Certified by .....
Gregory M. Papadopoulos
Professor, Electrical Engineering Department
Thesis Reader

Accepted by .....
Allan F. Henry
Chairman, Departmental Graduate Committee

Continuum Limit Of Lattice Gas Fluid Dynamics

by

Christopher M. Teixeira

Submitted to the Department of Nuclear Engineering
on August 14, 1992, in partial fulfillment of the
requirements for the degree of
Doctor of Philosophy

ABSTRACT

The general theory for multiple-speed lattice gas algorithms (LGAs) is developed where previously only a single-speed theory existed. A series of microdynamical multiple-speed models are developed that effectively erase the underlying lattice from the macroscopic dynamics allowing the LGA to reproduce the results of continuum hydrodynamics *exactly*. The underlying lattice is the 4D FCHC lattice. It is shown that this lattice: 1) Permits all integral energies, 2) Has sufficient symmetry to allow for an isotropic stress tensor for each energy individually, 3) Allows interaction amongst all energies, and 4) Has discrete microscopic Galilean invariance, all of which allows the extension of the model to higher-speeds. We show that this lattice is the *only* regular lattice with these remarkable properties, all of which are required to show that the discreteness artifacts completely disappear from the LGA in the limit of infinite speeds, so that correct continuum hydrodynamic behaviour results. Three finite-speed models that remove the discreteness artifacts are developed. A three-speed model is developed that reproduces macroscopically the behaviour of the continuity and Navier-Stokes equations. A four-speed model is developed that removes all but one of the artifacts from the mass, momentum and energy conservation equations. A five-speed model for low density flows is developed that removes *all* of the artifacts from these three equations. The mean dynamics of these models are unaffected by statistical fluctuations in the properties of the flow. This is the *Shot Noise Theorem* for LGAs. Extensive simulation results are presented for the three-speed model. We verify the removal of the discreteness artifacts from the momentum equation using a decaying shear wave experiment and show that they are still invisible for Mach numbers up to $M \sim .4$, beyond the theoretical limit. Flow between flat plates replicated the expected parabolic profile of Poiseuille flow in the mean when started from rest. Two separate measurements of the kinematic viscosity of the fluid (normal pressure drop and the microscopic particle force at the wall) agreed with each other and with the shear wave viscosity to better than 1%. Cylinder flow simulations accurately reproduced drag coefficients and eddy-length to diameter ratios for $Re \leq 45$ to within the error of experimental observation. At higher Reynolds number, $Re \simeq 65$, vortex shedding was observed to occur, with the Strouhal number being very close to the experimental value when corrected for the relatively large blockage, 18%, present in the simulation. CFD results for flow past cylinders at similar Reynolds numbers produce either erroneous results (significant errors in eddy length to diameter ratios) or rely on artificially perturbing the flow to cause phenomena that does not occur naturally in the method (vortex shedding).

Thesis Supervisor: Kim Molvig
Title: Professor, Nuclear Engineering Department

Thesis Reader: Gregory M. Papadopoulos
Title: Professor, Electrical Engineering Department

Acknowledgements

I would like to express my most sincere gratitude to my thesis supervisor, Professor Kim Molvig, for allowing me the opportunity to work on an exciting new way of understanding and simulating physical phenomena. Professor Molvig's dedication, capacity for physical insight, accessibility, encouragement and perseverance in convincing me of the fundamental nature of the work I was performing made this collaboration by far the most fortunate occurrence of my academic career here at M.I.T. A number of the innovations described herein are his and are included in order to present a complete picture of the potential of multiple-speed lattice gas algorithms. I am also grateful to Professor Gregory Papadopoulos for serving as my thesis reader and explaining to me the computational requirements for both the lattice gas algorithm and CFD. I would also like to thank Professor Jeffrey Freidberg for illustrating his rigourous approach to mathematical detail throughout the courses he has taught, of which I have been a student of many. This approach is one I have tried to adopt for my own throughout this work.

I would like to acknowledge the other students in our Lattice Gas group - Robert Bosch Jr., Saed Younis, Fernando Mujica - who (along with Prof. Molvig) ensured that the theory developed here could be verified via simulation.

I would like to thank the National Science and Engineering Research Council of Canada for their financial support throughout my time at M.I.T.

There is a shared exhilaration amongst those who have endured the same experience. To the many other "gradual" school students I have had the pleasure of meeting and sharing this time with - Christian Kurz, Gerasimos Tinios, Robert Gormley, Daniel Lo, James Wei, Michael Graf, Tom Hsu, Jim Reardon, Tony Hechanova amongst others - I look forward to our friendship being continued beyond graduation.

The companionship and encouragement of Miss J.S. Clowe provided a constant source of happiness that made the completion of this work all the more enjoyable.

Finally, I would like to dedicate this work to my family and in particular, my parents, Maureen and Michael Teixeira, for their constant encouragement, understanding, love and support.

Thank you Felix!

Christopher M. Teixeira

Contents

List of Figures

List of Tables

Chapter 1

Introduction

The descriptive equations of fluid dynamics are highly non-linear partial differential equations which allow analytical solutions in only the most specialized of cases. For most general flow scenarios, analytical development is not possible. As a result, up until about 20 years ago, the only way to obtain information about how a particular object would behave in a flow with particular characteristics was to actually build the object, place it in a wind tunnel and perform the experiment. With sophisticated non-intrusive diagnostics, gross properties of the flow such as drag and lift could be measured. With considerably more effort, information about the spatial dependence of some thermodynamic properties of the flow could be acquired.

With the advent of modern computers, it became possible, potentially, to do away with the cumbersome necessities of wind tunnel experimentation by simulating the equations of fluid behaviour numerically. Simulating fluid flow on computers in this manner is called Computational Fluid Dynamics (CFD). After

about 20 years of vigorous development[1], present day CFD calculations, when not rendered useless by unstable numerical algorithms, are severely constrained by the memory capacity and speed of available computing power[1, 2]. The volumetric resolution required in three dimensional fluids in order to simulate the small turbulent eddies needed to compute such practical quantities as the lift and drag of an airfoil are beyond the computational requirements presently available or even imagined today. For example, to simulate flow past an airfoil with a Reynolds number of about 1 million with the same accuracy as is now done in state of the art wind tunnels would require a simulation volume on the order of 10 trillion cells. A CRAY-2 supercomputer, working at a rate of 3×10^7 cell updates per second, would have to run continuously for over twenty thousand years to compute such a highly resolved flow[3, 4]. Put another way, at present, CFD methods can accurately simulate fluids in three dimensions, up to a Reynolds number of about 100 using about 1 million cells[3] which allows for full turbulence modelling to all scales. This corresponds to accurate simulation of flow around a car travelling at $\frac{4}{1000}$ kilometers per hour. For flows with very large Reynolds numbers, the effect of viscosity is limited to a thin layer near the solid surface, the so-called boundary layer. Outside of this layer, the flow is effectively inviscid. The width of the boundary layer scales with the inverse square root of the Reynolds number in this case[5]. For simulations of flows in this regime, it is possible to have the Reynolds number scale with the *square* of the number of sites in a linear dimension. This scaling improves the limit on Reynolds number in CFD simulation so that accurate simulation of flows around a car travelling at $\frac{1}{10}$ km/h is possible. This is obviously still VERY far from practical situations. Clearly, large improvements in algorithm reliability and almost unimaginable improvements in computing power are necessary if CFD is to become a general purpose alternative

to wind tunnel fluid experimentation.

In the last six years, *lattice gas algorithm* methods (LGA), motivated by the philosophical challenge of reducing physics to logic[6, 7, 8, 9], have been developed that provide a computational alternative to CFD. In the original development of the algorithm[11], abstract particles exist only at the vertices of a square lattice where time, space and direction has been discretized. All particles have the same speed and move along various links of the lattice from node to node. 'Speed' refers to the number of lattice sites a particle moves in one time step. At a particular node, particles are made to rearrange themselves (or collide with each other) in such a way that total particle number, momentum and energy (which is equal to mass in the single speed case) at a node remains constant consistent with the constraint that no more than one particle occupies a particular direction at a site per timestep. This is the exclusion principle of lattice gas algorithms. This simple system was observed to produce qualitatively correct macroscopic flow features in two dimensions using only logical operations for system updates.

Since then, a very general theory of these *single speed* lattice gases has been developed by several authors[12, 22] where an improved two-dimensional model[13] and a model that could be used to generate three-dimensional systems[14] has been proposed. The lattice gas algorithm should not be thought of as an oversimplified version of molecular dynamics[1] but rather as an discrete particle engine that obeys updating rules dictated by conservation requirements and lattice symmetries which results in qualitative behaviour similar to, but independent of, continuum fluid dynamics.

Nonetheless, existing lattice gases still have major limitations - *as models for*

[1]where the actual molecular characteristics of the fluid are specified[15]

real fluid dynamics. In 1991, in an introductory overview for a collection of state of the art lattice gas papers, Dr. J.P. Boon stated

> It should be stressed that contact between LGA simulations and laboratory experiments have been very scarce and quantitative comparison should be extremely valuable not only for the validation of the LGA method but also for an analytical understanding of the transitional regimes in the evolution towards turbulence. *J.P. Boon*[16]

In this thesis, we develop the general theory of *multiple* speed lattice gas algorithms and show how they can be made to accurately and efficiently model a true three-dimensional continuum fluid. We have found that although there are artifacts in the macroscopic behaviour of multiple-speed LGAs, these artifacts disappear *naturally* as higher speeds are added to the model. When a discrete continuum of infinite speeds has been added to the model, the lattice artifacts disappear completely leaving *only* the exact equations of continuum hydrodynamics. This behaviour is contingent on the underlying lattice having the structure known as the four-dimensional face-centred hypercube (4D FCHC), the simplest lattice that permits correct three-dimensional simulation[14] [2]. We have found that this lattice has the following key features: 1) It permits all integral energies to be represented, 2) The set of velocity vectors for each energy have sufficient symmetry to allow for an isotropic stress tensor at each energy *individually*, 3) All energies may interact via energy exchange collisions, and 4) Discrete microscopic Galilean invariance. All of these properties are required of the underlying lattice if we are to extend the LGA concept to infinite speeds. It is remarkable that a

[2]by projection from 4D down to 3D

lattice with all of these requirements exists. Moreover, we have found that the 4D FCHC is the *only* regular lattice with these properties.

The main theoretical advance, as outlined in this thesis, is the creation of a microdynamical system in which the lattice is entirely erased from the macroscopic dynamics for finite-speed systems. This amounts to forcing the artifacts to have the same values they would have in the continuum fluid for all times. This new system behaves as though it were a true continuum fluid without any artifacts of discretization. The lattice acts like an array of sampling points that do not contaminate the dynamics.

This fundamental advance is made possible by two main ingredients. First, particles with several speeds[29, 30, 33] are included so that energy becomes an independent degree of freedom. The structure of the underlying 4D FCHC lattice allows these particles of different speeds to exist independently on sufficiently symmetric sublattices while also allowing particles of different speeds to interact via energy exchange collisions. Secondly, we use different rates for forward and inverse processes[33] in the energy exchange collisions to introduce a new element of freedom into the algorithm. This variable rate coefficient can then be exploited to force the lattice artifacts to have the continuum values necessary for correct hydrodynamic behaviour. The validity of this method in removing the artifacts from the momentum equation at low-density, using a three-speed system, has already been demonstrated by Molvig *et al.*[35]. Here, we extend the theory by adding more rate coefficients so that all of the artifacts can be removed at arbitrary density.

In particular, we have developed a series of finite minimal-speed models that remove the lattice artifacts in stages with the highest-speed model — a five-speed

model — having the property that all artifacts are completely removed from the mass, momentum and energy equations. In essence, we have completely erased the effect of the underlying lattice — and with it its associated *discreteness artifacts* — from the dynamics of the lattice gas method. As a verification of the method, a computer code for the lattice gas model that completely removes all artifacts in the momentum equation [3] — a three speed model — was developed for the CRAY-2 supercomputer and several experimental tests were performed. These tests demonstrated that the artifacts had been removed and, as a result, *quantitatively* correct behaviour was demonstrated by the model when simulating standard fluid dynamics experiments such as Poiseuille flow (parabolic flow profile was developed in the mean with momentum lost down the length of the pipe being deposited to the walls) and flow past a circular cylinder (where the drag coefficient and length of characteristic downstream steady eddy length measurements agreed with experimental results within the experimental error, once the blockage effect in our simulations had been corrected for using a standard experimental technique, for the entire range of Reynolds numbers where this phenomenon occurs). An additional simulation demonstrates that the LGA model naturally allows vortex sheeding to occur, consistent with raising the Reynolds number above the threshold value of $Re \sim 45$. In contrast, the CFD results for similar simulations are either seriously in error (eddy length measurements) or rely on prior knowledge of the expected fluid behaviour to cause phenomena that would not occur naturally (vortex shedding).

Finally, because of the Boolean nature of the LGA algorithm, it is possible to devise massively parallel computer architectures[10, 75, 73] upon which the

[3]The LGA mass equation is identical to the continuity equation of continuum hydrodynamics

algorithm may be simulated. We show that the advantage in computing power of the LGA method over traditional floating point, finite-element, partial differential equations solvers is of such a fundamental nature that the LGA method requires about 1000 times fewer bit operations than the CFD method to update a similar size of fluid volume. Thus, the LGA method can simulate a volume about 1000 times larger than the CFD method *with similar computational power and effort* which permits a significant step towards the goal of accurate simulation of high Reynolds number hydrodynamic flows.

1.1 Comparison of LGA and CFD Theoretical Development

To describe the LGA method in broad terms, we compare conventional CFD simulation to the lattice gas approach, as illustrated in Figure 1.1. In both cases, we compare the path from the system we actually want to simulate - which is a real gas of particles that is not constrained in its phase-space motion in any way - to simulation output. Conventional CFD is based on the differential equations of fluid dynamics, the Navier-Stokes equations. These equations do not directly describe the actual real gas of particles but rather the mean dynamics of the mass, momentum and energy densities. The derivation of the Navier-Stokes equations from a real gas of molecules is a very complex piece of theoretical physics which is profound in the sense that it accounts for the development of irreversible thermodynamic behaviour from an underlying reversible microsystem. This development of physics was pioneered by Boltzmann about 150 years ago, and although considerable controversial debate ensued, the theory has been made rigorous to the

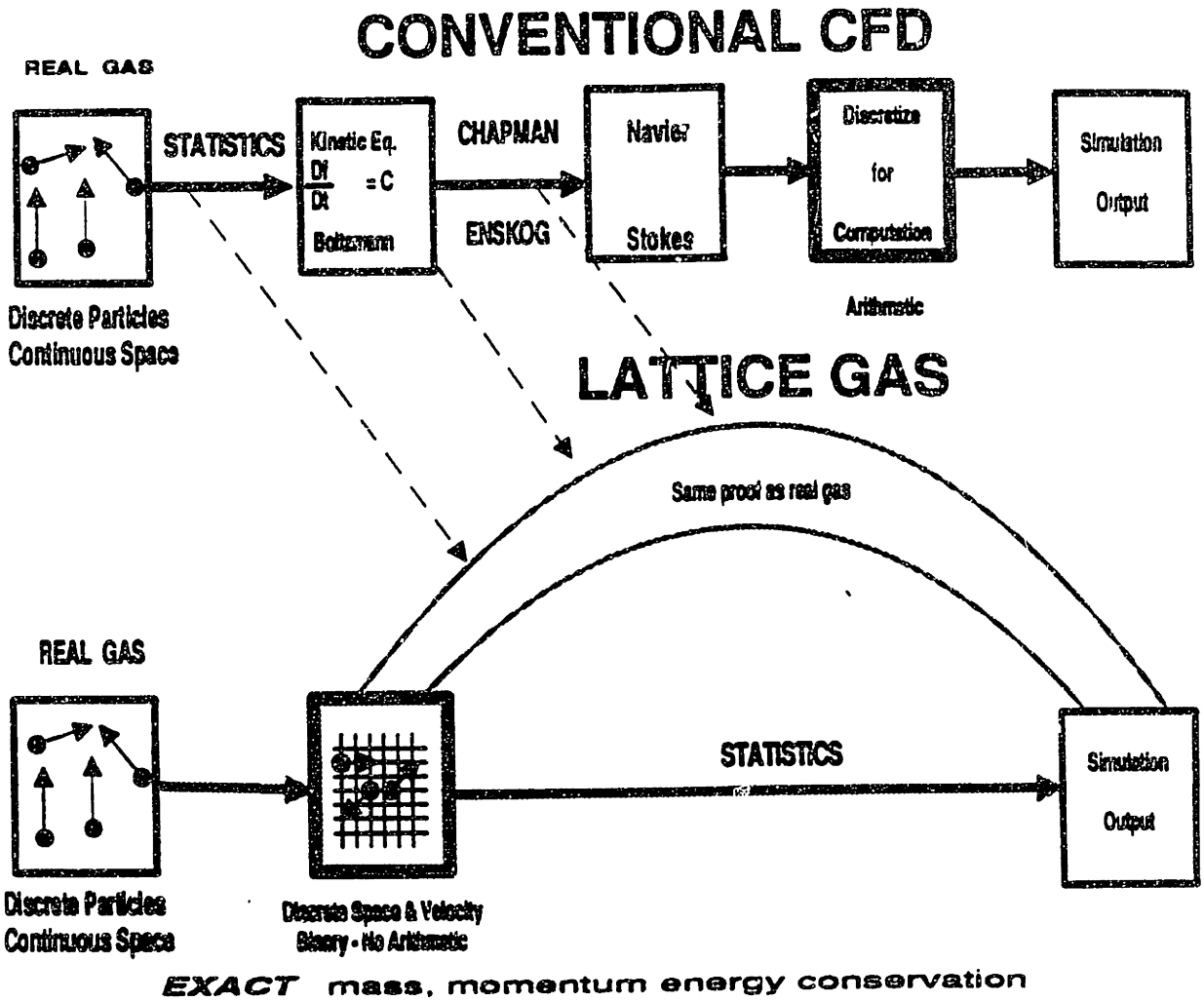

Figure 1.1: Comparison of conventional CFD and lattice gas simulation methods showing both simulation techniques evolution from real gas to simulation output.

point that it is now a cornerstone of statistical mechanics[31, 48]. This process requires statistical averaging of the discrete microsystem which leads to the kinetic equation of Boltzmann which is then expanded about its equilibrium solution to give the Navier-Stokes and energy equations.

Continuum differential equations cannot, of course, be solved on the inherently discrete medium of the computer. To make progress, these equations must be discretized by some sort of finite element approximation. Hardware implementation of floating point arithmetic has evolved to support this type of method. The numerical method of finding an adequate approximation to the Navier-Stokes equations has proved to be an extremely difficult one[51], as emphasized by the box for this step in Figure 1.1. This field is characterized by a diverse array of numerical instabilities and artifacts which often make it difficult to assess the accuracy of the simulation results. Nevertheless, since digital computers cannot fundamentally solve differential equations, something like this must be done and the result comes to us as the simulation output of the desired physical system.

By way of contrast, in the lattice gas method, the discretization necessary for computation occurs at the *microscopic* level. Beginning with the same real gas, we restrict the dynamics to a discrete space-time lattice such that particles can only reside at the lattice vertices at discrete time steps of the simulation. The lattice particles *are not* actual gas particles but can be considered large packets of individual gas particles lumped into a single *macroparticle*. Discretizing the system this way makes it possible to represent the microdynamical system of the lattice gas *exactly* with Boolean logic and to process it *exactly* on a digital computer. This system is very primitive; the microdynamics consist of a rectilinear particle movement between collisions (duplicated by moving bits on the lattice),

and collisions on the lattice sites that can also be processed in logic. Except for the discretized space-time domain, the lattice gas has dynamics identical to those of a real gas and mimics real gas behaviour in considerable detail, including the collisional generation of entropy and relaxation to a local thermodynamic equilibrium. These are the key attributes necessary to duplicate hydrodynamic behaviour[25]. In particular, the basic invariants that the Euler equations describe (mass, momentum, and energy) are conserved exactly by the lattice gas system at each site and for all times. It cannot possess numerical stabilities; in fact, the rapid generation of local entropy imbues the system with extraordinary - literally thermodynamic - dynamic stability.

The simulation is done on this microdynamical system with exact processing. The statistical accumulation of data to observe the hydrodynamic behaviour is done as a passive step, without impeding the continuing exact microdynamics. This statistical accumulation of information mimics precisely the theoretical development done on real gases to obtain the macroscopic equations. In this way, the hydrodynamic-like quantities of the lattice gas are measured.

There is an important difference, however. The discretized space-time simulation domain of the lattice gas does, in general, lead to observable consequences or *discreteness artifacts* at the macroscopic level. One can see the signature of the lattice macroscopically in much the same way that one can distinguish between a solid with a lattice structure and a fluid in the real world. For example, previous isotropic incompressible two-dimensional and three-dimensional single-speed lattice gas models yield, in the macroscopic limit, an Euler-like momentum equation of the form[14]:

$$\rho \frac{\partial \mathbf{u}}{\partial t} + \rho g(\rho)\mathbf{u} \cdot \nabla \mathbf{u} = -\nabla P_s, \tag{1.1}$$

where the pressure P_s is given by the equation of state for a lattice of dimension D

$$P_s = \frac{1}{2}\rho(1 - \frac{2}{D}u^2 g(\rho)), \tag{1.2}$$

and $g(\rho)$ is a known density dependent factor due to the lattice. This is the first of three *lattice artifacts* that become apparent in the general theory of lattice gas methods. The function $g(\rho)$ in front of the advective term of the momentum equation breaks the Galilean invariance found in real fluids; momentum is advected with velocity $g(\rho)\mathbf{u}$ instead of with the fluid velocity $\mathbf{u}$. Furthermore, the scalar pressure term contains an anomalous contribution proportional to the fluid kinetic energy, clearly an unphysical effect.

As previously mentioned, the main theoretical advance of this work is the creation of microdynamical system which results in the discreteness artifacts being removed from the macroscopic behaviour of the model. For example, by setting $g = 1$ in eqn. (1.1), we see that fluid is now advected with the correct velocity. For multiple-speed systems we will find that this condition also removes the dynamic pressure anomaly of eqn. (1.2). This new system behaves as though it were a true continuum fluid without any artifacts of discretization.

1.2 Outline of Analysis

In Chapter 2, we describe the physical model that is a lattice gas algorithm and demonstrate why the 4D FCHC lattice is the simplest lattice that will allow accurate simulation of three-dimensional fluids. Development of the microdynamical equations, which include explicitly the translation and collision operators for the model, follows. Rate coefficients for certain collision processes are introduced into

the microdynamics that will allow for later removal of the lattice artifacts. By ensemble averaging this equation, and using the Boltzmann approximation wherein all states are statistically independent of each other, we arrive at the kinetic equation for lattice gas algorithms. An equilibrium solution is derived and found to be of Fermi-Dirac rather than Maxwell-Boltzmann form.

In Chapter 3, the kinetic equation is expanded to first order in the Knudsen number and the Euler equations for a general multiple-speed LGA are derived. This derivation is accomplished by an expansion in the Mach number, subsidiary to the Knudsen number expansion. Expressions for the lattice artifacts in the three conservation equations are made explicit. We find that there are no artifacts in the mass equation, one artifact in the momentum equation, and two artifacts in the energy equation.

In Chapter 4, we examine the behaviour of lattice gas models with large numbers of speeds. We show that as the number of speeds becomes very large, the values of the artifacts converge towards the continuum values naturally (without the need for rate coefficients). In the limit of infinite speeds, we find that if the model is renormalized so that the distance between speeds becomes infinitesimally small, the artifacts become the continuum values *exactly*. It is not a simple matter to add higher speeds to a lattice gas algorithm. To do this requires some rather fortuitous properties of the 4D FCHC lattice that we demonstrate to exist. They are: 1) All integral energies are represented, 2) The set of velocity vectors for each energy have sufficient symmetry to allow for an isotropic stress tensor at each energy *individually*, and 3) All energies may interact via energy exchange collisions. Without these properties, the continuum limit on the lattice gas model could not be performed. The convergence of the lattice gas model to the continuum is shown

to scale linearly with the number of speeds added. We show that LGAs with a large number of speeds possess a form of discrete microscopic Galilean invariance that allows the lattice to be transformed by any lattice vector. Macroscopic equations derived from the transformed microdynamics result in lattice artifacts of the same form as derived in the stationary case, but they appear only as coefficients of velocities that are the difference between the actual fluid velocity and the closest lattice vector and so are inherently small terms. This transformation allows simulation of transonic simulations by lattice gas methods that have removed the lattice artifacts.

In Chapter 5, we find the minimal-speed lattice gas system that allows the artifacts to be removed using rate coefficients. We find that a three-speed model with one rate coefficient removes the g artifact from the momentum equation in arbitrary density systems. A four speed system with two rate coefficients is derived that either removes both the g artifact and the most significant artifact in the energy equation (related to the ratio of specific heats for the system) or reduces the errors in the two artifacts to insignificant levels ($< 1\%$). By performing an expansion in density, we show in principle that it is possible to remove all three artifacts. In the low density limit, we find that two of the artifacts collapse into one condition. We develop the complete description of the lowest speed model - the five speed model, with two rate coefficients - that can completely remove all three artifacts. The expressions for the rate coefficients are optimized so as to minimize their computational complexity to allow for ease in computer application.

In Chapter 6, we address the noise problems in lattice gas methods. We show that although the shot noise fluctuations in system properties from time-step to time-step are of the same order as the magnitudes of the properties themselves,

these large fluctuations do not effect the mean dynamics of the lattice gas model. Due to the Boolean nature of the lattice gas model, all terms that might appear nonlinearly in the collision operator can be reduced to linear terms. As a result, the collision operator is multi-linear. This means that shot noise does not contribute to second or higher order terms in the expansion of the collision operator about the mean, a result we call the *Shot Noise Theorem* for lattice gas methods. We demonstrate, by developing both an exact combinatorial and approximate theoretical calculation, that the magnitude of the remaining non-shot noise fluctuations scales inversely with lattice volume size. With a lattice volume of about one million sites, a typical value in our simulations, these remaining fluctuations are absolutely negligible in comparison with the mean dynamics. This justifies the Boltzmann approximation made in Chapter 2 to derive the kinetic equation as well as allowing us to conclude that if we remove the artifacts from the lattice gas method, then the correct hydrodynamic equations will be followed by the mean dynamics of the LGA despite fluctuations in local quantities that may leave the mean value submerged in noise.

In Chapter 7, we present our simulation results for the three-speed lattice gas model that removes the Galilean invariance artifact from the momentum equation. A brief description of the LGA code that has been developed to perform this task on the CRAY-2 supercomputer is presented. The simulation process is split into two sections, validation experiments and actual fluid flow experiments. The first set of simulation results demonstrates the validity of the method. In Section 7.2 we show, using a decaying shear wave experiment in an unbounded volume, that all artifacts in the momentum equation have been removed to within the level of statistical noise. The same experiment on a single-speed model clearly shows the expected anomalous behaviour. Since the model maintains a tight

thermodynamic equilibrium essentially down to the individual site level, accurate hydrodynamic behaviour is observed even for systems with perturbations as small as a few lattice sites in wavelength. The model also shows that the limit on low Mach number, $M \ll 1$, from theory is not necessary in practice as accurate hydrodynamic behaviour is observed for flows up to $M \sim .4$. In Section 7.3, for flow between two parallel plates - Poiseuille flow - we find that the expected parabolic profile is formed in the mean. We measure the viscosity of the fluid from both the momentum loss down the length of the pipe and from the momentum deposited to the walls. These two measurements agree with each other, and with the independent measurement of viscosity for a given density and temperature from the shear wave experiment, to within 1%. Finally, in Section 7.4, we present the results of flow past a cylinder for Reynolds numbers in the range $0 \leq Re \leq 65$. In the regime of attached eddies, $Re < 45$, our results for drag coefficient and eddy length measurement agrees with experimental results to within the experimental errors. In these results, we have employed the same relation for correcting for finite flow blockage that is used in actual wind tunnel experimentation. We show that CFD results are in error in this regime. The results for one flow where a vortex street is generated naturally by the model with $Re \simeq 65$ are shown. The Strouhal number for this flow is about 18% higher than what it should be, in comparison with zero-blockage fluid experiment results, due to blockage effects of the same magnitude in our experiment.

In Chapter 8, we compare the computational efficiency of the lattice gas model and present CFD models. We find that on computers that support 64-bit logical word operations, such as a CRAY, that the lattice gas requires about a tenth of the storage requirements of CFD while the two algorithms operate at essentially the same speed. We show that if the lattice gas method were employed on a computer

that had a processor specifically designed to perform the logical operations of the lattice collision operator, the same way the floating point processor on the CRAY is ideally suited to CFD needs, the LGA would then run about 100-1000 times as quickly as the CFD floating-point supported code.

In Chapter 9 we present our conclusions and recommendations for further work. Multiple-speed lattice gas methods can be used to accurately and efficiently simulate three-dimensional fluid dynamics behaviour. Since we have a fully developed model that removes the artifacts in both the momentum and energy equations, the next group of fluid experiments simulated should involve heat transfer.

Chapter 2

The Lattice Gas Algorithm

This chapter discusses the physical features needed to construct a lattice gas algorithm that can yield true fluid dynamics. This requires that the macroscopic behaviour of the lattice gas algorithm is described by the Navier-Stokes equations. Microdynamical equations for the evolution of the model as well as a formal expression for the dynamics (in binary arithmetic form) that describe all such systems are given. The microdynamical equations are then statistically averaged which allows us to develop the kinetic equation as well as the equilibrium distribution for this lattice gas model. The equilibrium distribution has Fermi-Dirac rather than the usual Maxwell-Boltzmann form. Details of specific implementations of lattice gas algorithms are discussed in Chapters 5 and 7 where the simulation results are presented.

2.1 The Physical Model

The general class of lattice gas algorithms that we are studying all have the following properties:

1. A population of particles that each have unit mass and may be categorized into species dependent on the speed of the particle. All particles within a species are identical and move the same number of lattice sites per time step - the particle 'speed'.

2. A totally discrete phase space (discrete values of position in all dimensions and discrete particle-velocity directions) and discrete time t. Discrete time means that the particles hop from site to site.

3. An underlying lattice on which the particles reside only at the vertices. There are many lattices to choose from but we will see that the four-dimensional lattice known as the face-centred hybercube (4D FCHC) is ideal.

4. A set of collision rules that allow collisions amongst particles of a particular species *and* amongst particles of differing species such that mass, momentum and energy (and no other property) are conserved. Particles interact with solid boundaries in a classical way (i.e. particles do not propagate through solid matter).

5. An exclusion principle so that at each vertex no two particles can have identical velocities. This limits the maximum number of particles of a given species at a vertex to the number of directions a particle with that speed can travel consistent with the structure of the underlying lattice.

The discrete nature of the microscopic behaviour of this system is quite different from that of a continuous Boltzmann gas where particles are free to move in any direction and have a continuous spectrum of speeds. The problem of finding an algorithm to do *true* hydrodynamics can be viewed as the problem of removing, from the macroscopic level, the consequences of the *discreteness* in the underlying dynamical system. Once the discreteness effects have been removed the finding of hydrodynamic behavior is in a sense obvious, since the microdynamical system conserves mass, energy and momentum.

The five principal artifacts of discreteness are:

1. non-isotropy of the stress tensor
2. Momentum non Galilean-invariance
3. dynamic pressure anomaly
4. Specific Heats ratio artifact
5. Energy non Galilean-invariance.

That certain lattices do in fact give an isotropic stress – the original discovery that gave much of the impetus to present lattice gas work – is by now well known [14]. With an appropriate lattice and a specific realization of the lattice gas algorithm described above, correct qualitative behaviour of real fluids has been reproduced (see Lim[17] and d'Humières et al.[18] who have separately collected the results from over 30 published experiments into two summary articles). The presence of the other four artifacts prevent correct quantitative results, however. Recently, Molvig, et.al. [35] have shown how the second two artifacts can be simultaneously removed by appropriately introducing an energy degree of freedom. The last two

artifacts are new, a result of an examination of the independent energy transport equation that results for multiple speed lattice gas models. Chapter 3 presents the derivation of expressions for all of the remaining artifacts while Chapter 5 describes how they may be removed.

The key new feature is the treatment of the energy degree of freedom. One must devise interactions that conserve mass, energy and momentum, which induce energy exchange or transitions among the energy states, while residing on the appropriate lattice. If we imagine a two-dimensional square lattice where there are stopped particles, particles that move along the links of the lattice (north, south, west and east) and particles that move diagonally, one example [11] of how an energy exchange collision can occur is illustrated in Figure 2.1 along with its inverse process[29]. Note that the vector lengths for the square lattice ensure that energy and momentum are conserved for interacting particles with equal masses. Algorithms that do not allow particles of multiple speeds cannot have energy exchange collisions and, as a consequence, may have a spurious momentum invariant [11] and cannot remove the other two momentum discreteness artifacts.

2.2 Choice of an Underlying Lattice

In the last section we indicated that the lattice must have a sufficient degree of symmetry to ensure that the stress tensor is isotropic *and* that its structure permits the existence and interaction of particles with different speeds. The stress tensor indicates the way the macroscopic fluid responds to shear stresses. A true fluid can react to a shear stress by moving equally freely in all directions which is what we mean by an isotropic stress tensor. We will quantify these requirements in

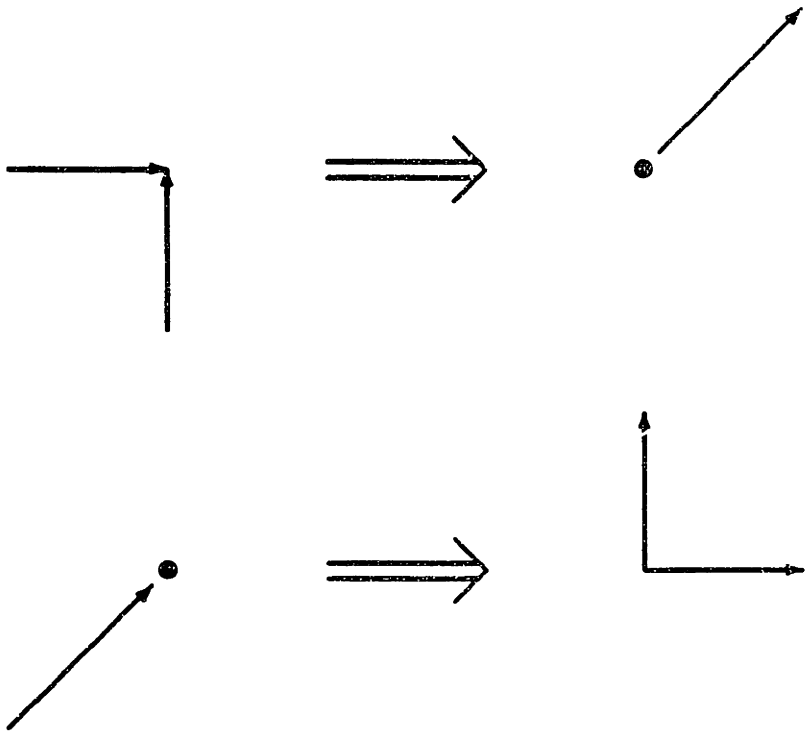

Figure 2.1: Example of energy exchanging interactions among particles. The lower event is termed the forward process while the upper one is the inverse process.

Chapter 3 but for now we will let these qualitative requirements guide us in the choice of a lattice.

The first fully deterministic lattice gas model with discrete time, positions, and velocities was introduced by Hardy, de Pazzis and Pomeau[11], a model now known as HPP. By a *deterministic* model we mean that specifying the intial distribution of particles on the lattice is enough to determine the later particle distribution at any time. In a deterministic model, there is only one possible output of a collision for a given input. The HPP model was a single speed deterministic model on a square two- dimensional lattice. Particles 'collided' when two particles entered

a lattice site head-on, resulting in a rotation 90 degrees. if the other two sites were empty. This procedure conserved mass and momentum (energy conservation is indistinguishable from mass conservation for single speed models) locally but also conserved momentum along each vertical and horizontal line, a set of spurious invariants. This, coupled with the fact that this lattice does not have the requisite symmetry for istotropic macroscopic flow, required that a different lattice be found if realistic fluid dynamics was to be simulated.

In 1986 a lattice model introduced by Frisch, Hasslacher, and Pomeau[13] removed the spurious invariants of the HPP model and had the required symmetry to allow qualitatively accurate fluid dynamics simulation for the first time. This model is also two-dimensional but is based on a hexagonal lattice rather than a square one. Particles, which all have the same speed, may move in any one of six directions defined by the lattice. Particles arriving at a site head-on collide, but now the outcome may be non-deterministic as the result may be a rotation of 60 degrees to the left *or* to the right. These head-on collisions conserve, in addition to mass and momentum, the difference of particle numbers in any pair of opposite directions on the lattice. To remove this spurious invariant, triple collisions or the addition of a zero-velocity 'rest-particle' was added to the model. These additions coupled with the possibility of a non-deterministic model allowed for experimentation with many different FHP models (e.g. see [12],[19],[20] or [21]) but there was still a major flaw with the model which prevented detailed comparison with true fluid flow results. Since the flow was still not Galilean invariant, velocity profiles of the lattice model became distorted once the mean velocity of the flow exceeded a critical value[24] and furthermore, the equation of state was dependent on this velocity, an unphysical feature that causes the dynamical pressure anomaly[25] mentioned as the third artifact above.

The originators of the FHP model[13] then began looking for a lattice that could be used to simulate fully three-dimensional fluid flow. Wolfram[22] had already shown that three dimensional regular lattices do not have enough symmetry to ensure macroscopic isotropy. A suitable four-dimensional model with requisite symmetry properties was introduced by d'Humiéres, Lallemand, and Frisch[29]. This lattice is face-centred hypercubic (FCHC), defined as the set of signed integers (x_1, x_2, x_3, x_4) such that $(x_1+x_2+x_3+x_4)$ is even. Each node is connected by links of length $c_1 = \sqrt{2}$ to 24 nearest neighbors, having two coordinates differing by an integer. The theory for single speed lattice gas systems on the 4D FCHC lattice has been developed in considerable generality by Frisch, et al.[14]. We will use their notation and formalism to extend the theory to multi-speed systems in this and remaining Chapters.

Three dimensional fluids reside in the projection of the FCHC lattice to three dimensions as shown in Figure (2.2). Note that the lattice sites of the fluid form an ordinary cubic lattice with unit lattice constant. Such a model may be thought of as a pseudo four-dimensional model[29] where there is unit perodicity, and hence no macroscopic structure, in the x_4 direction.

The nearest neighborhood of the FCHC lattice is thus described by the 24 displacement vectors obtained from the six permutations of $(\pm 1, \pm 1, 0, 0)$. A particle with one of these velocities has energy=1 (one-half times the mass of the particle times the magnitude of the velocity vector squared where the mass is unity) and has the lowest energy a moving particle may have. In the three-dimensional projection, as shown in Figure (2.2), twelve of these vectors do not have a fourth dimension component and can be thought of as moving diagonally in one of three planes of the cubic lattice. The other twelve vectors that do have a

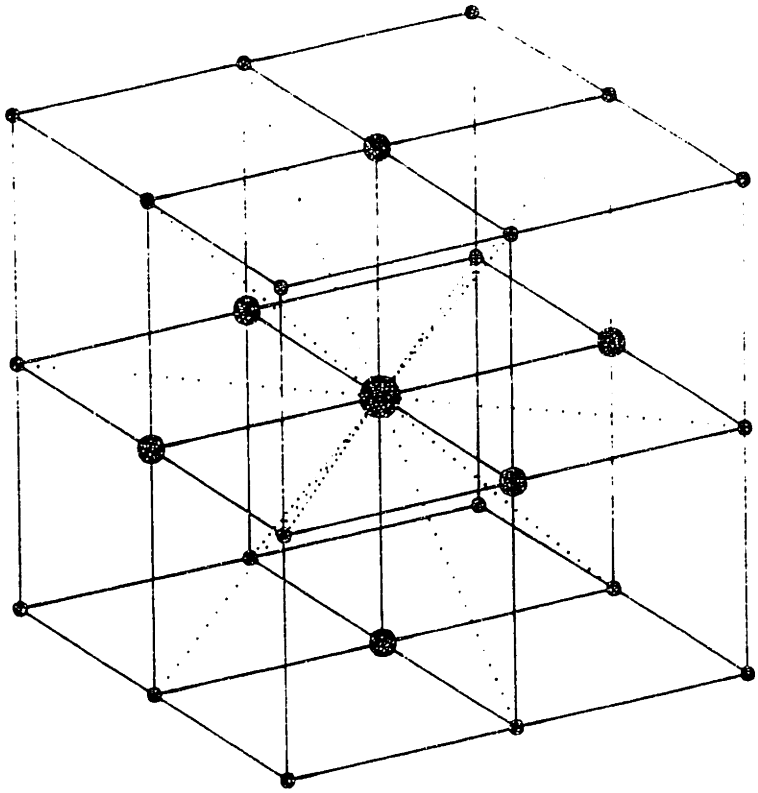

Figure 2.2: The 4D FCHC lattice projected to 3 dimensions. The neighborhood of one node is shown, displaying the links to nearest neighbors in the FCHC, 4D sense. Dotted lines indicate single links of the FCHC system with no displacement in the 4th dimension. Solid lines indicate links where up to two particles may propagate with 4-dimensional displacements of ± 1.

fourth-order component travel along one of the links of the cubic lattice. Up to two particles may occupy any one of these links in the three-dimensional projection but are differentiated in the fourth-dimension by the value of x_4 which is either ± 1. Higher order velocities, which can be expressed as a linear combination of some subset of these 24 'basis' vectors, also can be projected to the three dimensional lattice in the same way. Propagation and collisions proceed in this model as if a full 4D lattice was being used. Collision rules should conserve mass. all four components of momentum separately, and energy while avoiding spurious conservations. We denote the particle species or energy with the integer j index and a particular direction within a species with i. Thus the vector (j, i) indexes

the complete state space. In the formal developments that follow, we sometimes use the notation, $\mathbf{j} = (j, i)$ for this state vector. The unit energy particles have a velocity spectrum consisting of the 24 nearest neighbor vectors of the FCHC lattice, denoted $\mathbf{c_1} = \mathbf{c}_{1,i}$.

Next-nearest neighbors are reached by the displacements, $(\pm 2.0, 0, 0)$, and its four permutations, which form on hyperoctaedron (HO) and the 16 vectors $(\pm 1, \pm 1, \pm 1, \pm 1)$, which form a hypercube (HC). The union of the HO and HC gives the generic FCHC polytope[22]. In other words, the next-nearest neighbor sublattice also has the FCHC geometry. This feature is essential to the viability of the model, because it guarantees the needed isotropy of the fourth order tensors[13] for each particle type separately. The 24 velocity vectors of the type 2 particles are denoted $\mathbf{c_2} = \mathbf{c}_{2,i}$.

Next-next nearest neighors and so on may be discerned in a similar way. The number of displacements for a particular energy is equal to the number of velocity vectors (including permutations) that have the appropriate energy. Finally, we have zero-velocity rest particles that take part in energy exchange collisions. The number of rest particles per site is determined by the specific nature of the model. This relationship will be discussed in Chapter 5.

We have indicated that there are two types of collisions; collisions that occur within a particle species where all before and after collision particles have the same energy, and energy exchange collisions where the collision process alters the number of particles per species while still maintaing local conservation laws. The underlying lattice causes a major conceptual difference between the two types of collisions. Like-particle collisions result in the set of incoming particles being simply rotated about the net momentum vector into one of the other planes of

the FCHC lattice. These like particle collisions correspond to isometries of the underlying lattice [40]. Maintaining the lattice symmetry, dynamically, requires that such processes have identical rates for forward and inverse processes. Such a situation is called *detailed balance.*

In contrast, the energy exchange interaction is not related to any symmetry of the lattice. This means that it is possible (and as we will find later *necessary* to achieve true fluid dynamical behavior) to have the forward and inverse processes proceed at different rates. Variable rate coefficients are easily implemented in a lattice gas by utilizing a binary mask [35] whose density on the lattice is equal to the rate coefficient. Differing forward and inverse rates imply violation of detailed balance, of course. In fact, such an interaction does not even obey *semi-detailed balance*, a weaker condition thought [14] to be necessary to the proof of an H-theorem for the system. In spite of this, it turns out detailed balance can be recovered, after a kind of Boolean renormalization, for the interaction of quasi particles and quasi holes, leading to an H-theorem that guarantees the modified Fermi-Dirac distributions in equilibrium needed to provide true fluid dynamical behavior. This piece of theory is presented in the following section.

Finding similar energy exchanging interactions among equal mass particles in the other low lying *integer* energy states is not so simple. The constraint of the lattice and of integer values for energy and momentum severely restricts the possibilities for such interactions. It is indeed fortuitous that the FCHC lattice required for 3D isotropy allows the energy exchange collisions needed for thermalization to occur for the lowest energy states in the simple binary form illustrated above.

In fact, the 4D FCHC lattice has all the properties we would ever require, for,

as is shown in Chapter 4, not only can this lattice represent all integer values of energy, but the set of velocity vectors for each energy satisfy the symmetry requirements *individually* and collisions between all energy species are permitted. For these reasons, the 4D FCHC lattice is the underlying lattice on which we have chosen to conduct our multi-speed lattice gas experiments.

2.3 Microdynamical Equations

In this section we develop a set of microdynamical equations that describe the evolution of the lattice gas algorithm. The algorithm is constructed by attaching a *Boolean field*, $n_{\mathbf{j}}(t_*, \mathbf{r}_*)$, to each node $\mathbf{r}_*$ of the lattice at time t_*. The number of bits per lattice site, b, is equal to the number of different elements in the state vector, $\mathbf{j} = (j, i)$. Updating of the Boolean field in time consists of a propagation step,

$$n_{ji}(t_*, \mathbf{r}_*) \rightarrow n_{ji}(t_* + 1, \mathbf{r}_* + \mathbf{c}_{ji}) \tag{2.1}$$

followed by a collision step inducing a rearrangement of the b-bits on each lattice site. A possible state of the lattice site is given by the b-element vector s where

$$s = \{s_{\mathbf{j}} = 0 \quad \text{or} \quad 1, \mathbf{j} = 1, \ldots, b\} \tag{2.2}$$

and each element is 0 or 1 depending on whether a particle occupies that position in state-space or not. Thus there are 2^b possible states at each node. Following Frisch, et. al. [14] we describe a collision by a nondeterministic transition rule from an in-state $s = \{s_{\mathbf{j}}\}$ to an out-state $s' = \{s'_{\mathbf{j}}\}$, which has an assigned probability $A(s \rightarrow s') \geq 0$ of occurring. This probability must sum to unity over all out-states

$$\sum_{s'} A(s \rightarrow s') = 1 \tag{2.3}$$

and is dependent only on the lattice states, s and s', and not the lattice node.

The collisions will be constructed to conserve mass, energy and momentum, and assumed to be sufficiently complex to eliminate any spurious invariants. Invariance of the transition probability under all the isometries of the FCHC lattice is also assumed[14]. The transition probabilites may either obey the conditions of detailed balance

$$A(s \rightarrow s') = A(s' \rightarrow s), \quad \forall s, s' \tag{2.4}$$

which indicates equal rates of forward and backward collision processes between all pair combinations of states, or that of semi-detailed balance

$$\sum_{s} A(s \rightarrow s') = \sum_{s'} A(s \rightarrow s') = 1, \quad \forall s' \tag{2.5}$$

which states that if, before a collision, all states have equal probabilities, they stay so after collision, or they may obey neither of the two. The semi-detailed balance condition is trivially satisfied when the collision rule is deterministic and one-to-one. The nondeterministic nature of our algorithm does not obey this condition in this form. This is an important and necessary departure from previous work.

Apart from this important property, and the larger state space, the formalism is identical to that introduced by Frisch, et. al. [14]. The complete update rule is consequently formally identical. A Boolean function, $\xi_{ss'}$, implementing transitions between any pair of states, s and s', is introduced. The function, $\xi_{ss'}$, is effectively the lookup table of some computer implementation. Its ensemble average[31] is the transition probability discussed above,

$$\langle \xi_{ss'} \rangle = A(s \rightarrow s'), \quad \forall s, s' \tag{2.6}$$

and,

$$\sum_{s'} \xi_{ss'} = 1 \quad \forall s. \tag{2.7}$$

Since the ξ's are Boolean, this equation indicates that for a given s, $\xi_{ss'} = 0$ for all s' except one. Thus, for a given in-state s and realization of $\xi_{ss'}$, only one out-state s' is possible. We may now postulate a form of the microdynamical update rule,

$$n_{\mathbf{j}}(t_n + 1, \mathbf{r}_n + \mathbf{c}_{\mathbf{j}}) = n_{\mathbf{j}} + \Delta_{\mathbf{j}}(n_{\mathbf{j}}) \tag{2.8}$$

where $\Delta_{\mathbf{j}}(n_{\mathbf{j}})$ is the collision operator for the system. We wish to find an exact, explicit form for this function. The Boolean field $n_{\mathbf{j}}(t_n, \mathbf{r}_n)$ is also a series of b Boolean values which matches up with only one of all of the possible input states s. An identity for $n_{\mathbf{j}}$ is

$$n_{\mathbf{j}} = \sum_{s}(s_{\mathbf{j}}) \prod_{\mathbf{j}'} n_{\mathbf{j}'}^{s_{\mathbf{j}'}} (1 - n_{\mathbf{j}'})^{(1-s_{\mathbf{j}'})} \sum_{s'} \xi_{ss'}. \tag{2.9}$$

The function of the first sum over s is to cycle through all possible in-states, one of which will correspond to $n_{\mathbf{j}}$. Given a s, the product term compares all the Boolean elements of s with n and has the value 1 if *all* the elements of the two vectors are identical and zero otherwise. The identity $0^0 \equiv 1$ is used. The third sum has the value 1 and was tacked on for convenience. Similarly, if we use the fact that $\xi_{ss'}$ is non-zero for only one s' given s, we have an expression for the updated field

$$n_{\mathbf{j}}(t_n + 1, \mathbf{r}_n + \mathbf{c}_{\mathbf{j}}) = \sum_{s,s'} s'_{\mathbf{j}} \xi_{ss'} \prod_{\mathbf{j}'} n_{\mathbf{j}'}^{s_{\mathbf{j}'}} (1 - n_{\mathbf{j}'})^{(1-s_{\mathbf{j}'})}. \tag{2.10}$$

We sum over s until the product is non-zero. This means that the correct input state has been found. The factor $\xi_{ss'}$ ensures that we select the correct output state when summing over s' once the correct s has been found. If we combine the s and s' sums in eqn. (2.9) and then solve for the collision operator $\Delta_{\mathbf{j}}(n_{\mathbf{j}})$ in eqn. (2.8) plugging in from eqns. (2.9) and (2.10) we find

$$\Delta_{\mathbf{j}}(n_{\mathbf{j}}) = \sum_{s,s'} (s'_{\mathbf{j}} - s_{\mathbf{j}}) \xi_{ss'} \prod_{\mathbf{j}'} n_{\mathbf{j}'}^{s_{\mathbf{j}'}} (1 - n_{\mathbf{j}'})^{(1-s_{\mathbf{j}'})} \tag{2.11}$$

the explicit form we desired.

2.3.1 Conservation Laws

The collision function, Δ_j, is constructed so as to yield the conservation laws for mass, momentum, and energy. The mass conservation law,

$$\sum_{ji} m_j \Delta_{ji}(n_{ji}) = 0 \quad \forall n_{ji} \tag{2.12}$$

can be replaced by the moment of unity for the equal mass spectrum of the general b-bit model. Of course, particle number is not conserved for each particle type. Momentum conservation is

$$\sum_{ji} m_j \mathbf{c}_{ji} \Delta_{ji}(n_{ji}) = 0 \quad \forall n_{ji}. \tag{2.13}$$

The energy conservation law, unlike solitary speed models[14], is now different from mass conservation,

$$\sum_{ji} \tfrac{1}{2} m_j c_j^2 \Delta_{ji}(n_{ji}) = 0 \quad \forall n_{ji} \tag{2.14}$$

2.3.2 Recovering Detailed Balance for Quasi-Particles

It is desirable that the collision transition probabilities obey either detailed or semi-detailed balance in order to guarantee that an equilibrium exists due to the creation of an H-Theorem[31] for this system. In Section 2.2, we stated that collisions within a energy species obey detailed balance but that the need to have a variable rate for the energy exchange collisions required the abandonment of the balance conditions. We can recover a form of detailed balance for our class of models by absorbing the rate coefficient mask fields into the particle fields to form

a kind of quasi-particle for which the collision function will obey detailed balance. The theory allows any particle species to be renormalized in this manner.

First we simply rewrite the collision function by using the definition of the *Boolean hole* field, $\bar{n}_{ji} \equiv 1 - n_{ji}$,

$$\Delta_j(n_j) = \sum_{s,s'}(s'_j - s_j)\xi_{ss'} \prod_{j'} n_{j'}^{s_{j'}} \bar{n}_{j'}^{(1-s_{j'})}. \tag{2.15}$$

Now let $F^j_{ss'}$ be the Boolean mask whose statistical or ensemble average determines the rate of the forward process in a collision, $\langle F^j_{ss'} \rangle = F^j$, dependent only on the existence of particles of species j, and not on the details of the state. Similarly, let $I^j_{ss'}$ be the Boolean mask whose statistical average determines the rate of the inverse process. For example, if we have a three-speed system (energies 0,1 and 2) that undergoes energy exchange collisions as depicted in Figure 2.1, the equilibration condition for the energy exchange process on a specific two-dimensional plane of the FCHC lattice can be written,

$$F^0 n_0 n_{2i} \bar{n}_{1i} \bar{n}_{1i+1} = I^0 n_{1i} n_{1i+1} \bar{n}_0 \bar{n}_{2i} \tag{2.16}$$

where i and $i+1$ indicate directions that differ by 90 degrees. This equation indicates the Boolean nature of the model. For a forward process to occur, there must be a rest particle and a type 2 particle *and* two adjacent type 1 holes that the incoming particles can collide into. The inverse process has the opposite requirements. Equilibrium is reached when the rate of forward reaction is balanced by the inverse rate. For this case, we can associate the renormaliztion solely with the rest particles.

In the formal expression for the collision function, equation (2.11), these masks are part of the Boolean transition function, $\xi_{ss'}$, for the complete transition and

are not denoted explicitly. Note, however, that the energy exchange collisions always require the presence of a rest particle or rest hole, and therefore, the rate mask factors will only appear when rest particles and holes appear as non zero factors in the state product $\prod_{j'} n_{j'}^{s_{j'}}(1-n_{j'})^{(1-s_{j'})}$. Thus by defining the quasi-rest particle field,

$$\eta_0 \equiv F^0 n_0 \tag{2.17}$$

and quasi-rest hole field,

$$\bar{\eta}_0 \equiv I^0 \bar{n}_0 \tag{2.18}$$

we can extract the rate masks from the transition function and put them with the state product, now as part of the quasi particle density. This renormalization is trivially generalized

$$\eta_{ji} \equiv F^j n_{ji} \tag{2.19}$$

and quasi-rest hole field,

$$\bar{\eta}_{ji} \equiv I^j \bar{n}_{ji} \tag{2.20}$$

so that other processes may be rate controlled with direction independent masks that become part of the moving quasi particles. The collision function can now be written in terms of the quasi-particle fields,

$$\Delta_j = \sum_{s,s'}(s'_j - s_j)\xi'_{ss'} \prod_{j'} \eta_{j'}^{s_{j'}} \bar{\eta}_{j'}^{(1-s_{j'})} \tag{2.21}$$

where the function, $\xi'_{ss'}$, now leads to a transition probability, when ensemble averaged,

$$A'(s \rightarrow s') = \langle \xi'_{ss'} \rangle \tag{2.22}$$

that obeys the *detailed balance* condition,

$$A'(s \rightarrow s') = A'(s' \rightarrow s) \tag{2.23}$$

because for the quasi-particles and quasi-holes the forward and backward rates of *all* collisions are now equal. Since it is now the case that $\bar{\eta}_{ji} \neq 1 - \eta_{ji}$ we speak of quasi-particles and quasi-holes separately. In the next section we show that these equations assure that a thermal equilibrium exists and that it has Fermi-Dirac form.

2.4 The Kinetic Equation

The kinetic equation is obtained from the microdynamical equation (2.8) by statistical averaging and employing some assumptions about the correlations arising because of the nonlinearity in the microdynamics. For dilute gases, one usually assumes the Boltzmann approximation, wherein the probabilities for the different states in the in-state are independent and the statistical average of a product factors to the product of averages. In Chapter 6 we prove the validity of this assumption for the lattice gas models we are studying in the form of a *Shot Noise Theorem*. The result hinges on the absence of self-correlation effects from all lattice models and the negligible effect of non self-correlation terms in models of moderate size that obey detailed balance. Hence we will apply the Boltzmann postulate of equal *a priori* probabilities for all microscopic states that have the same macroscopic state for a system in thermal equilibrium. In standard Statistical Mechanics parlance[31], this means that in thermodynamic equilibrium the system under consideration is a member of a microcanonical ensemble. When we ensemble average some property of the system, we take the value of this property for every member of the ensemble and then normalize by the size of the ensemble. It is in this way that we can calculate continuous and ultimately macroscopic

properties of our microscopically discrete system.

Thus we define the average number of particles in state, $\mathbf{j} = (j, i)$, from the ensemble average as

$$N_{ji} = \langle n_{ji} \rangle \tag{2.24}$$

The average hole density is then,

$$\bar{N}_{ji} = \langle \bar{n}_{ji} \rangle = 1 - \langle n_{ji} \rangle. \tag{2.25}$$

Similarly, the average quasi-particle density is,

$$\mathcal{N}_{ji} = \langle \eta_{ji} \rangle = \langle F^j \rangle N_{ji} \tag{2.26}$$

while the quasi-hole density is,

$$\bar{\mathcal{N}}_{ji} = \langle \bar{\eta}_{ji} \rangle = \langle I^j \rangle \bar{N}_{ji}. \tag{2.27}$$

The rate factors were extracted from the transition matrix $\xi_{ss'}$ which indicates when a transition from state s to state s' is allowed. It is statistically independent of the $n_{\mathbf{j}}$. Thus, the ensemble average of a quasi-particle or hole is equal to the product of the average of the mask and appropriate density separately.

The kinetic equation is obtained by averaging the microdynamical update rule (2.8), using either equation (2.11) or (2.21) for the collision function and employing the Boltzmann assumption. The average collision function, or *collision operator* $C_{ji} \equiv \langle \Delta_{ji} \rangle$, can then be written in either of the two forms. In terms of the particle densities,

$$C_{\mathbf{j}}(n_{\mathbf{j}}) = \sum_{s,s'} (s'_{\mathbf{j}} - s_{\mathbf{j}}) A(s \rightarrow s') \prod_{\mathbf{j}'} N_{\mathbf{j}'}^{s_{\mathbf{j}'}} (1 - N_{\mathbf{j}'})^{(1-s_{\mathbf{j}'})} \tag{2.28}$$

or in terms of the quasi-particle densities,

$$C_{\mathbf{j}}(\mathcal{N}_{\mathbf{j}}) = \sum_{s,s'} (s'_{\mathbf{j}} - s_{\mathbf{j}}) A(s \rightarrow s') \prod_{\mathbf{j}'} \mathcal{N}_{\mathbf{j}'}^{s_{\mathbf{j}'}} \bar{\mathcal{N}}_{\mathbf{j}'}^{(1-s_{\mathbf{j}'})} \tag{2.29}$$

The collision operator vanishes when it operates on the particle distributions that correspond to thermal equilibrium. In this state, there is no net effect of the collision process on the system dynamics. In Frisch, et al. [14], an equilibrium solution for a single speed lattice gas system that obeys semi-detailed balance was found based on a series of provable lemmas. It is possible to generalize their lemmas to our multi-speed model that obeys detailed balance to obtain the following

Lemma 1 *The following statements are equivalent:*

- *The N_{ji} 's are a solution of the set of equations*

$$C_{\mathbf{j}}(n_{\mathbf{j}}) = \sum_{s,s'}(s'_{\mathbf{j}} - s_{\mathbf{j}})A(s \to s')\prod_{\mathbf{j}'} N_{\mathbf{j}'}^{s_{\mathbf{j}'}}(1 - N_{\mathbf{j}'})^{(1-s_{\mathbf{j}'})} = 0 \quad \forall \mathbf{j} \tag{2.30}$$

- *The N_{ji} 's are given by a generalized Fermi-Dirac distribution*

$$N_{ji} = \frac{r_j}{r_j + exp(\alpha m_j + \gamma m_j \mathbf{c}_{ji} \cdot \mathbf{u} + \beta \epsilon_j)} \tag{2.31}$$

where $r_j \equiv \langle I^j \rangle / \langle F^j \rangle$, is the rate coefficient factor, α, γ, β are arbitrary real numbers, and $\mathbf{u}$, is an arbitrary D-dimensional vector which we will take as the fluid velocity. The quantities, m_j, $\mathbf{c}_{ji}$, and $\epsilon_j = \frac{1}{2}m_j c_j^2$, are the microscopic mass, velocity and energy, respectively.

The lemma of Frisch, et.al. [14] applies by replacing the densities by quasi-densities. The proof is given in detail in Appendix A. The lattice gas model obtains a Fermi-Dirac distribution at equilibrium because of the built-in exclusion principle, not more than one particle may occupy a particular position in state space at a particular time.

To develop transport theory, or hydrodynamics, the difference equation (2.8) must be converted to a differential equation. This is done by first ensemble averaging the entire update equation and then Taylor expanding the displacement operator for slowly varying space and time scales. In the lattice model, the unit length is the lattice spacing while the unit time is the time required to traverse the lattice spacing. Because there may be many particles (with different velocities) occupying a lattice site, the probability of a collision occuring at any site is very high. This translates into a short free mean path of order the lattice spacing which means that the unit time is of order the collision time and particle microvelocities. c_j, are of order the sound speed. Thus the expansion of the ensemble averaged microdynamical equation is actually an expansion in the Knudsen number, $\kappa \sim \lambda/L$, where λ is the mean free path and L is a typical macroscopic scale length. This is the same expansion parameter used to develop the transport equations of hydrodynamics. As is standard with such expansions[31], all the transport effects are contained in the terms through $\mathcal{O}(\kappa^2)$ where the zeroth order gives the equilibrium distribution, first order gives the Euler equations and the second order gives the Navier-Stokes equation. Through this order the kinetic equation becomes,

$$\frac{\partial}{\partial t}N_{ji} + \nabla \cdot \mathbf{c}_{ji}N_{ji} + \frac{1}{2}\nabla\nabla : \mathbf{c}_{ji}\mathbf{c}_{ji}N_{ji} + \frac{1}{2}\frac{\partial^2}{\partial t^2}N_{ji} + \frac{\partial}{\partial t}\left(\nabla \cdot \mathbf{c}_{ji}N_{ji}\right) = C_{ji}. \quad (2.32)$$

We have already calculated the equilibrium distribution for this lattice gas system, eqn. (2.31). In the next Chapter, we develop the Euler equations.

Chapter 3

Euler Equations for the Lattice Gas

The Euler equations are the hydrodynamic equations describing the conservation of mass, momentum, and energy, in the limit when the transport coefficients (diffusivity, viscosity, thermal conductivity, etc.) are negligible. They arise formally from moments of the kinetic equation for kinetic distribution functions in local thermal equilibrium (when perturbations to the local equilibrium proportional to the spatial gradients are neglected as small)[31].

In this Chapter we develop the Euler equations for the multi-speed lattice gas model. When we compare these equations with the hydrodynamic equations, we find that the form of the lattice equations are correct but there are a few scalar coefficients that are different from the continuum equations. In the three conservation equations, these discrepancies can be summarized into three different terms or *lattice artifacts.* Deriving these artifacts is the purpose of the current

Chapter while showing how they may be removed (made to equal the continuum values) is the subject of Chapters 4 and 5.

In order that we may illustrate the method of calculation of the Euler equations as well as present the hydrodynamic results, we will sketch the calculation of the continuum Euler equations as described in any book on Statistical Mechanics (e.g. Huang[31]).

In the continuum, the microscopic distribution function is a continuous function of space, velocity and time, usually denoted $f(\mathbf{x}, \mathbf{v}, t)$ where $\mathbf{x}$ and $\mathbf{v}$ are D-dimensional vectors corresponding to the D dimensions of the volume. This function obeys the kinetic equation

$$\frac{\partial}{\partial t} f(\mathbf{x}, \mathbf{v}, t) + \nabla \cdot \mathbf{v} f(\mathbf{x}, \mathbf{v}, t) = C(f, f) \tag{3.1}$$

where $C(f, f)$ is the non-linear Boltzmann collision operator. If we multiply this function by any one of the mass, momentum or energy of the microscopic particles and then integrate over velocity we get a vanishing result since these three propertites must be conserved by the collision function

$$\int d^D v \begin{bmatrix} m \\ m\mathbf{v} \\ \frac{1}{2} m v^2 \end{bmatrix} C(f, f) = 0. \tag{3.2}$$

These are the only moments that cause this to happen. Thus, the mass, momentum and energy moments of the kinetic equation can be summarized in the general form

$$\frac{\partial}{\partial t} q(\mathbf{x}, t) + \nabla \cdot \Gamma_q = 0 \tag{3.3}$$

where

$$q(\mathbf{x}, t) = \int d^D v \, q(\mathbf{v}) f(\mathbf{x}, \mathbf{v}, t) \tag{3.4}$$

$q(\mathbf{v})$	$q(\mathbf{x},t)$	$\Gamma_q(\mathbf{x},t)$
m	ρ	$\rho\mathbf{u}$
	mass density	fluid momentum
mv	$\rho\mathbf{u}$	**S**
	fluid momentum	Stress Tensor
$\frac{1}{2}mv^2$	U	**Q**
	energy density	energy flux

Table 3.1: Summary of notation and names for different moments of the kinetic equation.

$$\Gamma_q(\mathbf{x},t) = \int d^D v\, q(\mathbf{v})\mathbf{v} f(\mathbf{x},\mathbf{v},t). \tag{3.5}$$

The notation that we will use for each of these moments when the conservation moments are performed is shown in Table 3. This notation will be used for both the continuum and the lattice gas system.

To find the Euler equations, we plug in the equilibrium distribution for $f(\mathbf{x},\mathbf{v},t)$ and calculate the conservation moments explicitly. In the D-dimensional continuum fluid, the equilibrium distribution has the form of a Maxwellian in velocity space

$$f(\mathbf{x},\mathbf{v},t) = \frac{n(\mathbf{x},t)}{(2\pi T(\mathbf{x},t)/m)^{D/2}} \exp[-m(\mathbf{v}-\mathbf{u}(\mathbf{x},t))^2/(2T(\mathbf{x},t)]. \tag{3.6}$$

We now can calculate the moments in eqns.(3.4). The results are

$$\rho = mn(\mathbf{x},t) \tag{3.7}$$

$$\rho\mathbf{u} = mn(\mathbf{x},t)\mathbf{u}(\mathbf{x},t) \tag{3.8}$$

$$\mathbf{S} = P_s\mathbf{I} + \rho\mathbf{u}\mathbf{u} = nT\mathbf{I} + \rho\mathbf{u}\mathbf{u} \tag{3.9}$$

$$U = U_p + \frac{1}{2}\rho u^2 = \frac{D}{2}nT + \frac{1}{2}\rho u^2 \tag{3.10}$$

$$\mathbf{Q} = (U_p + P_s + \frac{1}{2}\rho u^2)\mathbf{u} = (\frac{D+2}{D}U_p + \frac{1}{2}\rho u^2)\mathbf{u} \tag{3.11}$$

where $P_s = nT$ is the scalar or isotropic pressure and U_p is the internal energy. We see that

$$P_s = \frac{2}{D}U_p \tag{3.12}$$

which is the relation that describes equipartition of energy in an ideal gas. If we use the thermodynamic relation $P_s = (c_p/c_v - 1)U_p = (\gamma - 1)U_p$ [32], where $\gamma = c_p/c_v$ is the ratio of specific heats, we find that $\gamma = (D+2)/D$, the ideal gas relation.

In summary, we have the following conservation equations for the continuum gas. For mass the continuity equation

$$\frac{\partial}{\partial t}\rho + \nabla \cdot \rho\mathbf{u} = 0. \tag{3.13}$$

For momentum

$$\frac{\partial}{\partial t}\rho\mathbf{u} + \nabla \cdot (\mathbf{I}\frac{2}{D}U_p + \rho\mathbf{u}\mathbf{u}) = 0, \tag{3.14}$$

which may be alternatively written when we multiply the continuity equation by the flow velocity, $\mathbf{u}$, and subtract the result from above, as

$$\rho\frac{\partial}{\partial t}\mathbf{u} + \rho\mathbf{u} \cdot \nabla\mathbf{u} = -\nabla P_s. \tag{3.15}$$

Finally, the energy equation is

$$\frac{\partial}{\partial t}(U_p + \frac{1}{2}\rho u^2) + \nabla \cdot (\frac{D+2}{D}U_p + \frac{1}{2}\rho u^2)\mathbf{u} = 0. \tag{3.16}$$

3.1 General Form of the Lattice Moment Equations

The analysis leading to the Euler equations will treat a very general class of systems with a spectrum of masses and energies. Collisionality sufficient to achieve thermal equilibrium over all states during time scales of interest will be assumed. This section and the next will derive the Euler equations that result under those assumptions, and indicate the restrictions and conditions required to obtain true fluid dynamic behavior at the Euler level. The lattice system is characterized by the following parameters in a *species space* indexed by j and a *direction space* indexed by i

$$\begin{aligned}
N_{ji}(\mathbf{x},t) &= \text{microscopic distribution function} \\
m_j &= \text{microscopic mass} \\
\mathbf{c}_{ji} &= \text{velocity vector } (c_j = \text{ magnitude}) \\
d_j &= \text{number of directions per site} \\
\epsilon_j &= \tfrac{1}{2} m_j c_j^2 = \text{microscopic kinetic energy} \\
r_j &= \langle I^j \rangle / \langle F^j \rangle = \text{rate coefficient ratio.}
\end{aligned} \tag{3.17}$$

The Euler equations follow from the mass, momentum and energy moments of the lattice kinetic equation (2.32) through first order in the Knudsen expansion. Thus we have,

$$\sum_{j,i} \left(\frac{\partial}{\partial t} N_{ji}(\mathbf{x}, \mathbf{c}_{ji}, t) + \nabla \cdot \mathbf{c}_{ji}\ N_{ji}(\mathbf{x}, \mathbf{c}_{ji}, t) \right) \begin{bmatrix} m_j \\ m_j \mathbf{c}_{ji} \\ \epsilon_j \end{bmatrix} = 0 \tag{3.18}$$

where the collision operator on the right-hand side vanishes since collisions con-

serve mass, momentum and energy identically. There are two differences between this kinetic equation and the kinetic equation used for a continuum gas. First of all, in the continuum the velocity spectrum is continuous so one performs integrals over velocity to get the Euler equations. Here, the velocity spectrum is discrete so sums are taken rather than integrals. Secondly, as we have seen, the equilibrium relation for a real gas can be shown to be of Maxwell-Boltzmann form while for the lattice gas the equilibrium is Fermi-Dirac.

We now give the general results for the lattice Euler equations and discuss their consequences. Explicit calculations will be done in the next section. The mass moment gives the continuity equation directly,

$$\frac{\partial}{\partial t}\rho + \nabla \cdot \rho \mathbf{u} = 0 \tag{3.19}$$

where $\rho = \sum_{j,i} m_j N_{ji}(\mathbf{x}, \mathbf{c}_{ji}, t)$ is the fluid density. This equation is identical to the continuity equation of hydrodynamics. The momentum equation is

$$\frac{\partial}{\partial t}\rho\mathbf{u} + \nabla \cdot \mathbf{S} = 0, \tag{3.20}$$

where $\mathbf{S} = \sum_{j,i} m_j \mathbf{c}_{ji}\mathbf{c}_{ji} N_{ji}(\mathbf{x}, \mathbf{c}_{ji}, t)$, is the complete stress tensor, including the advection of fluid momentum. One finds [14] for systems with a lattice structure sufficient to guarantee isotropy of this tensor, that $\mathbf{S}$ can be written as

$$\mathbf{S} = \mathbf{I}P_s + g\rho\mathbf{u}\mathbf{u}, \tag{3.21}$$

where the factor g, which is a function of both density and temperature in multi-speed lattice systems, is not in general equal to unity as it is in hydrodynamics. If we multiply the continuity equation, eqn. (3.19), by the fluid velocity and then subtract the result from the momentum equation, eqn. (3.20), and substitute for the stress tensor using eqn. (3.21), we find

$$\rho\frac{\partial}{\partial t}\mathbf{u} + g\rho\mathbf{u} \cdot \nabla\mathbf{u} + \mathbf{u}\nabla \cdot (\rho\mathbf{u}(g-1)) = -\nabla P_s, \tag{3.22}$$

exhibiting, with $g \neq 1$, the generally non-Galilean invariant character of lattice gas hydrodynamics, since momentum is advected with velocity $g\mathbf{u}$ instead of $\mathbf{u}$. In previous models this problem was circumvented by restricting consideration to incompressible flows thereby eliminating the third term in equation (3.22) and by rescaling the time to put the second term in the proper hydrodynamic form. But this technique does not work when mixtures of fluids are being simulated ([36, 37]) since the velocity of the fluid interface is constrained by the conservation of particles to be equal to the average particle velocity and therefore cannot be subject to the same rescaling. Even when this rescaling may seem justified in a single fluid flow, the single-speed isotropic pressure is [14]

$$P_s = \frac{1}{2}\rho(1 - \frac{2}{D}u^2 g(\rho)) \tag{3.23}$$

where $D = 2$ for the FHP lattice and $D = 4$ for FCHC. This indicates that the pressure of the flow is velocity dependent. This unphysical result makes it very difficult if not impossible to quantitatively compare one-speed lattice results with actual flows. Furthermore, the dynamic pressure anomaly is the same order as the variation in the pressure that accounts for drag and lift on objects placed in fluid flow. This means that the simulated drag will vary from the actual value by order unity and will be dependent on the flow conditions. Similarly, one cannot correctly predict the pressure dependent flow separation phenomenon that is so critical in hydrodynamic design if this anomaly is present. Recently[38], it has been found that adding rest particles to a single-speed model allows the Galilean factor to be re-adjusted to the desired hydrodynamic value but at the expense of violating the semi-detailed balance condition. Thus, there is no longer an H-Theorem for this model and monotonic evolution to any equilibrium is not assured. In contrast, as described in Chapter 2, a multi-speed model with collision rate masks may be

renormalized so that detailed balance is obeyed.

In the multi-speed FCHC model, we will show that the isotropic pressure has the form

$$P_s = \frac{2}{D}\left[U_p + \tfrac{1}{2}\rho u^2(1-g)\right]. \tag{3.24}$$

We now notice that if $g = 1$, then both the non-Galilean invariant character of the advected momentum (eqn.(3.22) becomes identical to eqn.(3.15)) and the dynamic pressure anomaly are removed (eqn.(3.24) becomes identical to eqn.(3.12)). The energy equation had not been previously examined for single-speed lattice gas hydrodynamics since in existing algorithms it was identical to the continuity equation (3.19). The inclusion of an energy conservation constraint is what allows the possibility of the removal of the pressure anomaly in the multiple-speed case. The energy moment of eqn. (3.18) gives the energy equation in the correct form,

$$\frac{\partial}{\partial t}U + \nabla \cdot \mathbf{Q} = 0, \tag{3.25}$$

where $\mathbf{Q} = \sum_{j,i} \mathbf{c}_{ji}\epsilon_j N_{ji}$, is the full energy flux, including advection of the hydrodynamic energy density.

If the algorithm is to describe realistic hydrodynamics, the energy density U, must be the sum of the particle kinetic plus internal energy U_p plus the hydrodynamic flow energy $\frac{1}{2}\rho u^2$, eqn.(3.10). The lattice gas energy density does have this form. In addition, the energy flux must explicitly contain the fluid energy advection term $\frac{1}{2}\rho u^2\mathbf{u}$, in addition to the thermodynamic terms describing the consequences of distortion of the fluid element during flow. For the lattice gas, the energy flux takes the form

$$\mathbf{Q} = \left(\gamma U_p + g'\tfrac{1}{2}\rho u^2\right)\mathbf{u} \tag{3.26}$$

where γ is effectively the ratio of specific heats, and g' is the energy analog of the Galilean factor, g, that appears in the momentum equation. If we compare this with the actual relation, eqn.(3.11), we find that in eqn.(3.26), γ should equal (D+2)/D and g' should equal one. In general in the multi-speed lattice gas, this is not the case.

We now rewrite the lattice momentum and energy conservation equations so that each equation has two contributions, the correct hydrodynamic result and a portion due to the presence of the lattice. For the lattice stress tensor we write

$$\frac{\partial}{\partial t}\rho\mathbf{u} + \nabla\cdot(\mathbf{I}P_s + \rho\mathbf{u}\mathbf{u}) + \nabla\cdot[(g-1)\rho\mathbf{u}\mathbf{u}] = 0 \tag{3.27}$$

and for the energy equation

$$\begin{aligned}\frac{\partial}{\partial t}(U_p + \frac{1}{2}\rho u^2) \;&+\; \nabla\cdot(U_p + \frac{1}{2}\rho u^2 + P_s)\mathbf{u} \\ &+\; \nabla\cdot\left[(g-1)\frac{1}{D}\rho u^2 + \left(\gamma - \frac{D+2}{D}\right)U_p + (g'-1)\frac{1}{2}\rho u^2\right]\mathbf{u} = 0\end{aligned} \tag{3.28}$$

where the quantities in square brackets are artifact relations that vanish when the artifacts take on the continuum values. When this occurs, the remaining terms give the correct conservation equations precisely, eqns. (3.14) and (3.16). The g term appears in the energy equation when we substitute for $\frac{2}{D}U_p$ using eqn. (3.24) to give the isotropic pressure, P_s. Using the total derivative notation, $\frac{D}{Dt} \equiv \frac{\partial}{\partial t} + \mathbf{u}\cdot\nabla$, eqn. (3.27) becomes

$$\rho\frac{D\mathbf{u}}{Dt} = -\nabla P_s - \nabla\cdot\mathbf{A1} \tag{3.29}$$

where $\mathbf{A1} = (g-1)\rho\mathbf{u}\mathbf{u}$ is the artifact term for the momentum equation. If we dot this equation with the flow velocity, u, and use the continuity equation, rewritten in terms of the total derivative

$$\frac{D}{Dt}\rho = -\rho(\nabla\cdot\mathbf{u}) \tag{3.30}$$

we attain, after a bit of manipulation

$$\frac{D}{Dt}\tfrac{1}{2}\rho u^2 + \tfrac{1}{2}\rho u^2(\nabla\cdot\mathbf{u}) + \nabla\cdot\mathbf{u}P_s - P_s(\nabla\cdot\mathbf{u}) = -\mathbf{u}\cdot\nabla\cdot\mathbf{A1}. \tag{3.31}$$

The energy equation, eqn. (3.28), can also be manipulated to obtain

$$\frac{D}{Dt}(U_p + \tfrac{1}{2}\rho u^2) + (U_p + \tfrac{1}{2}\rho u^2)(\nabla\cdot\mathbf{u}) + \nabla\cdot\mathbf{u}P_s = -\nabla\cdot A2\mathbf{u} \tag{3.32}$$

where $A2$ contains all the artifact relations in the energy equation. Subtracting eqn. (3.31) from eqn. (3.32) and using eqn. (3.30) to substitute for the divergence of the velocity field, we arrive at

$$\frac{D}{Dt}U_p - \frac{(U_p + P_s)}{\rho}\frac{D}{Dt}\rho = -\mathbf{u}\cdot\nabla\cdot\mathbf{A1} - \nabla\cdot A2\mathbf{u}. \tag{3.33}$$

When $g = 1$, all artifacts in the momentum equation vanish and we get the equipartition of energy result $P_s = \frac{2}{D}U_p$ from eqn. (3.24). If we substitute for U_p into eqn. (3.33) , where now $\mathbf{A1} = \mathbf{0}$, we find

$$\frac{D}{Dt}P_s = \frac{D+2}{D}\frac{P_s}{\rho}\frac{D}{Dt}\rho - \nabla\cdot\left[\left(\gamma - \frac{D+2}{D}\right)P_s + (g'-1)\frac{1}{D}\rho u^2\right]\mathbf{u}. \tag{3.34}$$

The equation of state for the lattice gas fluid, like any other fluid, can be written in terms of three thermodynamic quantities. We choose pressure, density and entropy, S, as the three variables and solve the equation for the pressure, P_s

$$P_s \equiv P_s(\rho, S). \tag{3.35}$$

A small change in the pressure can be expressed in terms of small changes in the other two quantities

$$\frac{D}{Dt}P_s = c_s^2\frac{D}{Dt}\rho + \left(\frac{\partial P_s}{\partial S}\right)_\rho \frac{D}{Dt}S \tag{3.36}$$

where $c_s^2 \equiv (\partial P_s/\partial\rho)_S$ is the square of the sound speed for the flow.

We are examining the Euler equations for the lattice gas and so we have neglected all molecular transport effects in this analysis. In this situation, the flow is isentropic[65], $\frac{D}{Dt}S = 0$, so that eqn. (3.36) reduces to

$$\frac{D}{Dt}P_s = c_s^2 \frac{D}{Dt}\rho. \tag{3.37}$$

Upon comparing eqns. (3.37) and (3.34) we find that if the energy artifacts have been removed, $\gamma = \frac{D+2}{D}$ and $g' = 1$, then for a lattice gas

$$c_s^2 = \frac{D+2}{D}\frac{P_s}{\rho} \tag{3.38}$$

which is identical to the result in a true ideal gas. If the two energy artifacts have not been completely removed, we use eqn. (3.30) with eqn. (3.34) to get

$$\frac{D}{Dt}P_s = \left[\gamma\frac{P_s}{\rho} + (g'-1)\frac{1}{D}u^2\right]\frac{D}{Dt}\rho - \mathbf{u}\cdot\nabla\left[\left(\gamma - \frac{D+2}{D}\right)P_s + (g'-1)\frac{1}{D}\rho u^2\right] \tag{3.39}$$

which shows that the square of the sound speed is actually close to $c_s^2 \approx \gamma\frac{P_s}{\rho}$ in a lattice that has artifacts.

In summary, there are three lattice artifacts. One is in the momentum equation for both single- and multiple-speeds lattice gases in two separate places. While this artifact, g, is not in general equal to the Galilean invariant factor 1, we found that if $g = 1$, the momentum conservation equation for the multiple-speed lattice gas becomes correct while the single- speed result still has an unphysical feature. Furthermore, there are two artifacts in the energy equation, g' and γ, which are *not* in general equal to their hydrodynamic values of 1 and (D + 2)/D, respectively.

3.2 Calculating Expressions for the Artifacts

In this Section, we develop the Euler equations for the multiple-speed lattice gas model on the FCHC lattice based on an expansion of the equilibrium distributions, eqn.(2.31), for small fluid velocity **u** (or small Mach number) through third order in the Mach number. By expanding to this order, we capture all the artifacts that were described in the last Section which then allows a direct comparison with fluid dynamics results. This expansion [41, 14, 22] is in a sense subsidiary to the weak gradient expansion that underlies transport theory. It can be done in continuum kinetic theory as a convenience, but is often unnecessary since the velocity integrals over the Maxwellian distribution can be carried out in any case. For lattice gases, these integrals become sums that cannot be done without the subsidiary expansion.

In continuum mechanics, the form of the equilibrium Maxwellian is calculated from an H-Theorem and results in a function with three undetermined Lagrange multipliers, after we have made the identification that the momentum coefficient should be proportional to the fluid velocity, similar to the coefficients that appear in eqn.(2.31) for a lattice gas. In the continuum, these three coefficients are determined[31] by equating the mass, momentum and energy moments (the conserved quantitites) of the general Maxwellian to the known expressions for these three quantites (Table 3). We do the same procedure for the Fermi-Dirac relation while utilizing the Mach number expansion. We take moments of the equilibrium relation order by order where the form of the coefficients as functions of the fluid velocity is initially undetermined. This provides a freedom in the perturbation theory to structure the resulting equations in a most convenient manner. Exploiting this freedom is the key to obtaining the proper hydrodynamic equations.

The first step is to expand the coefficents, α, γ, and β, in eqn.(2.31) as a function of the fluid velocity $\mathbf{u}$ by noting that they are scalars and so can depend on $\mathbf{u}$ only through u^2 to the order we are carrying this expansion. Consequently, they may be expressed as

$$\begin{aligned} \alpha &= \alpha(u^2) &&= \alpha_0 + \alpha_2(u^2) \\ \gamma &= \gamma(u^2) &&= \gamma_0 + \gamma_2(u^2) \\ \beta &= \beta(u^2) &&= \beta_0 + \beta_2(u^2) \end{aligned} \tag{3.40}$$

where the subscripts denote the order in u. One can anticipate that β_0 will correspond to the thermodynamic expression $\beta_0 = 1/kT$.

Plugging the above into the equilibrium relation eqn. (2.31) and then expanding N_{ji} in powers of u yields

$$\begin{aligned} N_{ji} = N_j[1 &+ N_j'\gamma_0 m_j \mathbf{c}_{jli}\cdot\mathbf{u} \\ &+ \tfrac{1}{2}N_j''\gamma_0^2 m_j^2(\mathbf{c}_{jli}\cdot\mathbf{u})^2 + N_j'(m_j\alpha_2 + \epsilon_j\beta_2) \\ &+ N_j'\gamma_2 m_j \mathbf{c}_{jli}\cdot\mathbf{u} + \frac{1}{6}N_j'''\gamma_0^3 m_j^3(\mathbf{c}_{ji}\cdot\mathbf{u})^3 + N_j''(\gamma_0 m_j \mathbf{c}_{jli}\cdot\mathbf{u})(m_j\alpha_2 + \epsilon_j\beta_2) \\ &+ \mathcal{O}(u^4)] \end{aligned} \tag{3.41}$$

where

$$N_j = \frac{r_j}{r_j + exp(\alpha_0 m_j + \beta_0\epsilon_j)} = F(-\ln r_j + \alpha_0 m_j + \beta_0\epsilon_j), \tag{3.42}$$

is the zero order, isotropic, Fermi-Dirac equilibrium density (per direction), and $F(x) = 1/(1+e^x)$. The term N_j has been pulled out of the expansion so that the coefficients N_j', N_j'', and N_j''' have the simplest possible form. The form of these coefficients, which are easily calculated from repeated differentiations of the function $F(x)$, are

$$N_j' = \frac{F'}{F} = -(1 - N_j) \tag{3.43}$$

$$N_j'' = \frac{F''}{F} = (1 - N_j)(1 - 2N_j) \tag{3.44}$$

$$N_j''' = \frac{F'''}{F} = -(1 - N_j)(1 - 6N_j + 6N_j^2). \tag{3.45}$$

Note that r_j does not appear in the expressions as written above. It only enters in the equilibrium relations relating the various densities, N_j in equation (3.42).

When taking the mass, momementum and energy moments of the above expanded distribution function, we have to sum over particle species j, and direction , i. The result of the direction sum indicates whether a lattice is sufficiently symmetric. This is the case when the direction vectors, $\mathbf{c}_{ji}$, give rise to isotropic tensors of both the second and fourth rank when summed over directions. As mentioned in Chapter 2, this is a feature assured by the FCHC lattice for all particle speeds *individually*. This will be shown in Chapter 4.1.1. It means that

$$\sum_i \mathbf{c}_{ji}\mathbf{c}_{ji} = \frac{d_j}{D} c_j^2 \mathbf{I}, \tag{3.46}$$

and

$$\sum_i \mathbf{c}_{ji}\mathbf{c}_{ji}\mathbf{c}_{ji}\mathbf{c}_{ji} = \frac{d_j}{D(D+2)} c_j^4 \Delta^{(4)}, \tag{3.47}$$

where we have adopted the notation of Wolfram [22], defining $\Delta^{(4)}$ as the completely symmetric 4th rank tensor,

$$\Delta^{(4)}_{\alpha\beta\gamma\delta} \equiv \delta_{\alpha\beta}\delta_{\gamma\delta} + \delta_{\alpha\gamma}\delta_{\beta\delta} + \delta_{\alpha\delta}\delta_{\gamma\beta}. \tag{3.48}$$

Because of the symmetry of the direction vectors, sums over an odd number of $\mathbf{c}_{ji}$'s vanish[22]

$$\sum_i \mathbf{c}_{ji} = \mathbf{0} \tag{3.49}$$

$$\sum_i \mathbf{c}_{ji}\mathbf{c}_{ji}\mathbf{c}_{ji} = \mathbf{0}. \tag{3.50}$$

Of course, a sum over directions of a quantity that does not depend on direction results in the factor d_j, $\sum_i = d_j$, for a particular speed.

To facilitate the summation over species space, four inner products are defined

$$\begin{aligned}
(\mathbf{a},\mathbf{b})_0 &\equiv \sum_j d_j N_j a_j b_j \\
(\mathbf{a},\mathbf{b})_1 &\equiv -\sum_j d_j N_j N_j' a_j b_j \\
(\mathbf{a},\mathbf{b})_2 &\equiv \sum_j d_j N_j N_j'' a_j b_j \\
(\mathbf{a},\mathbf{b})_3 &\equiv -\sum_j d_j N_j N_j''' a_j b_j.
\end{aligned} \tag{3.51}$$

where **a** and **b** are any system vectors over species space such as mass or energy.

Because of the symmetry relations eqns. (3.46), (3.47), (3.49), only the zeroth and second order moments of mass and energy are non-zero while the first and third moments of momentum survives. This gives six equations which should in principle allow us to solve for the six coefficients $\alpha_0, \alpha_2, \gamma_0$, etc. so that these moments give the correct hydrodynamic values. We will then calculate the stress tensor and energy flux vector using these results to make the form of the artifacts explicit and to complete the calculation of the lattice Euler equations.

3.2.1 Mass and Energy Coefficients

We begin with the mass and energy moments, evaluated order by order. The lowest order result, where $N_{ji} = N_j$, defines the zero order mass and energy densities according to

$$\rho^{(0)} = \sum_{j,i} m_j N_j = \sum_j m_j d_j N_j = (\mathbf{m},\mathbf{1})_0 \tag{3.52}$$

and

$$U^{(0)} = \sum_{j,i} \epsilon_j N_j = \sum_j \epsilon_j d_j N_j = (\epsilon, \mathbf{1})_0. \tag{3.53}$$

There is no first order contribution to the mass and energy densities since $N_{ji}^{(1)}$ has a single $\mathbf{c}_{ji}$ which is annihilated by the direction sum. There are two second order terms, the terms on the second line of eqn. (3.41). Second order expressions are

$$\rho^{(2)} = \sum_{j,i} m_j N_{ji}^{(2)} = \sum_{j,i} m_j N_j N_j'(m_j\alpha_2 + \epsilon_j\beta_2) + \sum_{j,i} m_j^3 N_j N_j'' \tfrac{1}{2}\gamma_0^2(\mathbf{c}_{ji}\cdot\mathbf{u})^2 \tag{3.54}$$

and

$$U^{(2)} = \sum_{j,i} \epsilon_j N_{ji}^{(2)} = \sum_{j,i} \epsilon_j N_j N_j'(m_j\alpha_2 + \epsilon_j\beta_2) + \sum_{j,i} \epsilon_j m_j^2 N_j N_j'' \tfrac{1}{2}\gamma_0^2(\mathbf{c}_{ji}\cdot\mathbf{u})^2. \tag{3.55}$$

The third order contribution to mass and energy also vanish due to eqns. (3.49).

We may make the left sides of the zeroth and second order equations anything we like and solve for the coefficients $\alpha_0, \beta_0, \alpha_2, \beta_2$. Usually this expansion is developed so that all the mass is contained in $\rho^{(0)}$ through second order so that the mass of the fluid is not velocity dependent. Thus one utilizes the freedom in the perturbation theory (underdeterminedness of the coefficient equations) to set $\rho^{(2)} = 0$. Then, $\rho = \rho^{(0)}$, to second order and the continuity equation is complete.

The energy moment is different since there may be both a zeroth and second order contribution. There is the particle kinetic energy, U_p, which is zeroth order and the energy associated with the fluid flow, $\frac{1}{2}\rho u^2$, which is second order in u.

In summary, we identify

$$\rho^{(0)} = \rho \qquad \text{and} \qquad U^{(0)} = U_p \tag{3.56}$$

which allows us, in principle, to solve for α_0 and β_0. Since we have already identified β_0 as being related to temperature through the equation of state, we

conclude that α_0 allows us to specify the density. To obtain the correct second order values of density and energy, we solve for the coefficients, α_2, and β_2 so that

$$\rho^{(2)} = 0 \qquad \text{and} \qquad U^{(2)} = \tfrac{1}{2}\rho u^2. \tag{3.57}$$

The result will be left in terms of the momentum coefficient γ_0 to be computed subsequently. Thus, both density and energy will agree with the true fluid dynamics relations (eqn. (3.10)).

Utilizing the notation of eqns. (3.51) and the direction symmetry relations, eqns. (3.54) and (3.55) can be written as

$$(\mathbf{m},\mathbf{m})_1\alpha_2 + (\mathbf{m},\epsilon)_1\beta_2 = \frac{1}{D}\gamma_0^2 u^2(\mathbf{m}^2,\epsilon)_2 \tag{3.58}$$

$$(\mathbf{m},\epsilon)_1\alpha_2 + (\epsilon,\epsilon)_1\beta_2 = \frac{1}{D}\gamma_0^2 u^2(\mathbf{m}\epsilon,\epsilon)_2 - \tfrac{1}{2}\rho u^2 \tag{3.59}$$

Equations (3.58) and (3.59) are soluble provided the determinant of this two equation, two unknown system,

$$A \equiv (\mathbf{m},\mathbf{m})_1(\varepsilon,\epsilon)_1 - (\mathbf{m},\epsilon)_1^2 \tag{3.60}$$

does not vanish. But $A \neq 0$ is the condition that the mass and energy "vectors" are not collinear. This is just the independence of the mass and energy properties that the present, multiple-speed, algorithm exhibits. This is not the case for single-speed systems. Thus, A is not equal to zero in all cases for the multiple-speed algorithm. Solving for α_2 and β_2 yields

$$\alpha_2 = \frac{1}{A}\left[(\mathbf{m},\epsilon)_1\tfrac{1}{2}\rho u^2 + \frac{1}{D}\gamma_0^2 u^2\left((\epsilon,\epsilon)_1(\mathbf{m}^2,\epsilon)_2 - (\mathbf{m},\epsilon)_1(\mathbf{m}\epsilon,\epsilon)_2\right)\right] \tag{3.61}$$

$$\beta_2 = -\frac{(\mathbf{m},\mathbf{m})_1}{A}\tfrac{1}{2}\rho u^2 + \frac{1}{AD}\gamma_0^2 u^2\left((\mathbf{m},\mathbf{m})_1(\mathbf{m}\epsilon,\epsilon)_2 - (\mathbf{m},\epsilon)_1(\mathbf{m}^2,\epsilon)_2\right) \tag{3.62}$$

This completes the solution of the mass and energy coefficients up to third order. The equations are retained in the most general form here. Simplifications

will be indicated as the conditions needed to obtain hydrodynamic behavior are derived subsequently.

3.2.2 Momentum Coefficients

We now calculate the coefficients γ_0 and γ_2 from the first and third orders momentum moments respectively since the zeroth and second order contributions vanish due to the vector symmetry relations. The first order momentum moment, which should be equal to the first order term $\rho\mathbf{u}$, is

$$\begin{aligned}\rho\mathbf{u} &= \sum_{j,i} m_j \mathbf{c}_{ji} N_{ji}^{(1)} = \gamma_0 \sum_{j,i} N_j N_j' m_j^2 \mathbf{c}_{ji}\mathbf{c}_{ji}\cdot\mathbf{u} \\ &= -\gamma_0 \frac{2}{D}(\mathbf{m},\epsilon)\mathbf{u} \end{aligned} \tag{3.63}$$

which gives the coefficient, γ_0, in terms of the equilibrium quantities,

$$\gamma_0 = -\frac{D}{2}\frac{\rho}{(\mathbf{m},\epsilon)}. \tag{3.64}$$

We have made the density ρ a zeroth order quantity. Thus, the fluid momentum, $\rho\mathbf{u}$, is purely first order. Requiring that all momentum be contained in $\rho\mathbf{u}$ through third order determines the second momentum coefficient, γ_2.

$$\begin{aligned} 0 &= \sum_{j,i} m_j \mathbf{c}_{ji} N_{ji}^{(3)} \\ &= \sum_{j,i} m_j \mathbf{c}_{ji} N_j \left[N_j' \gamma_2 m_j \mathbf{c}_{ji}\cdot\mathbf{u} + \frac{1}{6} N_j''' \gamma_0^3 m_j^3 (\mathbf{c}_{ji}\cdot\mathbf{u})^3 + N_j''(\gamma_0 m_j \mathbf{c}_{ji}\cdot\mathbf{u}) \times \right. \\ &\quad \left. (\alpha_2 m_j + \epsilon_j \beta_2)\right] \\ &= -\gamma_2 \frac{2}{D}(\mathbf{m},\epsilon)_1 \mathbf{u} + \frac{2\gamma_0}{D}\left[\alpha_2(\mathbf{m},\mathbf{m}\epsilon)_2 + \beta_2(m\epsilon,\epsilon)_2\right]\mathbf{u} \\ &\quad + \frac{1}{2}\gamma_0^3 \sum_j N_j N_j''' g_j \frac{m_j^4 c_j^4}{D(D+2)} u^2 \mathbf{u} \end{aligned} \tag{3.65}$$

$$= -\gamma_2 \frac{2}{D}(\mathbf{m},\epsilon)_1 \mathbf{u} + \frac{2\gamma_0}{D}\left[\alpha_2(\mathbf{m},\mathbf{m}\epsilon)_2 + \beta_2(\mathbf{m}\epsilon,\epsilon)_2\right]\mathbf{u}$$
$$- \gamma_0^3 \frac{2}{D(D+2)}(\mathbf{m}^2,\epsilon^2)_3 u^2 \mathbf{u}$$

where we have used the fact that $(\Delta^{(4)} : \mathbf{uu}) \cdot \mathbf{u} = (2\mathbf{uu} + u^2\mathbf{I}) \cdot \mathbf{u} = 3u^2\mathbf{u}$. Solving for γ_2 gives

$$\gamma_2 = \frac{-\gamma_0^3 u^2}{(D+2)} \frac{(m^2,\epsilon^2)_3}{(\mathbf{m},\epsilon)_1} + \frac{\gamma_0}{(\mathbf{m},\epsilon)_1}\left[\alpha_2(\mathbf{m}^2,\epsilon)_2 + \beta_2(m\epsilon,\epsilon)_2\right]. \tag{3.66}$$

Plugging in for γ_0, α_2, and β_2 from eqns. (3.64), (3.61) and (3.62) respectively, gives γ_2 in terms of equilibrium quantities only.

With all of the coefficients now determined, we may now calculate the stress tensor and energy flux vector.

3.2.3 Stress Tensor

To third order in u the pressure tensor is,

$$\begin{aligned}
\mathbf{S} &= \sum_{j,i} m_j \mathbf{c}_{ji}\mathbf{c}_{ji} N_{ji} \\
&= \sum_{j,i} m_j N_j \left[\mathbf{c}_{ji}\mathbf{c}_{ji} + \tfrac{1}{2}N_j'' \gamma_0^2 m_j^2 (\mathbf{c}_{ji}\mathbf{c}_{ji}\mathbf{c}_{ji}\mathbf{c}_{ji} : \mathbf{uu}) + N_j'(m_j\alpha_2 + \epsilon_j\beta_2)\mathbf{c}_{ji}\mathbf{c}_{ji}\right] \\
&= \mathbf{I}\frac{2}{D}[U^{(0)} - (\mathbf{m},\epsilon)_1\alpha_2 - (\epsilon,\epsilon)_1\beta_2] + \Delta^{(4)} : \mathbf{uu}\frac{2\gamma_0^2}{D(D+2)}(\mathbf{m}\epsilon,\epsilon)_2.
\end{aligned} \tag{3.67}$$

Again we use $\Delta^{(4)} : \mathbf{uu} = 2\mathbf{uu} + u^2\mathbf{I}$ so that eqn. (3.67) can be written as

$$\begin{aligned}
\mathbf{S} &= \mathbf{I}\frac{2}{D}[U^{(0)} - (\mathbf{m},\epsilon)_1\alpha_2 - (\epsilon,\epsilon)_1\beta_2 + (\mathbf{m}\epsilon,\epsilon)_2\frac{\gamma_0^2 u^2}{2(D+2)}] \\
&+ \frac{4\gamma_0^2}{D(D+2)}(\mathbf{m}\epsilon,\epsilon)_2\mathbf{uu}.
\end{aligned} \tag{3.68}$$

Substituting $U^{(0)} = U_p$, eqn. (3.64) for γ_0, and eqns. (3.61) and (3.62) for α_2 and β_2, the stress tensor becomes, after some algebra,

$$\begin{aligned}\mathbf{S} &= \mathbf{I}\frac{2}{D}\left[U_p + \tfrac{1}{2}\rho u^2 - \tfrac{1}{2}\rho u^2\left(\frac{D}{D+2}\frac{(\mathbf{m}\epsilon,\epsilon)_2}{(\mathbf{m},\epsilon)_1^2}\rho\right)\right] \\ &\quad + \left(\frac{D}{D+2}\frac{(\mathbf{m}\epsilon,\epsilon)_2}{(\mathbf{m},\epsilon)_1^2}\rho\right)\rho\mathbf{uu}. \end{aligned} \tag{3.69}$$

This is of the form anticipated in eqns. (3.21) and (3.24) with the Galilean factor, g, given by

$$g = \frac{D}{D+2}\frac{(\mathbf{m}\epsilon,\epsilon)_2}{(\mathbf{m},\epsilon)_1^2}\rho. \tag{3.70}$$

3.2.4 Energy Flux

Finally, we calculate the energy flux, $\mathbf{Q}$, to third order in u, giving

$$\begin{aligned}\mathbf{Q} &= \sum_{j,i}\epsilon_j N_{ji}\mathbf{c}_{ji} \\ &= \sum_{j,i}\epsilon_j N_j\left[(\gamma_0+\gamma_2)N_j' m_j\mathbf{c}_{ji}\mathbf{c}_{ji}\cdot\mathbf{u} + \frac{1}{6}N_j'''\gamma_0^3 m_j^3\mathbf{c}_{ji}\mathbf{c}_{ji}\mathbf{c}_{ji}\mathbf{c}_{ji}\cdot\mathbf{uuu}\right. \\ &\quad \left. + N_j''\gamma_0 m_j(\alpha_2 m_j + \epsilon_j\beta_2)\mathbf{c}_{ji}\mathbf{c}_{ji}\cdot\mathbf{u}\right] \\ &= -(\gamma_0+\gamma_2)\frac{2}{D}(\epsilon,\epsilon)_1\mathbf{u} - \gamma_0^3\frac{2}{D(D+2)}(\epsilon,m\epsilon^2)_3 u^2\mathbf{u} \\ &\quad + \frac{2}{D}\gamma_0\left[\alpha_2(m\epsilon,\epsilon)_2 + \beta_2(\epsilon^2,\epsilon)_2\right]\mathbf{u} \end{aligned} \tag{3.71}$$

Substituting for γ_0 and γ_2 we get the following form of the energy flux moment.

$$\begin{aligned}\mathbf{Q} &= \rho\mathbf{u}\frac{(\epsilon,\epsilon)_1}{(m,\epsilon)_1}\left[1 + \left\{\alpha_2\left[\frac{(m^2,\epsilon)_1}{(m,\epsilon)_1} - \frac{(m\epsilon,\epsilon)_2}{(\epsilon,\epsilon)_1}\right] + \beta_2\left[\frac{(m\epsilon,\epsilon)_2}{(m,\epsilon)_1} - \frac{(\epsilon^2,\epsilon)_2}{(\epsilon,\epsilon)_1}\right]\right\}\right] \\ &\quad + \tfrac{1}{2}\rho u^2\left[\frac{\rho^2 D^2}{2(D+2)(m,\epsilon)_1^3}\left\{(m\epsilon^2,\epsilon)_3 - \frac{(\epsilon,\epsilon)_1(m^2,\epsilon^2)_3}{(m,\epsilon)_1}\right\}\right]\mathbf{u}. \end{aligned} \tag{3.72}$$

The final thing to do is to substitute for α_2 and β_2, simplify the result, and we achieve the predicted form for the energy flux moment, eqn. (3.26)

$$\mathbf{Q} = \left(\gamma U_p + g' \tfrac{1}{2}\rho u^2\right)\mathbf{u} \tag{3.73}$$

where

$$\gamma = \rho \frac{(\epsilon,\epsilon)_1}{(m,\epsilon)_1 U_p} \tag{3.74}$$

and

$$\begin{aligned} g' \;=\; & \frac{\rho^2 D(\epsilon,\epsilon)_1}{2(m,\epsilon)_1^3}\left\{\left[\frac{(m\epsilon^2,\epsilon)_3}{(\epsilon,\epsilon)_1} - \frac{(m^2,\epsilon^2)_3}{(m,\epsilon)_1}\right]\frac{D}{D+2} + \right. \\ & \tfrac{1}{A}\left[(m^2,\epsilon)_2(\epsilon,\epsilon)_1 - (m,\epsilon)_1(m\epsilon,\epsilon)_2 + \frac{2}{D\rho}(m,\epsilon)_1^3\right]\left[\frac{(m^2,\epsilon)_2}{(m,\epsilon)_1} - \frac{(m\epsilon,\epsilon)_2}{(\epsilon,\epsilon)_1}\right] + \\ & \left.\tfrac{1}{A}\left[(m,m)_1(m\epsilon,\epsilon)_2 - (m,\epsilon)_1(m^2,\epsilon)_2 - \frac{2}{D\rho}(m,m)_1(m,\epsilon)_1^2\right]\left[\frac{(m\epsilon,\epsilon)_2}{(m,\epsilon)_1} - \frac{(\epsilon^2,\epsilon)_2}{(\epsilon,\epsilon)_1}\right]\right\} \end{aligned} \tag{3.75}$$

and A is the previously defined determinant (eq. 3.60).

In summary, we have the following conservation equations for the multiple-speed lattice gas. For mass the continuity equation

$$\frac{\partial}{\partial t}\rho + \nabla\cdot\rho\mathbf{u} = 0, \tag{3.76}$$

identical to the continuum result, eqn. (3.13). For momentum

$$\frac{\partial}{\partial t}\rho\mathbf{u} + \nabla\cdot\left(\mathbf{I}\frac{2}{D}\left[U_p + \tfrac{1}{2}\rho u^2(1-g)\right] + g\rho\mathbf{u}\mathbf{u}\right) = 0 \tag{3.77}$$

with g given by eqn. (3.70). When $g = 1$, this equation reduces to eqn. (3.14), the continuum momentum equation.

In the single-speed lattice gas, the isotropic pressure term had a dynamic anomaly that presisted despite the attainment of Galilean invariance, eqn. (3.23). For the multiple-speed case, however, we see that this anomaly can be eliminated

entirely by having the correct hydrodynamic energy together with Galilean invariance. Note that the term required for the cancellation of the second order energy, $\frac{1}{2}\rho u^2$ in eqn. (3.69), results from combining the terms involving α_2 and β_2, with the scalar part of $\Delta^{(4)}$: **uuu**. It cannot be related to any simple properties of the tensor $\Delta^{(4)}$. The cancellation of the pressure anomaly only seems to occur in general for systems which are purely kinetic energy systems. Molvig et al.[39] showed that when particles have an independent component of *internal* energy, as in the work of Chen et al.[42], the internal energy terms that propagate through the calculation remain uncancelled in the scalar pressure term and restore the pressure anomaly. This is because the stress tensor is basically a kinetic energy moment while the components α_2 and β_2 are calculated from a full (internal plus kinetic) energy moment. Thus, the internal energy contribution from these coefficients cannot be cancelled in the stress moment.

Finally, the energy equation is

$$\frac{\partial}{\partial t}(U_p + \frac{1}{2}\rho u^2) + \nabla \cdot (\gamma U_p + g' \frac{1}{2}\rho u^2)\mathbf{u} = 0 \tag{3.78}$$

which reduces to the continuum relation eqn. (3.16) when $\gamma = \frac{D+2}{D}$ and $g' = 1$.

In the next two Chapters, we examine how these three artifacts can be made to equal their continuum values so that the conservation equations for the lattice gas and continuum fluid are identical.

Chapter 4

Approach to Continuum Through Adding Higher Speeds

In the last Chapter, we derived quantities that represent the artifacts inherent to a multiple-speed lattice gas model in comparison with the continuum fluid result. These artifacts are present because of two physical reasons. First, while in the continuous Boltzmann gas, particles are free to move in any direction, the lattice case restricts particles to move only in a discrete set of directions that conform with the structure of the underlying lattice. Secondly, a real gas allows particles to have a continuous spectrum of speeds from zero to infinity (or the speed of light in relativistic treatments) while lattice gas models so far have been restricted to just one speed [14], [17],[18] or a few discrete speeds [39], [42]. In Chapter 5, we will examine how the rate of energy exchange collision coefficients, r_j, that were introduced into the general theory to recover detailed balance, can be exploited to remove these macroscopic artifacts in a finite but multiple speed system even though, microscopically, the reasons for the artifacts, as stated above, still exist.

In this Chapter, we examine the evolution of the lattice gas model as particles with higher and higher speeds are added to the algorithm without the rate factors. We show that the lattice algorithm approaches and then identically becomes the continuous model in the limit of infinite speeds being added to the lattice model. This means that the artifacts disappear in this limit. Intuitively, this seems possible since in the limiting case of the lattice model, particles of all speeds are permissable as in the continuous case. To show that this is true, there are a number of properties of the underlying lattice that are necessary. First of all, the lattice must possess enough symmetry that particles of all speeds can be represented. This requires that both the second and fourth order velocity tensors for all speeds are symmetric which results in the lattice exhibiting an isotropic stress *and* that there are no gaps in the particle energy spectrum. Both of these requirements are fortuitous properties of the underlying lattice we have chosen, the 4D FCHC lattice. The lattice must also allow energy exchange collisions between any groups of energies since it is these interactions that destroy evidence of the lattice, which it does. This makes the model 'discretely continuous' since the particle speeds are still discrete. A renormalization process allows us to reduce the width between speeds to an infinitesimally small value which permits passage to the full continuum. This is done in Section 4.1.2. Finally, we find that in the limit of the discrete continuum, the model possesses discrete *microscopic* Galilean invariance which allows translation of the lattice by any lattice vector without introducing discreteness artifacts. Thus a lattice gas model employed on the 4D FCHC lattice approaches a continuum model as higher speeds are added without the aid of the chemistry tricks needed for the finite speed case.

Although the lattice gas model approaches the continuum model as more speeds are added, the convergence is relatively slow. In fact, we find that the

convergence is linear with respect to the maximum energy allowed by the system. It was found that one must employ a model with at least seven different speeds in order to get any appreciable dynamical range where the artifacts are less than the error in the accuracy to which we can measure them, which is about 1% (this will be discussed in Chapter 7). This convergence may be aided by utilizing a hybrid model. Combining the chemistry tampering of present multi-speed lattice models with the convergence properties of a model with higher speeds allows the removal of discreteness artifacts from all of the conservation equations (mass, momentum *and* energy) as we show in Chapter 5.

The system we will be examining in this Chapter is the same one as in Chapter 3 except that we set $r_j \equiv 1$ for all j which now means that all collisions proceed at equal rates for forward and inverse processes and detailed balance is restored without the need for quasi-particle and quasi-hole definitions. The results are identical except that the zero-order isotropic Fermi-Dirac equilibrium density, eqn. (3.42), is now

$$N_j = \frac{1}{1 + exp(\alpha_0 m_j + \beta_0 \epsilon_j)}. \tag{4.1}$$

Another simplification that we use for the rest of the analysis is that the masses of all particles are identical and have the value unity. With $m_j \equiv 1$ for all species the microscopic kinetic energy, $\epsilon_j \equiv \frac{1}{2}c_j^2$, is the series of integers 0,1,2,... and is equivalent to the species index, $j \equiv \epsilon_j$. Thus a sum over species is equivalent to a sum over energies.

4.1 Continuum Values of the Artifacts

The approach to the continuum is begun by first making a series of assumptions about our system and then examining the consequences. Imagine that we can add particles of any desired energy (from zero to infinity) to our system to create a discrete infinite spectrum of particles speeds. This assumes that the FCHC lattice allows particles of any energy to be represented and that each set of velocity vectors for a particular speed possesses sufficient symmetry. That this is so will be shown in Section 4.1.1. Important macroscopic properties of the lattice fluid are calculated by taking moments of the microscopic distribution function. In the proposed discrete system, this is accomplished by taking a sum over discrete energies (from zero to infinity). For the sake of argument, imagine that these discrete sums can be turned into integrals over an energy variable ranging from zero to infinity and that the connection can be made in the following way. Using the definition for density as an example, (eqn. (3.52)) is transformed

$$\rho = \sum_{j=0}^{\infty} d_j N_j \Longrightarrow \int_0^{\infty} cE^n N dE \equiv \langle E^n \rangle \tag{4.2}$$

so that the sum over species j is replaced with an integral over energy which is denoted by E in the continuum case. As indicated, we have assigned the masses of all particles to be unity. The microscopic zero-order distribution function is now simply N where

$$N = \frac{1}{1 + a\exp(E/T)} \tag{4.3}$$

as indicated in eqn. (4.1) where $a \equiv \epsilon^{\alpha_0}$, the inverse fugacity, and we have identified $\beta_0 \equiv 1/T$, the temperature in energy units. The final identification is that the number of directions per site for species j (d_j) can be represented as proportional to the energy of that species raised to some power n. It is conjectured that the

value of this exponent should be

$$n = \frac{D-2}{2} \tag{4.4}$$

where D is the number of dimensions. Numerical and theoretical illustration of this will be presented in Section 4.1.1. Heuristically, if one imagines that d_j represents the density of states for species j, then this is equal to the number of velocity vectors that orignate from the origin of some space of dimension D and terminate at a distance between $\mathbf{v}$ and $\mathbf{v} + d\mathbf{v}$ so that the equivalent energy of all such vectors (where $m_j \equiv 1$) is j. The number of such vectors is equal to the surface area of a hypersphere of radius $\mathbf{v}$ which is proportional to v^{D-1}. If we then transfer to energy coordinates where $E \propto v^2$ then

$$\begin{aligned} d_j \Delta j &\propto v^{D-1} dv \\ &\propto v^{D-2} v dv \\ &\propto E^{\frac{D-2}{2}} dE \end{aligned} \tag{4.5}$$

so that d_j has the suggested behaviour. We will continue with the general exponent n and calculate what values of n (if any) will give the desired continuum values of the artifacts. The precise value of the proportional constant is not important for this analysis since this value cancels from the artifact expressions. A numerical value of this constant is calculated in the next section and is shown to be equal to a theoretical value that may be derived using number theory.

In a similar manner we can comprise a catalogue of all the moments that appear in the artifacts of Section 3.2. The moment notation of eqn. (3.51) requires sums over quantities of the form $N_j N_j^{(l)} = N^{(l)}$, in the notation of this Chapter, where l denotes the order of the derivative to be taken. These sums over various derivatives of the microscopic distribution function, upon being transferred into

integrals, can be partially performed using integration by parts to remove the derivatives from the moment definition (since the distribution function vanishes as the energy approaches infinity)

$$\begin{aligned}
U_p = &\quad \int_0^\infty cE^n ENdE &&\equiv \langle E^{n+1}\rangle \\
(1,1)_1 = &\quad n\int_0^\infty cE^{n-1}NdE &&\equiv n\langle E^{n-1}\rangle \\
(1,\epsilon)_1 = &\quad (n+1)\int_0^\infty cE^n NdE &&\equiv (n+1)\langle E^n\rangle \\
(\epsilon,\epsilon)_1 = &\quad (n+2)\int_0^\infty cE^{n+1}NdE &&\equiv (n+2)\langle E^{n+1}\rangle \\
(1,\epsilon)_2 = &\quad (n+1)n\int_0^\infty cE^{n-1}NdE &&\equiv n(n+1)\langle E^{n-1}\rangle \\
(\epsilon,\epsilon)_2 = &\quad (n+2)(n+1)\int_0^\infty cE^n NdE &&\equiv (n+1)(n+2)\langle E^n\rangle \\
(\epsilon,\epsilon^2)_2 = &\quad (n+2)(n+3)\int_0^\infty cE^{n+1}NdE &&\equiv (n+2)(n+3)\langle E^{n+1}\rangle \\
(\epsilon,\epsilon)_3 = &\quad (n+2)(n+1)n\int_0^\infty cE^{n-1}NdE &&\equiv n(n+1)(n+2)\langle E^{n-1}\rangle \\
(\epsilon,\epsilon^2)_3 = &\quad (n+3)(n+2)(n+1)\int_0^\infty cE^n NdE &&\equiv (n+1)(n+2)(n+3)\langle E^n\rangle.
\end{aligned} \tag{4.6}$$

We now calculate the continuum values of the artifacts g, g' and γ. We start with the expression for g (eqn (3.70)). Plugging in the appropriate moments from above we find that g is a function only of $\langle E^n\rangle$ moments which then cancel. The expression reduces to

$$g = \frac{D}{D+2}\frac{n+2}{n+1}. \tag{4.7}$$

This artifact is removed when $g = 1$ or when

$$n = \frac{D-2}{2} \tag{4.8}$$

which is the value conjectured in eqn (4.4). Next, the expression for γ (eqn (3.74)), in terms of the continuous moments, also permits some convenient cancellations and reduces to

$$\gamma = \frac{n+2}{n+1}. \tag{4.9}$$

The continuum value of γ is (D+2)/D. When we make the calculated value of γ equal to its correct value we get an expression equivalent to the expression for g calculated above. Thus, when $n = (D-2)/2$ both the g and γ artifacts are removed.

Finally, we examine the rather unwieldy expression for g' (eqn (3.75)). After plugging in the appropriate moments and performing some algebra we find

$$g' = \frac{n+2}{(D+2)(n+1)^2}\left[n(DK(n,a)+2) + (\frac{D^2}{2} - D)(1-K(n,a)) + 2\right] \quad (4.10)$$

where K(n,a) is a function of the energy moments and has the following form

$$K(n,a) = \frac{n}{n+1}\frac{\langle E^{n+1}\rangle\langle E^{n-1}\rangle}{\langle E^n\rangle^2}. \quad (4.11)$$

When the distribution function, N, has Fermi-Dirac form, $K(n,a)$ is a monotonically increasing function of n with a value at n=0 between 0.75 and 0.96 (dependent on $a \equiv e^{\alpha_0}$) which then approaches the value 1.00 asymptotically as $n \to \infty$. Appendix B discusses the behaviour of this function. When we now try to remove this artifact by making $g' = 1$ we find a quadratic equation for n with the roots

$$n = \frac{D-2}{2} \quad (4.12)$$

once again and

$$n = -2\left[1 - \frac{1/D}{1-K(n,a)}\right] \quad (4.13)$$

which is actually an implicit solution for n. The only roots from this second equation are for $a \ll 1.0$ where the solution for n is a function of a. The number of directions for a particular energy, which is a function of the underlying lattice, cannot depend on a characteristic property of the fluid such as the inverse fugacity. Thus, this second root is extraneous and can be ignored (see Appendix B).

We are left with the result that if we can make the transformation via a limiting process that will allow us to change our moment sums into integrals where the number of directions per site, d_j, is given the explicit relation of being proportional to $E^{(j-2)/2}$, then *all* three of the artifacts g, g' and γ disappear. If it is possible to develop a limiting procedure for our model that allows the addition of particle speeds up to infinity and transforms our discrete system into a continuum, our model will give true hydrodynamic continuum behaviour *exactly.* It is not surprising that once we have passed our discrete system to the continuum that the artifacts disappear because we could have done the same low Mach number expansion that we utilized here in the continuum where, of course, no artifacts would have resulted. What *is* surprising is that the model allows such a limiting procedure to occur. The demonstration of this is the topic of the next few sections.

4.1.1 Sums to Integrals - Preliminaries

Before proceeding with the mechanics of the limiting procedure we state and prove a few important characteristics of the underlying 4D FCHC lattice that make such a procedure possible. This lattice is defined as the set of signed integers (x_1, x_2, x_3, x_4) such that $(x_1 + x_2 + x_3 + x_4)$ is even. Because of this, it is possible to show that the magnitude of this vector is likewise also even. In fact, *only* quadruples that sum to an even number can give vector magnitudes (sum of the squares of the coordinates) that are even. The species index, j, is equivalent to the microscopic kinetic energy when the mass of all particles is given the value one

$$j \equiv \epsilon_j = \tfrac{1}{2}c_j^2 = \frac{1}{2}(x_1^2 + x_2^2 + x_3^2 + x_4^2) \tag{4.14}$$

which forces ϵ_j to be integer. From now on, j will be understood to stand for particle energy and we will use the terms particle 'energy' and particle 'species' interchangeably. We wish all energies to be represented in our model if a continuum spectrum is to be realized. This requires that all even numbers may be represented as the sum of four squares with the sum of the four numbers also being even. This is equivalent to requiring that every number can be represented as the sum of four squares. This conjecture, which has its roots in elementary number theory dating back to the time of Diophantus. was proved by J.L. Lagrange, with some help from Euler, in 1770 [44]. This is the minimum number of squares necessary to accomplish this. Because the sum of the four squares may take *any* even number, the energy, which is one-half of this value, may take any integral value. Thus, the species index, j, which is also the sequence of integers, is equivalent to the energy index. Since the macroscopic properties of the system are calculated by summing over the species index, or equivalently the particle energy, we find that the FCHC lattice allows all integer energies to be represented.

Knowing now that every energy may be represented in our model, we now examine the value d_j, the number of directions for each energy or equivalently, the number of ways the even integer $2j$ may be represented as the sum of four squares. In Section 4.1 we conjectured that

$$\begin{aligned} d_j &= c\epsilon_j^{\frac{D-2}{D}} \\ &= c\epsilon_j \end{aligned} \tag{4.15}$$

for D=4. We now show this experimentally and calculate the proportionality constant. In Figure 4.1, we see d_j plotted as a function of energy up to $\epsilon_{max} = 1024$ where d_j was calculated explicitly for each energy. For example, the vectors that make up a energy=1 particle are obtained from $(\pm 1, \pm 1, 0, 0)$ upon permuting the

indices and signs. Thus, $d_1 = 24$. Similarly, there are two separate vectors with energy=2, $(\pm 2, 0, 0, 0)$ and $(\pm 1, \pm 1, \pm 1, \pm 1)$, which, when all the permutations are counted, also gives $d_2 = 24$. Although there does not appear to be a linear relationship between the two quantities, if we form the accumulated sum of this quantity,

$$d_j sum = \sum_{k=1}^{j} d_k \tag{4.16}$$

and plot this as a function of energy, see Figure 4.2, a quadratic relationship between these two variables becomes apparent with a best fit resulting in

$$d_j sum = 9.88\epsilon_j^2. \tag{4.17}$$

with a very small fitting error in the slope of about 0.3%. To find the average value of d_j, denoted $\langle d_j \rangle$, from the above relation we note that

$$\sum_{k=1}^{j} k = \frac{j(j+1)}{2} \sim \tfrac{1}{2} j^2 \tag{4.18}$$

for large j so that the average can be deduced from

$$\sum_{k=1}^{j} d_k = \sum_{k=1}^{j} \langle d_k \rangle = 9.88\epsilon_j^2 \tag{4.19}$$

as

$$\langle d_j \rangle \sim 19.76\epsilon_j. \tag{4.20}$$

This is the *average* order of d_j if a large number of energies are included. This is further justification of our conjecture concerning d_j in eqn. (4.15). It has been found that the actual values of d_j, as shown in Figure 4.1, may be calculated using the following procedure.

Given an energy $\epsilon_j = j$, the number of different direction vectors, d_j is

$$d_j = 24\sigma(k) \qquad \text{where} \quad j = 2^n k,\ n \geq 0 \tag{4.21}$$

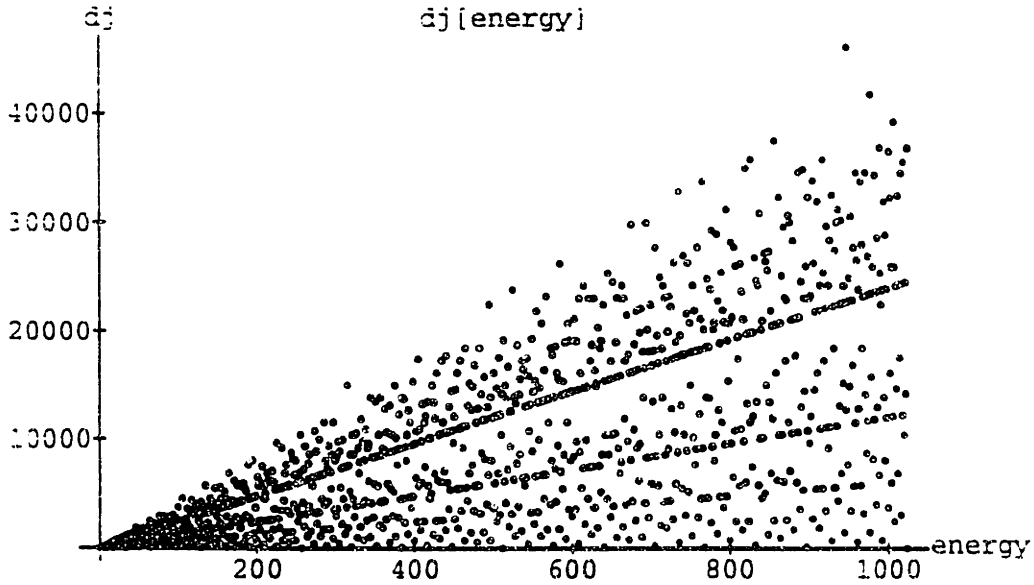

Figure 4.1: The number of directions for species j, d_j as a function of particle energy ranging from 0 to 1024.

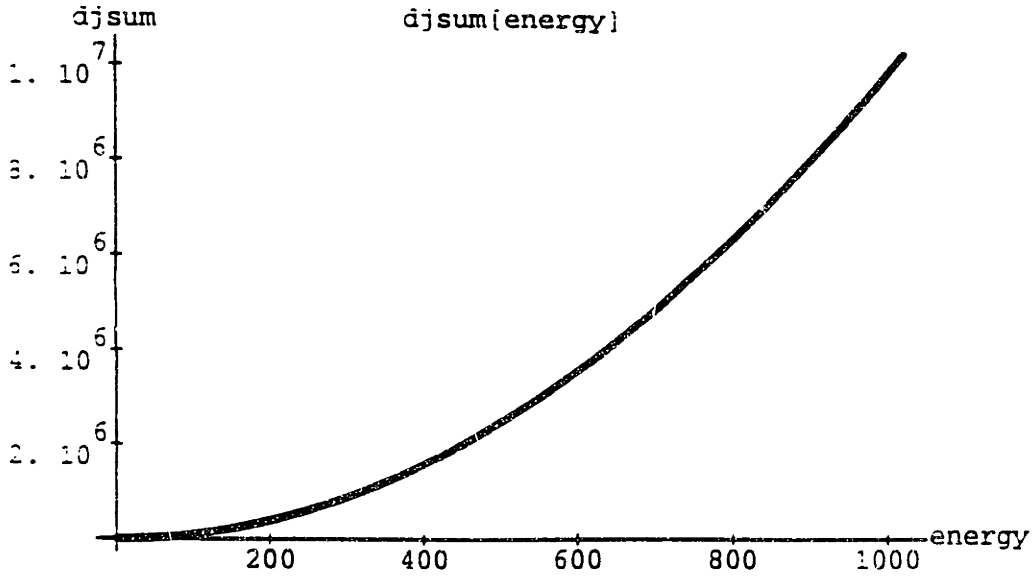

Figure 4.2: The accumulated sum of the number of directions for a given species j as a function of energy. The relationship is quadratic with $d_j sum = 9.88\epsilon_j^2$ being the best fit.

where $\sigma(k)$ is the sum of all the positive divisors of k, including 1 and k. It is possible to calculate $\sigma(k)$ explicitly once k has been completely factorised into prime numbers

$$k = p_1^{\alpha_1} p_2^{\alpha_2} p_3^{\alpha_3} ... p_n^{\alpha_n} \tag{4.22}$$

where $p_i \neq 2$ since all factors of 2 have been removed from j to give k. If k=1, $\sigma(1) = 1$, for $k > 1$ we find

$$\sigma(k) = \left(\frac{p_1^{\alpha_1+1} - 1}{p_1 - 1}\right)\left(\frac{p_2^{\alpha_2+1} - 1}{p_2 - 1}\right) \cdots \left(\frac{p_n^{\alpha_n+1} - 1}{p_n - 1}\right). \tag{4.23}$$

Equation (4.21), rewritten equivalently as

$$d_n = 24\sigma^o(n) \tag{4.24}$$

where $\sigma^o(n)$ is the sum of only the *odd* divisors of n, is another classical result of number theory first proved by Jacobi in 1828[44] as a consequence of his studies in the theory of elliptic functions. Actually, the result in eqn. (4.24) holds only for *even* values of n while a slightly different result holds for odd values of n. As shown in eqn. (4.14) the quantity we are really representing as the sum of four squares is $2j$ which is always even, as previously described. The factor of 2 only contributes *even* divisors so that it is irrelevant for calculating d_n, $d_{2j} = d_j$. A further dip into number theory will allow us to come up with theoretical values for the average orders of $d_j sum$ and d_j. It is known[44] that the average order of $\sigma(n)$, the sum of the divisors of n, is

$$\sigma(1) + \sigma(2) + ... + \sigma(n) = \frac{1}{12}\pi^2 n^2 + \mathcal{O}(n \log n). \tag{4.25}$$

To estimate the average order of $d_j sum$ however we only want to sum the *odd* divisors of the numbers 1 through n. The relationship between the sum of the

odd divisors and the above expression was found to be

$$\frac{\sum_{j=1}^{N}\sigma^{o}(j)}{\sum_{j=1}^{N}\sigma(j)} = \frac{\frac{1}{24}\sum_{j=1}^{N}d_j}{\sum_{j=1}^{N}\sigma(j)} \sim \frac{1}{2} \tag{4.26}$$

where N is some large integer ($N = 1024$ was used) so that $d_j sum$ is

$$d_j sum = \sum_{k=1}^{j} d_k = 24\sum_{k=1}^{j}\sigma^{o}(k) \sim 24\sum_{k=1}^{j}(\tfrac{1}{2})\sigma(k) \sim 24(\tfrac{1}{2})\frac{1}{12}\pi^2 j^2 \sim \pi^2 j^2. \tag{4.27}$$

Consequently, the average order of d_j is

$$d_j \sim 2\pi^2 j. \tag{4.28}$$

Numerically, $d_j sum \sim 9.87j^2$ and $d_j \sim 19.74j$ which agree with the values calculated 'experimentally' in eqns. (4.17) and (4.20) respectively within the error of the fit. As a final point on this topic, we calculate the above two relations using a geometric argument following Hardy[44]. The quantity d_n represents the number of lattice points on the hypersphere defined by $x_1^2 + x_2^2 + x_3^2 + x_4^2 = n$. The sum $d_j sum$ is one less (due to the value $d_0 = 1$) than the number of lattice points inside or on this same hypersphere. If we associate with each such lattice point a lattice hypercube in an uniform manner, the volume of the marked hypercubes is of the same order as the volume of the related hypersphere. A straightforward series of integrations illustrates that the volume of a four-dimensional hypercube with radius n is $\frac{\pi^2 n^2}{2}$. For our problem, we only want to include the *even* integers, i.e. sum over $2j$ where j ranges from 1 to $\frac{n}{2}$. A reasonable conjecture is that the even and odd radii contribute equally to the accumulation of volume inside the hypersphere. Thus, the value of $d_j sum$ should be one-half the total volume where $n = 2j$

$$d_j sum = \sum_{k=1}^{j} d_k \sim \tfrac{1}{2}(\frac{\pi^2(2j)^2}{2}) \sim \pi^2 j^2 \tag{4.29}$$

the same value calculated using the results of number theory.

We now see that the value of the proportionality constant in eqn. (4.15) is $2\pi^2$. Furthermore, with D=4, the relationship between d_j and the energy j is of linear order, precisely the relationship required to remove the lattice artifacts.

The second fortunate property of the FCHC lattice is that it is highly symmetric. One of the five principal artifacts of discreteness, as stated in Chapter 2, is that the stress tensor of the fluid may be non-isotropic due to preferred directions caused by the presence of the lattice. To ensure that this is not the case, the allowed velocity vectors, $\mathbf{c}_{ji}$, must give rise to isotropic tensors of both the second and fourth rank when summed over direction space for each energy *individually*. The conditions for this property were given in Chapter 3.2. They are restated here for convenience

$$\sum_i \mathbf{c}_{ji}\mathbf{c}_{ji} = \frac{d_j}{D}c_j^2\mathbf{I}, \tag{4.30}$$

and

$$\sum_i \mathbf{c}_{ji}\mathbf{c}_{ji}\mathbf{c}_{ji}\mathbf{c}_{ji} = \frac{d_j}{D(D+2)}c_j^4\Delta^{(4)}, \tag{4.31}$$

where $\Delta^{(4)}$ is the completely symmetric 4th rank tensor, as defined in eqn. (3.48),

$$\Delta^{(4)}_{\alpha\beta\gamma\delta} \equiv \delta_{\alpha\beta}\delta_{\gamma\delta} + \delta_{\alpha\gamma}\delta_{\beta\delta} + \delta_{\alpha\delta}\delta_{\gamma\beta}. \tag{4.32}$$

Wolfram[22], in an examination of the symmetry groups of the 4D FCHC lattice, states that the 24 vectors obtained from the six permutations of $(\pm1, \pm1, 0, 0)$ (what we would call a type or energy 1 vector) and the union of $(\pm2, 0, 0, 0)$ and its four permutations with the 16 vectors created by $(\pm1, \pm1, \pm1, \pm1)$ ($j = 2$ vectors) both satisfy the above symmetric relations separately. We would now like to examine if this symmetry holds for higher energies.

First of all, we look at the second rank tensor calculated using the left side of eqn. (4.30) for general energy j. All off-diagonal terms of this tensor are zero

since the sum over direction space allows each element in the vector $\mathbf{c}_{ji}$ to appear in each component with either sign an equal number of times. Thus a sum over non-equal elements will have each possible pair of components appearing with both positive and negative sign which then cancels, giving a total sum of zero. Likewise, all of the diagonal terms are equal since all elements appear in each component an equal number of times. We pick a particular direction component, α, and sum $c_{ji\alpha}^2$ over all directions. There are d_j terms which can be grouped into D (the number of dimensions) groups. Each one of these groups gives the sum c_j^2 (eqn. (4.14)). Thus we have shown that

$$\sum_i \mathbf{c}_{ji}\mathbf{c}_{ji} = \frac{d_j}{D}c_j^2\mathbf{I}. \tag{4.33}$$

for all energies j. Second order symmetry does hold for all energies in the 4D FCHC lattice.

Showing that fourth-order symmetry also holds for the FCHC lattice is a little more complicated and once again establishes a connection with number theory. Unlike the second order symmetry relation that holds for any lattice that allows both positive and negative components of the velocity vectors, fourth-order symmetry holds generally *only* for the four-dimensional FCHC lattice we are using as the framework for our lattice gas algorithm.

The fourth-order tensor calculated using the left side of eqn. (4.31) has entries that can be categorised into two groups. First of all, entries whose indices are identical in pairs. For $D = 4$, this includes entries where all four components are identical and entries that have two pairs of equal components. The second group includes all the entries not included in the first, that is entries with indices where a component appears an odd number of times. For $D = 4$ this includes entries where: 1) all four components are unequal, 2) three components are the

same, the other different and 3) one pair of equal components but the other two differ from each other. For the same reason that forced the off-diagonal elements of the second-order tensor to be zero, all elements that fall into the second group as described above also identically vanish when summed over all directions. We examine the two elements of the first group individually.

The number of different velocity vectors with energy j may be summarised in the list

$$(x_{1k}, x_{2k}, x_{3k}, x_{4k}) \tag{4.34}$$

where

$$x_{1k} \geq x_{2k} \geq x_{3k} \geq x_{4k} \geq 0 \tag{4.35}$$

for a set of vectors $k = 1$ to k_{max} that all have the same energy j. For $j = 1$, $k_{max} = 1$ and for $j = 2$, $k_{max} = 2$. For the same reason that caused all the diagonal elements of the second order tensor to be equal, all elements within each of these two sets are equal to all other members of that set. Consequently, we only need to examine one member of each of these sets. When all four components are equal in the fourth order tensor, we find that within the permutations allowed by a particular velocity vector of the set k, a sum over all fourth powers of the elements of these vectors is equivalent to summing over the fourth powers of the components of the velocity vector k and then dividing by D and multiplying by the number of permutations of the vector k. If we sum over all k we find that

$$\sum_{i=1}^{d_j} c_{ji\alpha}^4 = \sum_{i=1}^{d_j} \sum_{\alpha=1}^{D} \frac{x_{i\alpha}^4}{D}. \tag{4.36}$$

When there are two equal pairs of components in the fourth order tensor, denoted by subscripts α and β say, we find that the sum of the product of the squares of the α and β components of all velocity vectors within each vector k and its

permutations equals the sum of the product of the squares of separate components of the vector k taken two at a time multiplied by the number of permutations of this vector and divided by the number of different pairs of D objects. If we sum over all k we find that

$$\sum_{i=1}^{d_j} c_{ji\alpha}^2 c_{ji\beta}^2 = \sum_{i=1}^{d_j} \sum_{\alpha=1}^{D-1} \sum_{\beta=\alpha+1}^{D} \frac{x_{i\alpha}^2 x_{i\beta}^2}{\frac{D(D-1)}{2}} \tag{4.37}$$

where the expression $\frac{D(D-1)}{2}$ is the number of different pairs that can be formed from D objects. We now make use of the identity

$$\left(\sum_{\alpha=1}^{D} x_{i\alpha}^2\right)^2 = c_j^4 = \sum_{\alpha=1}^{D} x_{i\alpha}^4 + 2 \sum_{\alpha=1}^{D-1} \sum_{\beta=\alpha+1}^{D} x_{i\alpha}^2 x_{i\beta}^2 \tag{4.38}$$

by solving the above for the second term on the right side and substituting it into eqn. (4.37). The result is

$$\sum_{i=1}^{d_j} c_{ji\alpha}^2 c_{ji\beta}^2 = \frac{d_j c_j^4}{D(D-1)} - \frac{1}{(D-1)} \sum_{i=1}^{d_j} \sum_{\alpha=1}^{D} \frac{x_{i\alpha}^4}{D}. \tag{4.39}$$

The completely symmetric fourth-order tensor as given by eqn. (4.32) has the value 3 when all four components are equal, the value 1 when there are two different pairs of equal components and zero otherwise. This means that we require the left side of eqn. (4.39) to be one-third of the left side of eqn. (4.36). Equating the two

$$\frac{d_j c_j^4}{D(D-1)} - \frac{1}{(D-1)} \sum_{i=1}^{d_j} \sum_{\alpha=1}^{D} \frac{x_{i\alpha}^4}{D} = \frac{1}{3} \sum_{i=1}^{d_j} \sum_{\alpha=1}^{D} \frac{x_{i\alpha}^4}{D} \tag{4.40}$$

and solving for the right side gives

$$\sum_{i=1}^{d_j} \sum_{\alpha=1}^{D} \frac{x_{i\alpha}^4}{D} = \sum_{i=1}^{d_j} c_{ji\alpha}^4 = \frac{3 d_j c_j^4}{D(D+2)} \tag{4.41}$$

which is exactly the result needed for fourth order symmetry (eqn. (4.31)). Removing the common divisor of D we require that

$$\sum_{i=1}^{d_j} \sum_{\alpha=1}^{D} x_{i\alpha}^4 = \frac{3}{D+2} d_j c_j^4. \tag{4.42}$$

This can be compared with a relevant result from number theory, written using our notation

$$\sum_{i=1}^{d_j}(x_1^4 + x_2^4 + x_3^4 + x_4^4) = \tfrac{1}{2}d_j c_j^4. \tag{4.43}$$

when c_j^2 is any *even* integer. This result was stated by Liouville in 1858 but was first proved by Stern[45] in 1889. A proof of the above relation is given in Appendix C. As previously stated, c_j^2 is only an even integer. Equation (4.42) reduces to the above *only* when $D = 4$ and c_j^2 is even, the ingredients of the 4D FCHC lattice. Thus the 4D FCHC lattice ensures that the allowed velocity vectors, $\mathbf{c}_{ji}$, give rise to isotropic tensors of both the second and fourth rank when summed over direction space for each and any energy individually. What is remarkable is that the 4D FCHC lattice is unique in having this property. It is known [23, 22] that in five and higher dimensions the only regular polytopes that exist *do not* have the required fourth order symmetry for the base set of vectors that comprise these polytopes. Furthermore, in four dimensions[1] the only regular lattice with the required fourth order symmetry has FCHC form. Thus, we conclude that the 4D FCHC lattice is the *only* regular lattice that possesses all of the properties necessary to allow an extension of the lattice gas algorithm to infinite speeds.

This may be contrasted with two- (HPP[11],FHP[13]) or three-dimensional lattices that either do not have the required 4th order symmetry (in HPP or the 3D case) or cannot represent particles of higher energies (FHP). Even if the 3D lattice had the requisite symmetry this lattice could not represent all integral energies as it is another known result of number theory [44] that all integers of the form $4^n(8k + 7), n, k \geq 0$ *cannot* be represented as the sum of three squares.

[1]the lowest dimensional system that can represent all integral energies

This means there would be 'gaps' in the 3D energy spectrum amounting to at least one out of every eight of the energies. which prevents a complete spectrum from being represented.

In summary, we have shown that sums over particle species are equivalent to sums over particle energies, that the 4-dimensional FCHC lattice we are using allows *all* integral energies to be represented and that the set of velocity vectors for each energy, $\mathbf{c}_{ji}$ separately gives rise to isotropic tensors of both the second and fourth rank when summed over direction and it is the *only* regular lattice that has these properties. All of these properties are required if we are to make a connection between the discrete lattice gas algorithm and the true continuum. That such a lattice exists and, moreover, that it is unique, is a completely unexpected and remarkable result that permits the extension of the lattice gas algorithm to infinite speeds. Knowing that this extension is possible, we now perform a standard renormalization procedure that allows us to remove the discreteness artifacts from the macroscopic behaviour of the lattice gas algorithm entirely.

4.1.2 Sums to Integrals - The Limiting Procedure

We have shown in Section 4.1 that the artifacts disappear if the correct average value of the number of directions, d_j, is used and there is an infinite continuum of energies. This requires that the defining moments are integrals rather than discrete sums. The difference between a sum over some function and an integral over the same function is given by the *Euler-Maclaurin Summation Formula* [46]

$$\hat{T}(h) = \int_a^b f(x)dx + \frac{h^2}{12}[f'(b) - f'(a)] - \frac{h^4}{720}[f'''(b) - f'''(a)] + \ldots \qquad (4.44)$$

Trapezoidal Sum Approximation

Of An Integral with Step Size=h

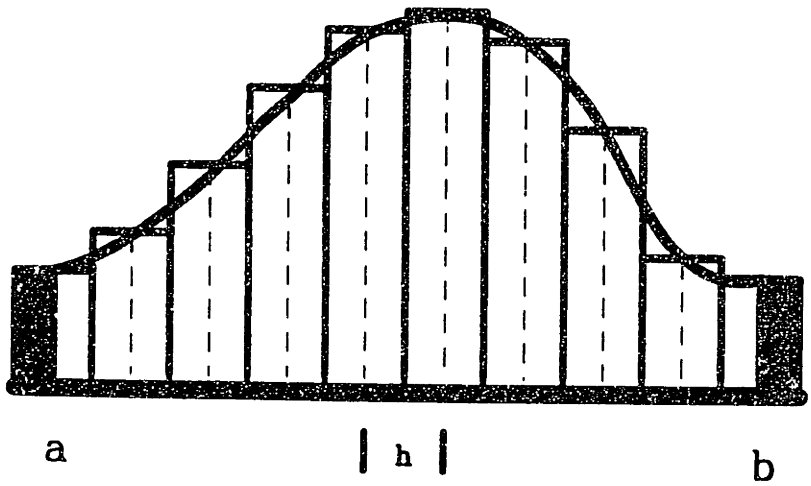

Figure 4.3: Illustration of the Euler-Maclaurin Summation Formula. The area under the curve is approximated by the sum under the rectangles. The error in accuracy is related to the step size, h.

where $\hat{T}(h)$ is the trapezoidal sum defined as

$$\hat{T}(h) = h \sum_{i=a}^{b} f_i - \tfrac{1}{2} h(f_a + f_b) \tag{4.45}$$

where h is the step size between adjacent values of f_i, see Figure 4.3. In the limiting process we are examining, we sum over all positive values of energy so that the limits are $a = 0$ and $b = \infty$. Secondly, we replace d_j with its average expression, as given in eqn. (4.15), since large values of energy are involved. As a consequence, the second and third terms in the definition of the trapezoidal sum, $\hat{T}(h)$ are zero. Finally, relabel the step size, h, as the step in energy space, $\Delta\epsilon$.

In the present discrete system. $\Delta\epsilon = 1$. The Euler-Maclaurin formula reduces to

$$\Delta\epsilon \sum_{\epsilon_j=0}^{\infty} f(\epsilon_j) = \int_0^{\infty} f(E)dE - \frac{f'(0)}{12}\Delta\epsilon^2 + \frac{f'''(0)}{720}\Delta\epsilon^4 - ... \qquad (4.46)$$

which illustrates that the error between the sum and the integral is second order in the step size. We see that if we can re-scale the width between energies so that $\Delta\epsilon \to 0$ then the sum becomes identical to the integral. This is, of course, the way an integral is *defined.* Examine the density relation where the largest value of energy is ϵ_{max} (we will ultimately take the limit $\epsilon_{max} \to \infty$)

$$\rho = \sum_{\epsilon_j=0}^{\epsilon_{max}} d_j N_j = \sum_{\epsilon_j=0}^{\epsilon_{max}} c\epsilon_j N_j \Delta\epsilon \qquad (4.47)$$

where N_j is given by eqn. (4.1), here slightly rewritten as

$$N_j = \frac{1}{1 + a \exp \epsilon_j/T} \qquad (4.48)$$

with $a \equiv e^{\alpha_0}$, the inverse fugacity, which is independent of energy and $\beta_0 = 1/T$. We define a rescaled energy, E, and temperature, T'

$$E \equiv \frac{\epsilon_j}{\epsilon_{max}^n} \qquad (4.49)$$

and

$$T' \equiv \frac{T}{\epsilon_{max}^n} \qquad (4.50)$$

where n is a real number arbitrarily close to, but less than, the value 1. For practical purposes, we may think of $n \equiv 1$ but for the purpose of the theoretical treatment we are performing, $n \equiv 1 - \delta^2$ where δ is arbitrarily small and real. Notice that

$$\frac{E}{T'} = \frac{\epsilon_j}{T} \qquad (4.51)$$

so that

$$N_j = \frac{1}{1 + a \exp \epsilon_j/T} = \frac{1}{1 + a \exp E/T'} \equiv N_E \qquad (4.52)$$

and the distribution function is unaffected by the rescaling. As ϵ_{max} is increased, we also increase T so that the rescaled temperature T' remains finite. We now perform the energy rescaling of eqn. (4.49) on the other elements of the density sum. In particular, we define

$$\Delta\epsilon = 1 = \frac{1}{\epsilon_{max}^n}\epsilon_{max}^n \equiv \Delta E \epsilon_{max}^n. \tag{4.53}$$

The density sum is now

$$\rho = \left[\sum_{E=0}^{\epsilon_{max}^{1-n}} cEN_E\Delta E\right]\epsilon_{max}^{2n} \tag{4.54}$$

where the sum is over the variable E and increments in steps of ΔE. This procedure can be repeated for all the moments that are needed, as listed in eqn. (4.6). We can make the notation of eqn. (3.51) very compact

$$(\epsilon^m)_k = (-1)^k \sum_{\epsilon_j=0}^{\epsilon_{max}} d_j N_j^{(k)} \epsilon_j^m \tag{4.55}$$

where k indicates that the *kth* derivative of N_j should be taken, i.e. $N_j^{(3)} = N_j N_j'''$ in the notation of Section 3.2. When $k = 0$ we get the zeroth-order moments for density (m=0) and energy (m=1). The re-scaled moments have the following form

$$\begin{aligned}(\epsilon^m)_k &= \left[(-1)^k \sum_{E=0}^{\epsilon_{max}^{1-n}} cEN_E^{(k)} E^m \Delta E\right]\epsilon_{max}^{n(2+m)} \\ (\epsilon^m)_k &= (E^m)_k \epsilon_{max}^{n(2+m)}.\end{aligned} \tag{4.56}$$

We now take the limit as $\epsilon_{max} \to \infty$. We see that the expression outside the square brackets, ϵ_{max} raised to some positive exponent, also approaches infinity. When we plug these expressions into the defining relations for the artifacts, eqns. (3.70), (3.74), and (3.75), the ϵ_{max} terms cancel. If we rescale the left-hand side of equation (4.56) with $\epsilon_{max}^{n(2+m)}$ we are left with the finite expression on the right-hand side, $(E^m)_k$, which is the new re-scaled generalized finite moment expression.

The step size, ΔE becomes infinitesimally small so that the difference between the sum and the integral, as given by the Euler-Maclaurin formula, eqn. (4.46), disappears. This means that

$$\lim_{\epsilon_{max}\to\infty} \sum_{E=0}^{\epsilon_{max}^{1-n}} f(E)\Delta E = \int_0^\infty f(E)dE \tag{4.57}$$

where $\lim_{\epsilon_{max}\to\infty} \epsilon_{max}^{1-n} = \infty$ because $1 - n = \delta^2 > 0$. The expressions for $(E^m)_k$, which are now integrals, are identical to the relations in eqn. (4.6). As calculated in Section 4.1, these relations for the moments cause the artifacts to become the correct continuum values. As an illustration of this, values of g and γ were calculated as functions of temperature, T' and the inverse fugacity $a \equiv e^{\alpha_0}$ that make up the continuum distribution function N_E, eqn. (4.52) with $\epsilon_{max} = 160$, a relatively large value. The results, as shown in Figure 4.4 for g and Figure 4.5 for γ, demonstrate that the continuum values, $g = 1$ and $\gamma = \frac{D+2}{D} = 1.5$ for $D = 4$, are reproduced for values of T' much smaller than ϵ_{max}. Similar behaviour is observed for the third artifact, g'. Truncation errors due to the finite range of energy cause g and γ to deviate from their continuum values at higher temperatures where contributions to the integral beyond ϵ_{max} are significant. A complete continuum is needed to make the artifacts disappear for all temperatures.

We have shown that the lattice gas model employed on the four-dimensional FCHC lattice directly and seamlessly reproduces true hydrodynamic behaviour as the upper bound on particle energy approaches infinity. Because this model can be made to approach a continuum via the limiting process described above, it is natural that the artifacts should disappear since the same low Mach number expansion that was used to generate expressions for the artifacts in this discrete system could have been used in the continuum case, where no artifacts would have resulted.

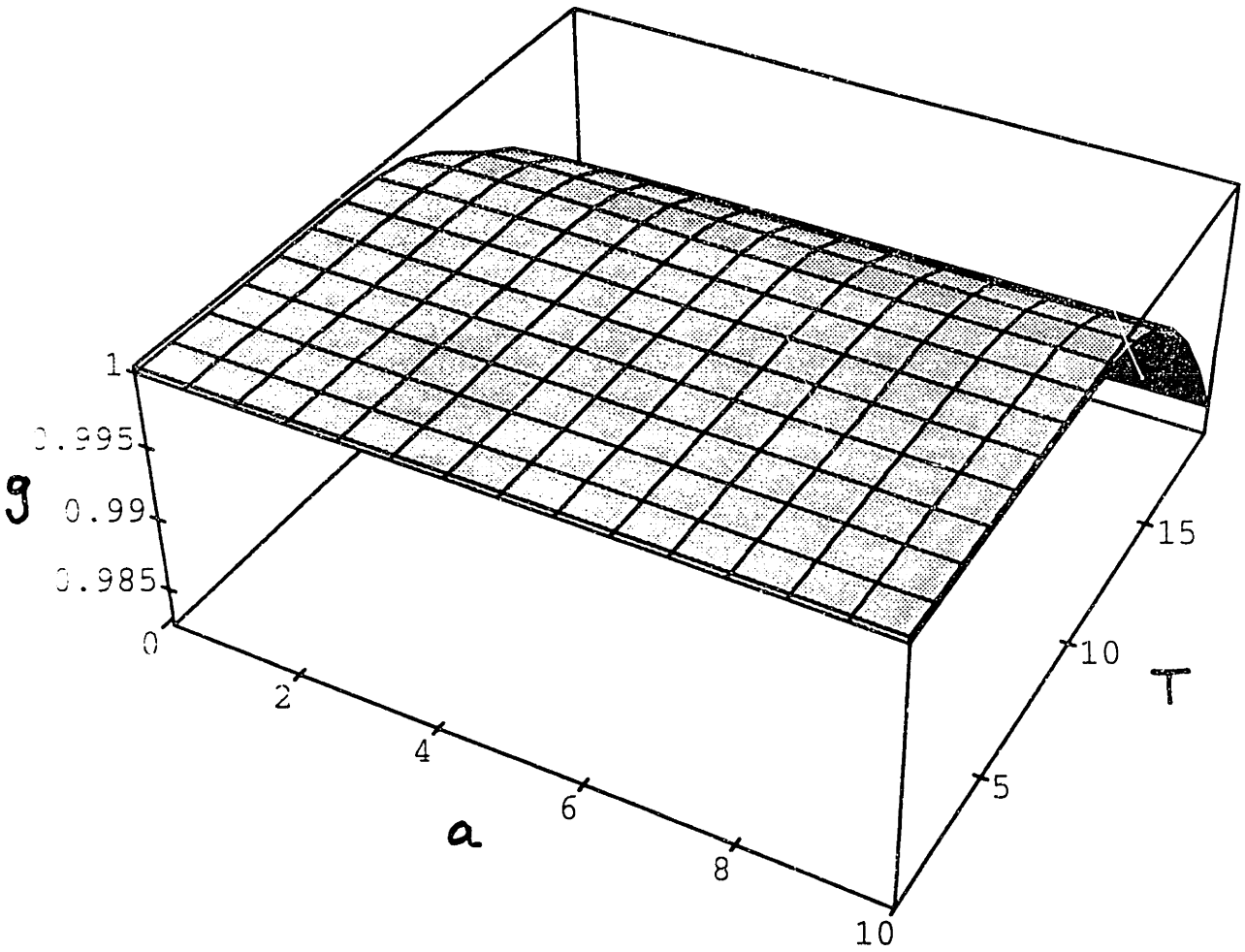

Figure 4.4: Calculation of g using integrals with $\epsilon_{max} = 160$ for $0 < a \leq 10$ and $0 < T \leq 19.2$. The result shows that this artifact is very close to its continuum value (1.0) at temperatures much less then the maximum energy.

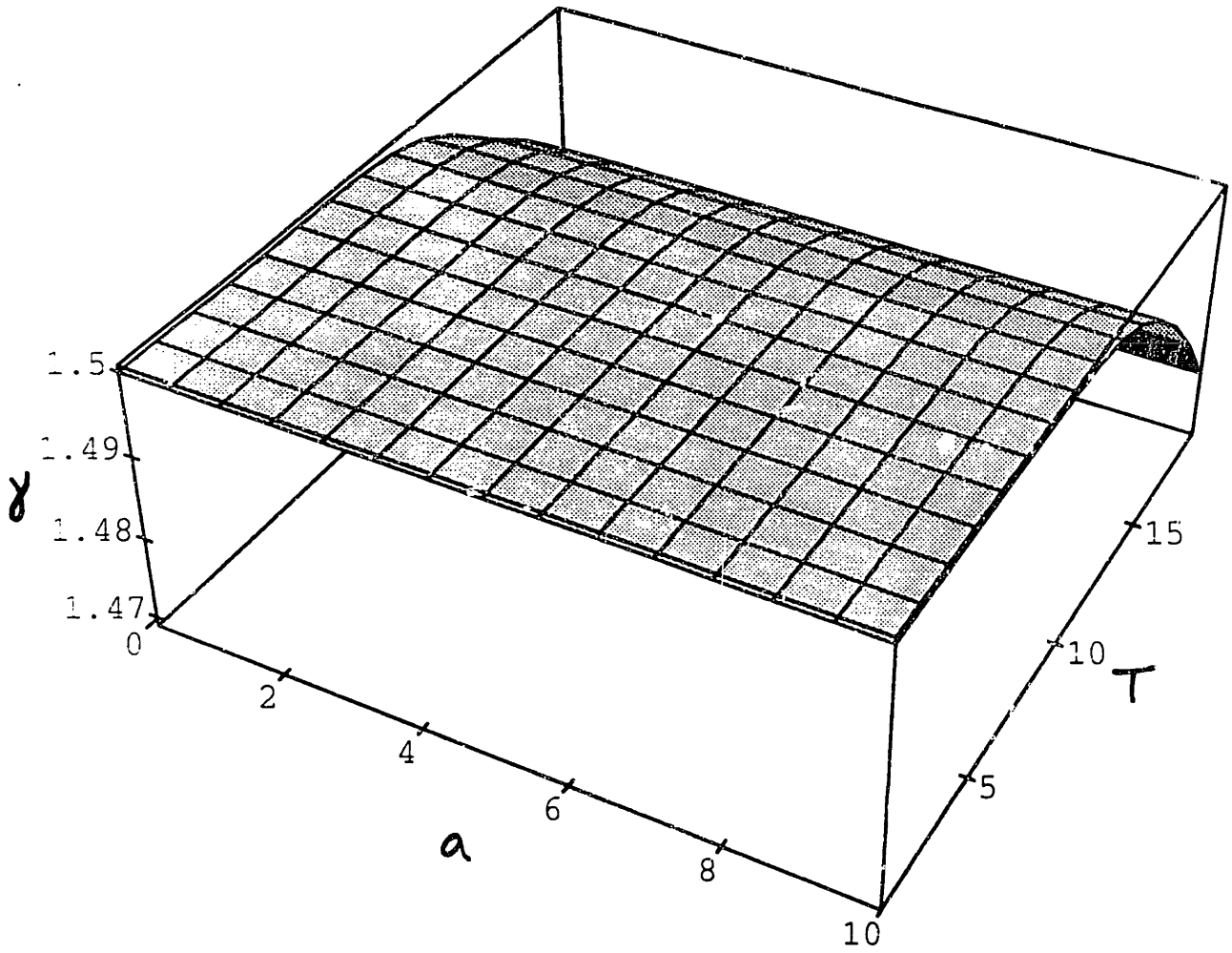

Figure 4.5: Calculation of γ using integrals with $\epsilon_{max} = 160$ for $0 < a \leq 10$ and $0 < T \leq 19.2$. The result shows that this artifact is very close to its continuum value (1.5) at temperatures much less than the maximum energy.

4.2 Convergence Properties of the Model

We now know that the artifacts acquire the correct continuum values when a complete spectrum of speeds are allowed in our lattice gas model. In this section we investigate the rate at which the artifacts converge to their continuum values as higher energies are added to a finite multiple-speed model. We will concentrate on the Galilean invariance factor g but what is found for this artifact has been shown to hold equally well for the other two artifacts.

It was demonstrated in Section 4.1.1 that every integral energy can be represented on the FCHC lattice. An energy ϵ_j has a particular number of allowable directions d_j that is given by eqn. (4.21) and for large enough energies can be accurately approximated with its average value as given in eqn. (4.28). To investigate the convergence of g to the continuum value, we calculate g from eqn. (3.70) for various values of the temperature T, and the inverse fugacity, a, as we raise ϵ_{max}. We wish to approximate an integral over all positive energies with a discrete sum over a finite range of energies. Thus, there are now two sources of error. The error as indicated by the Euler-Maclaurin Formula and the truncation error

$$\begin{aligned}\int_0^\infty f(\epsilon_j)d\epsilon_j &= \int_0^{\epsilon_{max}} f(\epsilon_j)d\epsilon_j + \int_{\epsilon_{max}}^\infty f(\epsilon_j)d\epsilon_j \\ &= \sum_{\epsilon_j=0}^{\epsilon_{max}} f(\epsilon_j) + -\tfrac{1}{2}(f(\epsilon_{max}) + f(0)) - \\ &\quad \left[\frac{f'(\epsilon_{max}) - f'(0)}{12} + \frac{f'''(\epsilon_{max}) - f'''(0)}{720} - \ldots\right] + \int_{\epsilon_{max}}^\infty f(\epsilon_j)d\epsilon_j \end{aligned} \tag{4.58}$$

where the step size $\Delta\epsilon = 1$. For every ϵ_{max}, it was desired to find the range over temperature where the root-mean square error in g from the value g=1 was less than 1%, because this was about the accuracy to which the Galilean invariance factor, g, could be measured ([39] or see Chapter 7). A number of interesting

properties were discovered. First of all, the error in g was largely independent of the inverse fugacity. Secondly, there seemed to be a lower limit on the value of T in order for the error to be about 1%. Reasons for this will be described shortly. Thirdly, it was found that the upper limit of T whereby the RMS error was 1% increased linearly with ϵ_{max} with a proportionality constant of about 0.12. Thus, it was found that the RMS error in g was about 1% or less for temperatures over the range

$$0.60 \leq T \leq 0.12\epsilon_{max}. \tag{4.59}$$

A consequence of this result is that there is no region where the error in g is less than 1% for $\epsilon_{max} \leq 5$. The RMS error in g for many values of ϵ_{max} may be found in Table 4.1 while the results for $\epsilon_{max} = 10$, 40, and 160 are in Figures 4.6, 4.7 and 4.8 respectively. The tabulated results show that the RMS error in g remains at a value of about 1% as the upper bound of temperature is increased linearly with the maximum value of energy. From the indicated figures, we see that the calculated value of g differs from the value $g = 1$ for both extremely high and low values of the temperature. For an explanation of this we must examine the terms in eqn. (4.58) that indicate the difference between the continuum and discrete system. Besides the errors related to derivative values of the integrand, there is an error related to the truncation at a finite value of ϵ_{max}, quantified by the terms $-\frac{1}{2}f(\epsilon_{max})$ and the integral from ϵ_{max} to infinity, and an error related to the value of the integrand at $\epsilon_{max} = 0$, which is $\frac{1}{2}f(0)$. The truncation errors while being significant at low values of ϵ_{max} become negligible at large upper limits in energy. This effect is responsible for the small improvement in the RMS error of g as ϵ_{max} increases from a value of 10 to 30 but above this value, the effect is negligible and the error remains relatively constant. The other error, related to the value of the integrand at $\epsilon_j = 0$, is non-zero only for non-energy moments

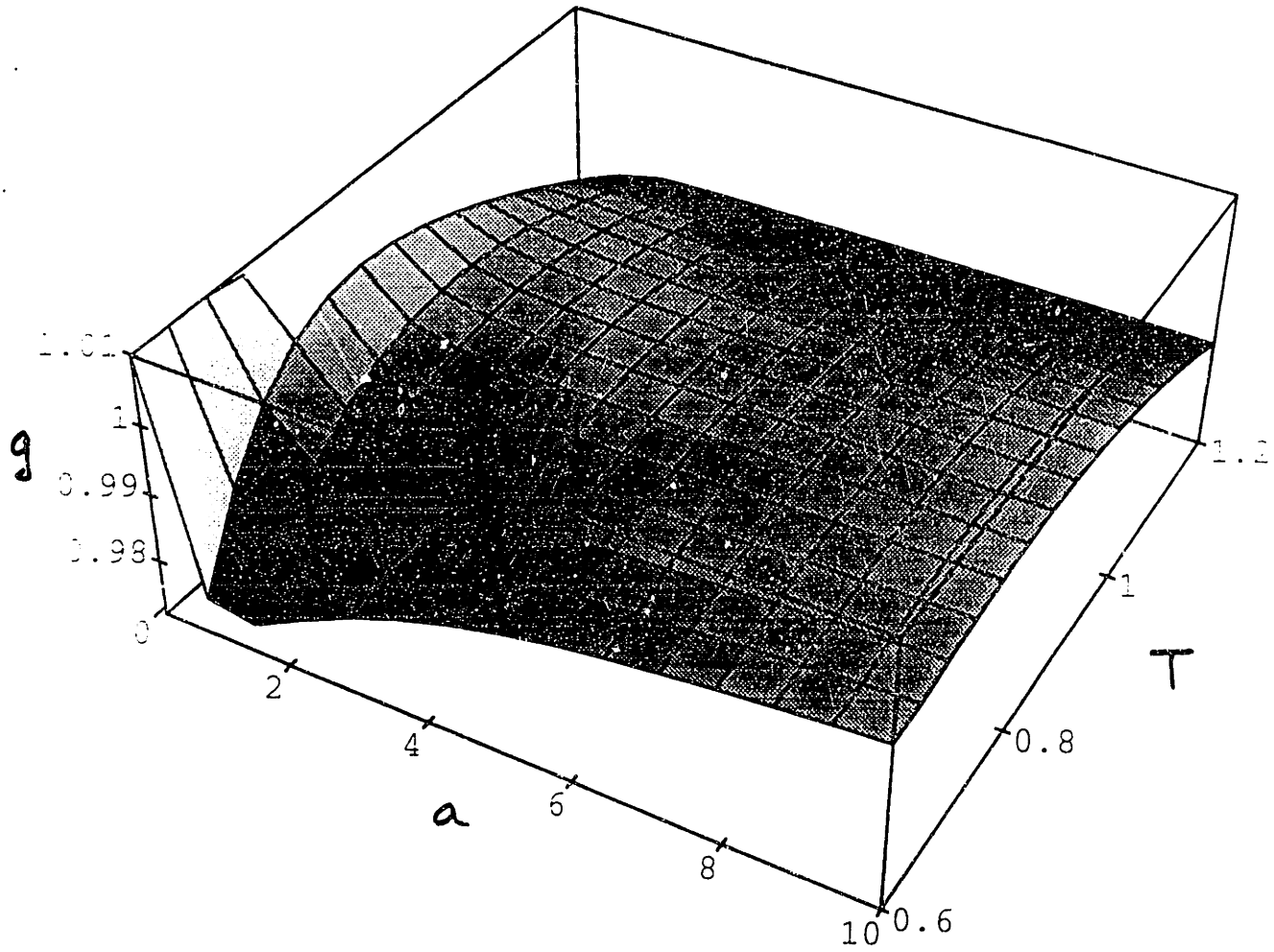

Figure 4.6: Calculation of g using discrete sums with $\epsilon_{max} = 10$ for $0 < a \leq 10$. and $0.6 \leq T \leq 1.2$. The RMS error in g over the plotted range is 1.13%.

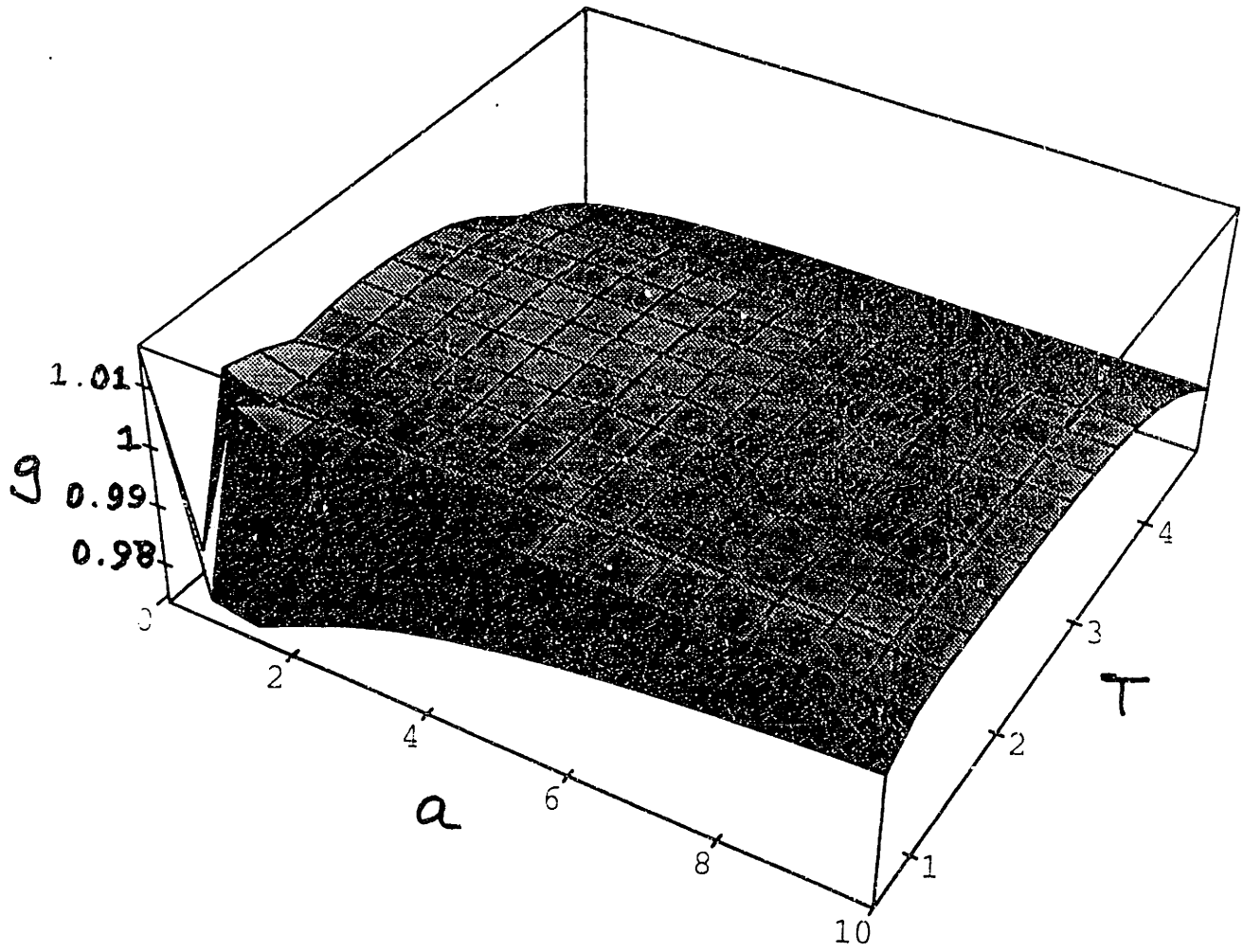

Figure 4.7: Calculation of g using discrete sums with $\epsilon_{max} = 40$ for $0 < a \leq 10$. and $0.6 \leq \mathrm{T} \leq 4.8$. The RMS error in g over the plotted range is 0.93%.

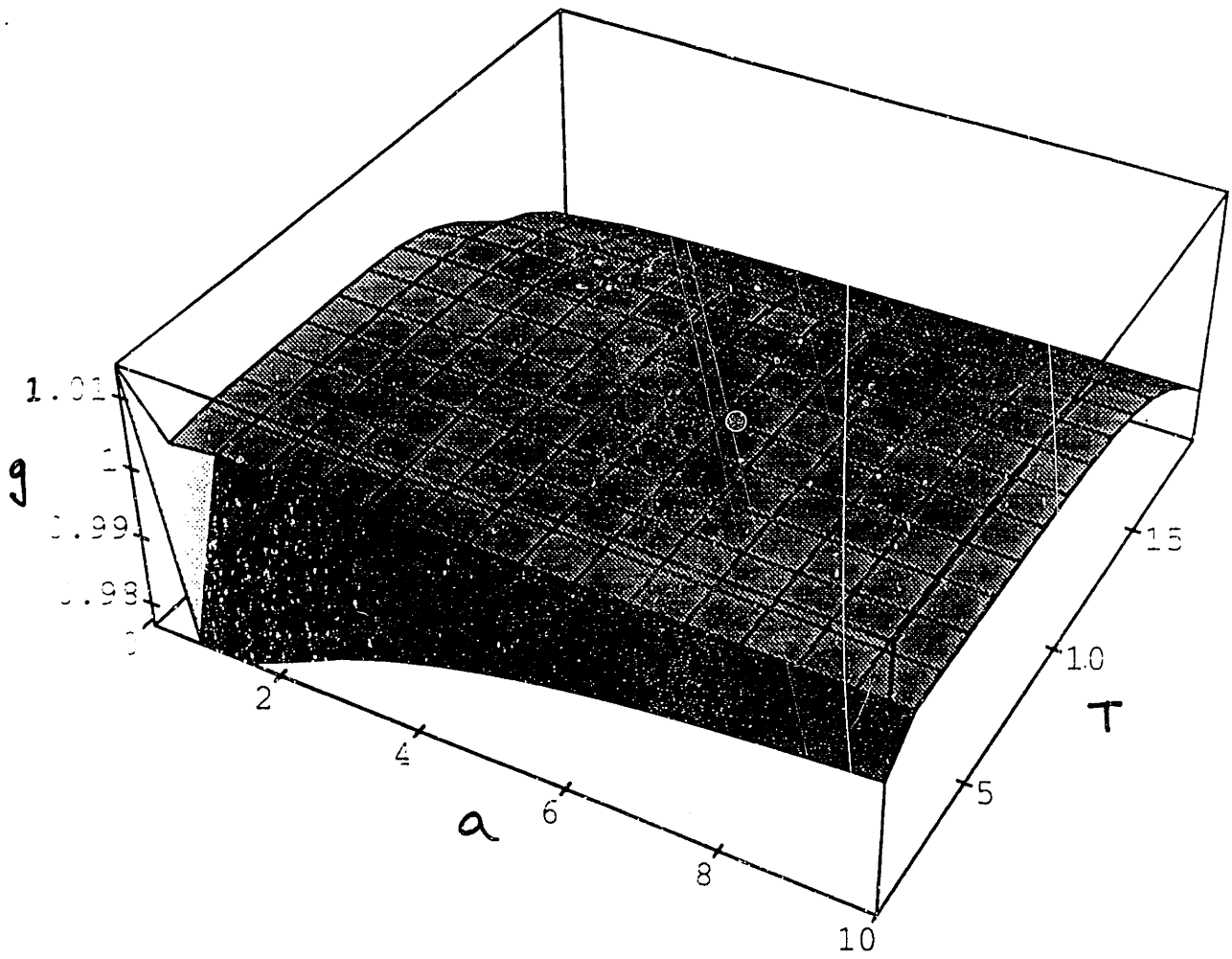

Figure 4.8: Calculation of g using discrete sums with $\epsilon_{max} = 160$ for $0 < a \leq 10$. and $0.6 \leq T \leq 19.2$. The RMS error in g over the plotted range is 0.91%. When $T_{max} = 0.12\epsilon_{max}$, the error remains constant at about 1%.

ϵ_{max}	RMS error in g $0.60 \leq \mathrm{T} \leq 0.12\ \epsilon_{max}$
5	No Range
10	1.13 %
20	0.98 %
30	0.91 %
40	0.93 %
60	0.91 %
80	0.92 %
160	0.91 %

Table 4.1: The range of temperature, T, that allows a RMS error in g of about 1% increases linearly with the largest allowed energy in the system, ϵ_{max}.

such as the density or the first-order mass moment $(\mathbf{m}, \mathbf{m})_1$ which appear in the expressions for the artifacts. Thus, when calculating g from sums for finite speed systems, there will be a constant difference between this quantity and the value of g calculated from integrals due to the finite value of particle number at an energy of zero. This effect becomes larger as you lower the temperature as lower energy states are more populated when the temperature is low. It was found that for a temperature lower than 0.60, this error would be large enough to cause an overall error in g of greater than 1%. Even if this contribution to the error along with the truncation error could be removed there would still be a finite error between the discrete and continuum calculation of the artifacts. The limiting procedure described in Section 4.1.2 is required to reduce the step size to zero and make the

error in g vanish completely. Passage to the continuum was made by re-scaling the energy and temperature parameters with the quantity ϵ_{max}^n where n is arbitrarily close to, but less than, the value of one. If we do this re-scaling on the present system we find that the range of re-scaled temperature, T' (eqn. (4.50)), that results in errors of less than 1%, from eqn. (4.59), is

$$\frac{0.60}{\epsilon_{max}^n} \leq T' \leq 0.12\epsilon_{max}^{1-n}. \tag{4.60}$$

When we take the limit where ϵ_{max} approaches infinity, the lower limit on T' approaches zero while the upper limit approaches infinity since $1-n > 0$. In fact, we know from the analysis of Section 4.1.2 that the error for the whole range of temperature becomes zero in this limit.

In summary, we have found a range of temperature for a given 4D FCHC lattice model that allows particles with energies up to ϵ_{max} where the Galilean invariance factor artifact, g, is within 1% of its correct continuum value. This range of temperature increases linearly with the maximum energy allowed in the system. A corollary of this is that the convergence of the discrete model to the continuum model is linear.

4.3 Discrete Microscropic Galilean Invariance

We have investigated what happens to our model when we add higher speeds by examining the convergence of the artifacts to their continuum values. However, the artifact expressions we have been using were calculated using a low Mach number or subsonic expansion. To fully utilize the benefits of adding higher speeds to our model, we would like to be able to use fluid velocities that were comparable to any allowable microscopic velocity. Moreover, we would like the

physics in the frame moving at this finite fluid velocity to be the same as if we were in a stationary frame. This requires the model to have discrete microscopic Galilean invariance. Previously, we found that the artifacts g and g' indicated the presence of macroscopic non-Galilean invariance. We now show that the same artifacts exist, using a velocity transformed definition of eqn. (3.51) over species space, in the transonic case. Before beginning the transonic derivation we must ensure that our model can accomodate a velocity transformation. If we transform the stationary basis vectors, $\mathbf{c}_{ji}$ to a new set of vectors, $\mathbf{c}_{j'i}$ using the arbitrary lattice vector $\mathbf{c}_J$

$$\mathbf{c}_{ji} = \mathbf{c}_{j'i} + \mathbf{c}_J \tag{4.61}$$

we require that there be only one stopped particle so that the Fermi exclusion principle, which states that there can only be one particle with a particular velocity at any one site, is not violated. We also require a infinite spectrum of energies, or at least an upper bound that is much larger than any vector, c_J, we may be transforming by, to ensure that the set of transformed vectors, $c_{j'i}$, is complete for each energy. We have already shown in Section 4.1 that the FCHC lattice allows an infinite set of particle energies to be represented with sufficient symmetry to ensure isotropic stress tensors. We now assume there is a zeroth order fluid velocity, $\mathbf{u}$ where

$$\mathbf{u} = \mathbf{c}_J + \delta\mathbf{u} \tag{4.62}$$

where c_J is the closest lattice vector to the fluid velocity and $\delta\mathbf{u}$ is the error between the two. The magnitude of this vector is always less than or equal to $\frac{1}{2}$ and so is inherently small. In Chapter 7 we will show that even when the magnitude of $\delta u = .5$, the errors in the artifacts are still less than 10%. In effect, this small vector is quantifying the discreteness error in the system. The system,

due to its discrete nature, may not be able to exactly represent the fluid velocity with a single lattice vector. If we solve eqn. (4.62) for $\mathbf{c}_J$ and then substitute this relation into eqn. (4.61) we find

$$\mathbf{c}_{ji} = \mathbf{c}_{j'i} - \delta\mathbf{u} + \mathbf{u}. \tag{4.63}$$

We know that for the discrete lattice gas, the equilibrium distribution has Fermi-Dirac form (eqn. (2.31) with $r_j \equiv 1$). It is possible to complete the square in the exponent of this relation for $\mathbf{c}_{ji}$ and derive a relation that is dependent only on the difference between the microscopic velocity vector and the fluid velocity. Since $\mathbf{c}_{ji} - \mathbf{u} = \mathbf{c}_{j'i} - \delta\mathbf{u}$, we may make this substitution and expand the exponent out again to get the transformed distribution function

$$N_{j'i} = \frac{1}{1 + exp(\alpha^* m_{j'} + \gamma^* m_{j'} \mathbf{c}_{j'i} \cdot \delta\mathbf{u} + \beta^* \epsilon_{j'})} \tag{4.64}$$

where $\alpha^*, \gamma^*, \beta^*$ are still arbitrary real numbers and the definition of the transformed energy is

$$\epsilon_{j'} = \tfrac{1}{2} m_{j'} c_{j'}^2. \tag{4.65}$$

We now proceed as was done in Section 2.4 to expand the distribution function in terms of the inherently small factor $\delta\mathbf{u}$. This justifies only expanding the distribution function to second order in this small term, even though the total fluid velocity can be quite large. All the moments are now over the transformed energy space, denoted by $\epsilon_{j'}$. We calculate the macroscopic properties to third order in this small quantity but expect that all physical properties should now appear at the lowest order since the fluid velocity is now zeroth order. All higher order contributions are now artifacts. Upon doing this calculation we find that the mass, momentum and energy moments of the kinetic equation, eqn. (3.18), gives conservation equations for these three quantities that have the correct form

as outlined in eqns. (3.19), (3.20), and (3.25). A summary of the important moments follows:

Density

$$\sum_{j',i} m_j N_{j'i} = \rho = \rho^{(0)} \tag{4.66}$$

Momentum

$$\sum_{j',i} m_j \mathbf{c}_{ji} N_{j'i} = \rho \mathbf{u} = \rho \mathbf{u}^{(0)} \tag{4.67}$$

Energy

$$\sum_{j',i} \tfrac{1}{2} m_j c_j^2 N_{j'i} = U_p + \tfrac{1}{2}\rho u^2 = U^{(0)} \tag{4.68}$$

where

$$U_p = \sum_{j'} d_{j'} \epsilon_{j'} N_{j'}. \tag{4.69}$$

Note that the energy has the correct hydrodynamic form as given by eqn. (3.10).

Stress Tensor

$$\sum_{j',i} m_j \mathbf{c}_{ji} \mathbf{c}_{ji} N_{j'i} = \frac{2}{D} U_p \mathbf{I} + \rho \mathbf{u}\mathbf{u} + \left[\frac{1}{D} \rho \delta u^2 (1-g) \mathbf{I} + \rho (g-1) \delta \mathbf{u} \delta \mathbf{u} \right] \tag{4.70}$$

where the square bracketed term is second-order. The zeroth order term is completely correct with

$$P_s = \frac{2}{D} U_p \tag{4.71}$$

as required. The expression for g in the above is identical to eqn. (3.70) except that the inner products are now over the transformed energy spectrum. Once again, we see that if $g = 1$, then the higher order contributions are removed and we are left with the zeroth order term for the stress tensor which is identical to the continuum value.

Energy Flux

$$\begin{aligned}\sum_{j',i} \tfrac{1}{2} m_j c_j^2 \mathbf{c}_{ji} N_{j'i} &= \left(\frac{D+2}{D} U_p + \tfrac{1}{2}\rho u^2\right)\mathbf{u} + \left(\gamma - \frac{D+2}{D}\right) U_p \delta\mathbf{u} \\ &+ \rho(1-g)\delta\mathbf{u}\cdot\left[\frac{1}{D}\delta\mathbf{u}\mathbf{u} - \mathbf{u}\delta\mathbf{u}\right] \\ &+ \rho\delta u^2 \delta\mathbf{u}\left[\frac{D-1}{D}(1-g) - \tfrac{1}{2}(1-g')\right]\end{aligned} \tag{4.72}$$

where the zeroth order term is as required for hydrodynamics, eqn. (3.11). The first-order term is the γ artifact with γ given by eqn. (3.74) with moments over the transformed energy spectrum. The Stress tensor Galilean term, g, is also important in the energy flux relation at second order and third order. Finally, the g' artifact, as given by eqn. (3.75) using the transformed energy spectrum, appears as a third order error. All three artifacts appear in the energy flux relation. When the artifacts take on their correct continuum values, all of the higher order contributions to the energy flux vanish. Only the hydrodynamically correct zeroth order contribution remains.

These results illustrate that artifacts appear only as coefficients of the small error velocity $\delta\mathbf{u}$ and that the artifacts we find here are the same three that were calculated in the small Mach number case. If the fluid velocity happens to correspond exactly with a lattice vector, $\mathbf{u} = \mathbf{c}_j$, then all artifacts vanish. This shows how it is possible to get accurate hydrodynamic results from a supersonic lattice gas when the macroscopic flow velocity is equal to one of the microscopic particle velocities. Furthermore, if we make the fluid velocity small in the above treatment by setting $\mathbf{u} = \delta\mathbf{u}$ and simplifying, we reproduce the results for the stress tensor and energy flux vector given by eqns. (3.21), (3.24), and (3.26) of Section 3.1. Since the artifacts may be removed by adding higher speeds to the model, we have shown that the 4D FCHC lattice gas model may be used to

simulate transonic flows because the system permits discrete microscopic Galilean invariance. Because the new transformed velocity, $\delta\mathbf{u}$, is still small, it is not necessary to go beyond the 4th order symmetry requirements of the FCHC lattice to be able to remove the artifacts at large Mach numbers. Since the second order expansion in velocity was sufficient in the low Mach number case, it is also sufficient here since the small velocity term in the transonic case will never be larger than the largest velocity that was found to still produce accurate results in the low Mach number models (presented in Chapter 7). The lattice gas model is not restricted to simulating subsonic flows, as was previously thought[14, 39].

Chapter 5

Removing the Artifacts

In Chapter 4 we demonstrated that the three lattice artifacts uniformly approach their hydrodynamic values as higher speeds are added to the lattice gas model. However, the convergence rate is linear, which is slow. When an additional speed is added to the algorithm, the additional amount of computational effort required to move the new particles also increases linearly since the number of added directions increases linearly with speed (eqn. (4.28)). On the other hand, the computational work required to collide these new particles with all existing particles is proportional to the total number of particles in the model, which grows quadratically with speed (eqn. (4.27)). Consequently, the amount of work we have to do grows quadratically while the convergence of the artifacts is only linear if we rely solely on adding higher energy particles in order to remove the artifacts.

In this Chapter, we show how the artifacts can be removed in a finite speed system. Because of the disproportionate amount of incremental work when a new speed is added, it is always desirable to use the lowest speed model that will allow

the desired artifacts to be removed. The key elements that allows us to do this are the collsion rate coefficients that we introduced into the microdynamics in Chapter 2. Basically, the freedom created by the introduction of the adjustable decay rates will be utilized to impose the desired conditions of: i) Galilean invariance, ii) equipartition, and iii) an Adiabatic equation of state energy equation. The first two of these are conditional on the g artifact while the third depends on the values of the γ and g' artifacts.

From the standpoint of kinetic theory, what will be done is to set the appropriate higher order moments to the values required by the requisite macroscopic features. Without the adjustable decay rates, the moments are fixed by the Fermi-Dirac distributions (equation (3.42) with $r_j = 1$), once the density and temperature are known. Thus all the equilibrium density ratios, $N_j/N_{j'}$, are determined by ρ, and U_p. The introduction of the decay rates r_j allows these individual particle densities to be somewhat adjustable, even for ρ and U_p fixed.

While the density, momentum and energy moments cannot be tampered with, the higher order moments, such as $(m\epsilon, \epsilon)_2$, do not have any restrictions on their values (except they must remain positive, of course). This allows us to establish relationships for these moments which force the artifacts to have the correct values. These relationships are realized by adjusting the rate coefficients.

The value of g when $r_j = 1$ for all energies, j, is illustrated in Figures 4.6, 4.7 and 4.8 for values of $j_{max} = \epsilon_{max}$=10,40 and 160, respectively. Except for very small values of $a \equiv e^{\alpha_0}$ and temperature, g is always smaller than the continuum value of one. Thus, we wish to raise the value of g to its correct value by an amount dependent on the lattice site's local density and temperature. The equation for

g, eqn. (3.70), is

$$g = \frac{D}{D+2}\frac{(\mathrm{m}\dot{\epsilon}, \epsilon)_2}{(\mathrm{m}, \epsilon)_1^2}\rho. \tag{5.1}$$

If we want to raise the value of g, we need to raise the value of the moment $(\mathrm{m}\epsilon, \epsilon)_2$. Similarly, both γ and g' are everywhere smaller than their continuum values but while γ is actually closer to its desired value than g is, g' differs from its desired value in a much more complicated way, as the expression for g', eqn. (3.75) might suggest. As a result, when we make $g = 1$, the other artifacts stray further away from their desired values and other moments must be alterred to return them to the continuum values.

The momentum equation is contaminated only by the g artifact. Making $g = 1$ causes our lattice momentum equation to become identical to the hydrodynamic result (eqns. (3.22) and (3.23)). Thus, we start our analysis with the g artifact with the goal of finding the smallest system that will allow it to be removed. A three speed system with a solitary rate coefficient, r_0, allows us to remove this artifact for a limited but substantial range of density and temperature. The next important artifact is the ratio of specific heats γ which appears as a first order of the Mach number quantity in eqn. (3.26). This quantity must be set to the ideal gas value (D+2)/D if the lattice model is to simulate heat transfer correctly. The nature of the g and γ equations is such that a simultaneous solution is not possible for a large range of density and temperature. We find in a four speed system with two separate rate coefficients that when an exact solution is not possible, it is still possible to make the errors in the artifacts smaller than 1%, an acceptable level. The final coefficent, g', is a third order effect in both the small Mach number, eqn. (3.26), and transonic, eqn. (4.72), energy equations so that its impact on the dynamics is limited. Still, we may attempt to remove it, along with the other

artifacts, but we find that there is no simultaneous solution for general density. Furthermore, unlike the g and γ case, there are no set of rate coefficients that make the errors small in a low speed model. We do find that if the equilibrium density is small, tractable results for removing all three artifacts do occur. In this low density regime, the γ relation collapses to the g relation so that there are really only two artifacts. We again find that a three speed model removes both g and γ while a five speed model is required to remove all three. Complete solutions as well as the range of applicability for all results in the cases described above will be presented in this Chapter.

5.1 Making g=1 − 3 Speed Model

The zeroth order density and energy equations, eqns. (3.52) and (3.53), specify the coefficients α_0 and β_0. Requiring $g = 1$ adds an additional equation to the system so that one additional variable is required to solve the system completely. This means that only one rate coefficient is required, the rest may be set equal to one. The rate coefficients only affect energy exchange collisions. Thus, we must have a system that allows particles to exchange energies during a collision. The smallest system that has this property is the three speed model where particles with $\epsilon_j = j = 0, 1$ and 2 are allowed (we have set all masses in the system equal to one). The energy exchange collision occurs when two type 1 particles collide at right angles to produce a stopped particle and a type 2 particle, as in Figure 2.1. We will associate the rate coefficient with the stopped particles, r_0, for algebraic simplicitly since the stopped particle distribution does not appear in the energy moments. The relation for g, eqn. (3.70), is in terms of moments of the equilibrium

distribution function, eqn. (3.42) which we rewrite once again as

$$N_j = \frac{yr_j}{yr_j + z^j} \tag{5.2}$$

where $y \equiv e^{-\alpha_0}$, the fugacity, $y \equiv a^{-1}$ as defined in Chapter 4, and $z \equiv e^{\beta_0}$, a quantity related to temperature. When simulating a lattice gas model, we like to specify the density and temperature of the equilibrium fluid. This means that we will treat density, ρ, and the temperature related variable, z, as input parameters while y is a variable that must be tuned to give the desired density. The internal energy, U_p, is then calculated from the equation of state using ρ and z. Thus the unknowns are the fugacity, y, and the rate coefficients, r_j.

For the three speed model, we keep r_0 and set $r_1 = r_2 = 1$. As calculated in Section 2.2, the number of directions for the energy=1 particles is $d_1 = 24$ as it is for energy=2, $d_2 = 24$. For reasons that will be explained shortly, we set the maximum number of stopped particles allowed at a site to six, $d_0 = 6$. Using eqn. (5.2), the equilibrium distributions for this model are

$$\begin{aligned} N_0 &= \frac{yr}{yr+1} \\ N_1 &= \frac{y}{y+z} \\ N_2 &= \frac{y}{y+z^2}. \end{aligned} \tag{5.3}$$

We have dropped the subscript on the rate coefficient, r, since there is only one in this model. The equations defining the density and energy, together with the Galilean invariance condition ($g = 1$), form three equations which in principle allow determination of the Lagrange multipliers, α_0, and β_0, as well as the rate coefficient, r. The resulting equations are quartic in the fugacity, y, with analytic solutions that are neither insightful nor useful. A more practical approach, as

stated above, is to treat z as a temperature input parameter and use an expansion in the density, essentially a virial expansion, that will turn out to be rapidly convergent. In this expansion, we use the quantity, $f \equiv \rho/d_1 = \rho/24$, to represent the density. This is a characteristic bit occupation density and will be smaller than unity in all applications we investigate.

Thus we have the density relation for the three speed model, eqn. (3.52)

$$f = \frac{1}{4}N_0 + N_1 + N_2 = f(y, r, z) \tag{5.4}$$

the Galilean invariance condition, eqn. (3.70) with D=4 for the 4D FCHC lattice, written out using the notation of eqns. (3.51) is

$$g = \frac{2}{3}\frac{[N_1(1-N_1)(1-2N_1) + 4N_2(1-N_2)(1-2N_2)]}{[N_1(1-N_1) + 2N_2(1-N_2)]^2} f = 1 \tag{5.5}$$

which may be rewritten as a function, $gcond(y, z, f) = 0$,

$$0 = f[N_1(1-N_1)(1-2N_1)+4N_2(1-N_2)(1-2N_2)] - \frac{3}{2}[N_1(1-N_1)+2N_2(1-N_2)]^2 \tag{5.6}$$

which allows us to solve for y as a function of the input parameters f and z. Knowing $y(f, z)$ will allow us to find $r(f, z)$ from eqn. (5.4).

The virial expansion is established by developing the fugacity, y, in a power series,

$$y = y_1 f + y_2 f^2 + y_3 f^3 + y_4 f^4 + \cdots. \tag{5.7}$$

Plugging this relation into eqn. (5.6) and setting the result equal to zero order by order in f, the coefficients $y_j(z)$ may be calculated as rational polynomials,

$$y_1 = \frac{z}{3}\left(2 - \frac{8}{(2+z)^2}\right) \tag{5.8}$$

$$y_2 = \frac{32(-1+z)z^3(4+z)}{9(2+z)^5} \tag{5.9}$$

$$y_3 = \frac{-8z^2(4+z)(64+48z-152z^2+344z^3-68z^4-12z^5+z^6)}{27(2+z)^8} \tag{5.10}$$

$$y_4 = \frac{128(z-1)z^3(4+z)(-384-208z+748z^2-870z^3-2z^4+41z^5)}{81(2+z)^{11}}. \tag{5.11}$$

It turns out that, in spite of the complexity of these coefficients, this series is rapidly convergent for most physically useful temperatures. The coefficients y_j are of order unity for values of z in the range $.1 \rightarrow 10$, which corresponds to almost a doubling in temperature. The relationship between z and the temperature, T, will be derived in Section 5.4. Neglected terms, if the series is retained to this order, contribute less than 1% even for a density of $f \sim \frac{1}{2}$, or $\rho = 12$.

If the corresponding power series for the rate coefficient r is developed from equation (5.4), one does not obtain the same accuracy - possibly related to the poor convergence properties of the series for $1/(1+x) = 1 - x + x^2 - x^3 \cdots$. However (5.4) can be solved exactly for r as a rational function of the fugacity, y,

$$r = \frac{-4(-2y^2+fy^2-yz+fyz-yz^2+fyz^2+fz^3)}{y(-9y^2+4fy^2-5yz+4fyz-5yz^2+4fyz^2-z^3+4fz^3)} \tag{5.12}$$

and the *accurate* series for y through fourth order in f may be substituted. This will provide an accurate expression for the rate coefficient for all usable densities.

In a similar manner, we can compute the energy,

$$U_p = 24(N_1 + 2N_2) = 24\left(\frac{y}{y+z} + \frac{2y}{y+z^2}\right) \tag{5.13}$$

and by substituting the series for y through fourth order, we obtain the equation of state.

The accuracy of this procedure can be established first from the magnitude of the y_i coefficients, displayed graphically as a function of z in Figure 5.1. The coefficient y_1 would be off-scale on this plot. Note that the magnitude of y_4 is

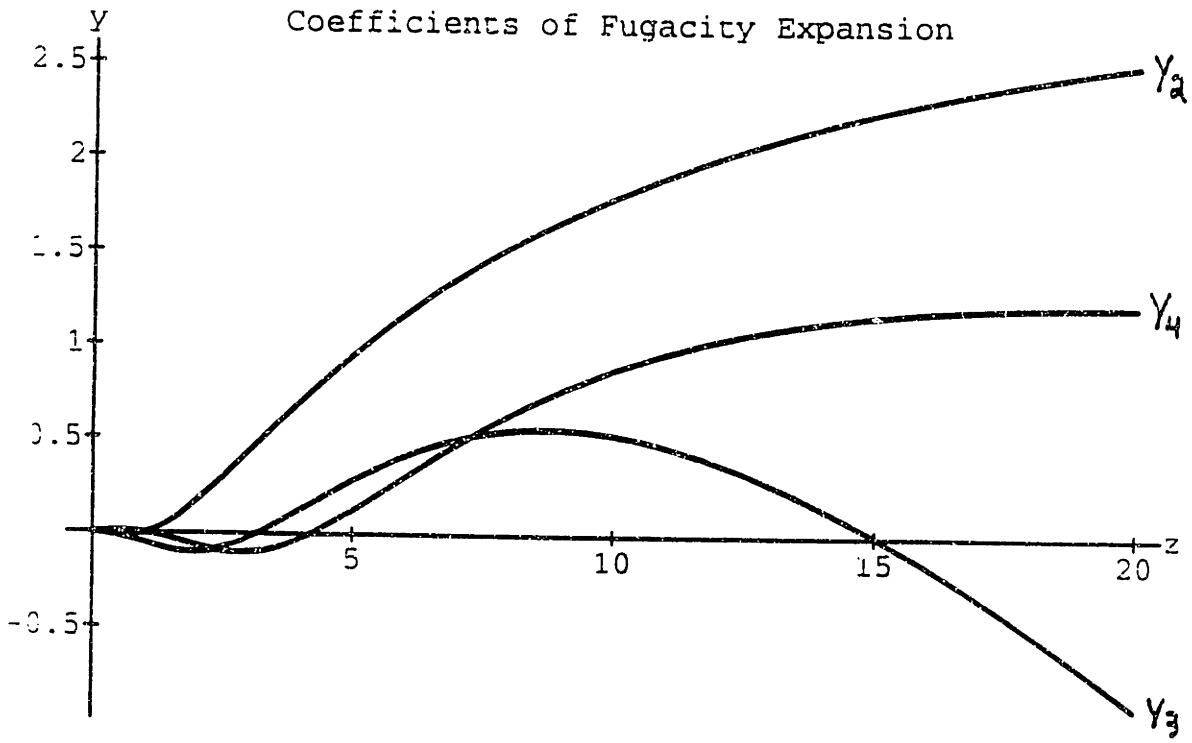

Figure 5.1: Expansion coefficients in the density expansion for the fugacity. Coefficients y_2, y_3, and y_4 are shown.

less than 1. over the range $0 \leq z \leq 15$. It is straightforward to calculate the magnitudes of higher coefficients by extending the fugacity expansion. eqn. (5.7), to higher orders in f. Explicit calculation shows that the magnitude of y_5 is less than 0.5 while y_6 is bounded by 0.2 in this range. This implies correction terms to y order $\sim .5f^5$, or .016 for densities up to $f \sim .5$ which is less than 1% of the value of y at this density and temperature. At lower values of f and z, the correction effect is even smaller. The full expression for the fugacity, through order f^4, is plotted as a function of f and z in Figure 5.2.

The key factor limiting the dynamical range and the applicability of the entire lattice gas method, is the rate coefficient. r. The coefficient must be positive, of course. To maintain rapid thermalization within the flow, in practice. r cannot be

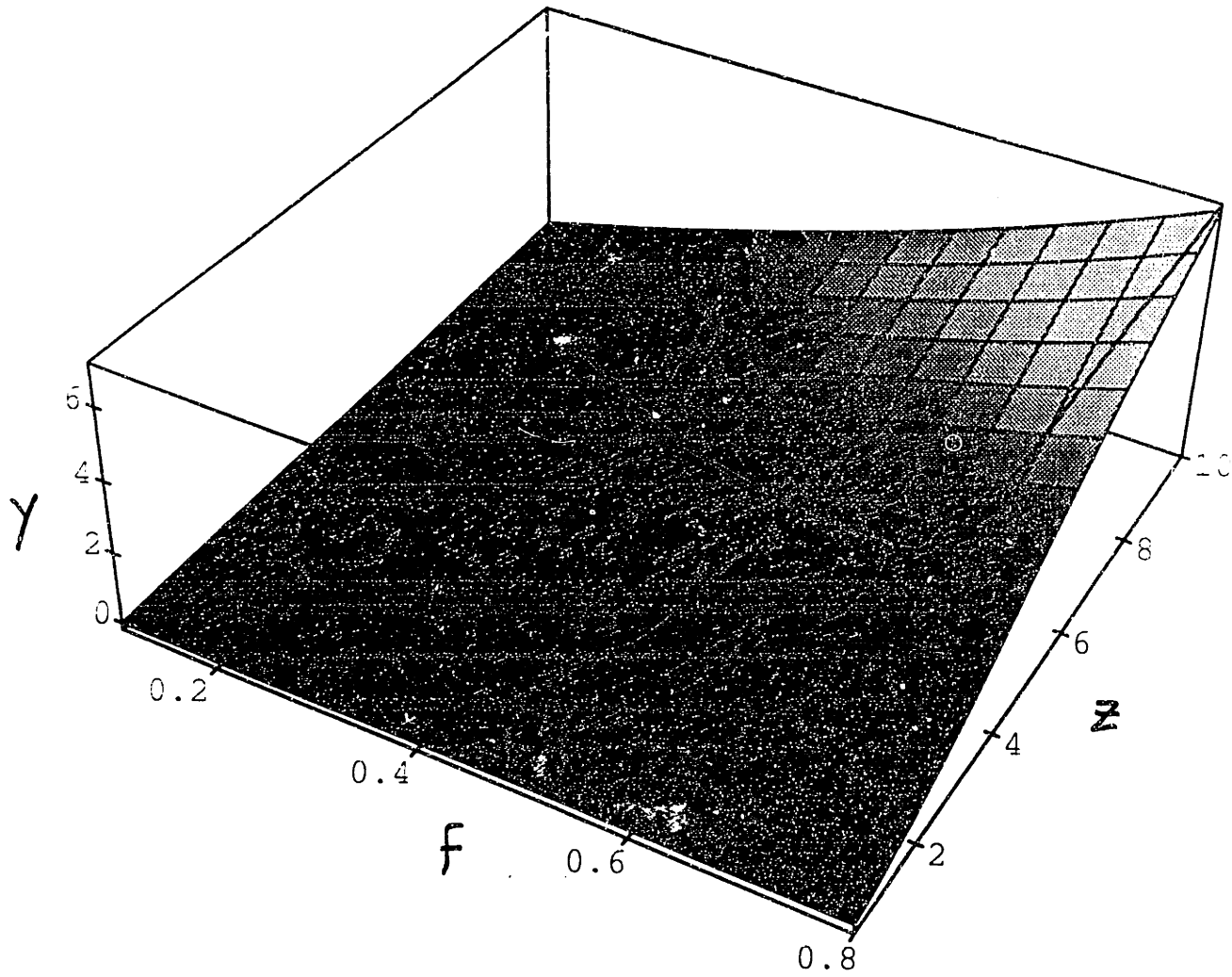

Figure 5.2: Fugacity from the 4^{th} order expansion as a function of density, $.1 \leq f \leq .8$ and the temperature variable, $.5 \leq z \leq 10$.

too large or too small. Typical allowed values would be in the range $.1 < r < 10$ although the closer to the 'natural' value of $r = 1$, the easier it is to maintain. As the three-dimensional plot of r as a function of density and the temperature variable, z, shows in Figure 5.3, r is positive and within the acceptable range when $f < .56$ and for all z, $.5 \leq z \leq 10$. For increased densities, $f \geq .56$, the range of z for which r is positive becomes constricted until for $f \geq .75$ where $r < 0$ for all z and there is no longer a physical solution. For the range $0.56 \leq f \leq .75$, the algorithm can no longer access low z flows. Figure 5.4 shows a cross-section of r with $f = 2/3$ which shows the constricted range of z where realistic flow is still attainable. In this regime, care would have to be taken to assure the simulation didn't require temperatures in the unphysical range.

The range for which r is positive is strongly dependent on the number of stopped particles in the model. The maximum value of f that allows a positive solution for r over the range of z, $.1 \leq z \leq 10$. for various values of d_0 is shown in Table 5.1.

d_0	f_{max}
1	0.13
3	0.33
6	0.56
10	0.82

Table 5.1: The limit on density to assure that r is positive as a function of the number of stopped particles in a three-speed model.

Clearly, the more stopped particles the better. We limit ourselves to $d_0 = 6$ for

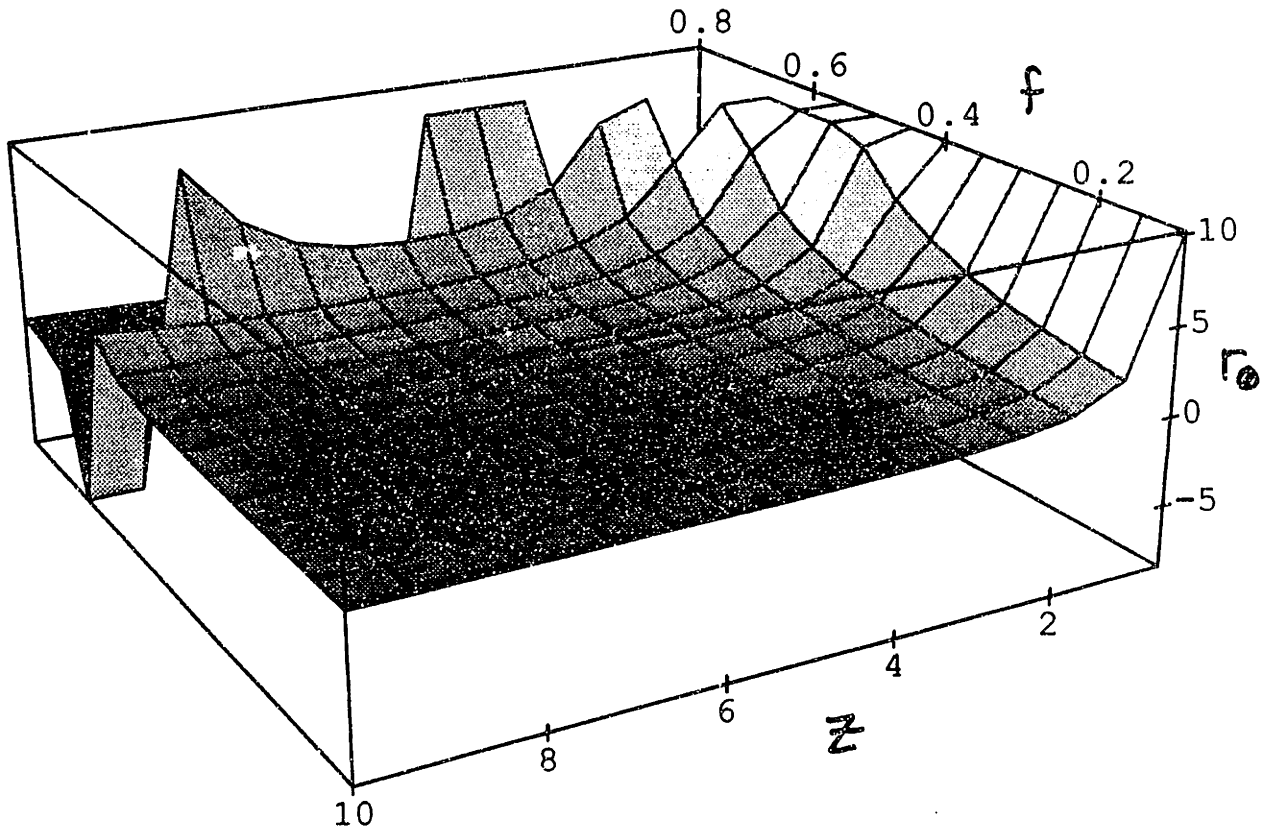

Figure 5.3: Three speed model rate coefficient for $.1 \leq f \leq .8$ and $.5 \leq z \leq 10$. showing the plateau topography over the main dynamical range. For $f \geq .56$, $r < 0$ for some z which is unphysical.

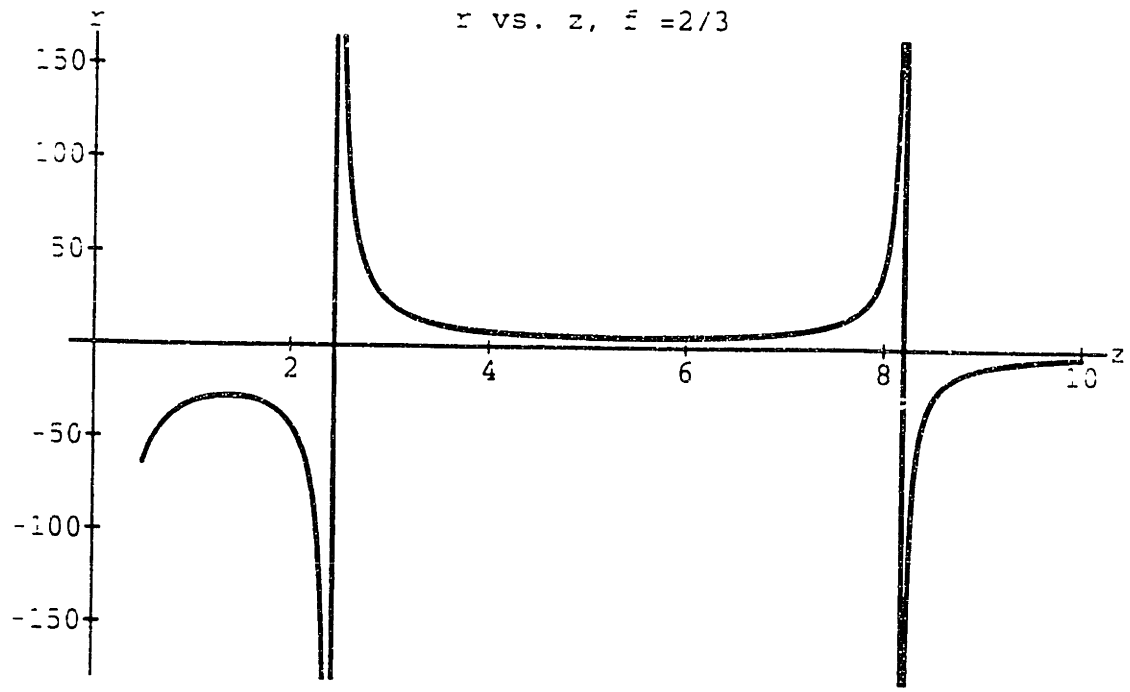

Figure 5.4: Rate coefficient as a function of temperature, z. at a density of f=2/3. The negative ranges of r correspond to regions where realistic (Galilean invariant and non-anomalous pressure) flow cannot be obtained with this algorithm.

practical reasons. First of all. we anticipate that we will not be pushing this model beyond $f = .5$ so that six stopped particles are sufficient to assure positive values of r up to this limit. Furthermore. with six stopped particles we may associate a stopped particle with each of the six orthogonal intersecting planes in a 4D cartesian coordinate system. Thus at any site, it is possible to have a stopped particle to permit an energy exchanging collision in each orthogonal plane. With less stopped particles, fewer energy exchanging collisions can occur, which reduces the algorithm's ability to maintain $g = 1$. This is reflected in the reduced range of possible density as d_0 is decreased. Of course. if we wish to transform the lattice to the frame of any velocity vector. we require $d_0 = 1$ to maintain the exclusion

principle. In models with larger speeds, we will find that the $d_0 = 1$ requirement is not as restrictive as it is in this case.

The removal of all artifacts from the momentum equation has been demonstrated using this technique for the three speed model in extensive simulation results, which will be discussed in Chapter 7. Once the removal of the g artifact had been established, a number of standard fluid dynamical experiments, such as flow in pipes or flow around bluff objects, were run with this model to illustrate that the system transferred momentum correctly. In these dynamical cases, it was possible that the local values of temperature and density could change significantly if a simulation was started off far from equilibrium. For this reason, it was necessary to have a rate coefficient that exhibited very little dependence on these quantities, such as the large plateau region of r in Figure 5.3. Another way of assuring r remains at the appropriate value is to create a feedback system that can sense the local density and temperature (z) and then alter the collision mask accordingly.

If the zero order distributions, N_j, can be measured directly, the local density, f, can be calculated from eqn. (5.4) and z can be calculated from eliminating the variable y from the expressions for N_1 and N_2 in eqns. (5.3)

$$z = \frac{\hat{N}_1}{\hat{N}_2} \tag{5.14}$$

where $\hat{N}_j \equiv \frac{N_j}{1-N_j}$. Knowing f and z, we can calculate the updated values of y and r from eqns. (5.7) and (5.12) respectively. Unfortunately, it is not possible to sense the N_j ***directly*** in a system with a non-zero fluid velocity. This is not an issue for the density measurement since all contributions from the mass moment over N_{ji} vanish except the zeroth order but it does become important for the z measurement. What we ***can*** do is sum the local density N_{ji}, eqn. (3.41), over

direction and then divide by the number of directions to get an averaged zero order density for energy j

$$\langle N_j \rangle \equiv \frac{\sum_i N_{ji}}{d_j} = N_j \left[1 + N_j'(\alpha_2 + \epsilon_j \beta_2) + N_j'' \frac{\gamma_0^2}{D} \epsilon_j u^2 \right] = N_j \left[1 + \chi_j u^2 \right] \tag{5.15}$$

which is different from the desired quantity N_j by the second order quantity $\chi_j u^2$. Normally, such a small error could be ignored but since the mask is being used to remove an effect that is second order [1], we must remove second order errors from the value of the mask. Since $N_j = \langle N_j \rangle / [1 + \chi_j u^2]$, we can substitute this into eqn. (5.14) to obtain z in terms of the measured zero order densities

$$z = \frac{\langle \hat{N}_1 \rangle}{\langle \hat{N}_2 \rangle} \frac{\left(1 + \frac{\chi_2}{\langle \overline{N_2} \rangle} \right)}{\left(1 + \frac{\chi_1}{\langle \overline{N_1} \rangle} \right)} \tag{5.16}$$

where $\langle \overline{N_j} \rangle = 1 - \langle N_j \rangle$. This relation is correct to second order in the fluid velocity. The quantity χ_j contains moments of the zero order distribution function through the coefficients γ_0, α_2, and β_2. For these calculations, the averaged distribution $\langle N_j \rangle$ may be used since this adds second order errors to the χ_j result which, in turn, is a fourth order error in z, which is negligible. Since the length scale for gradients in macroscopic variables such as fluid velocity or global density is much larger than the lattice spacing, we do not need to set the mask separately at each site. It is sufficient to set one value of the mask based on the average density and temperature over a region of the lattice, the size of which corresponds to the smallest macroscopic scale length. This feedback technique was used successfully to maintain the removal of the g artifact in simulations where local values of the

[1] The pressure anomaly is second order, eqn. (3.24)

density and temperature changed significantly (i.e. region behind a bluff object with flow accelerating from rest - see Chapter 7).

As a final observation on this model, we calculate the other two artifacts γ and g' to see how far away they are from their hydrodynamic values, shown in Figures 5.5 and 5.6 respectively. Since there is no further freedom in this model, these quantities remain artifacts and affect the energy equation. We find that setting $g = 1$ pushed $\gamma > 1.5$, its correct value for a four-dimensional degree of freedom lattice, although the error is small at low density and becomes worse as the density is increased. This is because the rate coefficient, Figure 5.3, becomes larger at higher densities which means the constitutive moments of the artifact relations change by a greater amount at larger densities. On the other hand, g' has values both greater and smaller than unity, attaining unphysical negative values for large density, low temperature regimes. There is a region of parameter space, $0.4 \leq f \leq 0.6$ and $4 \leq z \leq 8$, however, where the value of g' is very close to the value 1.

5.2 Making g=1 and $\gamma = 1.5$ – 4 Speed Model

In order to accurately simulate low Mach number heat transfer, it is necessary that both the g and γ artifacts have their correct hydrodynamic values, 1 and 1.5 respectively in a four-dimensional volume. Requiring $\gamma = 1.5$ adds another equation to the system that, in turn, requires a further free variable that can be tuned to give this result. This means that we need to add another rate coefficient to the system. Although the γ artifact is quite small once g=1, as illustrated in the 3-speed model, it cannot be completely removed at all densities and temperatures

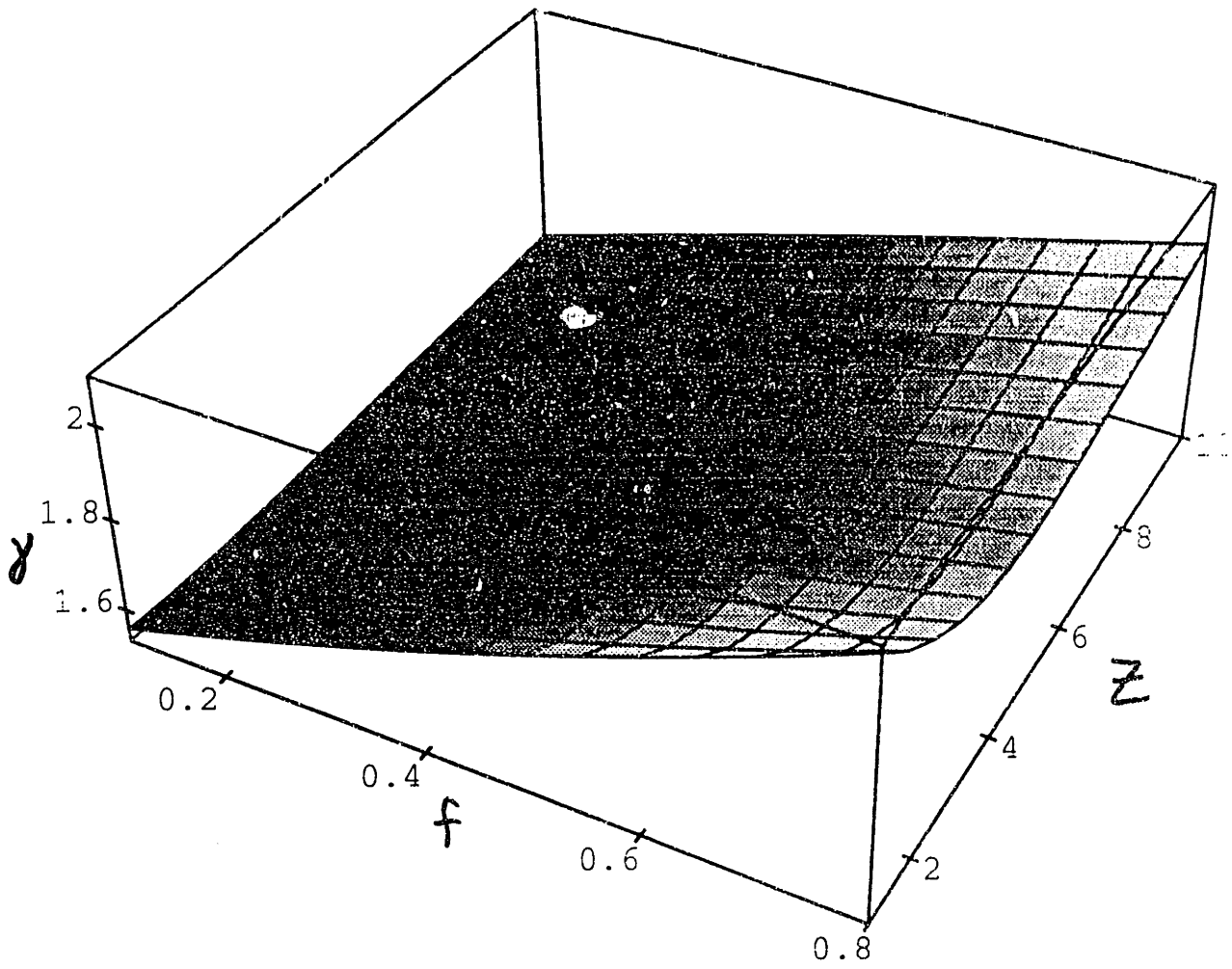

Figure 5.5: The artifact γ as a function of density, f, and energy, z using the solutions for the 3 speed model that makes $g = 1$. Although close to the continuum value of 1.5 at low density, the discrepancy grows with density although the largest error for $f = .5$ is limited to 17%

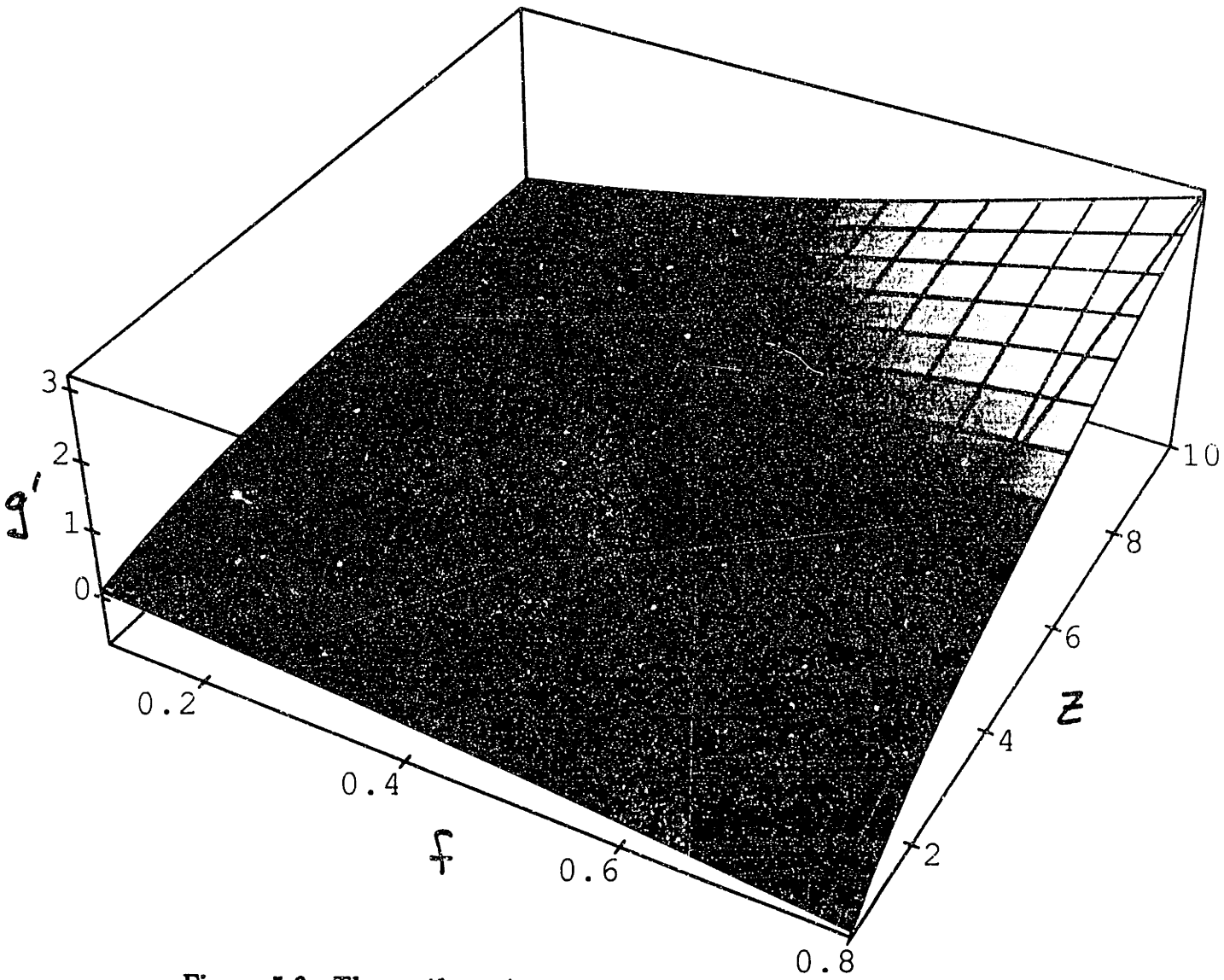

Figure 5.6: The artifact g' as a function of density, f, and energy, z using the solutions for the 3 speed model that makes $g = 1$. Note the proximity of g' to the hydrodynamic value $g' = 1$ in the range $0.4 \leq f \leq 0.6$ and $4 \leq z \leq 8$.

in low speed models.

That the error in γ is small once g has been corrected can be shown by isolating for the ratio $\rho/(1,\epsilon)_1$ in the g artifact when g=1. Since this same ratio appears in the expression for γ, eqn. (3.74), we can substitue the result from the g relation. We use the fact that higher order moments can be written in terms of lower order moments, specifically

$$(1,\epsilon)_1 = U_p - \sum_j d_j N_j^2 \epsilon_j \tag{5.17}$$

$$(\epsilon,\epsilon)_2 = (\epsilon,\epsilon)_1 - 2\sum_j d_j N_j^2 (1-N_j)\epsilon_j^2. \tag{5.18}$$

where the correction terms are at least quadratic in the zero-order density N_j, to rewrite γ

$$\begin{aligned}
\gamma &= \frac{(\epsilon,\epsilon)_1}{U_p}\left[\frac{D+2}{D}\frac{(1,\epsilon)_1}{(\epsilon,\epsilon)_2}\right] \\
&= \frac{D+2}{D}\left[\left(1-\frac{\sum_j d_j N_j^2\epsilon_j}{U_p}\right)\left(1+\frac{2\sum_j d_j N_j^2(1-N_j)\epsilon_j^2}{(\epsilon,\epsilon)_2}\right)\right] \\
&= \frac{D+2}{D} - \frac{D+2}{D}\frac{\sum_j d_j N_j^2\epsilon_j}{U_p} + \frac{D+2}{D}\frac{2}{U_p}\frac{(U_p-\sum_j d_j N_j^2\epsilon_j)}{(\epsilon,\epsilon)_2}\sum_j d_j N_j^2(1-N_j)\epsilon_j^2
\end{aligned} \tag{5.19}$$

which clearly shows that at low density γ approaches the continuum value $\gamma \to (D+2)/D = 1.5$, for the 4D case. As the density is increased, the two higher order terms in eqn. (5.19) contribute significantly and push γ away from 1.5. By adding another rate coefficient we could attempt to force the two higher order terms to cancel each other. To examine this requirement more rigorously, we make the expansion in density explicit by defining the notation

$$< \epsilon^n >_k \equiv \sum_j d_j N_j^k \epsilon_j^n, \tag{5.20}$$

the nth energy moment of the zero-order density distribution raised to the kth power. All of these moments are necessarily positive quantities. N_j is the prob-

ability of particle occupation and so must be less than 1. In this notation, the relevant moments in the g and γ relations are, using eqns. (3.51)

$$\begin{aligned} U_p &= <\epsilon>_1 \\ (1,\epsilon)_1 &= <\epsilon>_1 - <\epsilon>_2 \qquad (5.21) \\ (\epsilon,\epsilon)_1 &= <\epsilon^2>_1 - <\epsilon^2>_2 \\ (\epsilon,\epsilon)_2 &= <\epsilon^2>_1 -3<\epsilon^2>_2 +2<\epsilon^2>_3 . \qquad (5.22) \end{aligned}$$

Using the above, eqn. (5.19) becomes

$$\gamma = \frac{D+2}{D}\left(1 + \frac{2<\epsilon^2>_2<\epsilon>_1 - <\epsilon>_2<\epsilon^2>_1}{<\epsilon>_1<\epsilon^2>_1} + \mathcal{O}(N_j^2)\right) \qquad (5.23)$$

so that the second rate coefficient must force

$$2<\epsilon^2>_2<\epsilon>_1 = <\epsilon>_2<\epsilon^2>_1 \qquad (5.24)$$

for γ to be correct at low to moderate densities. The following relationships hold amongst the moments

$$<\epsilon^2>_1 \;>\; <\epsilon>_1 \;>\; <\epsilon>_2 \qquad (5.25)$$

$$<\epsilon^2>_1 \;>\; <\epsilon^2>_2 \;>\; <\epsilon>_2 \qquad (5.26)$$

for all N_j in the physical range $0 \leq N_j \leq 1$. The rate coefficient cannot alter these relations. The determination of which of the pair $<\epsilon^1>$ and $<\epsilon^2>_2$ is larger depends on N_j.

In the 3-speed model, the left-side of eqn. (5.24) is larger than the right since $\gamma > 1.5$ when $q = 1$. This means we would like to increase the value of the largest moment $<\epsilon^2>_1$ to balance the two sides. We may make this moment larger by preferentially increasing the number of particles with higher speeds. This can

be accomplished by associating the new rate coefficient with the highest speed distribution in the model, $r_{j_{max}}$. At low densities and temperatures, $< \epsilon^2 >_1 \sim < \epsilon >_1$ and $< \epsilon^2 >_2 \sim < \epsilon >_2$ since there are very few particles in higher energy states. This along with the relations in eqns. (5.25) and (5.26) indicates why the first order in density contribution to γ, eqn. (5.23), is positive. As the density and temperature increase and more particles are in the highest speed, the rate coefficient is more effective in reducing the discrepancy between the two sides of eqn. (5.24). Still, if j_{max} is too small, it may not be possible to increase the value of $< \epsilon^2 >_1$ enough over the other moments to satisfy eqn. (5.24) due to the requirements of eqns. (5.25) and (5.26). In these cases, there is a value of the rate coefficient that minimizes the error in the artifacts g and γ. If this error is acceptably low[2], then this approximate solution is acceptable. We know that the balancing of eqn. (5.24) must become easier as higher speeds are added since the artifacts naturally vanish as the discrete continuum is approached, as shown in Chapter 4.

The smallest system that might be able to remove both of these artifacts is again the 3-speed model with two rate coefficients, the previous r_0 to remove g and the new rate r_2, to set γ correctly. When we attempt to solve eqns. (3.70) and (3.74) simulataneously for y and r_2 with $j_{max} = 2$, we find that no exact solutions are possible, for the reasons described above. Moreover, at typical densities and temperatures, the minimum errors attainable in the artifacts are greater than 5%, which is too large to be practically useful.

The next smallest system is the four-speed model where we add particles with energy=3. The velocities for this energy are all the signed permutations

[2]below the threshold of being measured

of (2,1,1,0), of which there are 96, $d_3 = 96$. As does any complete set of velocity vectors for a given speed, j, on the 4D FCHC lattice, the set of $j = 3$ vectors are sufficiently symmetric to ensure an isotropic stress tensor. We associate the rate coefficient r_3 with this energy so that $N_3 = \frac{yr_3}{yr_3+z^3}$ and eqn. (5.4) becomes

$$f = \frac{1}{4}N_0 + N_1 + N_2 + 4N_3 = f(y, r_0, r_3, z) \tag{5.27}$$

from which we can solve for r_0 analytically

$$\begin{aligned} r_0 \;=\; & [-4(-6r_3y^3 + fr_3y^3 - 5r_3y^2z + fr_3y^2z - 5r_3y^2z^2 + fr_3y^2z^2 \\ & - 4r_3yz^3 - fr_3yz^3 - 2y^2z^3 + fy^2z^3 - yz^4 + fyz^4 - yz^5 + fz^6)]/ \\ & [y(-25r_3y^3 + 4fr_3y^3 - 21r_3y^2z + 4fr_3y^2z - 21r_3y^2z^2 + 4fr_3y^2z^2 - 17r_3yz^3 \\ & + 4fr_3yz^3 - 9y^2z^3 + 4fy^2z^3 - 5yz^4 + 4fyz^4 - 5yz^5 + 4fyz^5 - z^6 + 4fz^6)]. \end{aligned} \tag{5.28}$$

The equations we use to solve for y and r_3 are

$$g = \frac{2}{3}\frac{[N_1(1-N_1)(1-2N_1) + 4N_2(1-N_2)(1-2N_2) + 36N_3(1-N_3)(1-2N_3)]}{[N_1(1-N_1) + 2N_2(1-N_2) + 12N_3(1-N_3)]^2}f = 1 \tag{5.29}$$

and

$$\gamma = \frac{[N_1(1-N_1) + 4N_2(1-N_2) + 36N_3(1-N_3)]}{[N_1(1-N_1) + 2N_2(1-N_2) + 12N_3(1-N_3)][N_1 + 2N_2 + 12N_3]}f = \frac{3}{2}. \tag{5.30}$$

Again we find that it is not possible to find an exact solution for all density and temperatures with this model but the errors are much smaller than in the $j_{max} = 2$ model. For example, Figure 5.7 shows the $g = 1$ and $\gamma = 1.5$ contours as functions of y and r_3 for a typical case where $f = .26$ and $z = 5.5$. Although the curves come very close to each other, they do not intersect which indicates there is no solution (y, r_3) that removes both artifacts simultaneously. However, we see that as r_3 increases, the two curves approach each other to a point of minimum distance

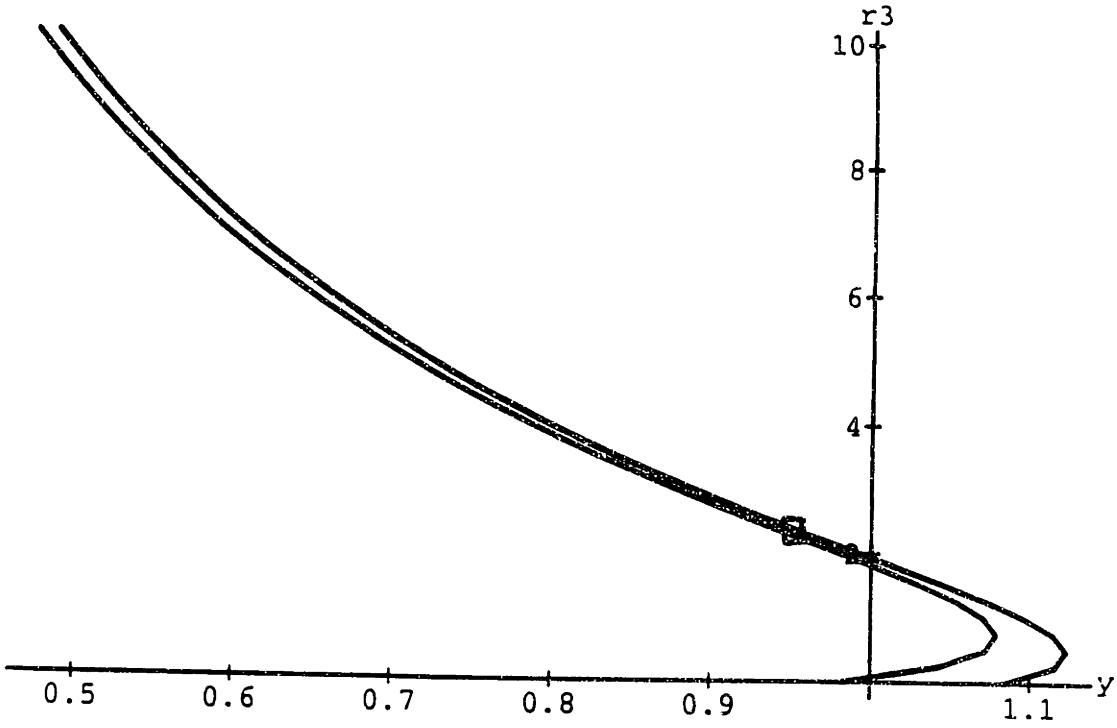

Figure 5.7: Contours of $g = 1$ and $\gamma = 1.5$ as functions of the fugacity, y, and the rate coefficient, r_3, for $f = .26$, $z = 5.5$ in a four-speed model. Since the contours do not intersect, there is no simultaneous solution for the artifacts at this density and temperature. The point where the curves are closest together, as indicated, results in an error in both artifacts of only .5%, which is acceptable.

and then diverge. If we select the point midway between the two curves at the point of closest approach, $y = 0.95$, $r_3 = 2.34$, the error in either artifact is only .5%, which is smaller than the accuracy to which we can measure the artifacts in a simulation. Thus, we can use this point as a solution for the system.

On the other hand, at higher densities and values of z, it becomes possible to calculate an exact solution to the system. As shown in Figure 5.8 for the case $f = .44, z = 9.35$, the two contours do intersect at $y = 3.76, r_3 = 4.40$, so that the two artifacts can completely be removed in this case.

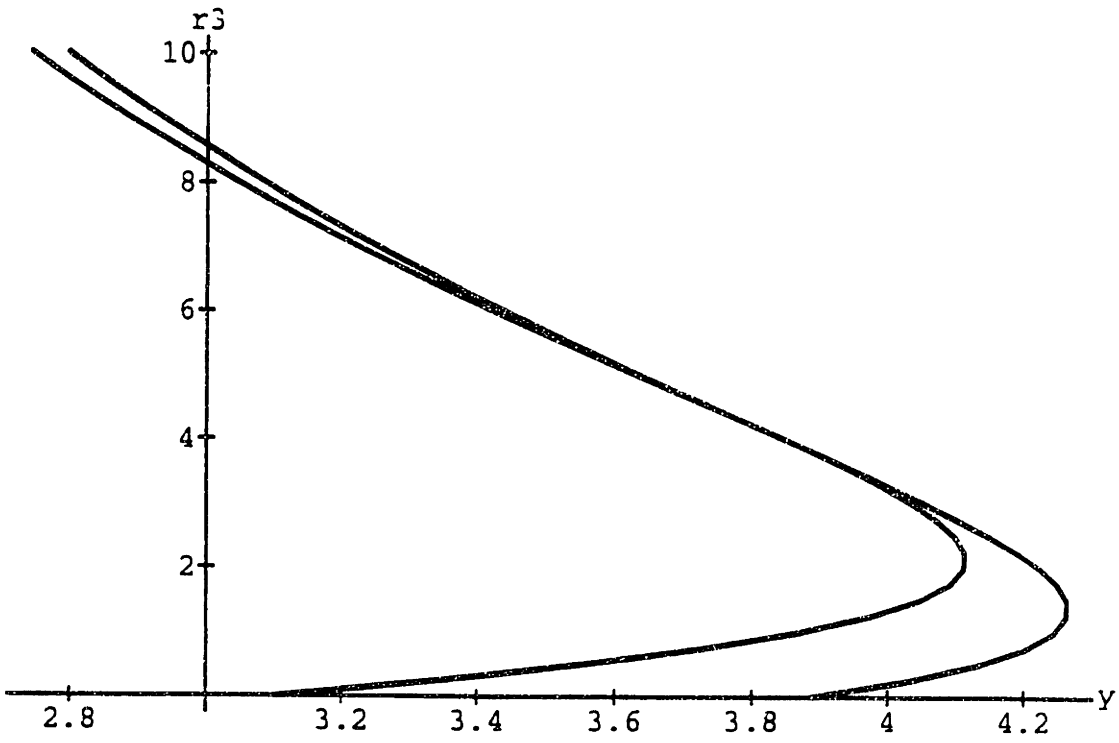

Figure 5.8: Contours of $g = 1$ and $\gamma = 1.5$ as functions of the fugacity, y, and the rate coefficient, r_3, for $f = .44$, $z = 9.35$ in a four-speed model. In this case, the contours do intersect so that an exact solution for removing the artifacts is possible.

There are two regions of solution for this system. A region where the solution is exact at high density and z and the rest of parameter space where no exact solution is possible, but a 'solution' that minimizes the errors in the artifacts may be found. The 'solutions' in this second region can be used only if the errors in the artifacts are 1% or less so that there is no detectable evidence of the artifacts in the macroscopic behaviour of the model. Figures 5.9, 5.10, 5.11 illustrate the solutions y,r_0, and r_3 to this system. Although the numerically calculated solutions y and r_3 appear planar for the most part, there is some slight curvature so that the

best-fit equations to these curves in the approximate solution region are

$$\begin{aligned} y(f,z) &= 0.01 - 1.49f + 4.59f^2 - 6.03f^3 + 1.03fz \\ &\quad - 1.64f^2z + 2.08f^3z - .025fz^2 + 0.129f^2z^2 \qquad (5.31) \\ r_3(f,z) &= 0.37 + 0.42f - 2.64f^2 - 0.29fz + 1.66fz^2 \\ &\quad + 0.095z^2 - 0.074fz^2 - 0.18f^2z^2. \qquad (5.32) \end{aligned}$$

The root-mean-square errors in these two relations with respect to the actual solutions are 1.5% and 2% respectively. Once we have y and r_3, r_0 is calculated using eqn. (5.28). For $z \geq 2.$, we see that the solution for r_0 is rather flat which is ideal for maintaining the correct values of the artifacts in a system where the density and temperature may be changing rapidly.

The curvature in the solution changes abruptly when the exact solution region is entered. The curve that separates the two solutions in parameter space is

$$z = 17.3 - 18.0f \qquad (5.33)$$

where approximate solutions solutions exist for z less than this relation and exact solutions exist for z greater than this relation. The best-fit equations to the solutions in the exact region are

$$\begin{aligned} y(f,z) &= 26.2 - 93.8f + 89.4f^2 - 2.18z + 8.45fz - 7.73f^2z \\ &\quad + .0643f^2z^2 \qquad (5.34) \\ r_3(f,z) &= -116 + 414f - 386f^2 + 8.62z - 31.0fz + 30.3f^2z \\ &\quad + .0754z^2 - .105f^2z^2. \qquad (5.35) \end{aligned}$$

Because the range in which an exact solution is possible is a small portion of the parameter space that we investigated, the above equations reproduce the data

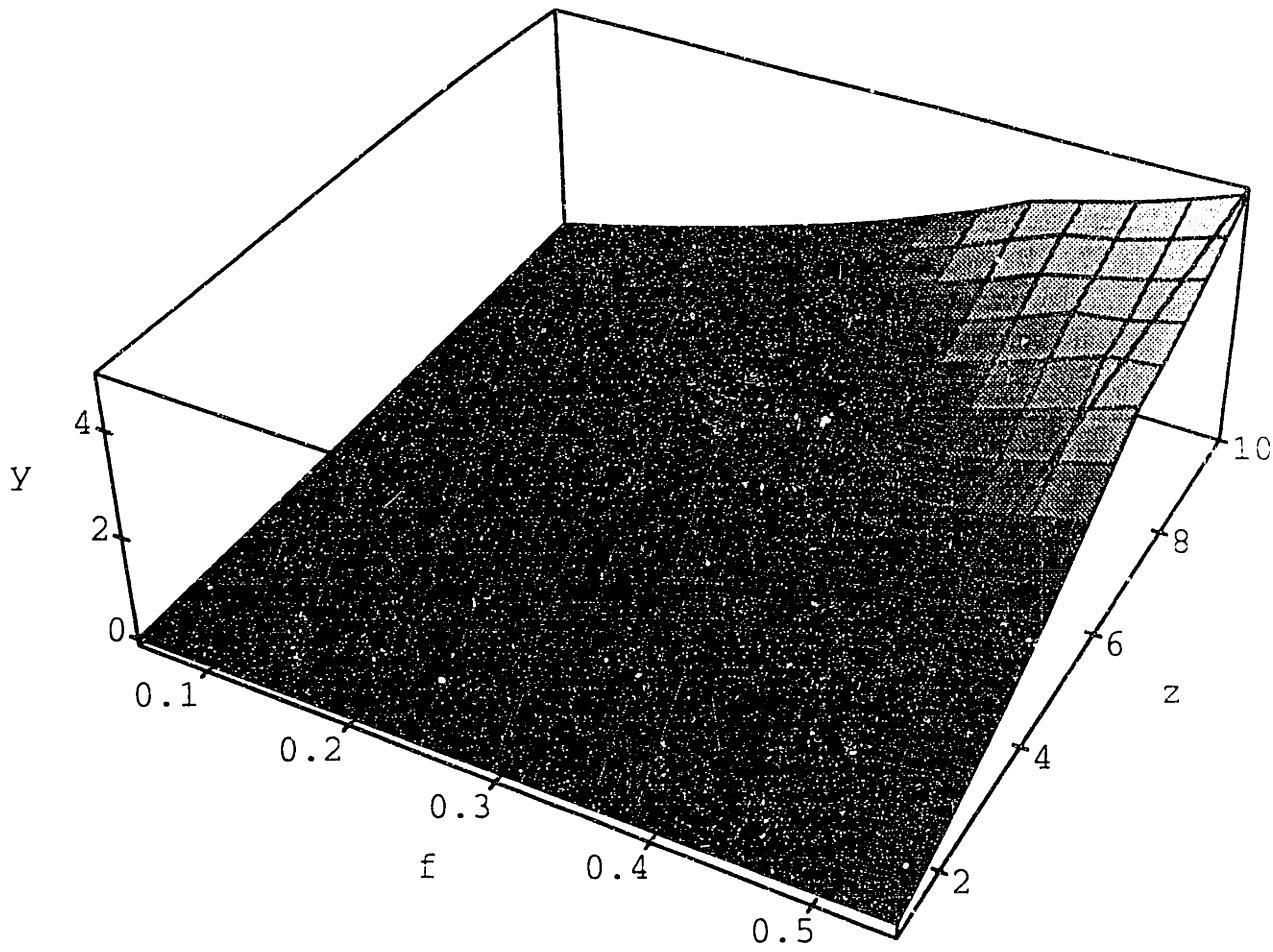

Figure 5.9: Fugacity as a function of density, f, and temperature, z for the four-speed model that gives $g \simeq 1$ and $\gamma \simeq 1.5$ in the region $z < 17.3 - 18.0f$ and an exact solution for $z \geq 17.3 - 18.0f$.

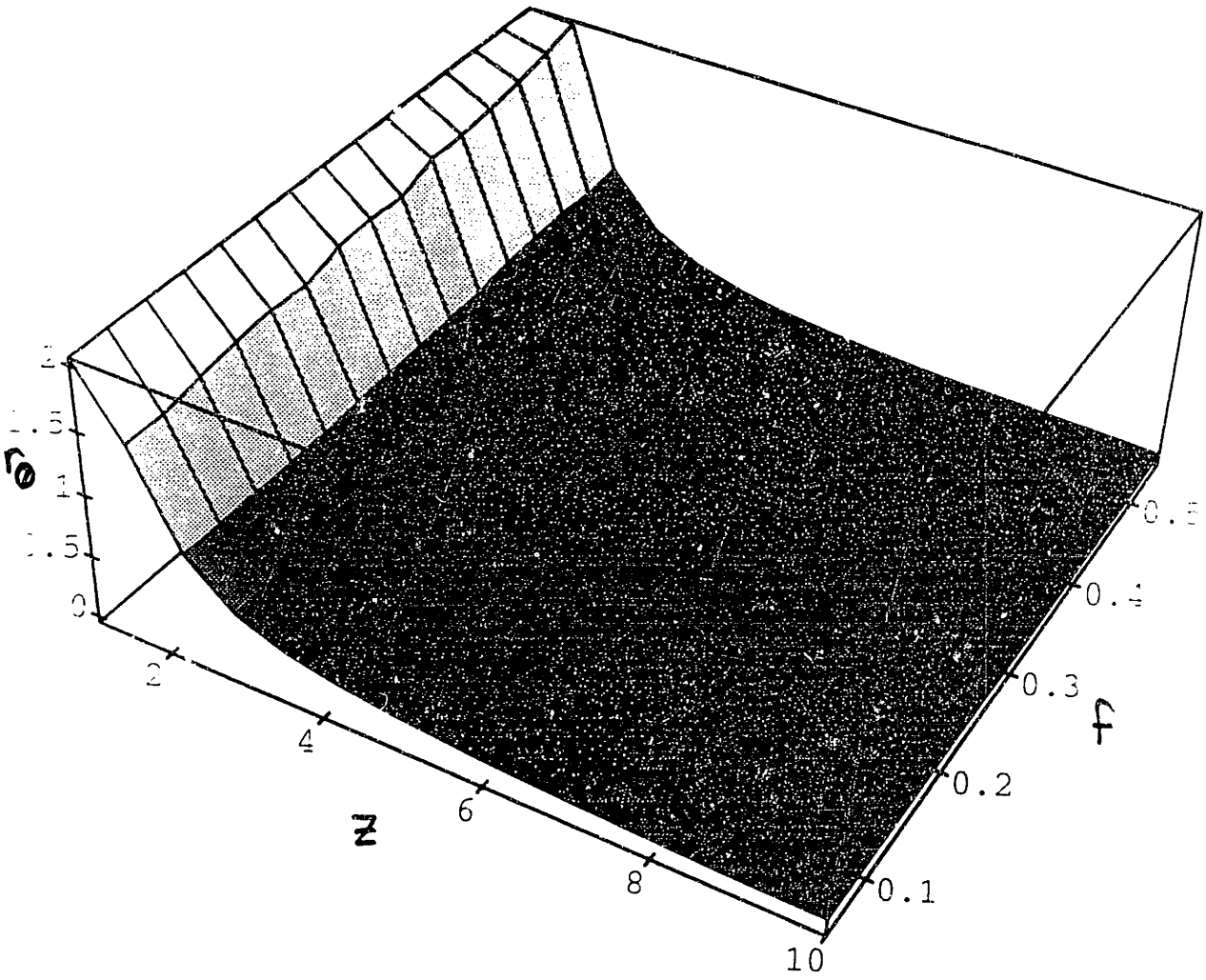

Figure 5.10: Rate Coefficient r_0 as a function of density, f, and temperature, z for the four- speed model that gives $g \simeq 1$ and $\gamma \simeq 1.5$ in the region $z < 17.3 - 18.0f$ and an exact solution for $z \geq 17.3 - 18.0f$.

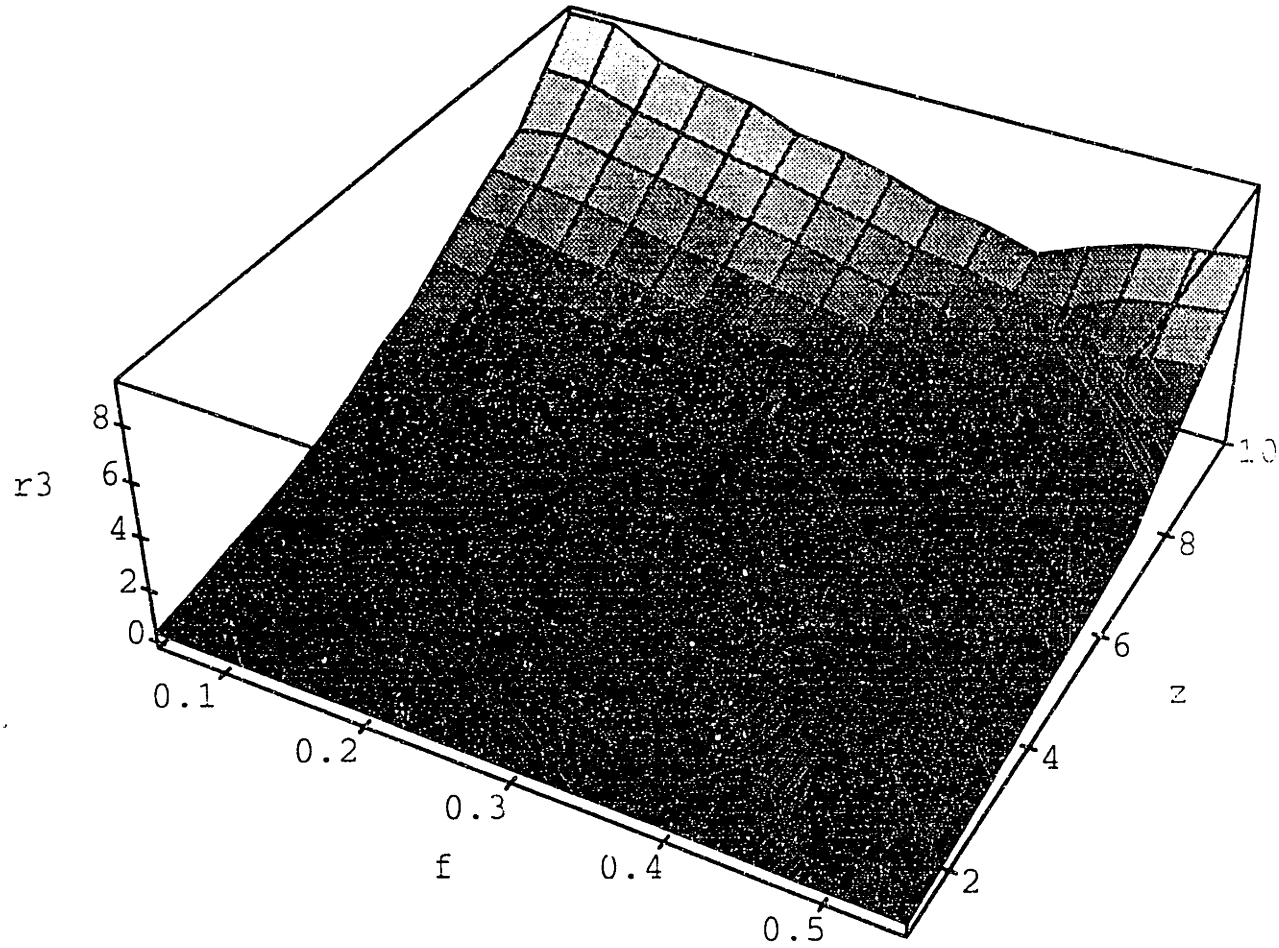

Figure 5.11: Rate Coefficient r_3 as a function of density, f, and temperature, z for the four- speed model that gives $g \simeq 1$ and $\gamma \simeq 1.5$ in the region $z < 17.3 - 18.0f$ and an exact solution for $z \geq 17.3 - 18.0f$.

points quite accurately, with an overall root-mean-square error of about 0.2% in both cases. In a simulation where the masks may be changing rapidly, requiring repeated calculation of the masks[3], it would probably be more computationally efficient to maintain a look-up table of the variables y and r_3 and interpolate when needed.

Figure 5.12 presents the maximum error from either g or γ for our solution. Of course, in the exact solution range the error is zero. The region of parameter space where the maximum error is 1% or less is given by

$$z \geq -3.4 + 26.9f - 23.9f^2 \tag{5.36}$$

which indicates that for $f \leq .15$, acceptable solutions exist for all z while at $f \sim .4$, only solutions where $z \geq 3.5$ are acceptable.

This solution used the value $d_0 = 6$, a maximum of six stopped particles per site. As in the 3-speed model, the range for which r_0 is positive and hence, physical, depends on the value of d_0 strongly. With $d_0 = 1$ there is only a very limited region of parameter space, $f \leq .2$ and $z \geq 4.$ where r_0 is positive. With $d_0 = 3$, this rate coefficient is positive for $0. \leq f \leq .275$ and $z \geq 2.$, which is entirely enclosed in the region where the errors in g and γ are bounded by 1%.

With the solution for the removal of g and γ system complete, we now calculate the final artifact, g' using the computed solutions and eqn. (3.75). The result, shown in Figure 5.13, shows that typically $g' \leq .6$ which is significantly different from the continuum value 1.

Unlike the 3-speed model where there was a range of parameter space with $g' \sim 1$, g' is everywhere smaller than unity in this case. To make $g' = 1$ as well

[3]Using the same feedback procedure as outlined in Section 5.1

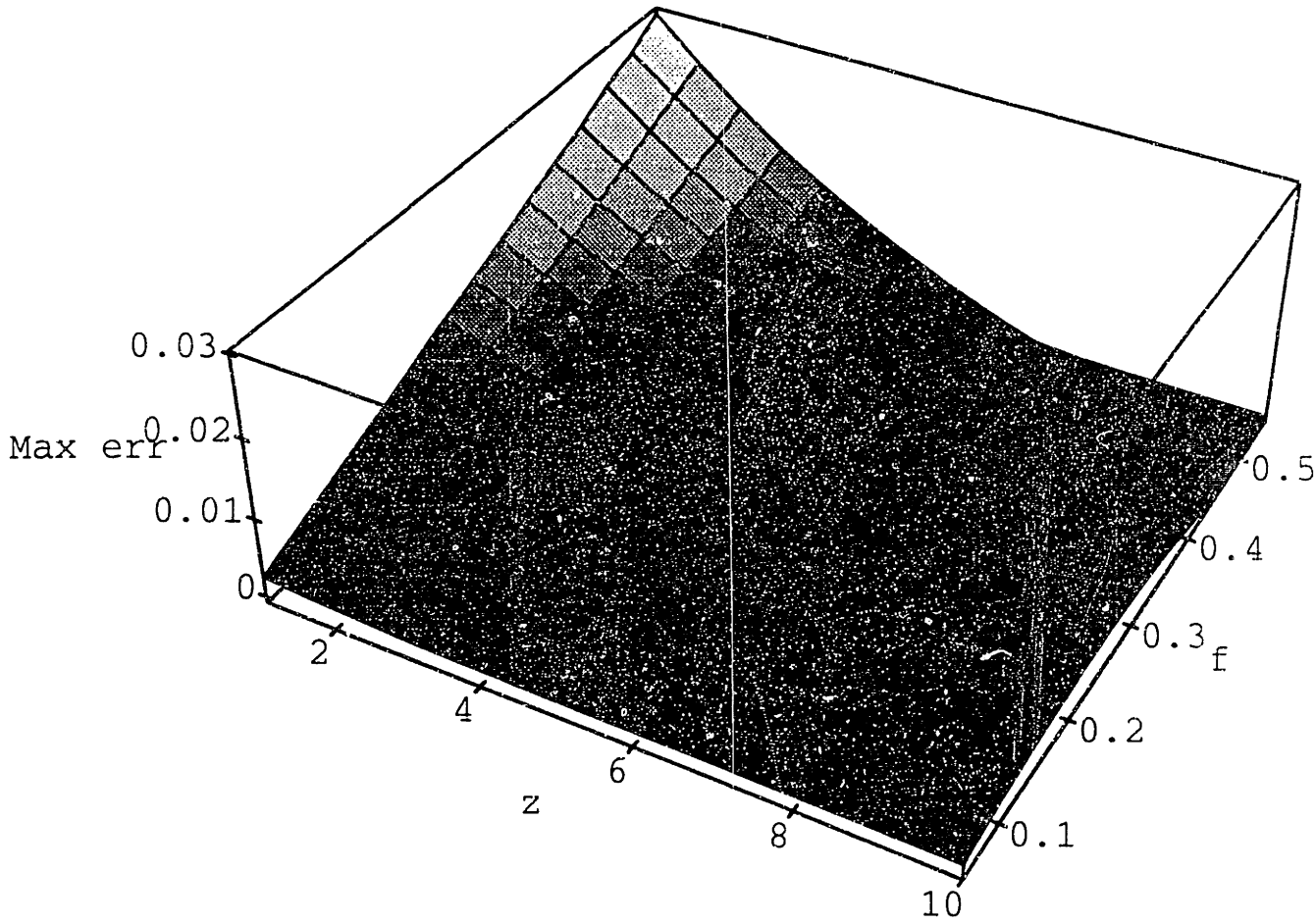

Figure 5.12: Illustrates the maximum error in the artifacts g and γ for the four speed model with two rate coefficients. For $z \geq -3.4 + 26.9f - 23.9f^2$, the maximum error is less than 1%. This is the usable range of this model.

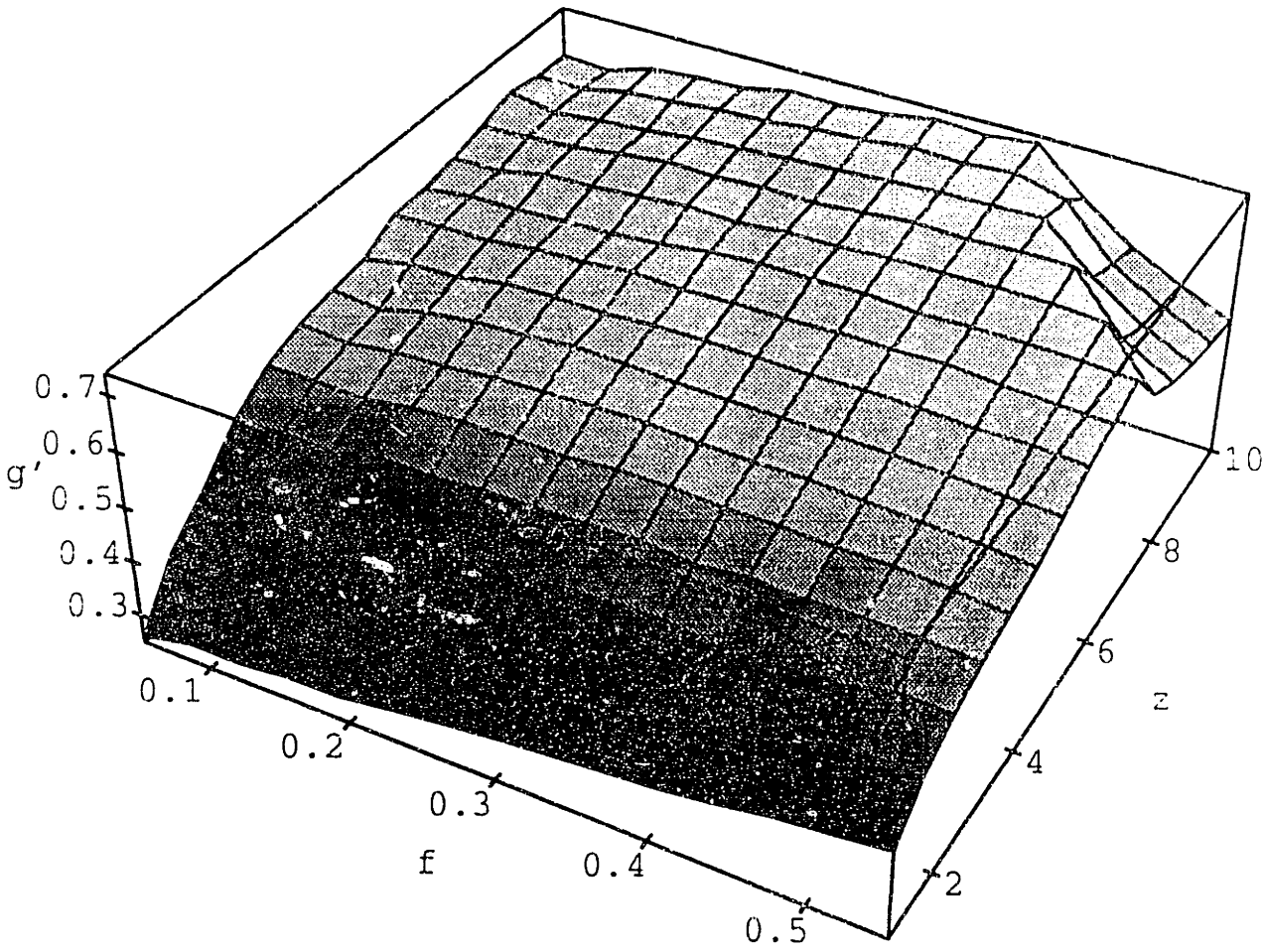

Figure 5.13: The artifact g' as a function of density, f, and energy, z using the solutions for the 4 speed model that makes $g \sim 1$ and $\gamma \sim 1.5$. g' is everywhere less than 0.7, for this model, which means the error in this artifact is at least 30% in this model.

would require another rate coefficient and higher speeds. The equation for g', eqn. (3.75) is so complicated that insight into what moments need to be alterred, as was possible for g and γ, is not possible. In a four-speed model with three rate coefficients, exploratory attempts to find full solutions resulted in no possible physical solutions for all densities and temperatures both large and small. Although the $g = 1$ and $\gamma = 1.5$ contours were once again very close together, the $g = 1$ contour was an order of magnitude displaced from the other two contours in parameter space. We prove in Section (5.4) that a five-speed model is the smallest system that can remove all three artifacts in the low-density limit. Thus, if a solution exists for general density, the system must have at least five speeds. If we move to a five-speed system and solve just for the g and γ artifacts by adding a r_5 rate coefficient, the range for which only approximate solutions are possible decreases slightly in comparison with the four speed model while the improvement in the minimum errors associated with artifacts in this region are only about 0.1% smaller, on average. Consequently, the additional computational effort required to add the fifth speed outweighs the slight improvement in the accuracy of the solution over the four speed model, when the removal of just the first two artifacts is the goal. On the other hand, a five speed system is the minimum model required to remove all three artifacts.

The four-speed model presented here can be used in simulations where the term including the remaining artifact is negligible. To find this range we examine the relative magnitudes of the two contributions to the energy flux vector, eqn.(3.26)

$$\mathbf{Q} = \left(\gamma U_p + g' \tfrac{1}{2}\rho u^2\right) \mathbf{u} \tag{5.37}$$

when the ratio of specific heats has its correct value, $\gamma = \frac{D+2}{D}$ and $g = 1$. For this

lattice gas, eqn. (3.38) indicates that

$$\frac{D+2}{D}U_p = \frac{D}{2}\rho c_s^2. \tag{5.38}$$

We then find that

$$\frac{\frac{1}{2}g'\rho u^2}{\gamma U_p} \simeq \frac{1}{D}g' M^2 \tag{5.39}$$

where M is the Mach number. We have seen that for this model $g' < 1$. We set $g' = 1$ in eqn. (5.39) to be conservative (and so that this calculation will hold for the case where *all* of the artifacts have been removed) and then calculate the Mach number that will keep the magnitude of the second-order contribution to the energy flux less than $\sim\leq 0.5\%$ of the zeroth order contribution. This value of Mach number is

$$M \leq 0.15. \tag{5.40}$$

Thus, we can use the four-speed model developed here to accurately simulate heat and momentum transfer in flows with a Mach number, $M \leq 0.15$.

5.3 Density Expansion of Artifact Relations

The Fermi-Dirac form of the equilibrium distribution complicates analytical computation of solutions for systems where the artifacts are removed. We were able to achieve a system where $g = 1$ by employing a virial expansion in the fugacity while a combination approximate-exact solution for the simultaneous $g = 1$ and $\gamma = 1.5$ case was possible only by numerical calculation. In low-speed models, it does not seem possible to remove all three artifacts or reduce the errors to an acceptable level in the arbitrary density case. In order to obtain some physical insight into how the artifacts are removed as well as to see if tractable solutions for

the removal of all three artifacts are possible at low densities. we now expand the artifact relations for small densities. We have written the equilibrium distribution N_{ji} as an expansion in Mach number, eqn. (3.41) so that it can be expressed as a function of the isotropic distribution function N_j. An expansion about small density proceeds by expanding N_j as a small quantity, using eqn. (5.2)

$$\begin{aligned} N_j &= \frac{yr_j}{yr_j + z^j} = \frac{\frac{yr_j}{z^j}}{1 + \frac{yr_j}{z^j}} \\ &= \frac{yr_j}{z^j} \sum_{i=0}^{\infty} (-1)^i \left(\frac{yr_j}{z^j}\right)^i \\ &\approx \frac{yr_j}{z^j} \sum_{i=0}^{k-1} (-1)^i \left(\frac{yr_j}{z^j}\right)^i \equiv (N_j^{LD})_k \end{aligned} \tag{5.41}$$

which is an expansion to order k around the low density equilibrium expression

$$N_j^{LD} = \frac{yr_j}{z^j} \equiv r_j e^{-\alpha_0} e^{-\beta_0 j}. \tag{5.42}$$

Incidentally, this low density distribution now has the Maxwell-Boltzmann form. The relative error in the truncated expansion can be shown to be

$$\frac{N_j - (N_j^{LD})_k}{N_j} = (-1)^k \left(\frac{yr_j}{z^j}\right)^k \tag{5.43}$$

so that if we wish to keep the error in a third order, or $k = 3$, expansion below 5%, we require that $N_j \leq .27$. We now expand all three artifacts to third order in the low density relation and attempt to remove the artifacts order by order.

The explicit expressions for the distribution function and its derivatives appear in the artifact calculations of Section 3.2 only in the moment relations, eqn. (3.51). Thus we do not need to repeat the calculation of the artifacts, we may simply expand the moments that appear in the artifact expressions about the low density function. All four moments of eqns. (3.51), expanded to third order, may be

summarised as

$$\begin{aligned}(\mathbf{a},\mathbf{b})_n &\simeq \sum_j d_j N_j^{LD}(1-2^n N_j^{LD}+3^n N_j^{LD^2})a_j b_j. \\ &\simeq < ab >_1 -2^n < ab >_2 +3^n < ab >_3 \end{aligned} \tag{5.44}$$

using the notation of eqn. (5.20).

As usual, we begin with the expansion of the g artifact, eqn. (3.70)

$$\begin{aligned} g &\simeq \frac{D}{D+2}\frac{(< \epsilon^2 >_1 -4 < \epsilon^2 >_2 +9 < \epsilon^2 >_3)}{(< \epsilon >_1 -2 < \epsilon >_2 +3 < \epsilon >_3)^2}(< \epsilon^0 >_1 - < \epsilon^0 >_2 + < \epsilon^0 >_3) \\ &\simeq \frac{D}{D+2}\frac{< \epsilon^2 >_1 < \epsilon^0 >_1}{< \epsilon >_1^2}\left[1+\left(4\frac{< \epsilon >_2}{< \epsilon >_1} - 4\frac{< \epsilon^2 >_2}{< \epsilon^2 >_1} - \frac{< \epsilon^0 >_2}{< \epsilon^0 >_1}\right)\right. \\ &\quad + \left(9\frac{< \epsilon^2 >_3}{< \epsilon^2 >_1} - 16\frac{< \epsilon >_2 < \epsilon^2 >_2}{< \epsilon >_1 < \epsilon^2 >_1} - 4\frac{< \epsilon >_2 < \epsilon^0 >_2}{< \epsilon >_1 < \epsilon^0 >_1}\right. \\ &\quad \left.\left. +4\frac{< \epsilon^2 >_2 < \epsilon^0 >_2}{< \epsilon^2 >_1 < \epsilon^0 >_1} + \frac{< \epsilon^0 >_3}{< \epsilon^0 >_1} + 12\left(\frac{< \epsilon >_2}{< \epsilon >_1}\right)^2 - 6\frac{< \epsilon >_3}{< \epsilon >_1}\right)\right]. \end{aligned} \tag{5.45}$$

To achieve hydrodynamics, the lowest order term in this expansion should have the value 1 while the higher order terms should vanish. We view this as three equations for the three moments $< \epsilon^2 >_n$. To give $g = 1$ at zeroth order requires that

$$< \epsilon^2 >_1 = \frac{D+2}{D}\frac{< \epsilon >_1^2}{< \epsilon^0 >_1} \tag{5.46}$$

while if the first order contribution is to vanish then

$$< \epsilon^2 >_2 = < \epsilon^2 >_1 \left(\frac{< \epsilon >_2}{< \epsilon >_1} - \frac{1}{4}\frac{< \epsilon^0 >_2}{< \epsilon^0 >_1}\right). \tag{5.47}$$

For notational convenience, we define

$$x \equiv \frac{< \epsilon >_2}{< \epsilon >_1} \sim \mathcal{O}(N_j) \tag{5.48}$$

a first order in density expansion parameter. The following are all combinations of moments that are zeroth order in density

$$\eta \equiv \frac{D}{D+2}\frac{< \epsilon^0 >_1}{< \epsilon >_1} \tag{5.49}$$

$$\kappa \equiv \frac{<\epsilon>_1 <\epsilon^0>_2}{<\epsilon^0>_1 <\epsilon>_2} \tag{5.50}$$

$$\xi \equiv \frac{<\epsilon>_1 <\epsilon^0>_3}{<\epsilon^0>_1 <\epsilon>_3} \tag{5.51}$$

$$\mu \equiv \frac{<\epsilon>_1 <\epsilon>_3}{<\epsilon>_2^2}. \tag{5.52}$$

Thus eqn. (5.46) is

$$<\epsilon^2>_1 = \frac{<\epsilon>_1}{\eta} \tag{5.53}$$

and eqn. (5.47) is

$$<\epsilon^2>_2 = \frac{<\epsilon>_1}{\eta} x \left(1 - \frac{\kappa}{4}\right). \tag{5.54}$$

Similarly, a straightforward calculation shows that the third order contribution to g in eqn. (5.45) vanishes if

$$<\epsilon^2>_3 = \frac{<\epsilon>_1}{\eta} \frac{x^2}{9} \left[(\kappa - 2)^2 + \mu(6 - \xi)\right]. \tag{5.55}$$

We now proceed to calculate γ, eqn. (3.74), in the same manner

$$\begin{aligned}
\gamma &\simeq \frac{(<\epsilon^0>_1 - <\epsilon^0>_2 + <\epsilon^0>_3)(<\epsilon^2>_1 - 2<\epsilon^2>_2 + 3<\epsilon^2>_3)}{(<\epsilon>_1 - 2<\epsilon>_2 + 3<\epsilon>_3)(<\epsilon>_1 - <\epsilon>_2 + <\epsilon>_3)} \\
&\simeq \frac{<\epsilon^0>_1 <\epsilon^2>_1}{<\epsilon>_1^2} \left[\frac{1 - \frac{<\epsilon^0>_2}{<\epsilon^0>_1} + \frac{<\epsilon^0>_3}{<\epsilon^0>_1}}{1 - 2\frac{<\epsilon>_2}{<\epsilon>_1} + 3\frac{<\epsilon>_3}{<\epsilon>_1}}\right] \left[\frac{1 - 2\frac{<\epsilon^2>_2}{<\epsilon^2>_1} + 3\frac{<\epsilon^2>_3}{<\epsilon^2>_1}}{1 - \frac{<\epsilon>_2}{<\epsilon>_1} + \frac{<\epsilon>_3}{<\epsilon>_1}}\right] \\
&\simeq \frac{D+2}{D} \left[1 + (1 - \frac{\kappa}{2})x + \frac{(4\xi\mu - 12\mu - \kappa^2 - 5\kappa + 14)}{6} x^2\right]
\end{aligned} \tag{5.56}$$

where in the last line we have substituted the relations for $<\epsilon^2>_n$ that make $g = 1$. As was found in Section 5.2, when $g = 1$, the zeroth order term in γ is correct, $\gamma = \frac{D+2}{D}$. From eqn. (5.56), we see that the first order contribution to γ vanishes if $\kappa = 2$ and if we plug this value into the second order contribution, this term also vanishes if $\xi = 3$, independent of μ.

To complete the expansion solution, we examine the third artifact g', eqn. (3.75). As before, we substitute for the various moments using eqn. (5.44) and then expand to second order in the density variable x. We then force the zeroth order term to have the value unity while the two higher order terms vanish using the three $< \epsilon^3 >_n$ moments. Although the calculation is straightforward, it is also tedious and the expansion terms are cumbersome. We simply state the results. The zeroth order term is

$$g' = \frac{D+2}{2}\left[\frac{< \epsilon^3 >_1}{< \epsilon >_1}\frac{1}{\eta^2} - 1\right] \tag{5.57}$$

so that $g' = 1$ if

$$< \epsilon^3 >_1 = \frac{D+4}{D+2}\frac{< \epsilon >_1}{\eta^2}. \tag{5.58}$$

Using this result, the first order term vanishes if

$$< \epsilon^3 >_2 = \frac{D+4}{D+2}\frac{3-\kappa}{4\eta^2} < \epsilon >_2 \tag{5.59}$$

while the second order term is zero if

$$< \epsilon^3 >_3 = \frac{(a-2)^2(48+10D-D^2)+4\mu(D+4)(9-2\xi)}{108\mu\eta^2(D+2)} < \epsilon >_3 \tag{5.60}$$

where we have used the results from the first two moments.

To summarize, it is possible to cause all three artifacts to have their correct hydrodynamic values through second order in the density expansion if, in the $D = 4$ FCHC system, $\kappa = 2$, $\xi = 3$ and

$$< \epsilon^2 >_1 = \frac{< \epsilon >_1}{\eta} \qquad < \epsilon^3 >_1 = \frac{< \epsilon >_1}{\eta^2}\frac{4}{3} \tag{5.61}$$

$$< \epsilon^2 >_2 = \frac{< \epsilon >_1}{\eta}\frac{x}{2} \qquad < \epsilon^3 >_2 = \frac{< \epsilon >_1}{\eta^2}\frac{x}{3} \tag{5.62}$$

$$< \epsilon^2 >_3 = \frac{< \epsilon >_1}{\eta}\frac{x^2}{3}\mu \qquad < \epsilon^3 >_3 = \frac{< \epsilon >_1}{\eta^2}\frac{4\mu x^2}{27} \tag{5.63}$$

where the $< \epsilon^2 >_n$ relations force $g = 1$. the $< \epsilon^3 >_n$ relations force $g' = 1$ and the conditions on κ and ξ force $\gamma = 1.5$.

In the arbitrary density case, the three artifact relations required three rate coefficients to make a solution possible. Now that we have performed a density expansion on the artifacts, we find that there are eight relations that need to be satisfied to remove all the artifacts. Although each of these relations are considerably simpler than the arbitrary density artifact equations, we still must solve a non-linear system of eight equations and eight unknowns where the number of speeds in the model as well as the density and temperature are parameters. Consequently, the complete solution is certainly not trivially attained.

5.4 Removal of Artifacts at Low Density

In the previous section, we examined the artifact relations when the Fermi-Dirac equilibrium was expanded in a power series of the low density equilibrium, eqn. (5.42). We now examine the artifact relations when the density expansion is truncated after the first term. In this low density limit, once there are two particles at a site that may collide, there is such a low probability that another particle will be occupying an output site for that collision that the probability of a hole site is $1 - N_j \simeq 1$ effectively. Thus, we assume if the input particles for a collision are present then the collision will occur without the need to check for output hole sites. This changes the collision dynamics from Fermi-Dirac back to the familiar Maxwell-Boltzmann which explains why the low density limit of the Fermi-Dirac distribution is in fact the Maxwellian

$$N_j^{LD} = r_j exp\left[-(\alpha_0 + \beta_0 \epsilon_j)\right] = r_j \, y \, z^{-j}. \tag{5.64}$$

This is also known as the "classical limit" of the Fermi-Dirac distribution[48].

We will show that in the low density limit, it is possible to analytically solve the artifact relations when sufficient number of rate coefficients and particles speeds have been added to the system. The artifact relations in the low density limit are the zeroth order terms of the artifact expansions of the last section. We will re-derive those results here in more detail.

In the low density limit, all the inner products of eqn. (3.51) reduce to

$$(\mathbf{a},\mathbf{b})_* \Longrightarrow \sum_j d_j N_j a_j b_j \qquad \text{for } * = 0,1,2,3. \tag{5.65}$$

Furthermore, all moments of eqn. (5.20) with $k > 1$ are no longer needed. We drop the subscript on the one remaining first order moment so that

$$< \epsilon^n > \equiv \sum_j d_j N_j j^n. \tag{5.66}$$

The low density expressions for the artifacts result from reducing all subscripts on the moments to zero. Thus, there are only four moments left in the system of equations, $< \epsilon^n >$ for n=0,1,2,3. We already have expressions for the moments where $n = 0$ and 1

$$< \epsilon^0 > = \rho \qquad < \epsilon^1 > = U_p \tag{5.67}$$

which allows us to solve for the coefficients α_0 and β_0. Thus, only the $n = 2$ and 3 moments are free to remove the three artifacts, which seems to leave the system unsolvable but it turns out to be exactly as many as are needed.

Because the masses of all particles have been set equal to unity, the mass density, ρ, equals the particle density, $\rho \equiv n$. We define a fluid temperature for this system in the same way that it is done for a continuum fluid

$$P_s \equiv nT = \frac{2}{D} U_p \tag{5.68}$$

where P_s is the scalar part of the pressure tensor, the Boltzmann constant for this system is taken as $k = 1$ and the second equality holds because of equipartition of energy in an ideal gas, which we know also holds for a multiple-speed lattice gas if $g = 1$, eqn. (3.24). Thus, $U_p = \frac{D}{2}nT$. We know in closed systems that the particle density must remain constant. If the system is also isothermal, U_p or equivalently $< \epsilon >$, remains constant.

The first artifact we will examine is the expression for g. The low density form of eqn. (3.70) is

$$g = \frac{D}{D+2}\frac{< \epsilon^2 >}{< \epsilon >^2}\rho = \frac{D}{D+2}\frac{< \epsilon^2 >}{U_p^2}n. \tag{5.69}$$

Since g is smaller than one in a system without rate coefficients, we must raise its value. Since n and U_p are constant in closed, isothermal systems, the only moment that is free is $< \epsilon^2 >$. It is clear that a rate coefficient must be used to preferentially increase the number of particles with higher speeds so as to increase the second energy moment to the level where $g = 1$. If we put $g = 1$ and then solve for $< \epsilon^2 >$ we find

$$< \epsilon^2 >= \frac{D+2}{D}\frac{U_p^2}{n}. \tag{5.70}$$

If we can force the second moment of energy to have this value, the first artifact will be removed. The low density expression for the second artifact, γ (eqn. (3.74)), is

$$\gamma = \rho\frac{< \epsilon^2 >}{< \epsilon >< \epsilon >} = n\frac{< \epsilon^2 >}{U_p^2}. \tag{5.71}$$

If we now plug in the relation for $< \epsilon^2 >$ that makes $g = 1$ we find that

$$\gamma = \frac{\rho}{< \epsilon >^2}\left[\frac{D+2}{D}\frac{< \epsilon >^2}{\rho}\right] = \frac{D+2}{D} \tag{5.72}$$

which is the required value for the ratio of specific heats in an ideal gas. The condition on $< \epsilon^2 >$ in eqn. (5.70) removes both the g and γ artifacts. In the last

section, we found that γ was correct to zeroth order when $g = 1$ and that only higher order contributions contaminated the value of γ. In the low density case, the higher order terms are not present and the value of γ is exactly correct when $g = 1$.

We now turn our attention to the final artifact, g', as given by eqn. (3.75). The low density value of this expression is

$$\begin{aligned} g' &= \frac{\rho^2 D < \epsilon^2 >}{2 < \epsilon >^3} \left\{ \left[\frac{< \epsilon^3 >}{< \epsilon^2 >} - \frac{< \epsilon^2 >}{< \epsilon >} \right] \frac{D}{D+2} + \right. \\ &\frac{1}{A} \left[< \epsilon >< \epsilon^2 > - < \epsilon >< \epsilon^2 > + \frac{2}{D\rho} < \epsilon >^3 \right] \left[\frac{< \epsilon >}{< \epsilon >} - \frac{< \epsilon^2 >}{< \epsilon^2 >} \right] + \\ &\left. \frac{1}{A} \left[\rho < \epsilon^2 > - < \epsilon >< \epsilon > - \frac{2}{D\rho} \rho < \epsilon >^2 \right] \left[\frac{< \epsilon^2 >}{< \epsilon >} - \frac{< \epsilon^3 >}{< \epsilon^2 >} \right] \right\} \end{aligned} \quad (5.73)$$

where

$$A = \rho < \epsilon^2 > - < \epsilon >^2 = \frac{2}{D} < \epsilon >^2 \quad (5.74)$$

substituting for $< \epsilon^2 >$ from eqn. (5.70). We now see that the second square-bracketed term on the second line and the first bracketed term on the third line (using the above identity for A) are both identically zero. When we substitute for $< \epsilon^2 >$ we can simplify the remaining portion of g' to

$$g' = \frac{D+2}{2} \left[\rho^2 \frac{< \epsilon^3 >}{< \epsilon >^3} \left(\frac{D}{D+2} \right)^2 - 1 \right]. \quad (5.75)$$

Like g, the natural value of g' is smaller than the desired value of 1. The only moment that can be alterred in this expression is the third energy moment $< \epsilon^3 >$. Once again, we wish to raise this moment using another rate coefficient so that g' becomes unity. The value of $< \epsilon^3 >$ that makes $g' = 1$ is

$$< \epsilon^3 > = \frac{(D+4)(D+2)}{D^2} \frac{< \epsilon >^3}{\rho^2} = \frac{(D+4)(D+2)}{D^2} \frac{U_p^3}{n^2}. \quad (5.76)$$

Of course, the required expressions for the low density second and third energy moments are identical to the lowest order density results shown in eqn. (5.61). With D=4 for the FCHC lattice, we find the following requirements for the four energy moments

$$< \epsilon^0 > = n \tag{5.77}$$

$$< \epsilon^1 > = 2nT \tag{5.78}$$

$$< \epsilon^2 > = 6nT^2 \tag{5.79}$$

$$< \epsilon^3 > = 24nT^3. \tag{5.80}$$

These four equations can be expressed in a very compact form. In fact the problem of removing the three artifacts in the low-density realization can be summarised as the following. We must solve the set of four equations

$$< \epsilon^k >= \sum_{j=0}^{j_{max}} d_j N_j j^k = n(k+1)!T^k \qquad \text{for k=0,1,2,3} \tag{5.81}$$

where n and T are the desired (input) density and temperature and

$$N_j = y r_j z^{-j} \tag{5.82}$$

for $y(n,T), z(n,T)$ and $r_j(n,T)$ where only one rate coefficient is needed to remove g and γ and two are needed to remove all three artifacts.

There is still a great deal of freedom in this system in deciding what value of j_{max} should be used and which energies should have masks. We address these issues in a systematic way in the remainder of this section with the goal of finding the lowest j_{max} that will allow a solution with an appreciable range in temperature, T. We wish to minimize j_{max} because the higher j_{max}, the larger the number of particles the lattice algorithm must move around and collide which means larger

computation time or, equivalently, slower computation speed per update cycle of the lattice. What we mean by appreciable range in T will be explained in the following section. We begin by examining the smallest system that permits the g and γ artifacts to be removed, $j_{max} = 2$.

5.4.1 Three Speed System

In Section 5.1 we used a three speed system (particles with energy 0,1 and 2) to remove the g artifact in an arbitrary density system. Obviously, there must be a low density solution as well that removes both g and γ. This is found by solving the first three equations of eqn. (5.81) putting $r_1 = r_2 = 1$, i.e. only the stopped particles have a mask, r_0, as we did for the arbitrary density system. If one of the other speeds had the mask we would still get a solution valid for the same range of T but the results are more algebraically complicated and so require more computational effort to employ in a simulation. With the above system, it is a straight forward matter to solve for the three unknowns (for the FCHC system, $d_1 = d_2 = 24$)

$$\begin{aligned} z = e^{\beta_0} &= \frac{2(2-3T)}{3T-1} \\ y = e^{-\alpha_0} &= n\frac{T(2-3T)^2}{6(3T-1)} \\ d_0 r_0 &= \frac{6(T-\frac{1}{3})(\frac{1}{12}+(T-\frac{1}{2})^2)}{T(T-\frac{2}{3})^2}. \end{aligned} \tag{5.83}$$

The dynamical range is set by the first of these three equations as the range where $z = e^{\beta}$ is positive and finite. Outside of this range, it is not possible to enforce $g = 1$. This range is $1/3 < T < 2/3$ which allows a doubling of the temperature in flow simulations. As a practical example, this range could be scaled to represent

temperatures of from 200 to 400 degrees Kelvin, which is more than sufficient for a simulation of the Earth's atmosphere. We see that, unlike in the arbitrary density case where the value of d_0 had a strong impact on the extent of the solution as a function of temperature, in the low density case d_0 affects only the magnitude of r_0 and does not affect the possible range of temperature. We can now set $d_0 = 1$ so that the system may be transformed by any lattice vector and still preserve the exclusion principle which permits us to extend the model to transonic speeds as shown in Section 4.3.

For fluid temperature, $T > 5/9$, the variable z is less than unity, implying a negative thermodynamic temperature. This means that the system has a population inversion with $N_2 > N_1$. It does *not* imply any kind of thermodynamic instability. To the contrary, this is a well-known feature of systems with a bounded energy spectrum[48]. One can show, explicitly [35] that lattice gas systems with this feature can equilibriate with positive temperature systems. Heat flows from low to high β_0, including the negative β_0 ranges. It is the fluid temperature, calculated by inverting eqn. (5.83)

$$T = \frac{z+4}{3(z+2)} \tag{5.84}$$

rather than the thermodynamic temperature, which provides the most useful parameter in the lattice gas dynamics. Figure 5.14 shows $T(z)$ as above while Figures 5.15 and 5.16 show $y/n(T)$ and $r_0(T)$ with one stopped particle per site as functions of temperature. We see that r_0 is within the acceptable range of $.1 \leq r_0 \leq 10$ for the majority of the allowable range of T and is close to unity for $T \leq 5/9$ where $z \geq 1$. Finally, we may take this solution that removes g and γ and calculate the final artifact using eqn. (5.75). The result simplifies to

$$g' = \frac{(3T-1)(2-3T)}{3T^2} \tag{5.85}$$

the structure of which shows explicitly its positive value within the range of allowable temperature, $\frac{1}{3} < T < \frac{2}{3}$. Figure 5.17 illustrates this relation. We see that $g' < .4$ for all T and so there is no range of temperature where $g' \sim 1$ for this system.

Solving three of the four equations of eqn. (5.81) corresponds to removing the two artifacts g and γ while allowing g' to be free. We now ask that all four equations be satisfied, thereby removing all three artifacts. We do this by adding the mask r_2, in addition to r_0, to make the fourth unknown. When we try to solve this system with only three speeds we find that the only solution with real roots is when $T = 0$ which, besides creating a trivial system, forces the mask r_2 to be negative. Since the masks represent a rate coefficient for collision processes between speeds, a negative value is unphysical. If we add the mask to the $j = 1$ species, r_1, instead of $j = 2$, we get the same result. There is no way to make all three of the artifacts disappear in a three speed system; we must go to a system with higher j_{max}.

5.4.2 Four Speed System

We now add an energy 3 particle, for which $d_3 = 96$[4], to create a four speed system. We begin the investigation of this system by putting $r_1 = r_2 = 1$ so that the four unknowns are y, z, r_0 and r_3. In this case, it is possible to solve eqn. (5.81) to get

$$z = e^{\beta_0} = -\frac{4T^2 - 5T + 2}{(2T-1)^2} \qquad \leq 0 \text{ for all } T$$

[4]With $j = 3$, there are 96 permutations of the velocity vector (2,1,1,0)

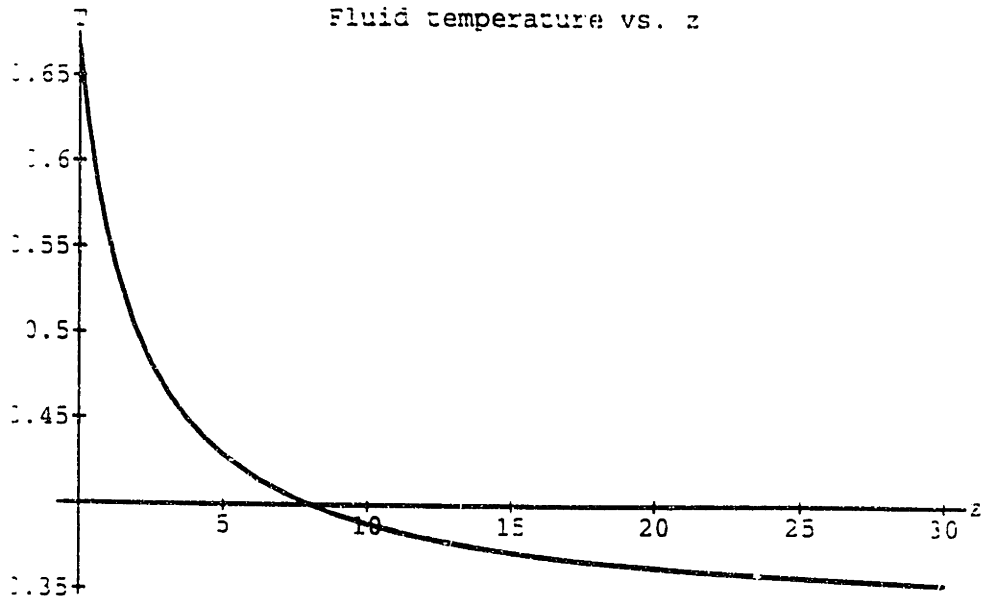

Figure 5.14: Fluid temperature for the three speed low density model as a function of z.

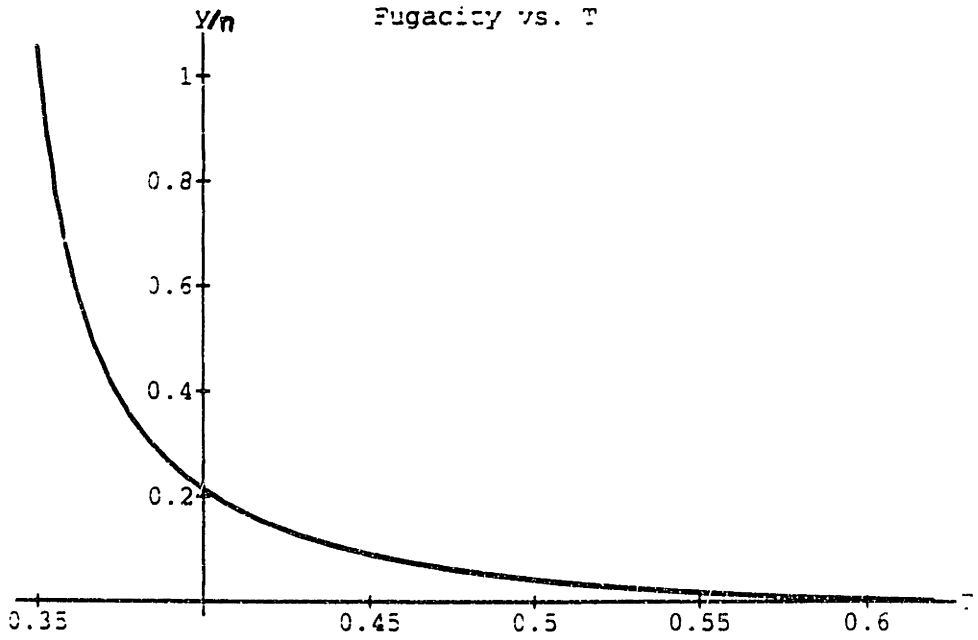

Figure 5.15: The density normalized fugacity y/n as a function of temperature in the allowable range $\frac{1}{3} < T < \frac{2}{3}$.

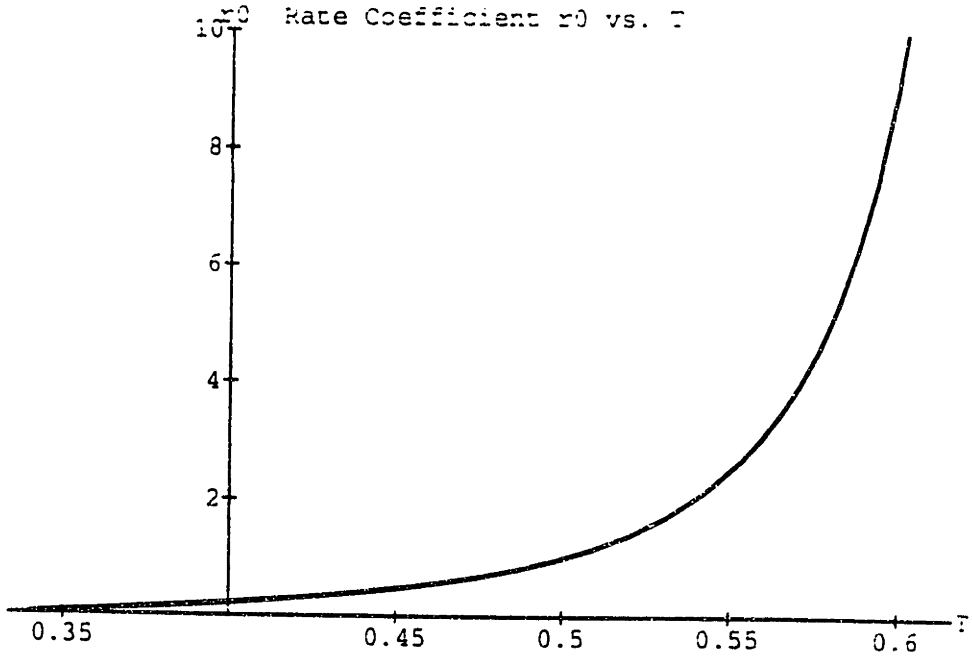

Figure 5.16: Rate coefficient r_0 that removed the artifacts g and γ as a function of temperature in the allowable range $\frac{1}{3} < T < \frac{2}{3}$ with $d_0 = 1$. The rate coefficient is not appreciably different from 1 for $T \leq 5/9$, the range for which $z \geq 1$.

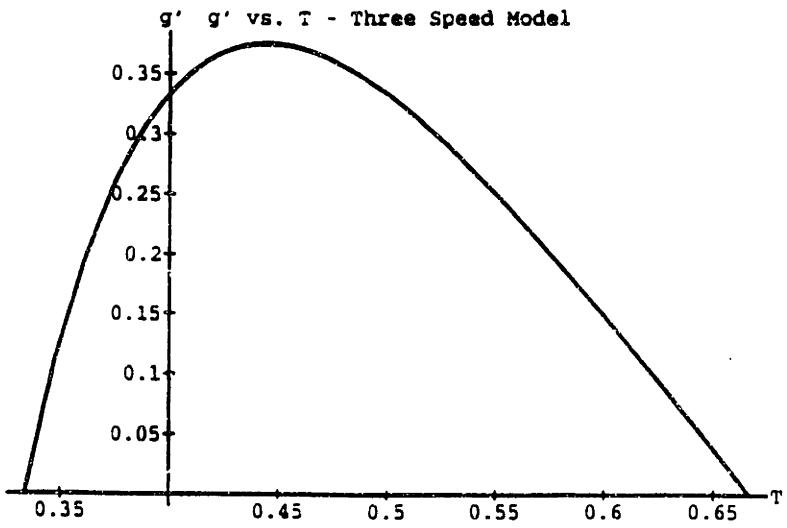

Figure 5.17: The third artifact $g'(T)$ as a function of temperature when the other two artifacts, g and γ, have been removed in a three speed model. Its value is always less than 0.4 so that g' is always significantly in error in this model since $g' = 1$ in the continuum.

$$
\begin{aligned}
y = e^{-\alpha_0} &= -\frac{n}{8}\frac{T(4T^2-5T+2)^2}{(2T-1)^2} \qquad \leq 0 \text{ for all } T \\
d_0 r_0 &= \frac{8(12T^3-18T^2+11T-3)(2T-1)^2}{3T(4T^2-5T+2)^2} \qquad \leq 0 \text{ for } T \leq .7 \\
r_3 &= \frac{(12T^2-9T+2)(4T^2-5T+2)}{36(2T-1)^4}.
\end{aligned} \tag{5.86}
$$

There are many problems with this system. Both the quantities y and z are exponentials that must be positive to be physical. As indicated above, for this system both y and z are negative for all temperatures so we must conclude that this system cannot be used. If we associate a mask with energy $j = 1$ or $j = 2$, instead of $j = 3$, we get the same result that both y and z are negative. Hence these solutions are also unusable. Finally, if we set up a linear relationship between two of the masks of the moving energies, such as $r_2 = ar_3$ where a is a positive constant, the solutions are still unphysical for all values of the temperature, T, and constant a. There is no way to remove all the artifacts within a system that has only four speeds. Once again, we are forced to add a higher speed.

5.4.3 Five Speed System

There are 24 energy $j = 4$ directions per lattice node, $d_4 = 24$ which come from the velocity vector (2,2,0,0) and its permutations. We first solve the set of four equations for the energy moments by setting $r_1 = r_2 = r_3 = 1$, and retain r_4. Since the equations are starting to get a little cumbersome, we will outline the process we went through to solve these equations. Starting with the second energy moment equation in eqn. (5.81), solve for y in terms of z, r_4, n and T. Plug this expression into the first energy moment equation and solve for r_4 in terms of z, n and T. Plug this back into the expression for y to get the fugacity as a function

of only these three parameters. Plugging these two expressions into the zeroth moment of energy (the density equation) allows r_0 to be solved in terms of z, n and T as well. Now take y and r_4 and plug them into the third energy moment equation (which is independent of r_0) and solve for $z(n,T)$. Finally, substitute this expression back into the other three terms to get the complete solution in terms of the density and temperature only.

When we solve this system using the above procedure, we get a positive solution for all four unknowns in the range $.39 \leq T \leq .82$. This range allows a doubling of T, about the same range that we found for the low-density three speed system. The problem with this system is that the expressions for the unknowns are quite complicated functions of T, involving fractional as well as very high powers of T. Raising a number to a fractional power is computationally intensive. This becomes a problem when we wish to update the masks dynamically throughout the simulation where constant recalculation of the mask is necessary. The mask calculations then become a computational bottle-neck. A further disadvantage of this method is that both r_0 and r_4 differ considerably from their natural value of 1 with $r_4 > 10$ and $r_0 < .7$ for all values of the temperature. This may make the system potentially unstable as small changes in the temperature may require significant changes in the masks (especially for r_4 which is quite large) to keep the lattice invisible. For the first time, we have found a physical system that allows the removal of all lattice artifacts for an appreciable range of temperature. Unfortunately, it is undesireable to implement this solution in practice due to computational problems that cannot be alleviated. We will attempt to find another solution that has the same range in T but without the problems described above.

If we put the mask in front of a different speed, we find that we get physical solutions but we still have the same problem with fractional roots *and* the value of mask becomes larger as we associate it with a lower speed. This indicates that the system is less perturbed by a mask associated with high speed particles. This is understandable since the number of particles decreases with higher speeds (the distribution is now Maxwellian) so that perturbing the higher speed particles has a smaller effect on the total system. We attempt to graduate the effect of the mask by giving two masks to the higher speeds but make them linearly related, i.e. $r_3 = ar_4$ where once again a is positive. With this scenario, the system once again becomes unsolvable with $z \leq 0$ for all a and T. When we put $r_2 = ar_4$ and $r_1 = r_3 = 1$, however, we find physical solutions again but only for the range $.37 \leq T \leq .53$ which is only about one-half the range of the previously calculated system which makes it unattractive.

The next logical step is to add three masks and have them all linearly related, $r_2 = br_4$ and $r_3 = ar_4$ where a and b are positive constants. With this system, a number of interesting results become apparent. First of all, it becomes possible to re-scale the four equations of eqn. (5.81) so that instead of two separate parameters, a and b, appearing in the equations, they only appear in a particular combination, K, where

$$K = \frac{b}{a^2}. \tag{5.87}$$

The re-scaled variables, denoted by primes, are related to the original variables using

$$\begin{aligned} z' &= az \\ y' &= ay \\ d_0 r_0' &= \frac{d_0 r_0}{a} \end{aligned} \tag{5.88}$$

$$r_4' = a^3 r_4.$$

The series of equations to solve is the same as eqn. (5.81) but we use an expression for N_j in terms of primed variables

$$N_j = y' r_j' z'^{-j} \tag{5.89}$$

where $r_1' = 1$, $r_3' = r_4'$ and $r_2' = K r_4'$ with K given by eqn. (5.87). With one parameter instead of two, the analysis of the solution to these equations becomes easier. Using the procedure outlined at the beginning of this subsection, the above system can be solved giving

$$\begin{aligned}
z' &= \left[-1 + \frac{1-3T}{4-15T+12T^2} \right. \\
&\quad \left. + \frac{1}{12}\sqrt{\frac{-24K(2-9T+12T^2)}{4-15T+12T^2} + \frac{(36-144T+144T^2)^2}{(4-15T+12T^2)^2}}\right]^{-1} \\
y' &= n\frac{T(-18z'^2 - 8z' - 2Kz'^3 + 18Tz'^2 + 6Tz' + 3KTz'^3)}{-144z' - 72 - 12Kz'^2} \\
d_0 r_0' &= \frac{-12(12z' + 6 + Kz'^2 - 32Tz' - 15T - 3KTz'^2 + 24T^2z' + 9T^2 + 3KT^2z'^2)}{Tz'(-18z' - 8 - 2Kz'^2 + 18Tz' + 6T + 3KTz'^2)} \\
r_4' &= \frac{(1-3T)z'^3}{-36z' - 16 - 4Kz'^2 + 36Tz' + 12T + 6KTz'^2}.
\end{aligned} \tag{5.90}$$

The above solutions are positive in the range $.386 \leq T \leq .807$ with the lower limit being a numerical approximation to the lowest positive root $4 - 15T + 12T^2$ which appears in the numerator of z' and the upper limit is needed to keep r_0 positive. We once again have an appreciable temperature range, slightly more than a factor of two in T, but z' requires a square root in its calculation. As previously mentioned, this is computationally undesireable. Unlike the previous case, there is still freedom in the solutions as illustrated by the presence of the factor K. This allows us to see if there a value of K that will make the expression

under the root sign in z' a perfect square so that the square root can be removed. A bit of algebra shows that if $K = 6$ then the expression under the root sign in the equation for z' becomes

$$\frac{(12-36T)^2}{(4-15T+12T^2)^2}. \tag{5.91}$$

In fact, $K = 6$ is the *only* value that will allow this convenient simplification to happen. The solutions are now merely rational functions of polynomials in T

$$z' = -\frac{4-15T+12T^2}{2-9T+12T^2} \tag{5.92}$$

$$y' = \frac{nT}{144}\frac{(4-15T+12T^2)(40-234T+471T^2-432T^3+144T^4)}{(3T-1)(2-9T+12T^2)} \tag{5.93}$$

$$r'_0 = -\frac{6}{T}\frac{(2-9T+12T^2)(24-164T+444T^2-657T^3+504T^4-144T^5)}{(4-15T+12T^2)(40-234T+471T^2-432T^3+144T^4)} \tag{5.94}$$

$$r'_4 = \frac{(4-15T+12T^2)^3}{4(2-9T+12T^2)(40-234T+471T^2-432T^3+144T^4)} \tag{5.95}$$

which shows that the solutions are functions of only five different polynomials in T. By only calculating these five polynomials, and then combining them to calculate the above parameters using only basic arithmetic procedures, we have minimized the amount of computational work needed to update the solution in a dynamical system. As in the three speed low density model, d_0 does not alter the allowable dynamical range of this system and so we may set it to the ideal value $d_0 = 1$. The expression for z' can be inverted to solve for T in terms of z'

$$T = \frac{15+9z' \pm \sqrt{33-18z'-15z'^2}}{24(1+z')} \tag{5.96}$$

where the negative root is taken when $.386 \leq T \leq .5$ and the positive root when $.5 \leq T \leq .807$ although, as we will show subsequently, it is possible to sense T directly in a low density system so that the conversion to z' is not necessary for the feedback procedure.

The next step in the optimization process was to find a value of a that minimized the deviance of the masks from their natural values, which is 1. This was done by calculating the root-mean-square difference of the masks r_0 and r_4 from the value 1 over the allowable range of T for a wide range of the parameter a (eqn. (5.88) is used to return to the original variables from the primed ones). The value of a that minimized the product of the RMS errors in the two masks was $a = .22$. Since $K = \frac{b}{a^2} = 6$, we find that $b \simeq .29$.

The solution is now complete. We have found a low density system that removes all of the artifacts while requiring only the basic arithmetic operations to calculate the solutions of this system. Furthermore, we have minimized the deviance of the masks from the value 1, their natural value. Graphical representations of this solution are shown in Figures 5.18, 5.19, 5.20 and 5.21 where z, y/n, $d_0 r_0$ and r_4 are shown, respectively. The factor n was incorporated into the defintion of y since it appears trivially in that expression. From Figure 5.20 we see that when $d_0 = 1$, as it should be, there is a wide range of T where r_0 has a value very close to the value 1. Similarly, although not as flat as r_0, r_4 does not differ considerably from the value 1 for a significant range of T. Again, it is not necessary that the value of the masks be close to 1 in order for the solution to work, it is expected, however, that the flatter the expression for the mask, the better the stability of the system when undergoing dynamical alterations. With the solutions for the four variables as functions of temperature and density, the zeroth order particle density for each species can now be calculated using eqn. (5.82).

In Section 5.1, we demonstrated a feedback system for the arbitrary density three speed model that sensed z from the averaged zero-order distribution functions $\langle N_j \rangle$ and then corrected for second order in velocity effects. In the low

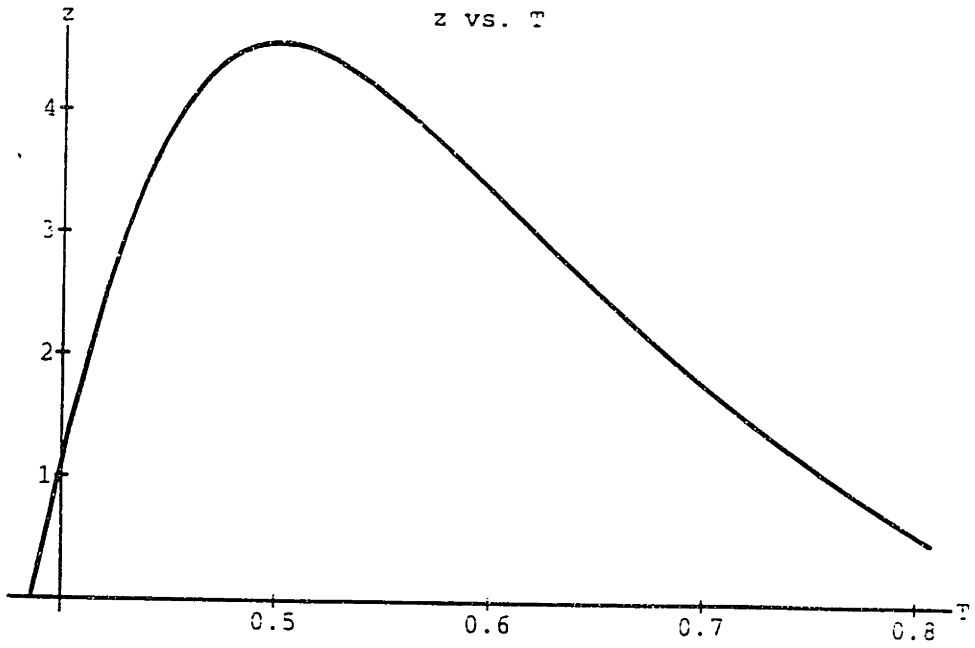

Figure 5.18: Variable $z(T) \equiv e^{\beta_0}$ as a function of temperature T in the range $0.386 \leq T \leq 0.807$ which permits all three artifacts to be removed in the five speed low density model.

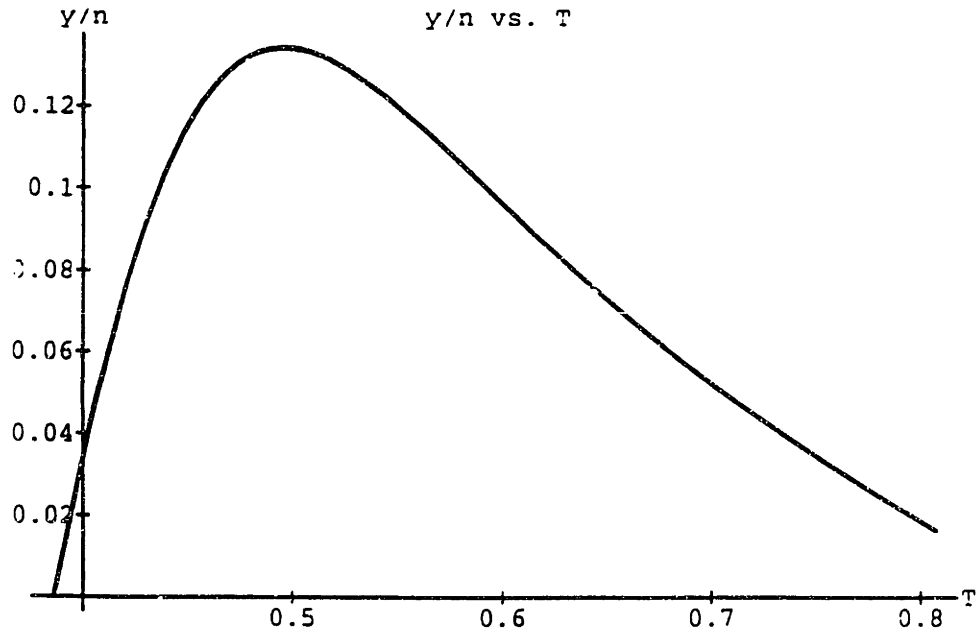

Figure 5.19: Variable $y/n(T) \equiv e^{-\alpha_0}/n$ as a function of temperature T in the range $0.386 \leq T \leq 0.807$.

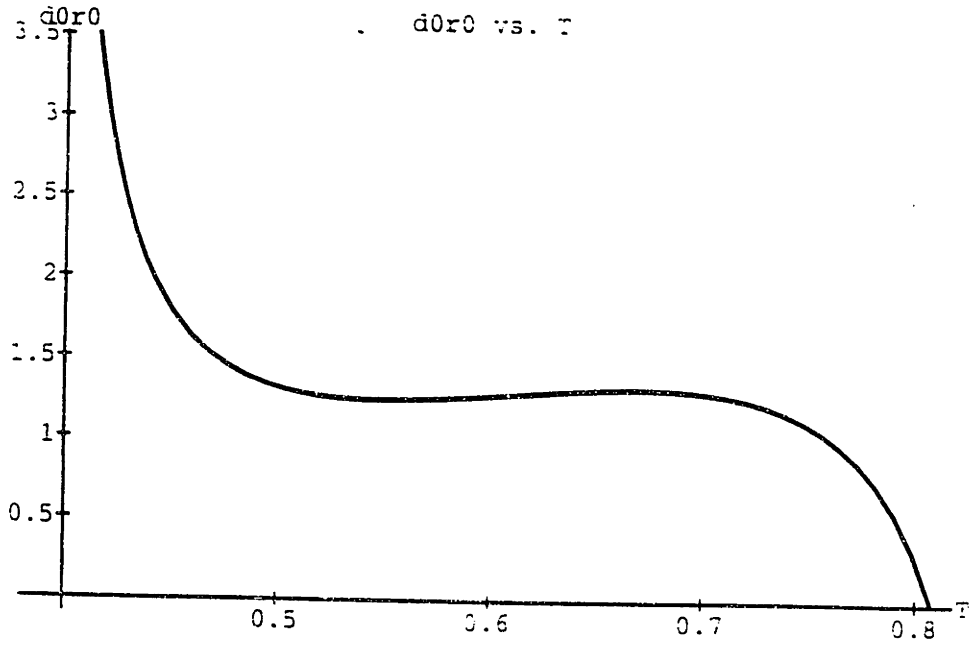

Figure 5.20: Rate Coefficient $r_0(T)$ as a function of temperature T in the range $0.386 \leq T \leq 0.807$. The large flat region where r_0 is close to 1 allows for a dynamically stable regime of operation.

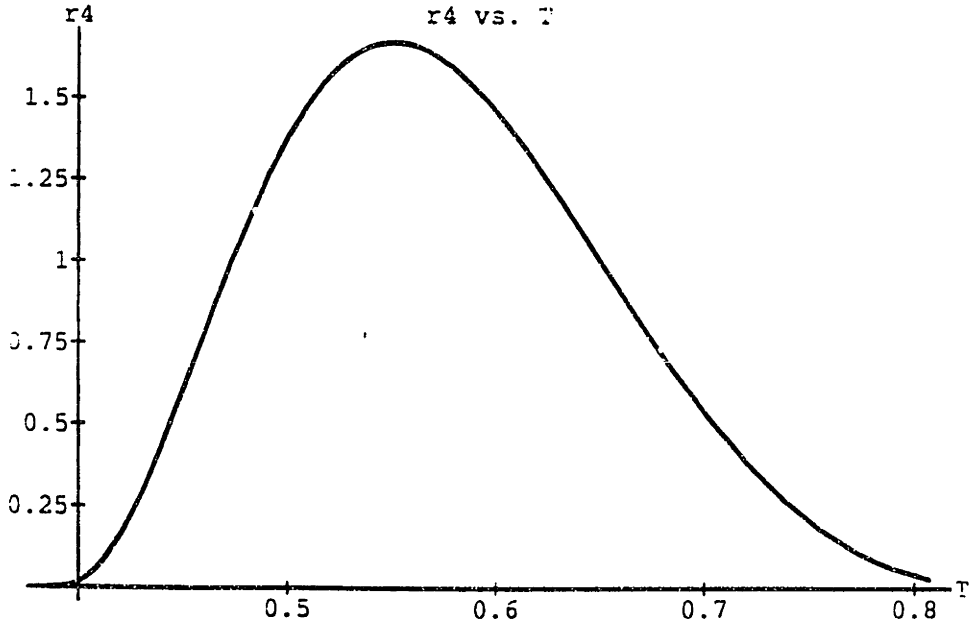

Figure 5.21: Rate Coefficient $r_4(T)$ as a function of temperature T in the range $0.386 \leq T \leq 0.807$. This mask's magnitude also is centred around the natural value of 1.

density system, however, it is possible to sense the temperature itself so that the procedure for first measuring the indirect temperature z and then correcting this measurement for velocity effects is not necessary. Once we have measured T, we can then calculate an updated value for the masks using eqns. (5.94) and (5.95). There may be many regions of the flow where the temperature varies significantly and where we would like to have local values of the masks. Furthermore, this updating procedure will have to be repeated many times throughout the course of the simulation. For these reasons, it was desirable to reduce the computational effort required for calculating the masks (by removing the calculation of fractional powers by tuning the value of K). To measure T we begin by measuring three local macroscopic properties of the flow, the density, momentum and energy

$$\rho = \sum_{ji} m_j N_{ji} = n \tag{5.97}$$

$$\rho \mathbf{u} = \sum_{ji} m_j \mathbf{c}_{ji} N_{ji} \tag{5.98}$$

$$U = \sum_{ji} \epsilon_j N_{ji} = U_p + \tfrac{1}{2}\rho u^2 = 2nT + \tfrac{1}{2} n u^2. \tag{5.99}$$

Once we know ρ and $\rho\mathbf{u}$ we can calculate the quantity $\frac{1}{2}\rho u^2$. Subtracting this from U, which gives U_p, and then dividing the result by two times the density will give us the temperature

$$T = \frac{U - \frac{1}{2}\frac{\rho\mathbf{u}\cdot\rho\mathbf{u}}{\rho}}{2\rho}. \tag{5.100}$$

exactly since $U_p = 2nT$ in a $D = 4$ system.

Low density solutions are only valid when $N_j \ll 1$. In order to find the limit in particle density to which the low density results still effectively remove the artifacts, the full Fermi-Dirac arbitrary density artifact relations were calculated using the five-speed low density model solution. Figure 5.22 shows the error in the Galilean invariance factor $g - 1$ as a function of temperature and particle number

at a site, n. Similar plots for $\gamma - 1.5$ and $g' - 1$ show that the errors in these values also increase sharply at low temperature and high density where $\gamma - 1.5$ is positive while $g' - 1$ is negative. Keeping in mind that an error equal to 1 represents a 100% error in g, which is totally untenable, we see that the low density system loses its viability for appreciable density as the temperature is decreased. In order for the errors in the artifacts to be less than 0.1, the density must satisfy the following inequality

$$n \leq 240T^2 - 188T + 40.8 \tag{5.101}$$

which gives a limit of $n = 4$ at $T = .4$ and $n = 20$ at $T = .65$. In a five speed system with one stopped particle the total possible number of particles at a site is $\sum_{j=0}^{4} d_j = 169$. This result agrees with the theoretical result that the classical limit, where the Fermi-Dirac distribution reduces to the Maxwell-Boltzmann relation, occurs in systems with sufficiently low densities or sufficiently high temperatures[48].

In this Chapter, we have outlined a series of potential lattice gas models that remove the lattice artifacts to varying degrees. In arbitary density systems, we found that a three speed model was required to remove the g artifact and this was done by implementing one rate coefficient, r_0, associated with the stopped particle distribution. A feedback procedure was outlined that will allow the rate coefficient to be updated dynamically to maintain $g = 1$. Extensive validation of this model is presented in Chapter 7. Although the second artifact, γ, has the correct value, $\gamma = \frac{D+2}{D}$, to leading order in the density when $g = 1$, it is impossible to remove the higher order errors in low speed models. For a four speed model, we found that these two artifacts could be removed to an accuracy of better than 1% for a large range of temperature and density by associating one rate coefficient,

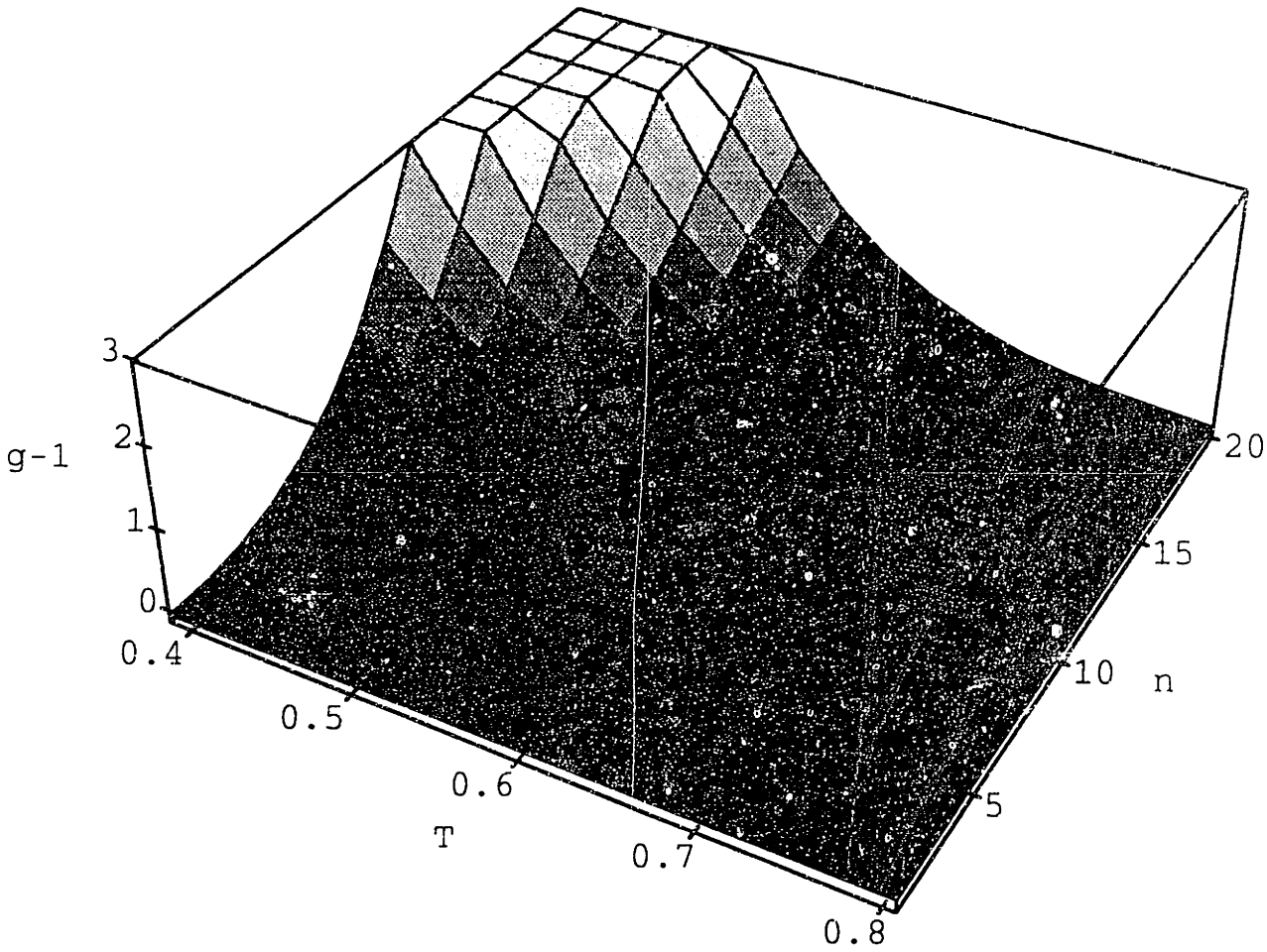

Figure 5.22: The error in the Galilean invariance artifact $g - 1$ when the low density five-speed model solution is used to calculate the arbitrary density value of g, eqn. (3.70). The error is sufficiently small at low densities and high energies.

r_0, with the stopped particles and another, r_3, with the energy $j = 3$ distribution. To remove all three artifacts in an arbitrary density system it is anticipated that a system with a significantly larger number of particles, perhaps one with seven or eight speeds, would have to be used. Since the g' appears as a coefficient of a third order quantity in the energy conservation equation while γ is a first order quantity, it is essential that γ has the continuum value if correct heat transfer is to be simulated while g' is a higher order effect. In the classical limit where the density becomes very small, the Fermi-Dirac distribution becomes Maxwell-Boltzmann. In this limit, the g and γ artifacts collapse into the same requirement. For a low density system, we once again find a three speed system that removes both g and γ but it is necessary to go to a five speed model to remove all three artifacts. The five speed model presented here has the usual r_0 rate coefficient as well as another coefficient r_4 that has been spread out over the highest three energies. This system has been optimized so as to minimize the computational effort required to update these coefficients in a dynamical simulation.

Chapter 6

Absence of Noise Effects on Lattice Gas Mean Dynamics

The lattice gas algorithm is a discrete Boolean algorithm. At any instant in time, a particular lattice site is either occupied by a particle or it is unoccupied. Despite this, the equilibrium distribution function is a continuous distribution function of Fermi-Dirac form, eqn. (2.31). As a result, at any particular time step of the simulation, the local macroscopic properties of the flow might vary significantly from the theoretical mean since the difference between the actual site density and mean theoretical density is of order unity. Consequently, we might feel that these significant fluctuations would have an adverse effect on the system's mean dynamics, preventing hydrodynamic results even when the lattice artifacts have been removed. Fortunately this is not true. In this Chapter, we demonstrate that lattice gas algorithms have the property that their mean statistical dynamics are unaffected by shot noise fluctuations, which can be quite large in lattice gas systems of practical interest. Furthermore all correlation functions between any

two non-equal states are negligible in comparison with the mean dynamics. This result justifies the Boltzmann approximation that we used to ensemble-average the lattice gas collision operator in Section 2.4. This result is demonstrated experimentally in the simulation results of Chapter 7 where we show that in systems where the Galilean invariance artifact has been removed, hydrodynamic behaviour is reproduced precisely.

6.1 Fluctuation and Nonlinear Effects in Simulation Methods

The computational efficiency of any particle simulation method depends on being able to accurately represent the macroscopic dynamics without explicitly following the dynamics of every molecule. Thus, in the lattice gas method, the particles represent macro-molecules of artificially large mass and are not intended to represent the precise gas microdynamics but are designed with the dynamics necessary to give the correct macroscopic behaviour. Intuition would say that good hydrodynamic behaviour cannot be obtained unless the number of these particles is so large that the averages taken at every time step accurately provide the hydrodynamic variables. Thus, it would seem that many lattice sites would be required per accurate hydrodynamic cell and the computational work would be prohibitive [49].

This intuition is in fact flawed - for both real fluids and lattice gases. What really counts for achieving accurate hydrodynamic behaviour is the shortness of the mean free path, not the statistical noise level. It is here that the discreteness of the lattice gas dynamics, so essential to the computational efficiency, confers

a key advantage. The lattice restriction forces many particles to reside on a lattice point at a given time (on the average, about 10 particles are resident on a lattice site) and they collide there very efficiently. We have found that in a typical lattice system, about 70% of the particles collide every time step. In fact, the inferred mean free path from the observed viscosity is actually less than the lattice length[1]. Thus, the lattice gas has an extreme statistical noisiness but very efficient collisionality. This is in marked contrast to a real gas which has extremely good statistical accuracy, but very inefficient collisionality. Because of the short range of the intermolecular force, molecules "miss" each other most of the time in air.

It is the size of the mean free path relative to the physical scale that determines the accuracy of the hydrodynamic behaviour in both the lattice gas and real air. Statistical fluctuations are irrelevant to the mean (hydrodynamic) behaviour of both, as we will show in the forthcoming sections of this Chapter.

The main reason for this is that lattice gases have a unique property which imbues them with a special immunity to shot noise fluctuations. This is a consequence of the logical - *Boolean* - character of the algorithm, and the *exact* conservation of the fundamental invariants, mass, momentum and energy. The mean dynamics of a lattice gas are completely independent of shot noise fluctuations (or self-correlations)- which are quite large in these Boolean systems. This is a property special to lattice gases, that more conventional particle simulation methods [50] do not possess. This means that the mean dynamics of small scale, very noisy, structures in the flow will obey hydrodynamics (or whatever the kinetic theory predicts for the mean behaviour if the lattice gas in question con-

[1]see Chapter 7 for description of viscosity measurement in a lattice gas system

tains discreteness artifacts), even if they are completely obscured by shot noise. *signal/noise* $\ll 1$. This counter-intuitive behaviour was first observed in the simulations of Molvig et al.[39]. This result can be explained by a *Shot Noise Theorem* that exists for lattice gasses, that demonstrates explicitly the absence of shot-noise effects on the mean dynamics.

Large scale structures and eddies, and quantities of practical interest such as lift, drag, and net heat flux, will have $s/n \gg 1$ and be clearly observable, of course. What the *Shot Noise Theorem* provides is a kind of guarantee that the smaller scale eddies that may not be visible are in fact providing precisely the correct[2] accumulated statistical effect on these larger scales.

In Section 2.3, we derived the form of the complete lattice gas microdynamical update equation, eqn. (2.8). There are two simple but profound properties of the microdynamical equation that are the basis of the extraordinary accuracy of these systems. Firstly, the advection of particles that will ultimately account for the fluid advection, is both linear and exact. All the nonlinearities in the dynamics are in the collision term. Secondly, the moments of the conserved quantities exactly annihilate the collision function on the right hand side of eqn. (2.8), as shown in Section 2.3.1. It is essentially these two properties that account for the accuracy and noise independence features of lattice gases that we develop in this Chapter.

The mean properties of the dynamics of equation (2.8) are obtained from ensemble averages. For the Boolean field n_j, which represents the particle occupancy per site in the lattice gas algorithm, we can write,

$$\langle n_j \rangle = N_j \tag{6.1}$$

[2]As predicted by kinetic theory for the mean dynamics.

where N_j is the (assumed continuous) distribution function. Fluctuations, δn_j can now be identified as the deviation of n_j from this mean value.

$$n_j = N_j + \delta n_j \tag{6.2}$$

The exact ensemble averaged microdynamics are obtained by averaging equation (2.8). The macrodynamics are obtained by taking the moments of this averaged equation with respect to the conserved quantities: mass, momentum, and energy. Since the fluctuations average to zero, $\langle \delta n_j \rangle = 0$, by definition, it is only through the non-linear terms that fluctuations can effect the mean dynamics. But when moments of the conserved quantities are taken to generate the macrodynamics, all the nonlinear terms, which are in the collision operator, vanish identically! The role of the collision operator (and all the nonlinearities in lattice gas algorithms) is to drive the system to local thermodynamic equilibrium, so that the moment equations can be closed in terms of the hydrodynamic variables alone. The nonlinear advection term of hydrodynamics, $\mathbf{u} \cdot \nabla \mathbf{u}$, arises from this local thermodynamic property - not from any nonlinearities in the advection dynamics.

This situation can be contrasted with other numerical methods, such as finite element approximations to Navier-Stokes[3] or direct particle simulation methods as used in Plasma Physics. In CFD, the incompressible Navier-Stokes equations,

$$\rho \left(\frac{\partial}{\partial t} \mathbf{u} + \nabla \cdot \mathbf{u}\mathbf{u} \right) = -\nabla P + \eta \nabla^2 \mathbf{u} \tag{6.3}$$

are discretized somehow, and when processed numerically give some approximation to the true hydrodynamics. We can represent this by writing the true fluid velocity, $\mathbf{u}$, as, $\mathbf{u} = \langle \mathbf{u} \rangle + \delta \mathbf{u}$, where $\langle \mathbf{u} \rangle$ is the numerical fluid velocity and $\delta \mathbf{u}$

[3]also known as Computational Fluid Dynamics - CFD

represents the fluctuation from the actual fluid velocity caused by the numerical approximation. The effect of the numerical approximations on the dynamics can be obtained by averaging the Navier-Stokes equation (6.3). The fluctuations contribute via the nonlinear terms, specifically the nonlinear advection term[4]. Averaging this term gives,

$$\nabla \cdot \langle \mathbf{uu} \rangle = \nabla \cdot \langle \mathbf{u} \rangle \langle \mathbf{u} \rangle + \nabla \cdot \langle \delta \mathbf{u} \delta \mathbf{u} \rangle \tag{6.4}$$

where the second term on the right hand side of equation (6.4) gives the "numerical" Reynolds Stress. This is the source of a variety of well known numerical artifacts such as numerical viscosity [51].

Similarly in plasma particle simulation, one solves the Vlasov equation,

$$\frac{\partial f}{\partial t} + \mathbf{v} \cdot \nabla f + \mathbf{a} \cdot \frac{\partial f}{\partial \mathbf{v}} = 0 \tag{6.5}$$

by numerical means. By identifying the fluctuating parts of both the acceleration, $\mathbf{a}$, and the distribution function, f, due to the simulation *discreteness*, one obtains a numerical discreteness term,

$$\frac{\partial}{\partial \mathbf{v}} \langle \delta \mathbf{a} \delta f \rangle \tag{6.6}$$

with well known consequences on the simulations[50].

Thus the lattice gas method does not produce either the discreteness Reynolds stresses of CFD, or the discreteness forces of particle simulation methods.

6.2 Shot Noise Theorem

For Boolean systems like the lattice gas, the shot noise, or self-correlation fluctuation level, can be calculated directly, and is usually quite large. Using, $n_j =$

[4]Which dominates the dynamics of practical high Reynolds number fluids.

$\langle n_j \rangle + \delta n_j$, we can square n_j, and use the Boolean relation.

$$n_j^2 = n_j \tag{6.7}$$

to find,

$$\langle n_j^2 \rangle = \langle n_j \rangle = \langle n_j \rangle^2 + \langle \delta n_j^2 \rangle \tag{6.8}$$

which gives the fluctuation level, $\langle \delta n_j^2 \rangle$, explicitly. The relative size of the fluctuations,

$$\frac{\langle \delta n_j^2 \rangle}{\langle n_j \rangle^2} = \frac{1}{\langle n_j \rangle^2} - 1 \tag{6.9}$$

is order unity or greater.

However, the mean kinetic theory dynamics of the lattice gas, obtained from averaging the microdynamical equation (2.8),

$$N_j(t_* + 1, \mathbf{r}_* + \mathbf{c}_j) - N_j(t_*, \mathbf{r}_*) = \langle \Delta_j \rangle \tag{6.10}$$

are independent of the shot noise, self-correlation level, $\langle \delta n_i^2 \rangle$. This is true to all orders and is in fact a theorem,

Theorem 1 (Shot Noise Theorem) *The mean kinetic theory dynamics of a lattice gas are independent of the shot noise fluctuation level. This result is true to all orders in the fluctuations. No dynamical dependence on $\langle \delta n_j^2 \rangle$ exists in the kinetic equation.*

This theorem will be demonstrated in detail in section (6.3).

Here we give the heuristic basis of the result, showing that it is a consequence of the Boolean nature of the algorithm. The collision operator is a sum of logical products, each of which tests for the existence of particles and their hole states, to determine if a transition will occur, eqn. (2.11). An example of a logical truth

condition which tests whether the transition of two particles in states i and i' to the resulting states i_o and i'_o - $i, i' \rightarrow i_o, i'_o$ - is allowed, is,

$$n_i \cdot n_{i'} \cdot \bar{n}_{i_o} \cdot \bar{n}_{i'_o} \tag{6.11}$$

where the overbar denotes logical complement, $\bar{n} = 1 - n$. Holes must be present in the out-state for the transition to occur. In no case does a particle appear logically ANDed with itself, for even if such terms arose from combinations of rules, the resulting product term, $n_i \cdot n_i$, would collapse to n_i anyway because of the Boolean relation (6.7). Since $n_i \cdot \bar{n}_i = 0$, no self product terms can arise from combinations of this type either.

6.3 The Collision Operator Expansion and Symmetries

The theory and formalism for single speed lattice gas systems has been developed in some detail by Hasslacher et. al. [14] This formalism was also used in Chapters 2 and 3 to develop a multiple speed lattice gas model that was free of discreteness artifacts. We continue using this formalism here in order to formulate a theory of fluctuations in lattice gases. The collision operator for the lattice gas system was written in terms of quasi-particles that contained rate coeffcients for energy exchange collisions which allowed the lattice artifacts to be removed eqn. (2.21). By doing this, detailed balance was restored to the multiple speed system, and a H-Theorem was proved for the general lattice gas model. We rewrite this collision operator here for convenience

$$\Delta_i(n_j) = \sum_{s,s'} (s'_i - s_i) \xi_{ss'} \prod_{j'} \eta_{j'}^{s'_{j'}} \bar{\eta}_{j'}^{1-s'_{j'}} \tag{6.12}$$

where η_j and $\overline{\eta}_j$ are related to the actual particle and hole fields by

$$\eta_j \equiv F_j n_j \tag{6.13}$$

$$\overline{\eta}_j \equiv I_j \overline{n}_j \tag{6.14}$$

where $\overline{n}_j = 1 - n_j$ but $\overline{\eta}_j \neq 1 - \eta_j$ and F_j and I_j are rate coefficients defined in Section 2.3.2. For lattice gases without this freedom, η and the density, n, are equal. The variables s and s' are strings of binary values corresponding to the input and output state, respectively, of the system. Furthermore, $\xi_{ss'}$ is a matrix that indicates when a transition from state s to state s' is allowed. It is statistically independent of the η_j.

In order to see the effect of fluctuations in the density on the mean dynamics we insert, $n_\mathbf{j} = N_\mathbf{j} + \delta n_\mathbf{j}$, where $N_\mathbf{j}$ is the mean value of $n_\mathbf{j}$

$$\left\langle n_\mathbf{j} \right\rangle = N_\mathbf{j} \quad ; \quad \left\langle \delta n_\mathbf{j} \right\rangle = 0 \tag{6.15}$$

into the collision operator, $\Delta_i(\{n_\mathbf{j}\})$, in the exact kinetic equation (6.10) and then expand the collision opertor about the mean value of $n_\mathbf{j}$.

$$\begin{aligned} \Delta_i(n_\mathbf{j}) &= \Delta_i(N_\mathbf{j} + \delta n_\mathbf{j}) \\ &= \Delta_i(N_\mathbf{j}) + \sum_l \delta n_l \frac{\partial \Delta_i(n_\mathbf{j})}{\partial n_l} \Big|_{n_\mathbf{j}=N_\mathbf{j}} \\ &\quad + \tfrac{1}{2} \sum_l \sum_m \delta n_l \delta n_m \frac{\partial^2 \Delta_i(n_\mathbf{j})}{\partial n_m \partial n_l} \Big|_{n_\mathbf{j}=N_\mathbf{j}} + \cdots \end{aligned} \tag{6.16}$$

where the sums are over all velocity vectors in the model. Now the equation for mean dynamics is easily found by averaging eqn. (2.8) which gives

$$N_\mathbf{j}(t_* + 1, \mathbf{r}_* + \mathbf{c}_j) - N_\mathbf{j}(t_*, \mathbf{r}_*) = \langle \Delta_i(n_\mathbf{j}) \rangle \tag{6.17}$$

where

$$\left\langle \Delta_i(n_\mathbf{j}) \right\rangle = \left\langle \Delta_i(N_\mathbf{j}) \right\rangle + \tfrac{1}{2} \sum_l \sum_m \langle \delta n_l \delta n_m \rangle \left\langle \frac{\partial^2 \Delta_i(n_\mathbf{j})}{\partial n_m \partial n_l} \right\rangle \Big|_{n_\mathbf{j}=N_\mathbf{j}} + \cdots \tag{6.18}$$

calculated from eqn. (6.16). The only fluctuating quantity in $\Delta_i(N_j)$ that is affected by the averaging process is $\xi_{ss'}$ such that $\langle \xi_{ss'} \rangle = A(s \to s')$, eqn. (2.22), the transition probability of going from state s to s'. Furthermore, the average of the second order term may be split up into two terms as shown, since $\xi_{ss'}$ is independent of the density fluctuations.

Since we have an exact expression for $\Delta_i(n_j)$ it is possible to calculate the expansion derivatives exactly. A straightforward series of differentiations on

$$\langle \Delta_i(N_j) \rangle = \sum_{s,s'} (s_i' - s_i) A(s \to s') \prod_{j'} \mathcal{N}_{j'}^{s_{j'}} \overline{\mathcal{N}}_{j'}^{\overline{s}_{j'}} \tag{6.19}$$

eqn. (2.29), shows that

$$\begin{aligned} \left\langle \frac{\partial \Delta_i(n_j)}{\partial n_l} \Big|_{n_j = N_j} \right\rangle &= \sum_{s,s'} (s_i' - s_i) A(s \to s') \prod_{j'} \langle F^{j'} \rangle^{s_{j'}} \langle I^{j'} \rangle^{\overline{s}_{j'}} \times \\ &\quad \prod_{j' \neq l} N_{j'}^{s_{j'}} \overline{N}_{j'}^{\overline{s}_{j'}} \left[s_l N_l^{s_l - 1} \overline{N}_l^{\overline{s}_l} - \overline{s}_l \overline{N}_l^{\overline{s}_l - 1} N_l^{s_l} \right] \qquad (6.20) \\ &= \sum_{s,s'} (s_i' - s_i) A(s \to s') \prod_{j'} \mathcal{N}_{j'}^{s_{j'}} \overline{\mathcal{N}}_{j'}^{\overline{s}_{j'}} (s_l - N_l) \frac{1}{N_l \overline{N}_l} \end{aligned}$$

From eqn. (6.21), the only possible dependence on N_l is in the square bracketed term

$$\begin{aligned} \left[s_l N_l^{s_l - 1} \overline{N}_l^{\overline{s}_l} - \overline{s}_l \overline{N}_l^{\overline{s}_l - 1} N_l^{s_l} \right]_l &= 1 \qquad \text{if } s_l = 1 \\ \left[s_l N_l^{s_l - 1} \overline{N}_l^{\overline{s}_l} - \overline{s}_l \overline{N}_l^{\overline{s}_l - 1} N_l^{s_l} \right]_l &= -1 \qquad \text{if } \overline{s}_l = 1. \end{aligned} \tag{6.21}$$

Thus eqn. (6.21) is independent of N_l. This illustrates that the collision operator is a multilinear function of the microscopic densities N_j. This is a result of the Boolean character of the n_j's.

The second derivative is

$$\left\langle \frac{\partial^2 \Delta_i(n_j)}{\partial n_m \partial n_l} \Big|_{n_j = N_j} \right\rangle = \sum_{s,s'} (s_i' - s_i) A(s \to s') \prod_{j'} \mathcal{N}_{j'}^{s_{j'}} \overline{\mathcal{N}}_{j'}^{\overline{s}_{j'}} \frac{(s_l - N_l)}{N_l \overline{N}_l} \frac{(s_m - N_m)}{N_m \overline{N}_m} \tag{6.22}$$

and

$$\left\langle \frac{\partial^2 \Delta_i(n_j)}{\partial^2 n_l} \mid_{n_j=N_j} \right\rangle = 0$$

since the collision operator, as just shown, is multilinear. Thus there are no contributions to the mean collision operator, eqn. (6.18), by self-correlations of the form $\langle \delta n_l^2 \rangle$. This proves the *Shot Noise Theorem*, stated in the last section, for this class of lattice gas algorithms.

The only remaining noise quantity left in the mean equation is the non-self correlation term $\langle \delta n_l \delta n_m \rangle$, $l \neq m$, in (6.18). We calculate this quantity explicitly in the next section with the goal of showing that it contributes negligibly to the mean dynamics.

In the remainder of this section, we examine the symmetry properties of the expanded collision operator. First of all, there is a distinction to be made between the equilibrium and non-equilibrium state of the system. In equilibrium

$$\langle \Delta_i(N_j) \rangle = 0 \tag{6.23}$$

which we know results in the Fermi-Dirac equilibrium distribution function for N_j, see Appendix A. Another consequence of equilibrium is that

$$\prod_j \mathcal{N}_j^{s'_j} \overline{\mathcal{N}}_j^{1-s'_j} = \prod_j \mathcal{N}_j^{s_j} \overline{\mathcal{N}}^{1-s_j} \qquad \forall s' \tag{6.24}$$

which is a result of detailed balance, $A(s \to s') = A(s' \to s)$.

This relation permits us to show that the first order collision operator is symmetric, or equivalently, parity invariant and microscopically reversible. Moving the product of particle and holes to the other side of eqn. (6.21) we see that

$$C_{il} \equiv \langle \frac{\partial \Delta_i(n_j)}{\partial n_l} \mid_{n_j=N_j,eqm} \rangle N_l \overline{N}_l = \sum_{s,s'} (s'_i - s_i) A(s \to s') \prod_{j'} \mathcal{N}_{j'eqm}^{s'_{j'}} \overline{\mathcal{N}}_{j',eqm}^{\overline{s'}_{j'}} s_l \tag{6.25}$$

where the term proportional to N_l in eqn. (6.21) is now zero due to the zeroth order equilibrium relation. If we reverse the direction of this collision, we simply interchange primed and unprimed s's and utilize the detailed balance condition and eqn. (6.24):

$$\begin{aligned} C_{il} &= \sum_{s,s'}(s_i - s_i')A(s' \to s)\prod_{j'}\mathcal{N}_{j',eqm}^{s_{j'}}\overline{\mathcal{N}}_{j',eqm}^{\bar{s}_j}s_l \\ &= \sum_{s,s'}(s_i - s_i')A(s \to s')\prod_{j'}\mathcal{N}_{j',eqm}^{s'_{j'}}\overline{\mathcal{N}}_{j',eqm}^{\bar{s}'_j}s'_l \\ &= -\tfrac{1}{2}\sum_{s,s'}(s_i' - s_i)A(s \to s')\prod_{j'}\mathcal{N}_{j',eqm}^{s'_{j'}}\overline{\mathcal{N}}_{j',eqm}^{\bar{s}'_j}(s'_l - s_l) \end{aligned} \tag{6.26}$$

where we have added up the two expressions for C_{il} and divided by two. The final expression for C_{il} explicitly shows the invariance of the collision operator under exchange of i, l particles *and* exchange of forward and inverse collision processes for a given particle pair in equilibrium. This is the expression that becomes the linearized collision operator of lattice gas transport theory, and can be used to calculate the transport coefficients explicitly (see Chapter 5 of Molvig et al.[39]). Because of this symmetry, the momentum moment of this term in the collision operator expansion vanishes. We know, of course, that the momentum moment of the *entire* collision operator expansion *must* vanish, eqn. (2.13). Finally, the first order collision operator vanishes from eqn. (6.16) once the ensemble average is taken since it is a coefficient of single fluctuating quantities, $\langle \delta n_i \rangle$.

In a non-equilibrium state C_{il} cannot be shown to be symmetric in this way since we cannot employ eqn. (6.24) upon reversing the direction of the collision.

The second-order operator may be written as

$$C_{iml} \equiv \left\langle \frac{\partial^2 \Delta_i(n_j)}{\partial n_m \partial n_l}\,|_{n_j=N_j} \right\rangle N_l \overline{N}_l N_m \overline{N}_m \tag{6.27}$$

$$= \sum_{s,s'}(s_i' - s_i)A(s \to s')\prod_{j'}\mathcal{N}_{j'}^{s_{j'}}\overline{\mathcal{N}}_{j'}^{1-s_{j'}}(s_l - N_l)(s_m - N_m) \quad (6.28)$$

which is symmetric for interchange of m and l indices but not for i paired with either m or l, regardless of whether the system is in equilibrium or not. Furthermore, although we have shown that $C_{ill} = 0$, this does not generalize to all triplets of coordinates. Thus, although the shot noise self-correlations do not enter at all into the mean dynamics, the correlations between differing particles are non-zero, generally. We must examine the correlations $\langle \delta n_l \delta n_m \rangle$ in order to account for all the noise effects on the mean dynamics.

6.4 Calculation of the Lattice-Gas Correlation Function

In this section, we develop techniques that will allow us to estimate the correlation function $\langle \delta n_l \delta n_m \rangle$ between two state variables. The shot-noise or self-correlation fluctuation level is known *a priori*, however, for Boolean systems. We calculated this value in eqn. (6.8), $\langle \delta n_i^2 \rangle = \langle n_i \rangle (1 - \langle n_i \rangle)$.

The shot noise contribution to the mean dynamics would be large if it weren't for the multilinear property of the collision operator which completely eliminates this effect. We can embody this in our expression for $\langle \Delta_i(n_j) \rangle$ explicitly by rewriting eqn. (6.18)

$$\langle \Delta_i(n_j) \rangle = \langle \Delta_i(N_j) \rangle + \sum_l \sum_{m<l} \langle \delta n_l \delta n_m \rangle \langle \frac{\partial^2 \Delta_i(n_j)}{\partial n_m \partial n_l} \rangle \mid_{n_j = N_j} \quad (6.29)$$

where we have ignored higher order contributions since they have only non-shot noise terms. We now calculate $\langle \delta n_l \delta n_m \rangle$ theoretically which will give us a closed-form differential equation for the correlation functions. Because this result is

not very amenable to practical calculation, we will use an approximate treatment from equilibrium statistical mechanics to calculate explicitly the behaviour of the non-shot noise fluctuations as the size of the system increases.

6.4.1 Hierarchy of Correlation Functions

In this section, we proceed formally to calculate the first two terms of the BBKGY hierarchy[53] for lattice gas models. This follows the analysis of Chopard[52].

We begin by restating the microdynamical equation

$$n_j(t_* + 1, \mathbf{r}_* + c_j) = n_j(t_*, \mathbf{r}_*) + \Delta_i(n_j) \tag{6.30}$$

where n_j has a mean and fluctuating part eqn. (6.15). If we ensemble average eqn. (6.30) we find

$$\begin{aligned} N_j(t_* + 1, \mathbf{r}_* + c_j) - N_j(t_*, \mathbf{r}_*) &= \langle \Delta_j(n) \rangle \\ &= \Delta_j(N_j) + \sum_l \sum_{m<l} C_{lm} \langle \frac{\partial^2 \Delta_i(n_j)}{\partial n_m \partial n_l} \rangle \mid_{n_j = N_j} + \cdots \end{aligned} \tag{6.31}$$

where N_j is the mean value of n_j and

$$C_{lm}(\mathbf{r}_*, \mathbf{r}'_*, t_*) \equiv \langle \delta n_l(\mathbf{r}_*, t) \delta n_m(\mathbf{r}'_*, t) \rangle \tag{6.32}$$

the non-self correlation function. To derive an equation for C_{lm} we begin by multiplying eqn. (6.30) by the same equation for $n_i(t, \mathbf{r}')$ to obtain

$$\begin{aligned} n_j(t+1, \mathbf{r} + c_j) n_i(t+1, r' + c_j) &= n_j(t, \mathbf{r}) n_i(t, \mathbf{r}') + n_j(t, \mathbf{r}) \Delta_i(n(t, \mathbf{r}')) \\ &+ \Delta_j(n(t, \mathbf{r})) n_i(\mathbf{r}, t) + \Delta_j(n(\mathbf{r}, t)) \Delta_i(n(\mathbf{r}', t)) \end{aligned} \tag{6.33}$$

Doing the same to eqn. (6.32) results in

$$\begin{aligned} N_j(\mathbf{r} + c_j, t+1) N_i(\mathbf{r}' + c_i, t+1) &= N_j(\mathbf{r}, t) N_i(\mathbf{r}', t) + N_j(\mathbf{r}, t) \langle \Delta_i(n(t, \mathbf{r}')) \rangle \\ &+ \langle \Delta_j(n(t, \mathbf{r})) \rangle N_i(\mathbf{r}', t) + \langle \Delta_j(n(t, \mathbf{r})) \rangle \langle \Delta_i(n(t, \mathbf{r}')) \rangle \end{aligned} \tag{6.34}$$

If we now average eqn. (6.34) and then subtract eqn. (6.35) we find that

$$\begin{aligned} C_{ji}(r'+c_j,\mathbf{r}'+c_i,t+1) &= C_{ji}(\mathbf{r},\mathbf{r}',t)+\langle\delta n_j(\mathbf{r},t)\Delta_i(\mathbf{r}',t)\rangle \\ &+ \langle\Delta_j(\mathbf{r},t)\delta n_i(\mathbf{r}',t)\rangle+\langle\Delta_j(\mathbf{r},t)\Delta_i(\mathbf{r}',t)\rangle \\ &- \langle\Delta_j(\mathbf{r},t)\rangle\langle\Delta_i(\mathbf{r}',t)\rangle \end{aligned} \tag{6.35}$$

To get everything in terms of correlation functions we expand the collision operator in terms of the density fluctuations up to second order. This results in a closed form expression for the time evolution of the second order correlation function

$$\begin{aligned} C_{ji}(\mathbf{r}+c_j,\mathbf{r}'+c_i,t+1) - C_{ji}(\mathbf{r},\mathbf{r}',t) = \\ \sum_l\left[C_{jl}(\mathbf{r},\mathbf{r}',t)\frac{\partial\Delta_i(N(\mathbf{r}',t))}{\partial n_l}+C_{il}\frac{\partial\Delta_j(N(\mathbf{r},t))}{\partial n_l}\right] \\ +\sum_{k,l}\left[\frac{\partial\Delta_i(N(\mathbf{r},t))}{\partial n_k}\frac{\partial\Delta_i(N(\mathbf{r}',t))}{\partial n_l}C_{kl}(\mathbf{r},\mathbf{r}',t)\right] \end{aligned} \tag{6.36}$$

Equations (6.32) and (6.36) represent the first two equations of a BBKGY hierarchy for lattice-gas models since the left-hand sides of both equations are differential operators on the unknown. The first and second order collision operators are known explicitly as functions of N_j. Thus, eqns. (6.32) and (6.36) represent two coupled non-linear partial differential equations for the nonequilibrium density N_j and correlation function C_{ij}. Rather than struggle with this formidable analytical problem we will examine the more tractable problem of calculating C_{ij} in equilibrium where explicit calculation is possible.

6.4.2 Microcanonical Distribution and the Equilibrium Fluctuations

In equilibrium statistical mechanics, the probability distribution in phase space is given by the so-called microcanonical distribution. This distribution assumes that

when equilibrium has been reached all microscopic configurations of the particles that have the equilibrium energy, U, occur with the same probability[31]. Armed with this hypothesis it is now possible to estimate the equilibrium values of density correlations.

The method will be demonstrated using the three speed model we discussed in Section 5.1 that removed the Galilean invariance artifact, g. Let $N0, N1$, and $N2$ be respectively the total number of stationary, energy=1, and energy=2 particles, and let Ω be the number of sites in the lattice. Furthermore, the microscopic Boolean variables $n0_i(\mathbf{r}_j), n1_i(\mathbf{r}_j)$ and $n2_i(\mathbf{r}_j)$ indicate, respectively, whether a stationary, speed 1 or speed 2 particle exists at lattice site $\mathbf{r}_j$ in direction i. The number of possible "directions" at any lattice site for a particular speed is indicated, as usual, by d_0, d_1 and d_2 respectively. Now our hypothesis states that all configurations with $N1 + N1 + N2 \equiv F$ particles and a given energy, $N1 + 2N2 = U$, are equiprobable. Call this probability p. All other configurations cannot occur in this system. A configuration of the lattice is determined by the set of all Boolean quantities $n0_i$, $n1_i$ and $n2_i$ for $i = 1$ to $d0, d1$ or $d2$ and $k = 1$ to Ω. Thus the probability of a certain configuration $P(n0, n1, n2)$ occuring in this system is given by

$$P(n0,n1,n2) = \left\{ \begin{array}{l} \\ \sum_{i=1}^{d_0}\sum_{k=1}^{\Omega} n0_i(\mathbf{r}_j) + \sum_{i=1}^{d_1}\sum_{k=1}^{\Omega} n1_i(\mathbf{r}_j) + \sum_{i=1}^{d_2}\sum_{k=1}^{\Omega} n2_1(\mathbf{r}_j) = F \\ p \text{ if} \\ \sum_{i=1}^{d_1}\sum_{k=1}^{\Omega} n1i(\mathbf{r}_j) + 2\sum_{i=1}^{d_2}\sum_{k=1}^{\Omega} n2_i(\mathbf{r}_j) = U \\ \\ 0 \text{ otherwise} \end{array} \right\} \tag{6.37}$$

where the configuration $(n0, n1.n2)$ is defined by

$$(n0, n1, n2) \equiv (n0_1(\mathbf{r}_1), \ldots n0_{d_0}(\mathbf{r}_1), n1_1(\mathbf{r}_1), \ldots n1_{d_1}(\mathbf{r}_1), n2_1(\mathbf{r}_1), \ldots n2_{d_2}(\mathbf{r}_\Omega)).$$

To find the value of p, we now must find the number of ways we can arrange $N0, N1, N2$ on $d_0\Omega, d_1\Omega, d_2\Omega$ lattice sites respectively such that

$$F \equiv N0 + N1 + N2 \tag{6.38}$$

$$U \equiv N1 + 2N2 \tag{6.39}$$

for each realization. The probability of any one of these arrangements is then merely $1/p$ due to the microcanonical hypothesis. A straightforward combinatoric calculation shows that

$$\frac{1}{p} = \sum_{N2=max[O,U-F]}^{U/2} \left(\begin{array}{c} d_2\Omega \\ N2 \end{array} \right) \left(\begin{array}{c} d_1\Omega \\ U - 2N2 \end{array} \right) \left(\begin{array}{c} d_0\Omega \\ F - U + N2 \end{array} \right). \tag{6.40}$$

We allow the energy=2 density, $N2$, to vary and define the other two energies in terms of $N2$ and the two constant quantities using eqns. (6.38) and (6.39). The upper bound on the value of $N2$ is to ensure that $N1$ is positive while the lower bound ensures that $N0$ is positive. We use the usual combinatoric notation

$$\left(\begin{array}{c} A \\ B \end{array} \right) = \frac{A!}{B!(A-B)!}. \tag{6.41}$$

From this result, we can calculate $\langle n2_i(\mathbf{r}) \rangle$, the average type 2 density travelling in direction i in equilibrium

$$\begin{aligned} \langle n2_i(\mathbf{r}) \rangle &= \sum n2_i P(n0, n1, n2) \\ &= 0 \cdot p \cdot \sum_{N2} \left(\begin{array}{c} d_2\Omega - 1 \\ N2 \end{array} \right) \left(\begin{array}{c} d_1\Omega \\ U - 2N2 \end{array} \right) \left(\begin{array}{c} d_0\Omega \\ F - U + N2 \end{array} \right) \end{aligned} \tag{6.42}$$

$$+ \quad 1 \cdot p \cdot \sum_{N2} \begin{pmatrix} d_2\Omega - 1 \\ N2 - 1 \end{pmatrix} \begin{pmatrix} d_1\Omega \\ U - 2N2 \end{pmatrix} \begin{pmatrix} d_0\Omega \\ F - U + N2 \end{pmatrix}$$

$$= \sum_{N2=max[1,U-F]}^{U/2} \begin{pmatrix} d_2\Omega - 1 \\ N2 - 1 \end{pmatrix} \begin{pmatrix} d_1\Omega \\ U - 2N2 \end{pmatrix} \begin{pmatrix} d_0\Omega \\ F - U + N2 \end{pmatrix} \cdot p$$

where the above sum is over all configurations $(n0, n1, n2)$ but only the configurations with a particle in $n2_i$ that also satisfy F and U contribute. Note that the lower limit of the sum has now moved up to at least 1 to ensure that configurations without $N2$ particles do not contribute to $\langle n2_i(\mathbf{r}) \rangle$.

We may now calculate the quantity $\langle n2_i(\mathbf{r}) n2_j(\mathbf{r}) \rangle$ at equilibrium in a similar manner. We already know the result when $i = j$ and $\mathbf{r} = \mathbf{r}'$, eqn. (6.8), so we will only do the non-self-correlation calculation:

$$\begin{aligned} \langle n2_i(\mathbf{r}) n2_j(\mathbf{r}') \rangle &= \sum n2_i n2'_j P(n0, n1, n2) \\ &= \sum_{N2=max[2,U-F]}^{U/2} \begin{pmatrix} d_2\Omega - 2 \\ N2 - 2 \end{pmatrix} \begin{pmatrix} d_1\Omega \\ U - 2N2 \end{pmatrix} \begin{pmatrix} d_0\Omega \\ F - U + N2 \end{pmatrix} p \end{aligned} \tag{6.43}$$

where now we put two $N2$ particles in specific sites and rearrange all the other particles in all possible arrangements. Again the lower bound of the sum has been raised to assure that there are at least two $N2$ particles in the configuration.

These results, although explicit, are not that amenable to calculation. To facilitate this we first notice the identities

$$\begin{aligned} \begin{pmatrix} N - 1 \\ n - 1 \end{pmatrix} &= \frac{n}{N} \begin{pmatrix} N \\ n \end{pmatrix} \\ \begin{pmatrix} N - 2 \\ n - 2 \end{pmatrix} &= \left(\frac{n}{N}\right)^2 \begin{pmatrix} N \\ n \end{pmatrix} \frac{\left(1 - \frac{1}{n}\right)}{\left(1 - \frac{1}{N}\right)}. \end{aligned} \tag{6.44}$$

Thus for notational purposes, we may write

$$\begin{aligned}\langle n2_i(\mathbf{r})\rangle &= \frac{\sum_{N2=max[1,U-F]}^{U/2}\left(\frac{N2}{d_2\Omega}\right)\begin{pmatrix} d_2\Omega \\ N2\end{pmatrix}\begin{pmatrix} d_1\Omega \\ U-2N2\end{pmatrix}\begin{pmatrix} d_0\Omega \\ F-U+N2\end{pmatrix}}{\sum_{N2=max[0,U-F]}^{U/2}\begin{pmatrix} d_2\Omega \\ N2\end{pmatrix}\begin{pmatrix} d_1\Omega \\ U-2N2\end{pmatrix}\begin{pmatrix} d_0\Omega \\ F-U+N2\end{pmatrix}} \\ &= \frac{\sum_{N2}\left(\frac{N2}{d_2\Omega}\right)f(N2)}{\sum_{N2}f(N2)} = p\sum_{N2}\left(\frac{N2}{d_2\Omega}\right)f(N2) \\ &\equiv \langle\frac{N2}{d_2\Omega}\rangle \end{aligned} \tag{6.45}$$

since $p^{-1}=\sum_{N2}f(N2)$, eqn. (6.40). Similarly, we may rewrite eqn. (6.44)

$$\langle n2_i(\mathbf{r})n2_j(\mathbf{r}')\rangle = \left\langle\frac{1-\frac{1}{N2}}{1-\frac{1}{d_2\Omega}}\left(\frac{N2}{d_2\Omega}\right)^2\right\rangle = \frac{1}{1-\frac{1}{d_2\Omega}}\left[\left\langle\left(\frac{N2}{d_2\Omega}\right)^2\right\rangle - \frac{1}{d_2\Omega}\left\langle\frac{N2}{d_2\Omega}\right\rangle\right] \tag{6.46}$$

and we note that the bottom bound of the summations for the numerator and denominator may be different.

We now may calculate the correlation function for this case since

$$\begin{aligned}\langle\delta n2_i(\mathbf{r})\delta n2_j(\mathbf{r}')\rangle &= \langle n2_i(\mathbf{r})n2_j(r)\rangle - \langle n2_i(\mathbf{r})\rangle\langle n2_j(\mathbf{r}')\rangle \\ &= \frac{1}{1-\frac{1}{d_2\Omega}}\left[\left\langle\left(\frac{N_2}{d_2\Omega}\right)^2\right\rangle - \frac{1}{d_2\Omega}\left\langle\frac{N2}{d_2\Omega}\right\rangle\right] - \left\langle\frac{N_2}{d_2\Omega}\right\rangle^2 \\ &\approx \left\langle\left(\frac{N_2}{d_2\Omega}\right)^2\right\rangle - \left\langle\frac{N2}{d_2\Omega}\right\rangle^2 + \frac{1}{d_2\Omega}\left[\left\langle\left(\frac{N2}{d_2\Omega}\right)^2\right\rangle - \left\langle\frac{N2}{d_2\Omega}\right\rangle\right]\end{aligned} \tag{6.47}$$

to first order in $1/d_2\Omega$. Since Ω is the number of lattice sites, which is typically on the order of 10^5 to 10^6 in simulations, this is a good expansion parameter. As well, $d_2 = 24$ is also large. If we can show that the terms in the square brackets are order unity or smaller with respect to the lattice volume and that the first

two terms combine to leave a term of order $1/d_2\Omega$, then the two point correlation function is inversely related to the volume and so becomes vanishingly small as the volume $\Omega \to \infty$. Thus, in large enough systems, the non-self correlation functions can be made negligibly small.

The rest of the correlation functions can be calculated in a similar manner. Written in the above notation, they are

$$\begin{aligned}
\langle n1_i(\mathbf{r})\rangle &= \left\langle \frac{U-2N2}{d_1\Omega}\right\rangle = \frac{U}{d_1\Omega} - 2\left\langle \frac{N2}{d_1\Omega}\right\rangle = \frac{U}{d_1\Omega} - 2\frac{d_2}{d_1}\langle n2_i(\mathbf{r})\rangle \\
\langle n0_i(\mathbf{r})\rangle &= \left\langle \frac{N2+F-U}{d_0\Omega}\right\rangle = \frac{F-U}{d_0\Omega} + \frac{d_2}{d_0}\langle n2_i(\mathbf{r})\rangle \\
\langle \delta n0_i(\mathbf{r})\delta n0_j(\mathbf{r}')\rangle &= \frac{1}{1-\frac{1}{d_0\Omega}}\left[\left\langle\left(\frac{F+N_2-E}{d_0\Omega}\right)^2\right\rangle - \frac{1}{d_0\Omega}\left\langle\frac{F+N_2-E}{d_0\Omega}\right\rangle\right] \\
&\quad - \left\langle\frac{F+N2-E}{d_0\Omega}\right\rangle^2 \\
\langle \delta n1_i(\mathbf{r})\delta n1_j(\mathbf{r}')\rangle &= \frac{1}{1-\frac{1}{d_1\Omega}}\left[\left\langle\left(\frac{U-2N2}{d_1\Omega}\right)^2\right\rangle - \frac{1}{d_1\Omega}\left\langle\frac{U-2N2}{d_1\Omega}\right\rangle\right] \\
&\quad - \left\langle\frac{U-2N2}{d_1\Omega}\right\rangle^2 \qquad (6.48) \\
\langle \delta n2_i(\mathbf{r})\delta n1_j(\mathbf{r}')\rangle &= \frac{d_2}{d_1}\left[\frac{U}{d_2\Omega}\left\langle\frac{N_2}{d_2\Omega}\right\rangle - 2\left(\frac{N_2}{d_2\Omega}\right)^2\right] - \left\langle\frac{N2}{d_2\Omega}\right\rangle\left\langle\frac{U-2N2}{d_1\Omega}\right\rangle \\
\langle \delta n2_i(\mathbf{r})\delta n0_j(\mathbf{r}')\rangle &= \frac{d_2}{d_0}\left[\left\langle\left(\frac{N_2}{d_2\Omega}\right)^2\right\rangle + \frac{(F-U)}{d_2\Omega}\left\langle\frac{N_2}{d_2\Omega}\right\rangle\right] \\
&\quad - \left\langle\frac{N_2}{d_2\Omega}\right\rangle\left\langle\frac{F-U+N2}{d_0\Omega}\right\rangle \\
\langle \delta n1_i(\mathbf{r})\delta n0_j(\mathbf{r}')\rangle &= \frac{U(F-U)}{d_0d_2\Omega^2} + \frac{(3U-2F)}{d_0\Omega}\left\langle\frac{N_2}{d_2\Omega}\right\rangle - 2\frac{d_2}{d_0}\left\langle\left(\frac{N_2}{d_2\Omega}\right)^2\right\rangle
\end{aligned}$$

To calculate the moments of the form $\left\langle\frac{N_2}{d_2\Omega}\right\rangle$, we use the result from statistical mechanics that

$$\begin{pmatrix} N \\ n \end{pmatrix} \approx P_M(n) \approx \frac{2^N}{\sqrt{2\pi\sigma^{*}}}\exp\left[-\frac{(n-\langle n\rangle)^2}{2\sigma^{*2}}\right] \qquad (6.49)$$

as $N \rightarrow \infty$ where

$$\begin{aligned} \langle n \rangle &= N/2 \\ \sigma^{*2} &= \frac{\sigma^2}{1-\frac{1}{N}} \;\; ; \;\; \sigma^2 = N/4. \end{aligned} \tag{6.50}$$

Furthermore, in the limit of large N

$$\sum_{n=0}^{N} \left(\begin{array}{c} N \\ n \end{array} \right) \rightarrow \int_{-\infty}^{\infty} P_M(n) dn. \tag{6.51}$$

Since the indicated integrals over Maxwellians are analytically calculable, it becomes possible to calculate explicit values for the above $N2$ moments. The large parameter N in eqn. (6.51) corresponds to the volume quantity $d_2\Omega$ in our analysis. This is the parameter we want to make very large to examine the behaviour of the correlation functions in the limit of large number of lattice sites. With the substitution indicated by eqn. (6.51), the expression for the probabilty p, eqn. (6.40), becomes an integral over a product of three Maxwellians which itself is a Maxwellian. Thus, this integral can be performed,

$$\begin{aligned} \sum_{N2} f(N2) &\approx \int_{-\infty}^{\infty} f(N2) dN2 \\ &\approx \int_{-\infty}^{\infty} \frac{2^{(d_0+d_1+d_2)\Omega}}{(2\pi)^{3/2}\sigma_0^*\sigma_1^*\sigma_2^*} exp\left[-\frac{(N_2 - \frac{d_2\Omega}{2})^2}{2\sigma_2^{*2}} - \frac{(U - \frac{d_1\Omega}{2} - 2N2)^2}{2\sigma_1^{*2}} \right. \\ &\qquad \left. - \frac{(N_2 - \frac{d_0\Omega}{2}U + F)^2}{2\sigma_0^{*2}} \right] dN_2 \\ &\approx K^* \int_{-\infty}^{\infty} \exp\left[\frac{-(N_2 - \frac{K_2}{2K_1})^2}{2/K_1} \right] dN_2 \\ &\approx K^* \sqrt{\frac{2\pi}{K_1}} \end{aligned} \tag{6.52}$$

where

$$\sigma_j^{*2} = \frac{g_j\Omega/4}{1 - 1/g_j\Omega} \propto \mathcal{O}(\Omega)$$

$$
\begin{aligned}
K_1 &= \frac{1}{\sigma_2^{*2}} + \frac{4}{\sigma_1^{*2}} + \frac{1}{\sigma_0^{*2}} \propto \mathcal{O}(\frac{1}{\Omega}) \\
K_2 &= \frac{d_2\Omega}{\sigma_2^{*2}} + \frac{4U - 2d_1\Omega}{\sigma_1^{*2}} + \frac{d_0\Omega + 2U - 2F}{\sigma_0^{*2}} \propto \mathcal{O}(1) \\
K_3 &= \frac{(d_2\Omega)^2}{\sigma_2^{*2}} + \frac{(U - \frac{d_1\Omega}{2})^2}{\sigma_1^{*2}} + \frac{\left(\frac{d_0\Omega}{2} + U - F\right)^2}{\sigma_0^{*2}} \propto \mathcal{O}(\Omega)
\end{aligned}
$$

and

$$
K^* = \frac{2^{(d_0+d_1+d_2)\Omega}}{(2\pi)^{3/2}\sigma_0^*\sigma_1^*\sigma_2^*} exp\left[\frac{-K_3}{2} + \frac{K_2^2}{8K_1}\right].
$$

Some straightforward, but cumbersome, manipulations of Maxwellian integrals give expressions for the moments in eqn. (6.48)

$$
\begin{aligned}
\left\langle \frac{N_2}{d_2\Omega} \right\rangle &= \frac{\int_{-\infty}^{\infty} \frac{N_2}{d_2\Omega} f(N_2) dN2}{\int_{-\infty}^{\infty} f(N_2) dN_2} = \frac{1}{d_2\Omega}\frac{K_2}{2K_1} \propto \mathcal{O}(1) \qquad (6.53) \\
\left\langle \left(\frac{N_2}{d_2\Omega}\right)^2 \right\rangle &= \left(\frac{1}{d_2\Omega}\right)^2 \left[\frac{1}{K_1} + \left(\frac{K_2}{2K_1}\right)^2\right] = \left(\frac{1}{d_2\Omega}\right)^2 \frac{1}{K_1} + \left\langle \frac{N_2}{d_2\Omega} \right\rangle^2 \propto \mathcal{O}(1)
\end{aligned}
$$

or

$$
\left\langle \left(\frac{N_2}{d_2\Omega}\right)^2 \right\rangle - \left\langle \frac{N_2}{d_2\Omega} \right\rangle^2 = \frac{1}{d_2\Omega}\left(\frac{1}{K_1(d_2\Omega)}\right) \propto \mathcal{O}\left(\frac{1}{d_2\Omega}\right). \qquad (6.54)
$$

Plugging these results into eqn. (6.48), we conclude that $\langle \delta n2_i \delta n2_j \rangle \propto \mathcal{O}\left(\frac{1}{d_2\Omega}\right)$, which is exactly the result we anticipated. Such calculations are possible for all the other correlation functions of eqns. (6.49). The results are summarized below:

$$
\begin{aligned}
\langle \delta n2_i \delta n2_j \rangle &\approx \frac{1}{d_2\Omega}\left[\frac{1}{K_1(d_2\Omega)} - \left\langle \frac{N_2}{d_2\Omega} \right\rangle \left(1 - \left\langle \frac{N_2}{d_2\Omega} \right\rangle\right)\right] \\
\langle \delta n1_i \delta n1_j \rangle &\approx \frac{1}{d_1\Omega}\left[\frac{1}{K_1(d_1\Omega)} - \left\langle \frac{U - 2N2}{d_1\Omega} \right\rangle \left(1 - \left\langle \frac{U - 2N2}{d_1\Omega} \right\rangle\right)\right] \qquad (6.55) \\
\langle \delta n0_i \delta n0_j \rangle &\approx \frac{1}{d_0\Omega}\left[\frac{1}{K_1(d_0\Omega)} - \left\langle \frac{N2 - (U - F)}{d_0\Omega} \right\rangle \left(1 - \left\langle \frac{N2 - (U - F)}{d_0\Omega} \right\rangle\right)\right]
\end{aligned}
$$

where the directions are different, $i \neq j$. In all three terms, the second term in the square brackets is the shot noise expression $\langle \delta n k_i^2 \rangle = \langle n k_i \rangle \left\langle \overline{n k_i} \right\rangle$ where k is

the particle energy, $k = 0, 1$ or 2. Since the moment of a constant is the constant itself, $\langle A \rangle \equiv A$, the only moment that requires calculation in the above results is $\left\langle \frac{N_2}{d_2 \Omega} \right\rangle$. The cross speed correlation functions are

$$\begin{aligned} \langle \delta n2_i \delta n1_j \rangle &\approx \frac{-2}{d_1 d_2 \Omega} \left(\frac{1}{K_1 \Omega} \right) \\ \langle \delta n2_i \delta n0_j \rangle &\approx \frac{1}{d_0 d_2 \Omega} \left(\frac{1}{K_1 \Omega} \right) \\ \langle \delta n1_i \delta n0_j \rangle &\approx \frac{-2}{d_0 d_1 \Omega} \left(\frac{1}{K_1 \Omega} \right) \end{aligned} \tag{6.56}$$

where

$$\frac{1}{K_1 \Omega} \approx \frac{1}{\frac{4}{d_0} + \frac{16}{d_1} + \frac{4}{d_2}} + \frac{\left(\frac{4}{d_0^2} + \frac{16}{d_1^2} + \frac{4}{d_2^2} \right)}{\left(\frac{4}{d_0} + \frac{16}{d_1} + \frac{4}{d_2} \right)^2} \frac{1}{\Omega} + \mathcal{O}\left(\frac{1}{\Omega^2} \right). \tag{6.57}$$

The above six non-shot noise correlation functions can be condensed into one summarising equation

$$\langle \delta n k_i \delta n l_j \rangle \approx \frac{1}{d_k \Omega} [1 - 3 (\delta^*_{10} + \delta^*_{21})] \left[\frac{1}{K_1 (d_l \Omega)} - \left\langle \delta n k_i^2 \right\rangle \delta_{kl} \right] \tag{6.58}$$

where the energy parameters k, l are any combination of the speeds 0,1,2 while the two particle speeds are not equal, $i \neq j$. The function δ_{kl} is the Kroenecker delta which has the value unity when $k = l$ and zero otherwise and δ^*_{ab} is defined as, $\delta^*_{ab} \equiv \delta_{ka}\delta_{lb} + \delta_{la}\delta_{kb}$, a function that is equal to one if $a \neq b$, $k = a$ and $l = b$ or vice-versa, equals two if $a = b$ and $k = l = a$, and zero otherwise. Since $1/K_1 \propto \mathcal{O}(\Omega)$, we see that non-self correlations are smaller than self correlations by a factor proportional to the inverse number of lattice sites in the model.

There are two main sources of error that we have introduced by switching from combinatoric expressions to Maxwellian distributions. First of all, we have gone from a discrete distribution to a continuous one and secondly, whereas the discrete distribution only allowed contributions from a finite range of $N2$ (from

max[0,U-F] to $U/2$), we are integrating the Maxwellian distribution for values of $N2$ from $-\infty$ to ∞. For a broad yet strongly peaked distribution the difference between the two should be small since the contribution outside the denied range of $N2$ will be negligible.

To see the effect of these assumptions, numerical results using equations (6.45) and (6.46) to calculate the value of $\langle \delta n2_i(\mathbf{r}) \delta n2_j(\mathbf{r}') \rangle$ for specific values of U and F have been calculated and compared with the approximate theoretical analysis of equations (6.53) and (6.55). For these calculations, we take $U = 12\Omega$ and $F = 10\Omega$, which are typical values used in actual simulations, where Ω, the number of lattice sites, ranges from 1 to 20. These values of Ω are at least four orders of magnitude smaller than what would be used in an actual simulation. Since the purpose of this exercise is simply to demonstrate the $1/\Omega$ scaling of the non-self correlations, small values of Ω are ideal. Later we will calculate the sum of all the non-self correlation functions in an actual lattice gas model with a large number of sites to demonstrate the negligibilty of these terms. We also take $d_0 = 6, d_1, = 24, d_2 = 24$, the values that correspond to the three speed model we discussed in Section 5.1. Even in these calculations, although Ω itself may not be large, $\frac{1}{d_j \Omega}$ is still small. Table 6.1 shows a comparison between the approximate and directly calculated values of $\langle n2_i \rangle$ and $\langle \delta n2_i \delta n2_j \rangle$ for a range of Ω. These results show that the approximate analysis agrees quite well ($\leq\sim 15\%$ error) and improves as the number of lattice sites, Ω, increases. The most important result is that both calculations of the correlation function, $\langle \delta n2_i \delta n2_j \rangle$, show the expected $1/\Omega$ dependence, as illustrated in the last two columns of Table 6.1. Table 6.2 compares exact, eqns. (6.49), and theoretical, eqns. (6.58), results for the rest of the correlation functions at $\Omega = 1$. Even though the number of sites is not extremely large, we still see good qualitative agreement of the approximate method

Ω		EXACT eqn. (6.45) eqn. (6.46)	THEORY eqn. (6.53) eqn. (6.55)	ERROR	EXACT CORR. RATIO	THEOR. CORR. RATIO
1	$\langle n2_i \rangle$	0.1467	0.1445	-1.5 %		
	$\langle \delta n2_i \delta n2_j \rangle$	-4.565×10^{-3}	-3.869×10^{-3}	15 %		
5	$\langle n2_i \rangle$	0.1490	0.1475	1.0 %		
	$\langle \delta n2_i \delta n2_j \rangle$	-9.055×10^{-4}	-8.118×10^{-4}	10 %	5.04	4.77
10	$\langle n2_i \rangle$	0.1492	0.1478	0.94 %		
	$\langle \delta n2_i \delta n2_j \rangle$	-4.522×10^{-4}	-4.079×10^{-4}	9.8 %	2.00	1.99
20	$\langle n2_i \rangle$	0.1494	0.1480	0.94 %		
	$\langle \delta n2_i \delta n2_j \rangle$	-2.260×10^{-4}	-2.045×10^{-4}	9.5 %	2.00	1.99

Table 6.1: Calculation of average energy=2 density $\langle n2_i \rangle$ and energy=2 correlation function $\langle \delta n2_i \delta n2_j \rangle$ using both the exact, eqns. (6.45) and (6.46) and approximate theoretical, eqns. (6.53) and (6.55) methods for many different lattice sizes, Ω. The total number of particles in the system is $F = 10\Omega$ while the total energy is $U = 12\Omega$. The ratios in column 6 and 7 for a lattice of size Ω are found by dividing the value of the correlation function of next lower size to the current correlation value. That is, the ratio for $\Omega = 5$ is calculated from Ω_1/Ω_5. In column 6, we use the exact results and in column 7 we use the theoretical results. The ratios of the correlation functions for two different lattices, Ω_1 to Ω_2, are in the ratio $\frac{\Omega_2}{\Omega_1}$.

Correlation Function	EXACT eqn. (6.49)	THEORY eqn. (6.58)	ERROR
$\langle \delta n1_i \delta n1_j \rangle$	-3.610×10^{-3}	-5.654×10^{-3}	57%
$\langle \delta n0_i \delta n0_j \rangle$	-2.169×10^{-2}	-2.096×10^{-2}	3.4%
$\langle \delta n2_i \delta n1_j \rangle$	-1.684×10^{-3}	-2.564×10^{-3}	50%
$\langle \delta n2_i \delta n0_j \rangle$	3.368×10^{-3}	5.129×10^{-3}	52%
$\langle \delta n1_i \delta n0_j \rangle$	-1.188×10^{-2}	-1.026×10^{-2}	13%

Table 6.2: Calculation of the rest of the correlation functions using eqns. (6.49) to calculate numerical values and eqns. (6.58) for the approximate values with only one lattice site, $\Omega = 1$. The total number of particles in the system is $F = 10\Omega$ while the total energy is $U = 12\Omega$. The agreement between the two methods improves as Ω increases while the numerical values decrease as $\frac{1}{\Omega}$.

with the numerical results. In fact, we see that although most of the correlation functions are negative, there is one that is positive, $\langle \delta n2_i \delta n0_j \rangle$. The approximate method captures this result as well. As the number of lattice sites, Ω, is increased, the values of these correlations functions also decrease inversely with Ω while the quantitative errors in the approximate method decreases, similar to the way it does for $\left\langle \delta n_{2_i} \delta n_{2_j} \right\rangle$. Thus we find that although our approximate analysis introduces quantitative errors ($\leq\sim$ 50% at smallest Ω possible) the desired behaviour with increasing Ω is captured by our theoretical analysis.

Now that we have established that our approximate expressions for the correlation functions, eqns. (6.58), behave qualitatively the same as the exact eqns. (6.49), we can use the approximate expressions to compare the size of total contribution

of non-self correlation functions to the mean dynamics using eqn. (6.32). The zeroth order collision operator, eqn. (6.19), and the second order collision operator, eqn. (6.22), are of the same order of magnitude. Assume that they are both less than a quantity L. Then the two terms on the right-hand side of eqn. (6.32) can be combined

$$\Delta_i(N_j)+\sum_l \sum_{m<l} \langle \delta n_l \delta n_m \rangle \left\langle \frac{\partial^2 \Delta_i(n_j)}{\partial n_m \partial n_l} \right\rangle |_{n_j=N_j} \approx L \left(1 + \sum_l \sum_{m<l} \langle \delta n_l \delta n_m \rangle \right). \quad (6.59)$$

In the three-speed model for which our simulations have been carried out there are $d_0 + d_1 + d_2 = 54$ directions per lattice site. Writing eqn. (6.59) out explicitly in terms of the correlation functions, which are independent of direction, we find

$$\begin{aligned} \approx L \left(1 + \sum_{l=2}^{54} \sum_{m=1}^{l-1} \langle \delta n_l \delta n_m \rangle \right) &= L \left(1 + \{ 15 \langle \delta n0_i \delta n0_j \rangle + 24 \cdot 6 \langle \delta n1_i \delta n0_j \rangle \right. \\ &+ 276 \langle \delta n1_j \delta n1_j \rangle + \langle \delta n2_i \delta n2_j \rangle 276 \\ &+ \left. 24^2 \langle \delta n2_i \delta n1_j \rangle + 24 \cdot 6 \langle \delta n2_i \delta n0_j \rangle \} \right) \quad (6.60) \end{aligned}$$

where the numerical coefficient of each correlation function indicates the number of times it appears in the sum over l and m. We now calculate the values of the correlation functions using eqns. (6.58) in a system with $U = 12\Omega$, $F = 10\Omega$ and $\Omega = 64^3$, typical system parameters in the simulations of Chapter 7

$$\begin{aligned} L \left(1 + \sum_{l=2}^{54} \sum_{m=1}^{l-1} \langle \delta n_l \delta n_m \rangle \right) &\approx L \left(1 - \frac{4}{\Omega} \right) \\ &\approx L \left(1 - 10^{-5} \right). \quad (6.61) \end{aligned}$$

We see that the contribution due to non-shot noise correlations is down by 5 orders of magnitude and so is completely negligible in comparison with the mean collision operator contribution. Higher order non-shot noise correlations, which also scale inversely with the number of lattice sites, are even smaller. We have

justified that the equation for mean dynamics in a large lattice gas system is effectively

$$N_j(t_o + 1, r_o + c_j) - N_j(t_o, r_o) = \Delta_j(N_j) \tag{6.62}$$

which is equivalent to the equation obtained when assuming the Boltzmann approximation and ensemble-averaging the microdynamical equation, eqn. (2.8). We have verified that this assumption is valid in lattice gas systems of large enough size to be of practical interest.

6.5 Summary – Why the Mean Dynamics are Correct

This Chapter has been so awash in complex correlation function notation and mathematical gymnastics that the purpose of this exercise may have been lost. We restate the conclusions here. Intially, it was conjectured that the mean dynamics of lattice gas methods may be contaminated by the large inherent shot noise associated with any Boolean method. It turns out that this is not the case because the Boolean nature of the lattice advection term and collision operator results in a *Shot Noise Theorem* that states that the mean kinetic theory dynamics of a lattice gas are independent of the shot noise fluctuation level to all orders in the fluctuations. This remarkable result is due to the absence of non-linear terms in the lattice advection term[5] and the fact that the collision operator is multi-linear in the particle densities and so its second derivative with respect to any density is zero. While the shot-noise correlation functions are of the same order as the

[5]unlike the Navier-Stokes equations for fluid dynamics or the equations of plasma physics where the advection term is non-linear

densities themselves, all non-shot noise correlation functions decrease in a manner inversely proportional to the total state-space volume, and so become negligible at lattice volumes of practical interest.

The mean dynamics are correct despite the large statistical noise fluctuation level. This is because what is really needed to obtain accurate hydrodynamic behaviour is the ability to achieve and maintain a very tight thermodynamic equilibrium. This property depends on the existence of an abundance of collisions amongst the microscopic particles. In a lattice gas, at any instant in time the discreteness of the dynamics allows many particles travelling in different directions to occupy a particular lattice site which assures that they will collide efficiently there. It is not necessary to have an excessively large number of particles at each site as even with only 10 particles per site on average, the mean free path for collisions is actually less than the lattice length which assures that thermodynamic equilibrium is being held practically down to *lattice site scales.* Of course, another property of the microdynamics that is required to assure correct hydrodynamic behaviour is the exact conservation of mass, momentum, and energy, a property that lattice gas systems have precisely.

Consequently, we find that although macroscopic flow properties in a lattice gas may change significantly from time-step to time-step, the mean-value of these fluctuations is identical to the correct hydrodynamic values, if the lattice artifacts have been otherwise removed. All that needs to be done to observe the correct mean dynamics in a noisy lattice system is to average either over time, or if the system is changing quickly in time, over some spatial volume, to bring the signal to noise down to an acceptable level for which the averaged signal is the correct hydrodynamic result. This result will be repeatedly demonstrated in the

simulations of the next Chapter.

Chapter 7

Validation of Correct Hydrodynamic Behaviour in a Three-Speed Lattice Gas Model

In this Chapter, we verify some of the theoretical predictions we have made concerning the lattice gas algorithm and show by simulation that the lattice gas algorithm can be made to accurately reproduce hydrodynamics in low Mach number and Reynolds number flows. A computer code utilizing the three-speed lattice gas model that removes all lattice artifacts in the momentum equation[1] was developed for implementation on the CRAY-2 supercomputer. This code, from here on called the Lattice Gas Algorithm or LGA code, was used to confirm key predictions of the three speed model such as the absence of the Galilean invariance, g, and pressure anomaly artifacts for a large range of pressure and densities. The

[1]The model developed in Section 5.1

absence of these artifacts is the first reason that the lattice gas model can be used to accurately reproduce fluid dynamics. Although, in theory the simulations should be limited to low Mach number flows, $M \ll 1$[2], we have found that even for flows with Mach numbers approaching unity, where the small Mach number expansion and hence the underlying theory of the method breaks down, the pressure anomaly remains a small fraction of the dynamic pressure. Furthermore,the Galilean invariance factor, g, can be maintained at a value very close to the desired value of unity at Mach numbers up to $M = .4$ with non-hydrodynamic effects not becoming visible until $M = .5$. We also demonstrate that the model can maintain the proper hydrodynamic behaviour when disturbed by perturbations as small as two lattice sites in extent which shows the tightness of the lattice thermodynamic equilibrium - a consequence of small mean free path and effective collisionality at the lattice sites.

By simulating certain standard fluid dynamics experiments, such as flow between parallel plates and flow past a circular cylinder, where quantitative comparison of various flow properties with experimental results is possible, we demonstrate the second reason that the algorithm behaves accurately; the mean dynamics are independent of the high shot noise fluctuations. The pipe flow simulations demonstrate the development of the analytically calculable equilibrium parabolic profiles in the mean, despite the fact that the mean velocity signal was a small fraction of the velocity fluctuations from time-step to time-step. Also using pipe flow, we demonstrate that the force imparted to the walls by the fluid is equivalent to the stress transmitted by the pressure drop down the length of the pipe. This allows two independent calculations of the flow kinematic viscosity which can be com-

[2]See Chapter 3

pared with another independent measurement using the decay of a shear wave in an open system. We demonstrate that all three of these measurements agree with each other within 1% for systems with the same density and temperature.

The cylinder flow experiments tests the ability of the lattice gas model to reproduce very complex flow behaviour in a regime where analytical calculation is not possible for the most part, which it does accurately in the mean. The only important parameter in flows which are effectively incompressible is the Reynolds number, Re. We examine the flow around a circular cylinder as Re is increased from zero to about $Re = 65$ where many interesting and complex phenomena occur. In this range, recirculating eddies become apparent behind the object at $Re \sim 5$ and then grow steadily with a characteristic length until $Re \sim 45$ where the eddies become unstable and start to shed with a characteristic frequency which, when expressed non-dimensionally, is known as the Strouhal number. This frequency then increases as Re increases. We find that the LGA code correctly reproduces this phenomena with measured drag coefficients and eddy lengths for the examined range of Re being in agreement with experimental observations within the error of those observations. This is in contrast with recent CFD results which do not match the observations within the experimental error[56]. In fact, the CFD results for eddy length are significantly in error, probably attributable to discretization errors in the non-linear Navier-Stokes equations which can not be completely eliminated.

7.1 Brief Description of the LGA Code

Before describing the results of simulations done by the LGA code, we briefly describe the code itself. For a thorough, subroutine by subroutine explanation of the code's workings, see the master's thesis by F. Mujica[54].

The flow of the LGA code can be grouped into three main sections, the intialization routines, the routines that update the lattice from time-step to time-step and form the 'engine' of the algorithm, and the output or visualization routines. The way these groups flow together is demonstrated in Figure 7.1. The key to making this algorithm efficient is the fact that the entire lattice gas engine may be reduced to logical operations, the basic language of digital computers. Instead of representing flow parameters like fluid density or velocity as floating point numbers at each lattice site, we represent particles as bits in a computer 'word'.

On the CRAY computer, the word length is 64 bits long. Thus with one integer number, we can represent 64 particles. In the three-speed lattice gas model, the state-space has 54 elements: 6 stopped particle sites, 24 energy=1 particle sites and 24 energy=2 particle sites, at each lattice site for which the elements may be numbered 1-6 for the stopped particles, etc. Thus, we could let a single CRAY word represent an entire lattice site with ten bits left over as overhead. Because all collisions only happen amongst particles *at a particular lattice site*, this data structure is convenient for dealing with collisions as each lattice word is independent in this process. In other words, the collision process is a highly parallel operation. On the other hand, moving the particles is a complicated process in this notation because each particle must move in a different 'direction' to a different word which requires a fairly complicated sequence of bit manipulations

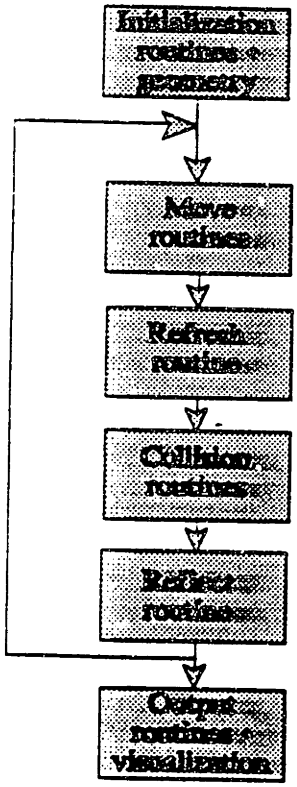

Figure 7.1: Flow chart demonstrating the interaction of the three groups of routines in the LGA code. The middle routines which are repeated once a time-step, form the 'engine' of the algorithm.

involving the state words of neighbouring sites.

Alternatively, we may think of each bit in a word as a different lattice site for a particular member of the state-space vector. With this structure, each 64 bit word represents a 3D subvolume of $4 \times 4 \times 4 = 64$ lattice sites in physical three-dimensional space. This means that for the three-speed model the complete state of this subvolume would be represented by a set of fifty-four 64-bit words. A particle is at a physical lattice site moving with a particular direction in the state-space if the bit corresponding to that site in the subvolume is turned on.

If the particle is not there, the bit is off. We then form the entire lattice out of as many subvolumes as the memory of the computer we are running LGA on permits.

The intialization routines set up the geometry on the entire lattice according to a user-specified function. Each subvolume has an additional word in the state-space vector that indicates whether the lattice sites of that subvolume are situated in the fluid or are part of some solid boundary, consistent with the user-specified geometry. Each of the bits in this additional word corresponds to a particular site in the subvolume. By setting the bits in this additional word, we can indicate whether a site is part of the fluid or is in a solid boundary. This information is needed to ensure that particles will not propagate through solid boundaries. Defining the way particles react when hitting a site marked as solid is how we set the boundary conditions in the LGA code. Once the geometry is set up, we proceed to seed all the lattice sites in a way that produces macroscopic flow properties such as density, temperature and flow velocity consistent with user-specified input parameters. This is done by seeding the particles with the probabilites equal to the equilibrium Fermi-Dirac distribution function calculated in Section 5.1. This ensures not only that the conserved quantities of mass, momentum and energy are as specified by the user, but that the Galilean invariant factor has been set to $g = 1$ as well. Since this is a Boolean system, the particle structure at any one site may be quite different from the theoretical distribution function. But, if we to were seed many lattices and then average over all of them, the resulting lattice would have a site population that would converge to the theoretical density. This procedure is a lengthy process since we must choose a random number between 0 and 1 for every lattice site and every member of the state-space vector and turn that site on if this number is less than the theoretical probability for that site and

leave it off if the opposite is true. Since it is only done once at the beginning of the simulation, it is not part of the actual engine. At this time, we also create a series of words corresponding to the forward and backward masks that effect the energy exchange collisions and force $g = 1$. Again, each word represents a subvolume and each bit a lattice site. If both the forward and backward mask bit at a particular site has been turned on, energy exchange collisions will be allowed at that site. The mask bits are set with the theoretical probabilty as calculated in Section 5.1 using the same method as was done for seeding the particles themselves. These series of mask words are then shuffled around the lattice at each time step to allow each site to sample a different mask vector. Once again, the average mask value at any site will be very close to the theoretical value.

We denote the i^{th} member of the fifty-four state-space vector at a particular site with $n_i(\mathbf{x})$, some of whose bits are turned on to indicate the presence of particles at this site. All the particles in this subvolume move in the same direction by virtue of being part of the same word

$$n_i(\mathbf{x}) \rightarrow n_i(\mathbf{x} + \mathbf{c}_i) \tag{7.1}$$

where $1 \times \mathbf{c}_i$ is the distance the particles moving in direction i move in one time-step. As a result, unlike the word-per-site data structure, the word-per-state structure allows the move operation to be done in parallel for many different sites and subvolumes. The only complication is moving particles from one subvolume to the next but this is a straightforward sequence of buffering and rotations which is done only on the surface area of the subvolume, rather than throughout the whole subvolume. We move particles in each direction, $+x, -x, +y, -y, +z, -z$, in turn, only moving the state-space vectors that have a component in the direction into which we are currently moving. The underlying lattice is the 4D FCHC lattice,

necessary for an isotropic stress tensor in three dimensions. Although each vector of the state-space may or may not have a component of velocity in the fourth direction, we only move particles in the first three. This corresponds to taking the three-dimensional projection of the four-D lattice, as described in Section 2.2.

We now describe the collision algorithm employed in the code. The theory considered in Chapter 2, utilized a collision function for the binary algorithm based on the binary function, $\xi_{ss'}$, which explicitly states the transition probabilty for any b-length state vector to any other b-length state vector. With $b = 54$ in our case, the literal implementation of this procedure would be a lookup table consisting of $(2^{54})^2 > 10^{32}$ elements! This is clearly unfeasible for any useful applications and is the main reason why most researchers in the lattice gas field have shied away from multiple-speed models[13, 11, 14]. Instead we will implement the collision function using a logical series of operations on the particles in which elemental collision types are called in sequence to accumulate a total state change.

Each collision is a binary collision occuring between two sets of paired particles taken from the state vector. If we denote this quadruplet as (i, j, k, l), where each letter represents some particular element of the 54 element state-space, this collision checks to see if particles i and j can collide to form output vectors in states k and l. We also check the inverse of this; k and l going to i and j. Of the over 8 000 000 possible quadruplets that can be chosen from fifty-four items, only 408[57] of these are unique collisions for which the input state is different from the output state *and* mass, momentum and energy are conserved by the collision on the FCHC lattice. This is now a manageable number which can be explicitly written out in the code and cycled through. In fact, there may be several realizations of this set in different order and at any time-step we choose one of

the realizations to use so as to randomize the collision sequence. Of these 408 collisions, 276 were chosen to implement into the code. It was determined that these 276 did just as good a job in colliding all the bits as the complete set of 408[58]. Let (i,j,k,l) be one of these 276 allowable collision where, for now, we stipulate that it is not an energy exchange collision. Thus all of the particles are either of energy=1 or energy=2. It is possible to outline the collision procedure completely in logic. We define the annihilation operator for particle i, A_i, and the creation operator for particle i, C_i, as

$$A_i = n_i \cdot n_j \cdot \overline{n_k} \cdot \overline{n_l} \tag{7.2}$$

$$C_i = \overline{n_i} \cdot \overline{n_j} \cdot n_k \cdot n_l \tag{7.3}$$

which state that a particle in state i will be annihilated by the above collision if both input particles are present and the two output states are empty (so that the forward collision can occur) and that a particle in state i will be created if itself and site j are empty with the other two sites occupied (the reverse collision). The dot indicates the logical AND operation while the overbar indicates the NOT operation. The collision operation can be represented as

$$\begin{aligned} n_i(t+\epsilon) &= n_i \cdot \overline{A_i} + \overline{n_i} \cdot C_i \\ &= n_i \cdot \overline{A_i} + C_i. \end{aligned} \tag{7.4}$$

This equation has a simple physical interpretation which can be read as follows. A bit is set after collision if it is set prior to collision and not annihilated or if it is not set before collision and created. All possible collisions can be described in this manner. Equation (7.4) can be written compactly,

$$n_i(t+\epsilon) = (A + C) \oplus n_i \tag{7.5}$$

where i now indicates any of the four particles in the quadruplet and the i subscript has been dropped from the A and C operators because they are the same for all four particles, as defined in eqns. (7.2) and (7.3). The logical operator '$\oplus$' is an 'exclusive or', the behaviour of which is described in Table 7.1.

X	Y	X $\oplus$ Y
T	T	F
T	F	T
F	T	T
F	F	F

Table 7.1: All possible outputs of the exclusive-or operator, $\oplus$, for given inputs.

To apply a collision rule, we perform the logic expression eqn. (7.5), using four 64-bit *words*. Thus, a single rule application updates sixty-four sites at once, again exhibiting a form of parallelism that can be utilized in the LGA code.

Because conventional computer processors provide word-oriented logical operations, the word-per-state representation is much more efficient on these machines when compared to the bit manipulation implied by the word-per-site representation.

If the collision quadruplet involves an energy exchange collision where the forward collision is masked by the Boolean variable F^j and the reverse collision by I^j, as introduced in Section 2.3.2, we simply tack them onto the definitions of the annihilation and creation operators. For example, in the three-speed model we are examining we have associated the masks with the stopped particle distribution.

Therefore, for an energy exchange collision we have

$$A = F^0 \cdot n_0 \cdot n_{2i} \cdot \bar{n}_{1i} \cdot \bar{n}_{1i+1} \tag{7.6}$$

$$C = I^0 \cdot n_{1i} \cdot n_{1i+1} \cdot \bar{n}_0 \cdot \bar{n}_{2i} \tag{7.7}$$

where i now indicates a direction within a particular energy. We now use eqn. (7.5) as before to update all four sites involved in the collision. The only difference between mono-energy collisions and energy exchange collisions is that the quadruplets associated with energy exchange have two extra words, corresponding to forward and backward masks, associated with them. The complete collision routine amounts to cycling through some order of the 276 collisions for each subvolume in the lattice, using eqn.(7.5) to update all sites. Because the collision operator is absolutely site independent, it is completely parallel and requires no interprocessor communication.

The only other collision process that may occur is when a particle collides with a solid boundary. In the real world, no matter how machined and polished an interface may be, at the microscopic level the boundary appears irregular so that incident particles bounce back in a seemingly random fashion. Since the lattice gas algorithm has neither the continuum of the fluid or the atomic scale resolution of the microscopic world, rules need to be created to define the way lattice particles will interact with solid matter. We of course require that the boundary does not create or destroy particles and that particles cannot propagate through the boundary. A further requirement is that for stationary boundaries, we require that the fluid velocity at the boundary be zero. An easy way to do this is to invoke a boundary 'bounce-back' rule. That is, particles that arrive at a site marked as a solid point simply reverse their direction. This operation can also be coded in logic and is facilitated by ordering the 54-element state vector in such a

way that parity directions are always a constant distance away from each other in the numbering scheme. This will clearly force the velocity at the boundary to be zero if we average over the before and after collision states.

In our simulations, we took a number of measurements, such as drag force, right on the surface of an object, in order to give us information about the bulk flow. This implicitly assumes that the behaviour of the fluid in the boundary layer is still hydrodynamic. However, it is known that near a solid-fluid interface there may exist a thin layer, with thickness on the order of the mean free path, in which the steady state is different from the bulk state[32]. This layer is known as the Knudsen layer and requires kinetic theory rather than hydrodynamics to describe it. If this were the case in our lattice gas algorithm, measurements near the wall would not be a good indication of bulk flow properties. Fortunately, it has been shown by Cornubert et al.[59] that reflection rules that combine bounce-back and specular reflection in any combination (which includes only bounce-back) do not build any Knudsen layer near the wall. While this result was done on the 2D FHP lattice, they suggest that it can be generalized to other lattices and we in fact, find it to be the case since we have found experimentally that measurements at the wall of the model do accurately describe bulk flow behaviour (for example, in Section 7.3 we compare the measurement of the force at the wall in a flow between two parallel plates to the force derived from the pressure drop down the length of the pipe and find them to agree to better than 1%).

The final routine that is performed every time step is the so-called 'refresh' routine. What this routine does is to update the boundaries of the physical lattice space. In some simulations, we may want all particles to wrap around toroidally[3]

[3]particles leaving one side of the lattice reappear at the opposite side, i.e. a particle exiting

so that the refresh routine does nothing. In other cases we may allow wrap-around on two sets of boundaries, top and bottom perhaps, and specify the boundary flow at the left and right boundaries. This situation is necessary if we wish to attain a steady flow in lattices that contain objects so that there is a pressure drop across the object. If we simply allow wrap-around, the flow will continuously lose momentum as it passes by the object and a steady-state will never be reached. If we continually replace the left- and right-most edges of the lattice with a particular flow , much the same way the end conditions in a wind tunnel are set by a fan at one end and suction at the other. we can acquire a steady-state situation. This is the way lattice-gas 'boundary conditions' are employed and again is in sharp contrast with differential equation methods that require macroscopic conditions at the boundaries. We will have more to say about lattice gas boundary conditions in the coming Sections but suffice it to say that the refresh routine simply, once a time step, replaces edges of the lattice that we do not want to toroidally wrap with some user-specified distribution function in order to attain a steady-state flow in the finite lattice volume.

The final step in the entire algorithm, a step that can be moved out of the lattice engine process if we accumulate particle statistices time- step to time-step, is the calculation of macroscopic properties of the flow and visualization thereof. At any site, the local value of fluid density, momentum, or any other macroscopic flow variable can be calculated by taking appropriate moments of the microscopic distribution. For example

$$\rho(\mathbf{x}) \;=\; \sum_{i=1}^{54} n_i(\mathbf{x})$$

---

from the top reappears at the bottom travelling upwards

$$\rho \mathbf{u}(\mathbf{x}) = \sum_{i=1}^{54} \mathbf{c}_i n_i(\mathbf{x}) \tag{7.8}$$

$$\mathbf{S} = \sum_{i=1}^{54} \mathbf{c}_i \mathbf{c}_i n_i(\mathbf{x})$$

calculates the local values of density, momentum and the stress tensor respectively accumulated over an *subvolume*. We would have to divide by the size of the subvolume (64 sites) if we wished to get an average quantity per lattice site. Note that the sum over the Boolean variables involves counting the number of bits that are 'on' in each word, not the integer sum of their values. This operation, usually denoted as a 'popcount' is a standard operation on computers that allow word-oriented logical operations, such as the CRAY. The macroscopic variables calculated above can then be averaged over space and time and displayed using a graphics package. It is the instantaneous values of these quantities that may be very noisy but whose mean we have proved follows the correct mean dynamics (Chapter 6).

7.2 Validation of Artifact Removal

In this Section we demonstrate that the three-speed lattice gas model with one rate coefficient for energy exchange collisions can remove the Galilean invariance artifact, g, which also removes the pressure anomaly, if the average rate coefficient equals the value calculated in eqn. (5.12) of Section 5.1. We do this by examining the relaxation of a shear wave with transverse velocity in an open system. That is, we seed the system with a particular density and temperature and an initial velocity field given by

$$\mathbf{u}_0(\mathbf{x}, t = 0) = u_T \mathbf{e}_y + u_L \sin(k\, y) \mathbf{e}_x \tag{7.9}$$

where k is the wavenumber of the perturbation. Having a non-zero streaming speed in the direction of the perturbation will allow g to be measured directly from the evolution of the perturbation. There is no flow velocity in the z direction. The evolution of this perturbation in time is given by the lattice Navier-Stokes equation,

$$\frac{\partial}{\partial t}\mathbf{u} + g\mathbf{u}\cdot\nabla\mathbf{u} = \nu\nabla^2\mathbf{u} \tag{7.10}$$

for incompressible, constant density and temperature flows. This equation comes from taking the momentum moment of the expansion of the lattice kinetic equation, eqn. (2.32), to second order in the small Knudsen number, κ. This quantity is the ratio of the mean free path to a relevant physical scale length and must be small for a valid transport theory to occur. The first order in κ term of the expansion gives the momentum Euler equation, eqn. (3.22). The left-side of eqn. (7.10) is simply this equation simplified for the incompressible, no pressure gradient open system we are using. The right-hand side shows the viscosity term resulting from the second-order expansion term. This term appears in a manner identical to the hydrodynamic incompressible viscosity term but the viscosity for the lattice model contains two contributions, the usual viscosity due to collisions and shear and another term due to the lattice itself - the so-called lattice viscosity. The sum of these two contributions can be shown to be positive-definite so that the total viscosity is always positive. All of the above results concerning the viscosity term in the lattice gas transport equations can be found in the work of Molvig et al.[39].

The solution for this equation with the initial conditions eqn. (7.9) can be calculated analytically by assuming that the spatial dependence of the solution is the same as the intial conditions and that only the magnitude of the velocity

changes. The solution is

$$\mathbf{u}(\mathbf{x},t) = u_T \mathbf{e}_y + u_L e^{-iku_T gt - \nu k^2 t} \sin(k\,y)\mathbf{e}_x \tag{7.11}$$

where we see that the time evolution of the phase and modulus of $\mathbf{u}(t)$ directly measure the g-factor and the kinematic viscosity ν. The presence of viscosity in the flow causes the shear to be destroyed. Eventually only the transverse flow remains.

Simulations were run on a $64 \times 64 \times 64$ lattice[4] for various values of density and temperature at low Mach number and for a low wavenumber perturbation. The values of g and ν were measured from the decay of the magnitude of the x-component of velocity. The robustness of the theory was tested by examining higher Mach number and perturbation wavenumber flows and noting when the algorithm was no longer able to keep $g = 1$. As a test of the validity of the H-Theorem derived for this lattice gas model in Section 2.4, some simulations were seeded with a distribution different from the derived equilibrium, eqn. (2.31). Such a system quickly alterred itself to the correct equilibrium in a few time steps which demonstrated the strong tendency of the model towards an unique H-Theorem based equilibrium state. Since we will be measuring the decay of the flow from $t = 0$ in these experiments, it is important that the intial relaxation phase is hydrodynamic and so we need to seed the bits correctly at $t = 0$. When seeded correctly, the total species populations remained constant to within the shot noise fluctuations during the decay[5].

[4]This required $54 * 64^2$ 64-bit CRAY words to represent the whole state-space

[5]Of course, TOTAL particle number, momentum and energy remained constant throughout the simulation

7.2.1 Galilean Invariance and Absence of Pressure Anomaly

These basic validation runs were done with $u_T = u_L = 0.1$ and a wavenumber of k= $2\pi/64$ which corresponds to one wavelength of the perturbation exactly fitting into the lattice volume. All macroscopic flow velocities are in units of number of lattice sites travelled per time step where a time step is the time required to update the entire state-space volume. The component of momentum in the x-direction was measured at every time step using eqn. (7.8) and then averaged over the y- and z- directions to reduce noise. This signal was then fourier transformed and the component with wavenumber k was extracted, all other fourier components being noise. This result was divided by u_L and then the phase and modulus of the remainder was calculated. When this was done for a large number of time steps, but smaller than the number of time steps it took for the perturbation to decay to noise after which there is no further decay, the slope of the modulus as a function of time was equal to to $-\nu k^2$ while the slope of the phase evolution was equal to gku_T. Since k and u_T are input parameters, it was possible to calculate g and ν from these slopes.

Representative plots of the phase and modulus for the first 500 time steps after perturbation for a run where the average number of particles per site was $\rho = 8$ and the temperature variable was $z = 5$ are shown in Figures 7.2 and 7.3 where the g factor and viscosity, ν can be measured respectively. A fit to the curves are shown but the accuracy of the model in reproducing the predicted linear decay makes the fluctuations almost imperceptible.

Observation of the exponential time dependence for the decay of both the modulus and phase of this perturbation is a good indicator of genuine hydrodynamic behaviour. Very small modifications to the microscopic rules, such as

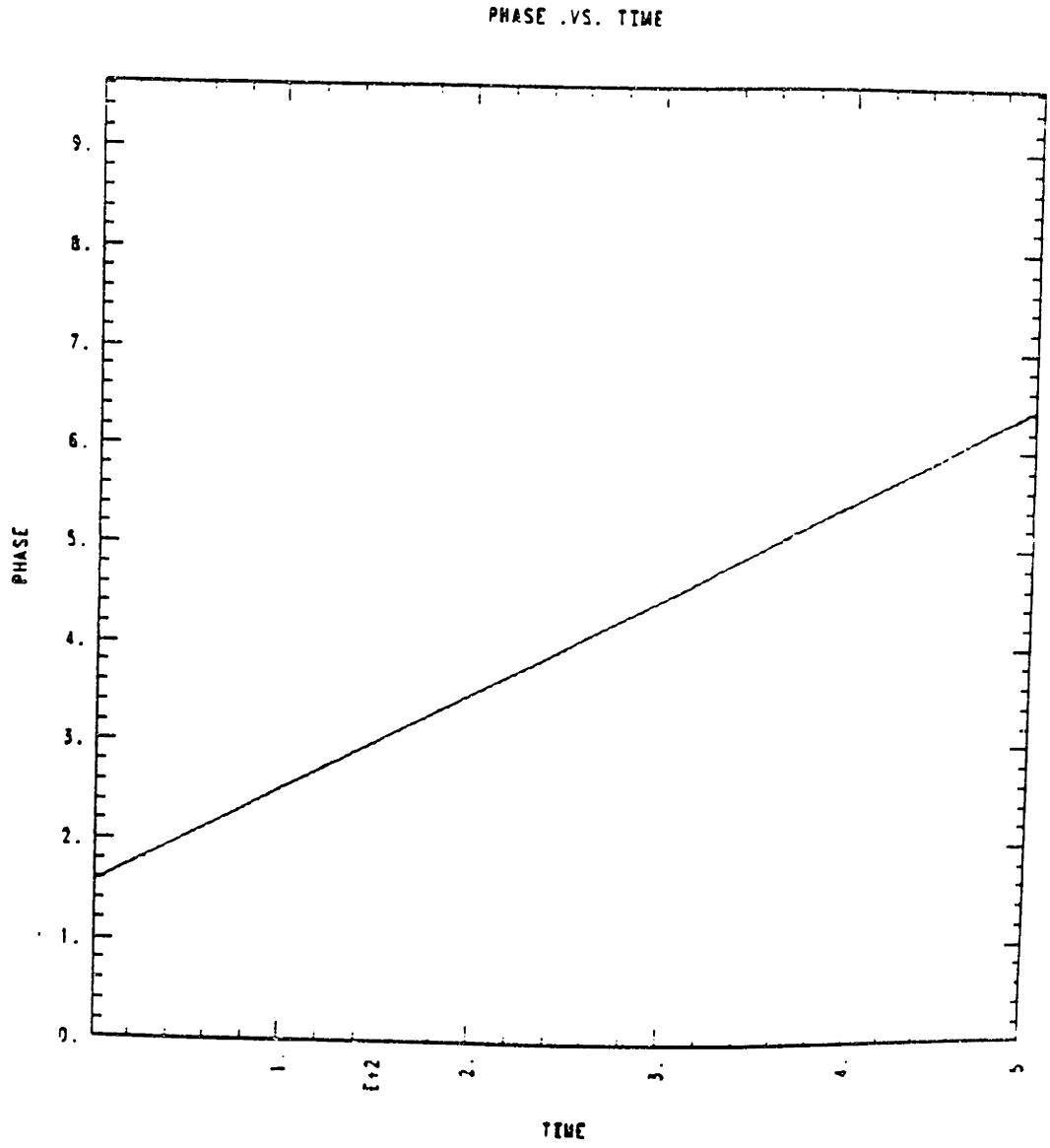

Figure 7.2: Phase of a decaying shear wave as a function of time for the case z=5, ρ=8. The slope of this line is equal to ku_Tg where $k = \frac{2\pi}{64}$ is the wavenumber and $u_T = .1$ the transverse velocity. A best fit to the slope results in the measurement $g = 1.006 \pm 0.005$

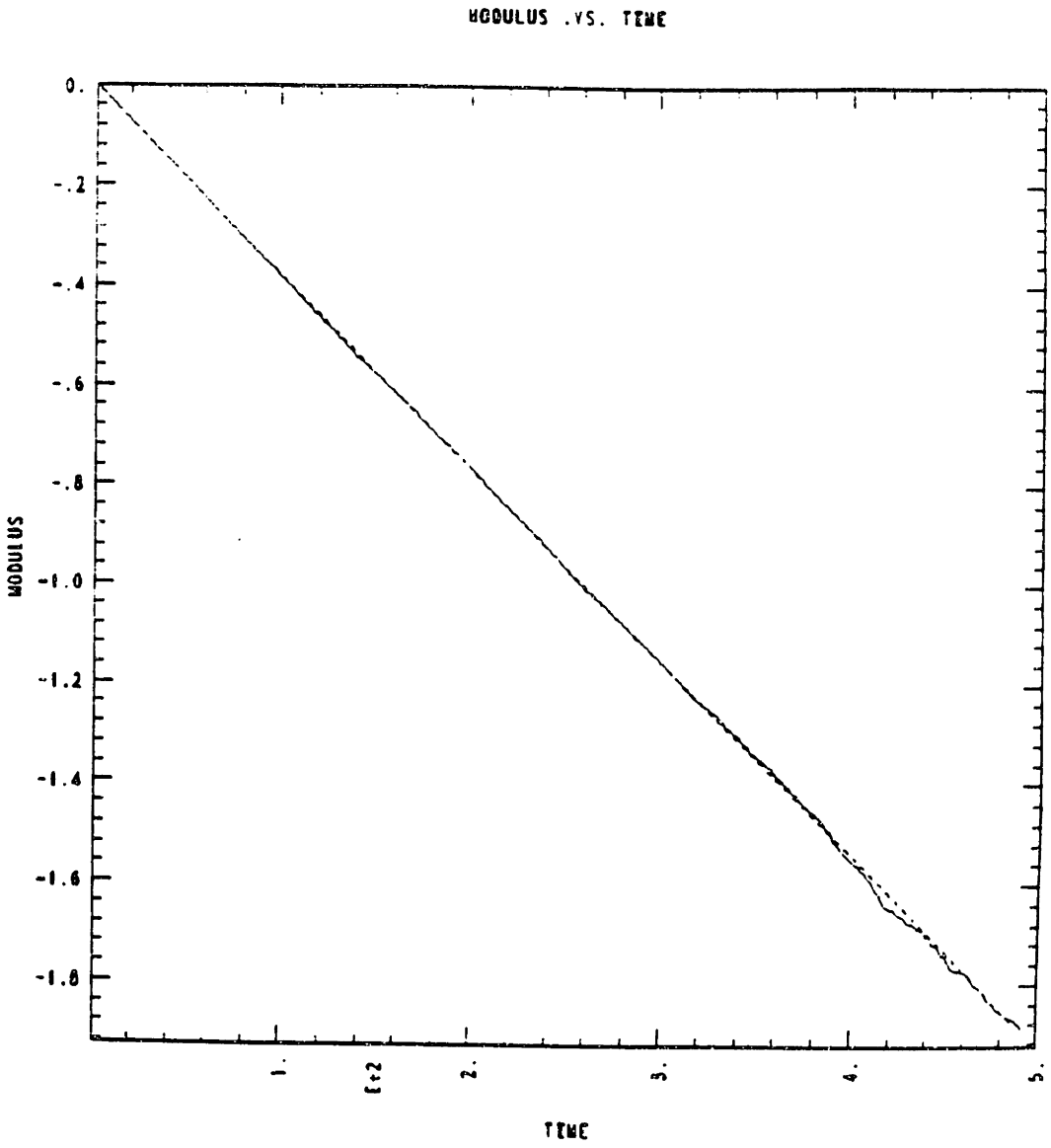

Figure 7.3: Modulus of a decaying shear wave as a function of time for the same run as in Figure 7.2. As predicted theoretically, the modulus decay is linear, corresponding to exponential decrease of the velocity amplitude from which the viscosity was measured. A best fit to the slope gives $\nu = 0.330 \pm .003$. Note that for $t > 380$, the phase becomes ragged indicating that the noise level has nearly been reached.

allowing particles to be created or destroyed, will destroy this characteristic time dependence. The results of calculating the Galilean factor, g, in this manner for a series of density and temperatures are collected in Table 7.2. We see that $g = 1$ to within 1% or better in all of these runs.

Similarly, we can demonstrate the absence of the pressure anomaly by calculating the stress tensor using eqns. (7.8). The value of the lattice stress tensor is given by eqn. (3.21)

$$\mathbf{S} = \frac{2}{D}\Big[U_p + \tfrac{1}{2}\rho u^2(1-g)\Big]\mathbf{I} + g\rho\mathbf{uu} \tag{7.12}$$

where the extra portion of the isotropic pressure proportional to the hydrodynamic flow energy $\frac{1}{2}\rho u^2$ is the pressure anomaly. If $g = 1$, the lattice stress becomes $\mathbf{S} = \frac{2}{D}U_p\mathbf{I} + \rho\mathbf{uu}$, the correct hydrodynamic expression. We calculate the component of the stress tensor S_{xx}, the momentum vector $\rho\mathbf{u}$, the total energy, U[6], and the density, ρ from the microscopic distribution. We calculate the flow energy using

$$\frac{1}{2}\rho u^2 = \frac{\rho\mathbf{u}\cdot\rho\mathbf{u}}{2\rho} \tag{7.13}$$

and then U_p from

$$U_p = U - \frac{1}{2}\rho u^2. \tag{7.14}$$

Subtracting this from S_{xx}, using eqn. (7.12), gives

$$S_{xx} - \frac{2}{D}U_p = g\rho u_x u_x + \frac{1}{D}\rho u^2(1-g) \tag{7.15}$$

where $D = 4$ for the FCHC lattice. If $g = 1$ then $S_{xx} - \frac{2}{D}U_p = \rho u_x u_x$, the same result as in hydrodynamics. We compare the volume averaged measurement in eqn. (7.15) with the volume averaged theoretical result for $\rho u_x u_x$ from eqn. (7.11)

[6] $U = \sum_{i=1}^{64} \epsilon_i n_i(\mathbf{x})$.

ρ	z	g ± 0.005	Pressure Anomaly	$\frac{1}{2}\rho u^2$	RMS Press. Fluc.	Shot Noise Level
5	2	1.012	0.026×10^{-2}	5.0×10^{-2}	0.30×10^{-2}	0.29×10^{-2}
5	5	0.988	0.006	5.0	0.27	0.29
5	8	1.003	0.024	5.0	0.25	0.29
8	2	1.000	0.035	8.0	0.35	0.36
8	5	1.006	0.004	8.0	0.31	0.36
8	8	1.001	0.018	8.0	0.28	0.36
10	2	1.004	0.005	10	0.39	0.39
10	5	0.992	0.020	10	0.33	0.39
10	8	0.995	0.025	10	0.30	0.39
12	2	1.005	0.051	12	0.40	0.42
12	5	1.001	0.043	12	0.37	0.42
12	8	1.005	0.017	12	0.32	0.42

Table 7.2: Measured values of the Galilean invariance factor g and the pressure anomaly for various densities, ρ, and temperatures, z using $k = \frac{2\pi}{64}$, $u_T = u_L = 0.1$. For all of the runs we find that $g = 1$ to better than 1% and that the pressure anomaly is much smaller than the dynamic pressure. In fact, the RMS fluctuations in the pressure anomaly is at the same level as the shot noise.

over time. Of course, if we average u_x over volume we get zero due to the sinusoidal dependence of u_x. Instead we calculate $(\rho u_x)^2/\rho$ at each site and then average this quantity. Doing this, we get a factor of $\frac{1}{2}$ from the volume averaged value of $\sin^2(k\,y)$ so that the theoretical result for the advected term is

$$\langle \rho u_x u_x \rangle = \frac{1}{2}\rho u_L^2 \exp(-2\nu k^2 t). \tag{7.16}$$

In Figure 7.4, we compare the theoretical value of $\rho u_x u_x$ to the measured value of $S_{xx} - \frac{2}{D}U_p$ for the case $\rho = 8$ and $z = 5$ with $u_T = u_L = .1$ as before. We see that the theoretical term, illustrated by the dotted line, delineates the mean of the fluctuations in the measured quantity precisely which clearly demonstrates the absence of any anomalous pressure term. At $t = 0$, $\rho u_x u_x = \frac{1}{2}\rho u_L^2 = 0.04$ for this case, which the measured value agrees with. If we now subtract $\rho u_x u_x$ from the $S_{xx} - \frac{2}{D}U_p$ measurement as shown in eqn. (7.15) only terms proportional to $(g - 1)$ remain. With $g = 1$, as we have forced, this residual pressure anomaly should be no more than noise. The rest of the columns in Table 7.2 illustrate that this is true in our simulations. The residual pressure anomalies were accumulated for the first 500 time steps and then averaged to get the value in the Table. The residual pressure anomaly is less than .2% of the dynamical flow energy, $\frac{1}{2}\rho u^2$, while the root mean square fluctuations of the residual pressure values are essentially equivalent to the shot noise we expect in the $\rho u_x u_x$ measurement. The shot noise for Boolean variables is known, as shown in Section 6.2, to have the value $\sqrt{\langle \delta n_i^2 \rangle} = \sqrt{\langle n_i \rangle (1 - \langle n_i \rangle)}$. The density is a Boolean variable with a mean value of ρ divided by the state-space size, in this case fifty-four. Thus, the shot noise level, SNL, is

$$SNL \sim u^2 \frac{\sqrt{\rho(54 - \rho)}}{54} \tag{7.17}$$

and if we plug in $u = .1$ and $\rho = 5$ we get $SNL \sim .0029$ as shown in Table 7.2.

The other components of the stress tensor were likewise examined and they all also displayed the predicted, hydrodynamic behaviour.

In contrast to the correct hydrodynamic behaviour of the multiple-speed model, when we ran the LGA code as a single-speed code [7] for the shear wave problem and performed the same comparison of $S_{xx} - \frac{2}{D}U_p$ (where now $U_p = \rho$ in the single-speed case) with $\rho u_x u_x$ we find a pressure anomaly far in excess of the noise fluctuations, as demonstrated in Figure 7.5. That this must be so can be shown by subtracting the required isotropic pressure, $\frac{2}{D}U_p$ from the lattice stress tensor, eqn. (3.21) using the single speed P_s expression. eqn. (3.23) so that

$$S_{xx} - \frac{2}{D}U_p = g\rho(u_x^2 + \frac{1}{D}u^2) \tag{7.18}$$

which is always non-zero for a flow with non-zero flow velocity.

7.2.2 Viscosity Measurements

We also measured the kinematic viscosity in this series of measurements, an example of which is shown in Figure 7.3. The values of the measured kinematic viscosity for the series of runs shown in Table 7.2 are shown in Table 7.3. The temperature variable z is related to the actual system temperature inversely in the three-speed model, see Figure (5.14). We see that as the temperature is increased (z is decreased) the kinematic viscosity also increases which is the same trend observed for gases such as air. Furthermore, the density dependence of the viscosity measurements, illustrated graphically in Figure 7.6, also demonstrates the correct behaviour for gases with kinematic viscosity decreasing monotonically as

[7] by not seeding any particles in the energy=0 or =2 states and removing energy exchanging collisions from the collision rule list

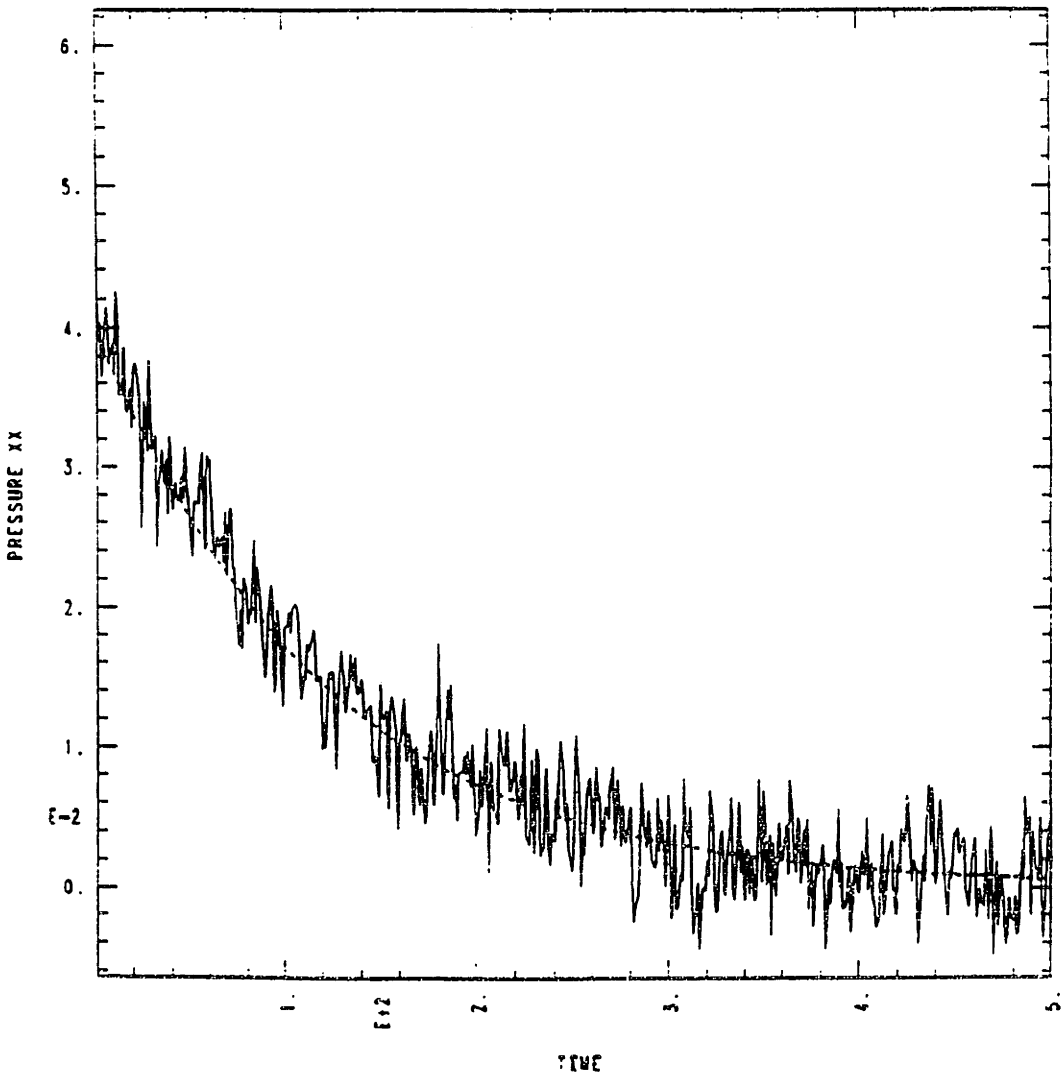

Figure 7.4: Stress component, $S_{xx} - \frac{2}{D}U_p$ compared to $\rho u_x u_x$ for the multi-speed case. The equivalence of these two quantities demonstrates that $g = 1$ and that there is no anomalous pressure contribution. Same run as in Figure 7.2.

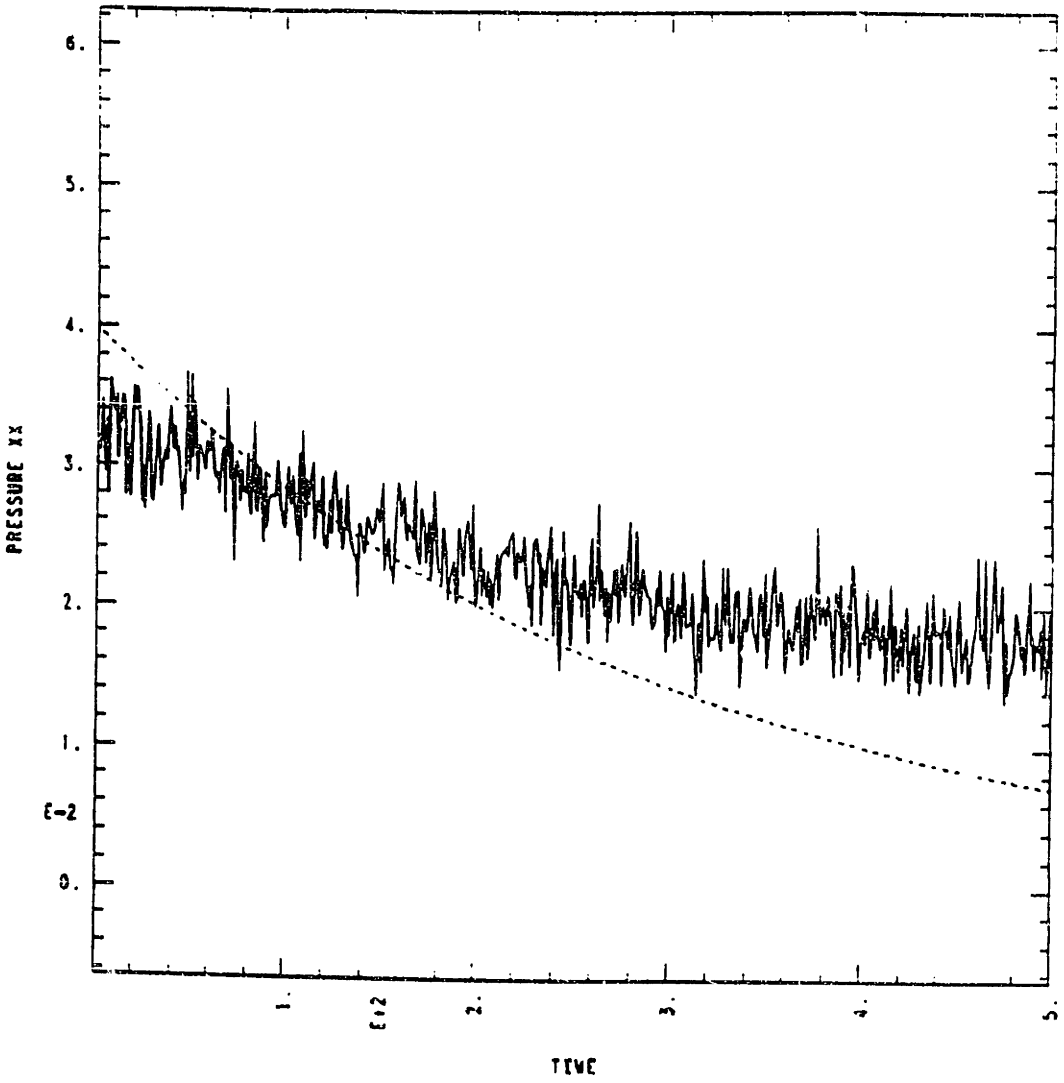

Figure 7.5: Stress component, $S_{xx} - \frac{2}{D}U_p$ compared to $\rho u_x u_x$ for the single-speed case showing the anomalous pressure contribution as in eqn. (7.18). Parameters have the same values as the run in Figure 7.2.

f	z	Kinematic Viscosity ± 0.003	$R^* = c_s/\nu$
0.208	2	0.502	1.72
0.208	5	0.450	1.78
0.208	8	0.422	1.84
0.333	2	0.376	2.30
0.333	5	0.330	2.43
0.333	8	0.311	2.49
0.417	2	0.340	2.55
0.417	5	0.299	2.68
0.417	8	0.285	2.72
0.5	2	0.341	2.54
0.5	5	0.281	2.85
0.5	8	0.275	2.54

Table 7.3: Measured values of the kinematic viscosity, ν for various densities, ρ, and temperatures, z using $k = \frac{2\pi}{64}$, $u_T = u_L = 0.1$. We observe that viscosity increases with temperature and decreases with density, as it does in a real gas (the temperature variable z is inversely related to the temperature T). The quantity R^* is the lattice local Reynolds number while the sound speed is $c_s = \sqrt{\gamma \frac{P}{\rho}} \simeq \sqrt{\frac{3}{2}\frac{P_s}{\rho}}$.

the density is increased. Best-fitting a relationship to the viscosity-density curve at $z = 5$ results in

$$\nu_{obs.}(f, z = 5) \simeq \frac{1.1}{\rho^{.55}} \tag{7.19}$$

essentially an inverse square root relationship. The kinematic viscosity of a fluid scales with collisional properties in the following way[16]

$$\nu \sim c_s \lambda \sim \frac{c_s^2}{\nu_c} \tag{7.20}$$

where c_s is the sound speed, λ is the mean free path and ν_c is the collisional frequency. In a lattice gas, the sound speed is of order 1 since particles, on average, move one lattice site per time step in the three-speed model. Equation (3.39) gave us an equation for the lattice gas sound speed when the energy equation artifacts have not been removed. From this equation, we find that for flows where the Mach number is small, the sound speed is given by $c_s \simeq \sqrt{\frac{\gamma P_s}{\rho}} = \sqrt{\gamma T}$, where the thermodynamic temperature is defined in the usual way, $P_s \equiv nT$ ($\rho = n$ since all particles have unit mass). The ratio of specific heats, γ, equals the correct ideal gas value to first order in the density (eqn. (5.19)) so that $c_s \simeq \sqrt{\frac{3}{2}T}$. Thus on an isotherm, the sound speed is constant and eqn. (7.20) states that the viscosity goes like $\nu \sim 1/\nu_c$. If we compare this with the observed dependence, eqn. (7.19), we find that

$$\nu_c \sim \rho^{\frac{1}{2}}. \tag{7.21}$$

This scaling happens to be the same behaviour we would expect in the shot noise of the Boolean variable density, eqn. (7.17) without the squared velocity term. The collision process reshuffles the particles at a lattice site by turning some bits 'on' and other bits 'off' while keeping the total density, momentum and energy at the site constant. This effectively causes fluctuations in the Boolean variables about the mean, the level of which is the known shot noise relation. Since higher

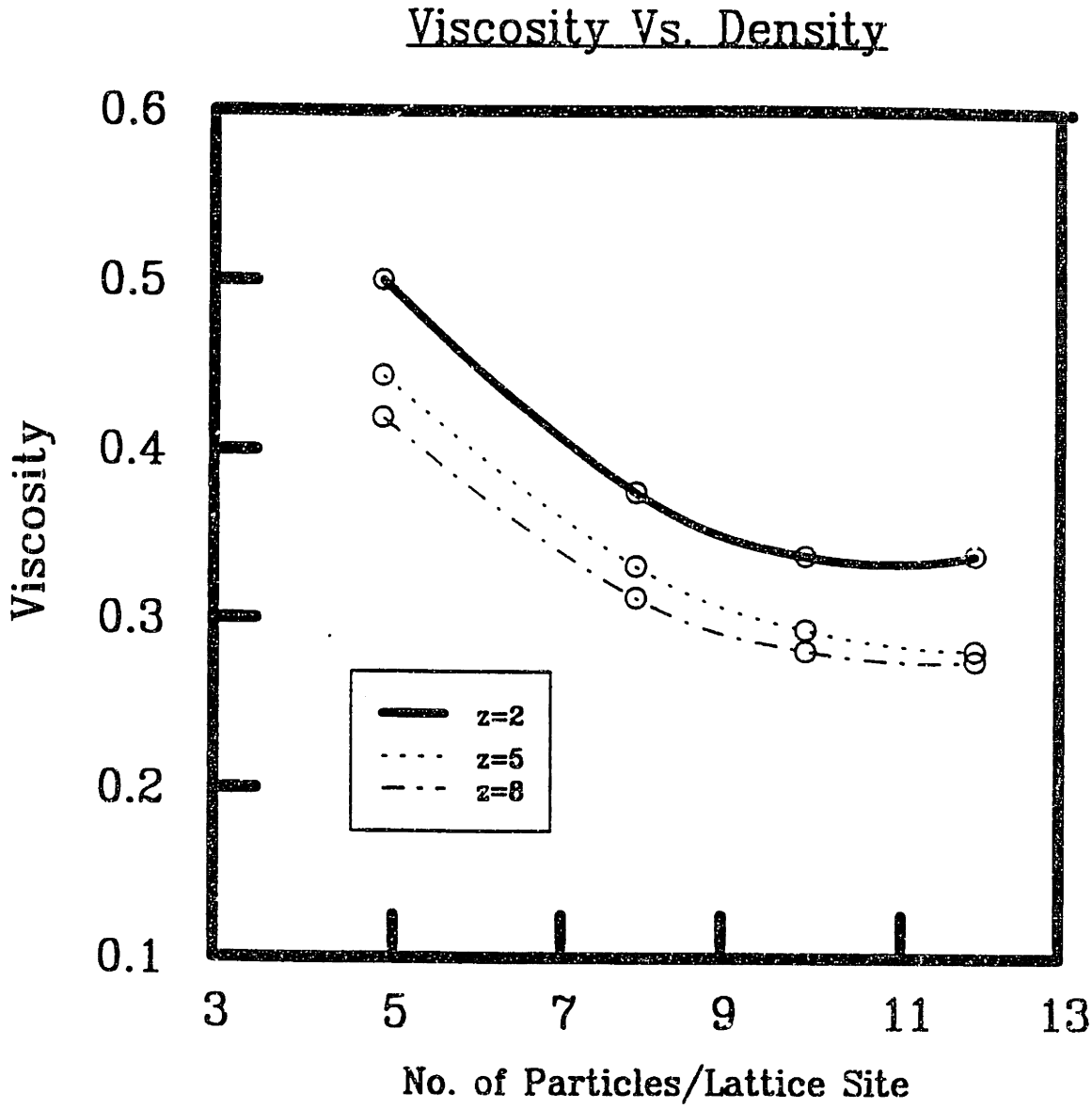

Figure 7.6: Measured value of kinematic viscosity as a function of density for a number of different temperatures. At $z = 5$, a best fit results in $\nu = \frac{1.1}{\rho \cdot 5T}$, essentially an inverse square root relationship.

densities mean more chance for a collision and hence higher collision frequency, more bits are shuffled in the process so that the collision frequency scales with density in the same way fluctuations scale. On the other hand, if the density becomes too large, then collisions are actually inhibited because hole sites are needed for a collision to occur. We see evidence of this in Figure 7.6 for the high z - low temperature flow where the viscosity has started to flatten out at high densities. At low temperatures most of the particles reside in the low speed sites which inhibits energy exchange collisions into or out of these energies.

The measured viscosity results also imply a further important property of lattice gases. From Table 7.3 we see that the measured viscosity is always less than 1. Since the sound speed is of order 1 we can use the viscosity scaling relationship eqn. (7.20) to deduce that the mean free path is also less than 1. This illustrates that the transport theory expansion is valid since $(\lambda/L) \ll 1$ and that a very tight equilibrium will be established since each lattice site will be in equilibrium with its neighbours.

As in a real fluid, the flow is completely characterized by the combination of flow parameters known as the Reynolds number where

$$Re = \frac{u\,L}{\nu} \tag{7.22}$$

where L is a characteristic length in terms of lattice spacings. Previous lattice gas treatments[14, 26] have rewritten this expression in terms of the Mach number, $M = \frac{u}{c_s}$ and a local model dependent Reynolds number so that

$$Re = M\,L R_n \tag{7.23}$$

where

$$R_n \equiv \frac{c_s g}{\nu} \tag{7.24}$$

and the Galilean artifact, g, is included in this definition. In our simulations, $g = 1$ so that $R_e = \frac{c_s}{\nu}$. The values of R_e shown in Table 7.3 establish contact with previous viscosity measurements on the FCHC lattice, specifically the one-speed measurements of Hénon[27] where he found that $R_e^{max} = 2$ for collisions chosen to preserve momentum using his so-called isometric algorithm. Our values of R_e are also in this range. It is desirable computationally to maximize the value of R_e to gain higher Reynolds numbers without having to increase resolution. To this end, improvement in this value for single-speed models has been made by choosing output states from a given input state in the collision process that minimizes viscosity. Using this technique, Hénon[60] later found that R_e could be improved to $R_e^{max} = 7.57$. Still later, Dubrulle *et al.*[38] experimented with the single-speed FCHC lattice model by adding rest-particles and attempted to maximize the Galilean g factor to raise R_e, eqn. (7.24), with the result that a value of $R_e^{max} = 13.5$ has been reported. While encouraging from a computational efficiency standpoint, these models still suffer from artifacts that make them unusable for accurate hydrodynamic experimentation. By adding rest-particles to their model, they have destroyed the semi-detailed balance condition that ensured a monotonic approach to equilibrium in the original single-speed model. Furthermore, by treating the Galilean factor as a free parameter that may be alterred to maximize R_e, rather than an artifact that must be removed by setting it to $g = 1$, they ensure that their model will continue to exhibit anomalous behaviour in comparison with actual fluid behaviour as predicted theoretically in Section 3.1 and shown experimentally in Section 7.2.1. The theory that Hénon developed for minimizing the viscosity in the single-speed case[26] has been generalized to multiple-speed models to some extent by Molvig *et al.*[39]. It appears that the viscosity minimization condition that appears in single-speed treatments does not

appear in such a straight-forward way in the multiple-speed case, making it difficult to create a set of optimal, viscosity minimizing collisions, in the multiple-speed case. Research in this area is ongoing.

Still, we have found experimentally that the set of 276 quadruplets that were chosen for the collsion operator in the three-speed model essentially minimized the attainable viscosity in our simulations. Using a longer string of collisions reduced the viscosity by only a few percent, making it not worth the additional computational effort to include them in the algorithm. The values of viscosity calculated here will be used in later simulations of flows around bluff objects.

7.2.3 Wavenumber Dependence – Scale Resolution

It is of interest to determine the wavenumber, or k, dependence of the phase and modulus in the decaying shear wave experiment. This has a bearing on the important issue of *scale resolution* in lattice gases. As the wavelengths approach the lattice spacing, one will lose hydrodynamic behavior, of course. The large k shear wave decay will show exactly how hydrodynamic behaviour is lost. This is one of the more demanding tests of small scale behaviour, since the free shear wave is unsupported by any driving effects and decays very rapidly at large k (for 16 period waves in the lattice volume, $k = 16 \times 2\pi/64$, the decay to noise takes less than 10 times steps for kinematic viscosity $\nu \sim .5$). Thus the time scale separation, between the phenomenon of collisional relaxation to local equilibrium and hydrodynamic behavior, is marginal at best. For eddies that are sustained against viscous decay by driving forces that increase the eddy lifetime, the accuracy of hydrodynamic behaviour would be much better.

We studied the k dependence by using a series of values of k in the intial seeding of the velocity shear field with $\rho = 8$, $z = 5$ and $u_T = u_L = 0.1$ as before. What the k dependence studies show, as reflected in Figs. (7.7) and (7.8) is that good hydrodynamic behavior of the shear wave persists up to normalized wavenumbers[8] of 16 (or 2 lattice sites per half wavelength). For larger k, there are not enough lattice points to represent even a crude approximation to a sine wave, and the behaviour observed is essentially that of noise. Notice, in particular, for the Galilean factor plotted in Fig. (7.7) that g remains essentially at unity up to $k = 16$, although the phase "signal" has become more noisy, making the slope measurement (and hence the value of g) more uncertain. An example of this is shown in the $k = 12$ phase plot of Figure (7.9). Note that the initial slope is very close to unity, but then drops off and starts to fluctuate rapidly as the amplitude approaches the shot noise level. The phase does begin to depart from the $g = 1$ line while the wave amplitude is still somewhat above the noise level. Comparisons with the spectrum of velocity fluctuations at other wavenumbers (not shown here) confirm this. This characteristic behaviour is seen in all the large k cases. We believe this departure from $g = 1$ behaviour is a failure to hold the equilibrium precisely at large k due to the weakness of the time scale separation. This would account for the correct behaviour initially since the equilibrium is properly seeded at this point. If the correct explanation, it also implies that either for increased collisionality (although it seems we have done about as best as we can in this area), or for slower evolution of the large k eddies (supported by driving effects) that the high k, small scale resolution would be improved.

[8] k / (2π /64)

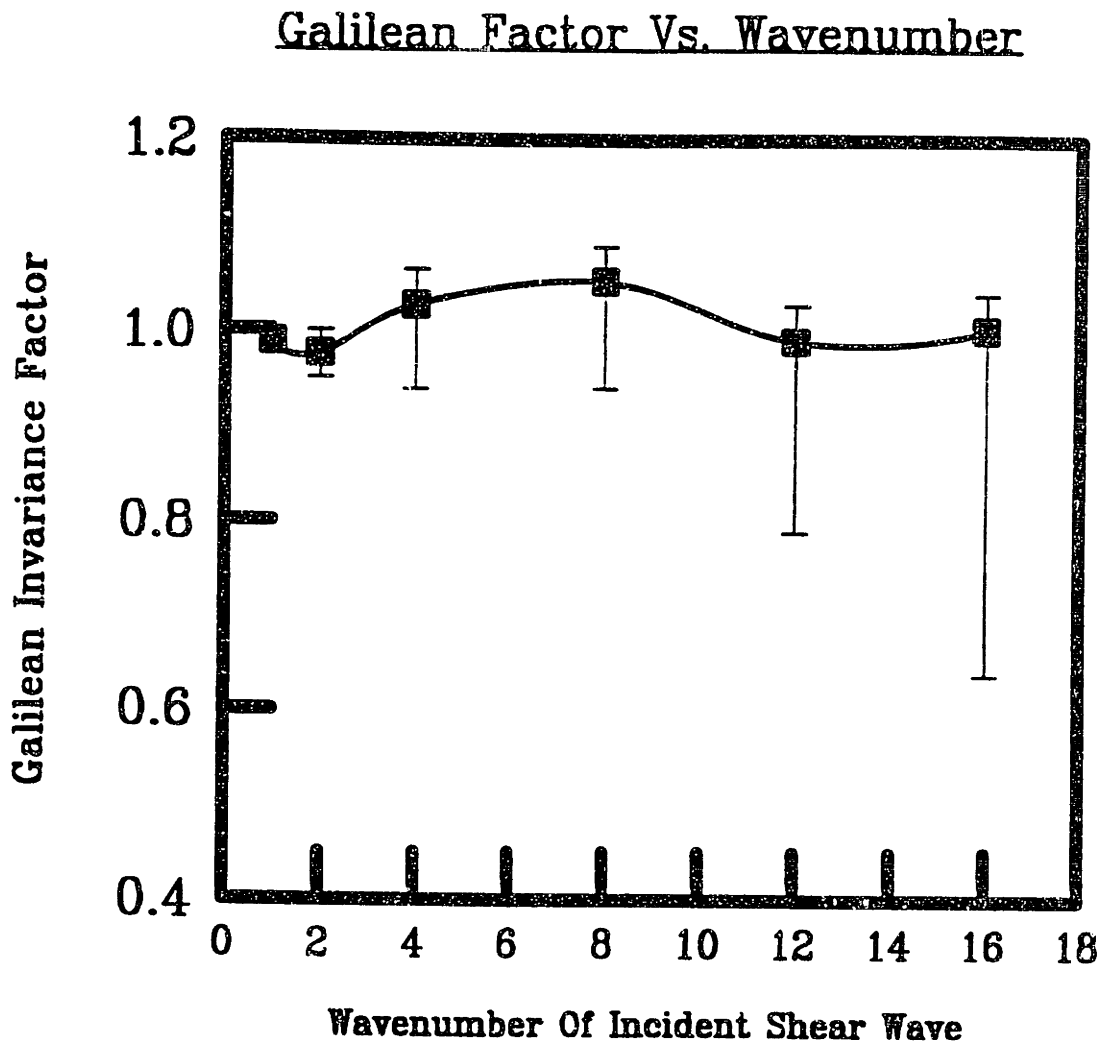

Figure 7.7: The value of g shown is calculated from the intial slope of the phase decay in the shear wave experiment for the case $z = 5, \rho = 8$. We see that Galilean invariance is being maintained intially, $g = 1$. despite the large uncertainities in the measurement (illustrated by the error bars) as the wavenumber increases causing the physical scale length to approach the lattice spacing.

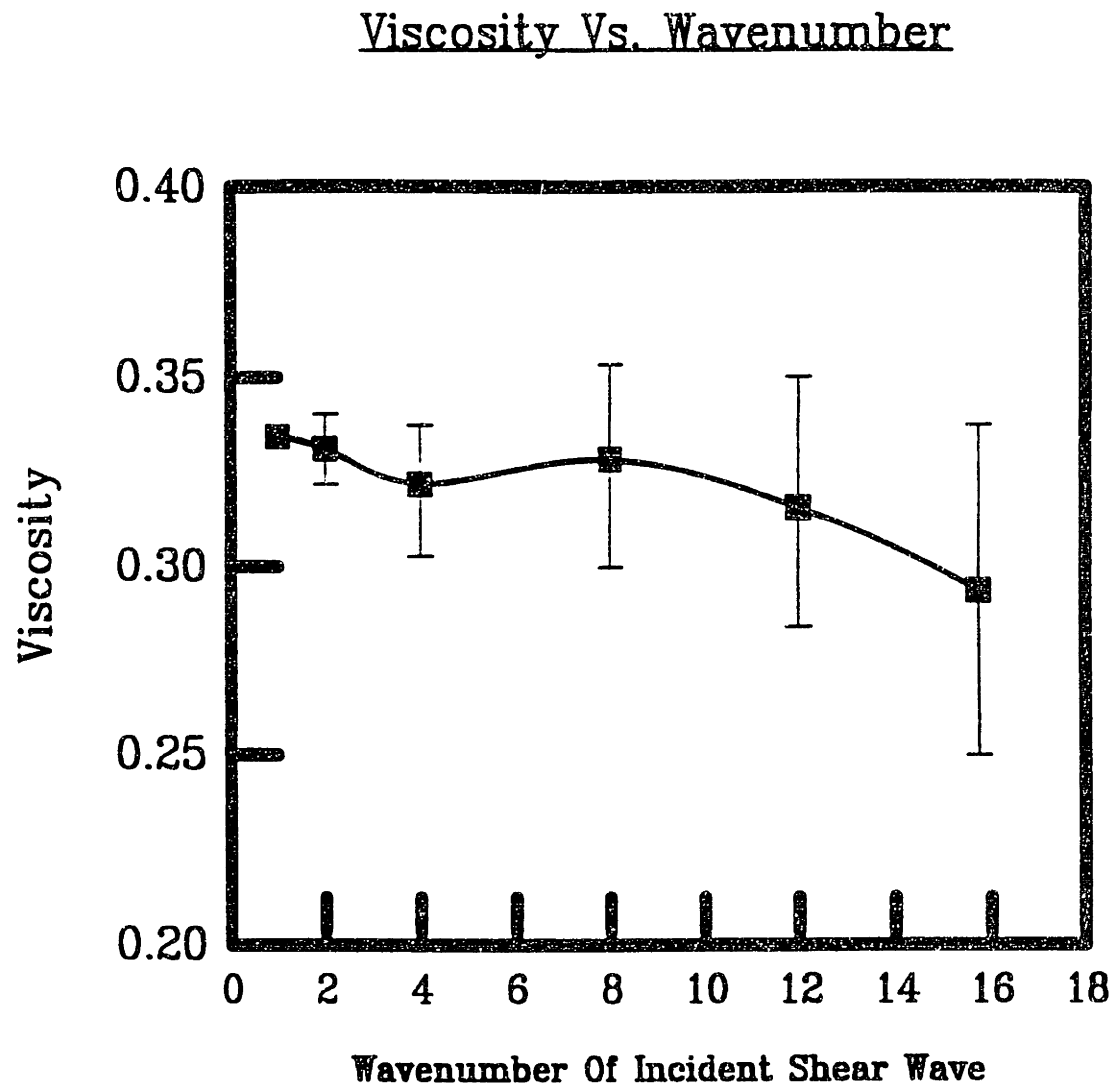

Figure 7.8: Viscosity measurements in the k dependence experiment, same runs as in Figure 7.7. Viscosity maintains the same value, within the region of uncertainity, for all values of the wavenumber.

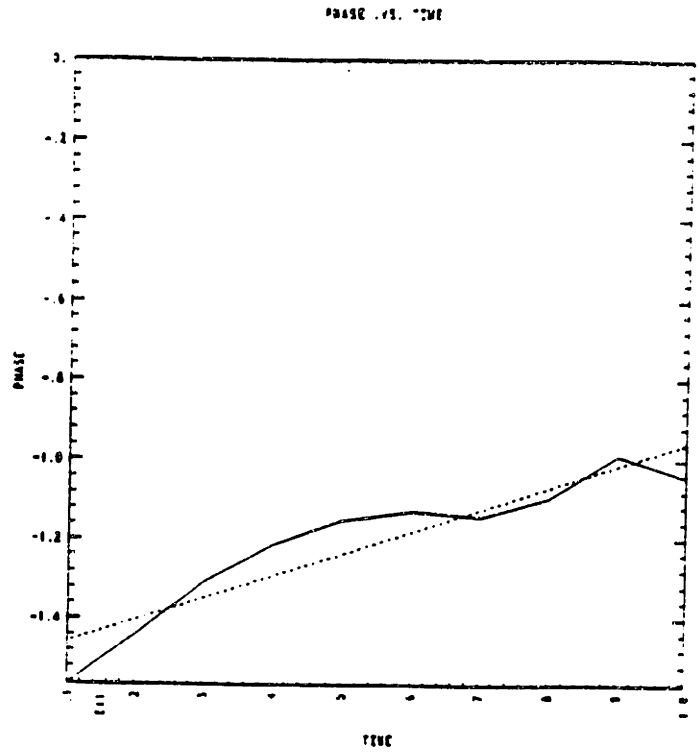

Figure 7.9: Phase of a decaying shear wave, from which we measure g, as a function of time for the wavenumber $k = 12$. Although the mean fit to this deacy, the dotted line, does not give good results, the value of g measured from the intial slope, $t \leq 30$, gives $g = 1$. The slope then drops below this level and fluctuates rapidly as the amplitude approaches the shot noise level.

7.2.4 Mach Number Behaviour

The final experiment we do with the shear wave is to examine the behaviour of the system at Mach numbers approaching unity by increasing the values of u_T and u_L. Since the relations for the artifacts were calculated using an expansion in Mach number, this is the regime where the theory breaks down. Even if the Mach number expansion for the Euler equations were carried beyond 3rd order, it is not known if the tensors generated by the FCHC basis vectors are isotropic beyond the 4th rank tensor of lattice velocities, eqn. (3.47). This means that we might expect that some high order graininess, reflecting the underlying lattice, would

Initial $u_T = u_L$	Mach	g	ν	Pressure Anomaly	$\frac{1}{2}\rho u^2$	$R^* = \frac{c_s}{\nu}$	Shot Noise Level
0.1	0.163	1.000	0.376	0.035×10^{-2}	8.0×10^{-2}	2.30	$.36 \times 10^{-2}$
0.2	0.327	0.985	0.368	0.092	32	2.36	.36
0.3	0.490	0.964	0.340	0.384	72	2.55	.36
0.4	0.653	0.933	0.307	1.479	130.0	2.82	.36
0.5	0.816	0.891	0.280	4.440	200.0	3.10	.36
0.6	0.980	0.824	0.260	12.508	288.0	3.33	.36

Table 7.4: Illustration of loss of $g = 1$ condition as the theory breaks down at high Mach number. We still see that $g = 1$ within 2% at values of Mach number up to $M \sim .4$ and does not become unacceptable until $M > .65$ where the pressure anomaly becomes significantly larger than the shot noise level.

start to appear at higher Mach numbers. Whether this would have a significant impact on the fluid behaviour is unclear, but the question is unlikely to have a satisfactory theoretical explanation. The best one can do here is explore the behaviour experimentally, with simulations, for indications of non-hydrodynamic behaviour. The results of such a study for increasing values of $u_T = u_L$ and $\rho = 8, z = 2$ are compiled in Table 7.4.

What one sees from the table is that, remarkably, reasonable hydrodynamic behavior persists to $M = .5$, well beyond what the underlying theory would give one any right to expect. At Mach numbers lower than this, even though g may vary from 1 by a few percent, the value of the pressure anomaly, as calculated in the inital validation experiments, is still at the shot noise level or less indicating that

deviations from hydrodynamics are indistinguishable from noise. Even for Mach numbers, $M = .98$, where the formulas for the rate coefficients would be expected to contain substantial errors, the Galilean factor is maintained reasonably close to unity, $g = .82$. The dynamic pressure anomaly does increase, so that by $M \sim .5$, it exceeds the noise fluctuations and becomes visible in the pressure plots. However, the dynamic pressure, $\frac{1}{2}\rho u^2$, also increases, so that the anomaly remains at 1% of the dynamic pressure at $M = .65$, and stays below 5% throughout the range indicated in the table, up to $M = .98$.

The results clearly suggest that our lattice model describes fluid dynamical behaviour correctly to about $M = .5$ in these low fluid velocity simulations. This corresponds to flow velocities up to $u \sim .5$ since $c_s \sim 1$. In Section 4.3, we showed that it was possible to rescale the equilibrium, and hence dynamical equations, of the lattice equilibrium expression for any flow velocity $\mathbf{u}$. This was done by finding the closest lattice vector, $\mathbf{c}_{ji}$ to the velocity $\mathbf{u}$ in a multiple- speed system and transforming the lattice by that velocity. This results in a residual velocity of $\delta\mathbf{u} = \mathbf{u} - \mathbf{c}_{ji}$ with magnitude necessarily less than or equal to 0.5. It was shown that this transformation is possible when the lattice exhibits discrete microscopic Galilean invariance, a property that the FCHC lattice attains *naturally* as higher speeds are added to the model. The result from the low Mach number experiments that indicate good hydrodynamical behaviour for $u \leq .5$ and the fact that we can rescale the model to any velocity as higher speeds are added where the residual velocity is always $\delta u \leq .5$, indicates that the model can be used to accurately simulate high Mach number flows as higher speeds are added.

7.3 Poiseuille Flow

Now that we have established that the three-speed LGA code correctly simulates hydrodynamic behaviour for a wide range of density, temperatures and velocities we examine some tradtional fluid dynamics experiments with the goal of further demonstrating the accuracy of our method. The first flow we will examine is unidirectional flow between two parallel plates, known as Poiseuille flow. This will allow us to examine the behaviour of the model in the presence of a pressure gradient. With the x-direction being aligned down the length of the pipe, the Navier-Stokes equation for this flow simplifies to

$$\frac{\partial}{\partial t}u_x = -\frac{1}{\rho}\frac{\partial}{\partial x}p + \nu\frac{\partial^2}{\partial y^2}u_x \tag{7.25}$$

with the other two spatial components of the equation being trivially satisfied. In steady state, with the conditions that the flow is zero at the walls and reaches a maximum in the centre, the solution is

$$\begin{aligned} u_x(y) &= -\frac{1}{\rho\nu}\frac{a^2}{2}\frac{\partial p}{\partial x}\left(1-\frac{y^2}{a^2}\right) \\ &= u_o\left(1-\frac{y^2}{a^2}\right) \end{aligned} \tag{7.26}$$

where a is the half-height of the channel centred around $y = 0$. Thus, in equilibrium, the velocity should attain a parabolic profile throughout the channel. From this result, a viscosity measurement can be obtained in two separate ways. The simplified Navier-Stokes equation for this steady-state problem is

$$-\rho\nu\frac{\partial^2}{\partial y^2}u_x = -\frac{\partial}{\partial x}p \tag{7.27}$$

where now each term is in units of force per volume. The term on the left-hand side represents the force deposited to the upper and lower walls and the term

on the right-hand side represents the force imparted to the system through the open ends and dissipated due to the pressure gradient. In equilibrium, these two terms must balance. Since we can measure both the total force on the walls and the pressure gradient down the pipe directly in our simulations, we can use the integrated form of eqn. (7.27) to calculate viscosity from both measurements since both the density and theoretical velocity profile are known.

The force deposited to the wall by one particle is simply the amount of momentum imparted to the wall by the particle over the duration of the collision. As described in Section 7.1, particles interact with solid boundaries by "bouncing-back" from them. This means that a particle imparts twice the value of its momentum directed into the wall. This is done over one time step, the smallest unit of time on the lattice. To find the total force on the wall, we simply take twice the value of the component of momentum directed into the wall for particles that collide with the wall. Thus the total force is

$$F_{wall} = 2\left(\sum_i \mathbf{c}_i n_i(\mathbf{x}) \mid_{\substack{top \\ wall}} \cdot \mathbf{e}_y - \sum_i \mathbf{c}_i n_i(\mathbf{x}) \mid_{\substack{bot. \\ wall}} \cdot \mathbf{e}_y\right) \tag{7.28}$$

summed over the entire upper and lower walls. To measure a value of viscosity from this, we also need to calulate the left side of eqn. (7.27). Plugging the solution, eqn. (7.26) into this relation gives

$$F = \nu \rho u_o \frac{2}{a^2} \times Volume \tag{7.29}$$

where u_o is the velocity down the centre of the pipe. To increase the accuracy of the centre velocity measurement, we measure the normalized momentum of the entire lattice volume and relate it to the momentum at $y = 0$

$$\langle \rho u \rangle \equiv \frac{\int_{-a}^{a} \rho u_o (1 - \frac{y^2}{a^2}) dy \Delta x \Delta z}{2a \Delta x \Delta z} = \frac{2}{3} \rho u_o \tag{7.30}$$

so that a much less noisy value of the median momentum is $\rho u_o = \frac{3}{2}\langle \rho u \rangle$. The total volume of the lattice is $2a\Delta x\Delta z$. We find a value of viscosity from the wall force measurement using eqn. (7.29)

$$\nu_{wall} = \frac{F_{wall}}{\langle \rho u \rangle} \frac{a}{6\Delta x \Delta z}. \tag{7.31}$$

Similarly, we can measure the pressure at all sites on the lattice, average over the y- and z- directions to find $p(x)$. Fitting a negatively sloped line to this measurement will give the pressure gradient, $-\frac{\partial}{\partial x}p$ and then the pressure drop down the length of the pipe, $\Delta P = \frac{\partial}{\partial x}p \times \Delta x$. Multiplying this value by the surface area of the outlet region gives us the total force imparted to the system by the flow. Using eqn. (7.29), another value of viscosity may be calculated

$$\nu_{press} = \frac{\Delta P}{\langle \rho u \rangle} \frac{a^2}{3\Delta x}. \tag{7.32}$$

If the system is transmitting momentum correctly, the two calculated values of viscosity should be the same since the force imparted to the volume through the inlet channel should be deposited on the walls. To cross-test these results, we compare these viscosity results with the viscosity calculated from the shear wave experiment using the same input parameters.

The simulation was started with the fluid at rest. Fluid was then injected at the entrance of the lattice at a particular velocity and the parabolic velocity profile evolved as predicted in about 1500 time steps. This profile evolved due to the effects of shear stresses near the wall (caused by the no-slip boundary conditions there) which resulted in the conversion of the normal pressure drop to tangential shear stress at the wall. This shear is absorbed as momentum into the wall. Once equilibrium was reached data was accumulated for another 1500 time steps to assure clean profiles and measurements. The results of a number of experiments

are shown in Table 7.5 where we see that the two different viscosity measurements agree with each other and also with the independent shear wave viscosity to within 1% for all cases. This is further strong evidence that the algorithm is behaving hydrodynamically in the mean. In all of these cases, the number of lattice sites down the length of the tube was $\Delta x = 352$, the total height was 56 so that $a = 28$ and the extent in the third dimension was just $\Delta z = 4$ for a total of about 80 000 lattice sites. This is a considerably smaller lattice than the 64^3 lattice we used in Section 7.2 because in this case we want to run the simulations for a very large number of time-steps to demonstrate the constancy of the mean flow quantities in equilibrium.

These cases were run at very slow speeds, $M \sim .05$, so that the noise level was extremely high. In fact, the instantaneous fluctuations in the velocity field at a lattice site were about 5 times the signal, or mean flow velocity, value. Figure 7.10 compares the instantaneous velocity profile in a single cross section of the pipe to the 1500 time step averaged value.

It is difficult to recognize any sensible mean flow from the instantaneous data. In fact, numerous points appear to exhibit "backflow" in the pipe. This is to be expected when the noise level is so high. On the other hand, it might seem that such an instantaneous flow field would not be able to accurately transmit the shear stress appropriate to a parabolic profile, which, of course, depends on the local gradients of the velocity field. But, as the data in Table 7.5 indicate, the accuracy with which the algorithm transmits the correct hydrodynamic stress — as though the profile were a very accurate parabola — is extremely good. The parabolic profile does eventually appear in the mean as statistics are accumulated over larger volumes of time and space.

ρ	z	Drag Force	Pressure Drop	Viscosity Norml Press.	Viscosity Wall Force	Viscosity Shear Wave
5	5.0	16.3	0.073	0.301 ±.002	0.301 ±.003	0.305 ±.003
8	2.0	29.2	0.130	0.448 ±.003	0.450 ±.004	0.450 ±.003
10.6	4.8	29.5	0.133	0.346 ±.002	0.343 ±.003	0.345 ±.003
10.6	6.0	26.0	0.116	0.302 ±.002	0.303 ±.002	0.300 ±.003

Table 7.5: Comparison of Viscosity measurements for various densities, ρ, and temperatures z (inversely related to T) for a low Mach number flow. Two measurements are from the pipe flow and they are compared with an independent measurement from the shear wave experiment. All three agree within the uncertainities for all cases.

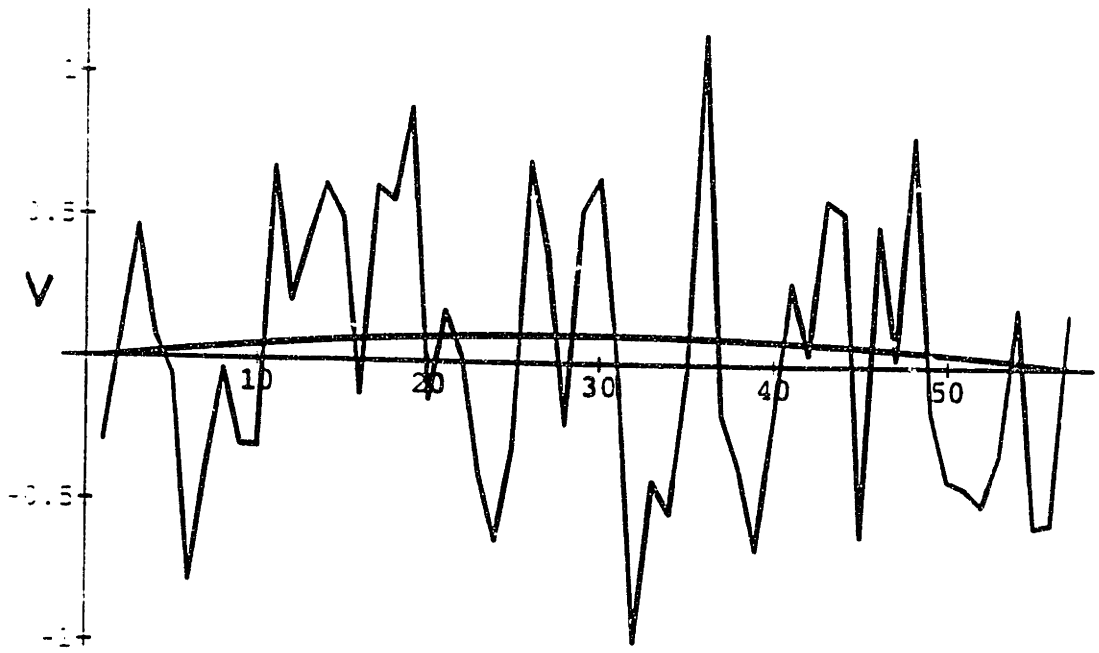

Figure 7.10: Comparison of jagged instantaneous velocity profile for a cross section of the pipe compared to the statistical mean value (over 1500 time steps).

Evidence of a persistent mean despite large shot noise flucutations was also seen in the wall force measurements. Although the mean value of the wall force was quite small (typically around 20 - 30 for a wall length of 352 lattice sites) due to the small velocity in the simulations, and hence quite noisy[9], the mean value from the accumulation of 1500 time steps of data remained constant within 2% over concurrent runs when equilibrium had been reached. The expected variation in a series of 1500 values that vary from their mean due to shot noise is $1/\sqrt{1500} \simeq$ 2.5 % so that our observed variation in the mean is within shot noise levels. This repeatability is a result of momentum being an exact invariant in our system.

The fact that the mean dynamics reproduces the expected results of hydrody-

[9]Signal / Noise $\approx$ 3

namics despite the high levels of noise is guaranteed by the shot noise theorem and subsequent conclusions of the absence of all noise effects on the mean dynamics derived in Chapter 6. If the instantaneous flow field shown in Figure (7.10) were that of a fluid obeying differential equations, or some numerical approximation to Navier-Stokes, the results would be much different and substantial errors would result as noise would have a significant effect on the mean dynamics in these methods, as shown in Section 6.1.

This experiment also revealed an interesting realism feature of the system in the way external boundaries behave. Boundary conditions in the differential equation sense do not occur. Rather one specifies the distribution of entering particles on the boundary[10]. The exiting particles — and thus all the net fluxes — are determined by the total system response. Even if external conditions are set inconsistently, the main flow will achieve correct hydrodynamic behaviour, forming very narrow boundary layers at the end to counteract the inconsistencies. The tendency to obtain thermal equilibrium is so strong that, for example, if flow is forced through the system without an imposed pressure gradient, the correct gradient will form naturally because hydrodynamics demands it. This is strikingly analogous to the way a real wind tunnel is driven — by a fan forcing particles through the tunnel — not by setting mathematical boundary conditions.

7.4 Flow Past a Circular Cylinder

The final flow experiment that was performed with the three-speed model was by far the most complex physically but was trivial to set up with the LGA code.

[10]using the Refresh portion of the LGA code in our case

Flow past a circular cylinder of a particular diameter was simulated by simply setting the fluid bits within a circular region of lattice sites to zero which ensured that all particles would be reflected at the surface of the cylinder in such a way as to keep the velocity zero there. By setting an initial density, temperature and flow velocity perpendicular to the axis of the cylinder, we could observe the evolution of the flow as it interacted with the solid cylinder for Reynolds numbers in the range $0 \leq Re \leq 65$. The Reynolds number is

$$Re = \frac{u\,d}{\nu} \tag{7.33}$$

where d is the diameter of the cylinder in lattice sites, u is the speed of the flow far from the cylinder and ν is the kinematic viscosity of the fluid near to the cylinder. As we increase Re by increasing both the initial flow velocity and cylinder diameter, a number of interesting phenomena occur that our model must accurately reproduce in order to verify its hydrodynamic behaviour. We will quantitatively perform this comparison by measuring flow properties such as drag and wake length in the range of Re where steady flow is maintained ($Re \leq 45$) and the frequency of shed eddies when the flow becomes unstable ($Re > 45$). We will compare our results with established experimental results for the same Reynolds number flows as well as results from recent CFD simulations.

There are two important geometrical issues that we must understand if we are to quantitatively compare our results to actual fluid experiments. These are the influence of surface roughness and blockage on the values of properties measured at the solid surface. The first issue concerns the degree to which we can delineate a continuously curving cylinder on a discrete lattice. It might appear that the surface of a simulation cylinder of relatively small diameter is significantly rougher than a true cylindrical surface, since it is restricted to be defined by the lattice

sites. Actually the scale of this roughness corresponds to a characteristic mean free path of a lattice gas particle. Thus, as long as the desired true surface has a scale length long compared to the mean free path, we would expect the lattice gas dynamics to effectively smooth this surface to become very close to the ideal shape as far as the macroscopic flow is concerned. However, this potential roughness phenomenon is difficult to analyze theoretically, and needs study by direct simulation to determine its importance.

The surface roughness of the lattice was found to be a very small effect, that we estimate to be below 1% for the radius 20 site cylinder we studied. This was the smallest radius that was used in the cylinder experiments and so it represents the case with the largest surface roughness effect. To make the effect extreme, we simulated flow using a pathologically "rough" cylinder (obtained by rotating the blocks in the data structure so as to create a distorted surface), as shown in Figure (7.11) where we compare it to the smoothest cylinder allowed by the lattice resolution. In spite of this extreme surface roughness — variations on the order of 10% of the radius — flow parameters such as drag and wake length, were affected very little. The drag measured using the pathologically "rough" cylinder was only 4% higher than the smooth case , at a Reynolds number of $Re \sim 30$. This result is another example of the continuum nature of the statistically averaged dynamics.

The second key geometrical consideration, which is also of vital importance in wind tunnel experiments, is the "blockage" or the ratio of the frontal projection area of the object to the total cross section area of the tunnel. Without extremely small blockages, the observations of drag, lift and so forth are affected by a variety of Venturi type effects, and differ significantly from free stream values. Even for blockages below 5%, which is a rule of thumb for accurate wind tunnel operation,

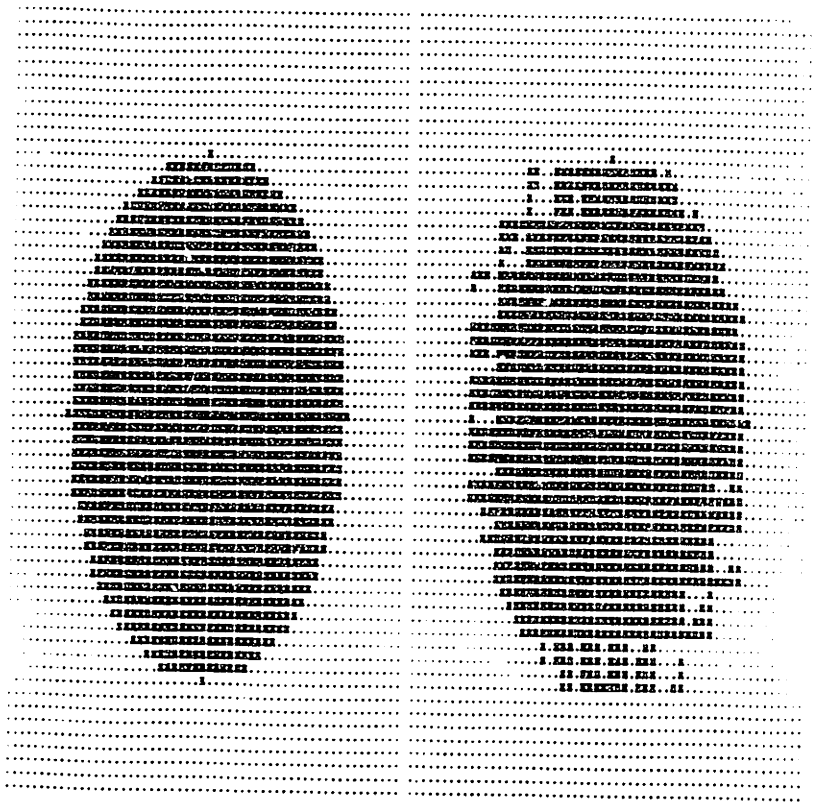

Figure 7.11: Comparison of smooth and pathologically rough cylinder cross sections used in the investigation of the effect of surface roughness on surface drag. At Re=30, the rough cylinder's drag was only 4% higher than the smooth result, a small effect.

corrections to the measured drag values need to be made. Even though the fluid in regions far from the object follows a fairly featureless potential type flow, it does succeed in transmiting significant stresses to the object which must be accounted for to obtain accurate results.

In CFD simulations this outer region can often be partially accounted for by so-called "potential flow boundary conditions". This does require some knowlege of the flow near the object, and can cause significant differences in answers if

not done correctly, but it does save significantly on computational work. For a previously untried flow object where the flow behaviour near the object is not known, this method requires many iterations to acquire this information before a stable result is found. Clearly, a simulation technique that does not require *a priori* information about the flow would be better suited to fluid dynamics research.

In the lattice gas method, boundary conditions of the differential equation type do not exist. A physical condition which accounts for the microscopic physics must be specified. In the present case. free slip walls are modelled by wrapping particles toroidally from the tunnel top to bottom, thereby forcing the flow to be parallel to a defined boundary without imparting any momentum to it. The only effective way to reduce blockage is to actually simulate a larger physical volume. This can be accomplished efficiently using the multigrid scheme that was developed by our research group and is described elsewhere[55] although we will describe its important features here.

The multigrid lattice that we are using is similar in concept to the multiple grid systems commonly used in CFD. An important difference is that while in CFD a grid may be tailored to conform with the expected geometry of the flow[51], we maintain a rectangular grid everywhere. By maintaining a higher resolution of lattice sites around an object we can be sure of capturing all the relevant phenomena there. Furthermore, by placing a coarse grid in regions far away from objects we wish to investigate, we reduce the computing power needed as well as create distance between the important object and the edge of the simulation volume. The multigrid we are using basically reduces the resolution by a factor of 2 in all three directions at a grid interface. The main requirement of the grid

interface is that all physical parameters (mass, momentum, energy) are continuous across the interface. The key to doing this is to keep the microscopic particle velocities, $\mathbf{c}_i$, unchanged. Particles have the same set of directions and speeds in all lattices. To counteract the eightfold change in lattice site density, we simply assign 8× the mass to particles in the coarse region and move them only half as much as the particles in the fine lattice to maintain the fundamental unit of time. This makes the microscopic dynamics *completely continuous*. Mass, momentum, and energy density are trivially continuous, and since the thermodynamics is identical, the sound speed is continuous as well. It has been theoretically asserted and verified by simulation that the multigrid algorithm we are using[55] preserves the Euler stresses continuously (effectively providing an Euler dynamics that is scale independent), and produces a discontinuity in the viscous stress corresponding to the increased mean free path in the coarser outer regions. As long as this viscosity change occurs in a region of potential flow, it will not change the results[11], a property that we verified directly by simulation. Of course, it is possible to have many multigrid stages with all the elements of the interface described above holding at each interface. In fact the only difference between the various lattices besides the aforementioned viscosity is the sampling accuracy per unit volume. The coarser regions are noisier which doesn't matter as long as the phenomena are resolved, the mean dynamics of all regions being unaffected by noise (see Chapter 6).

In the runs described here, a very simple multigrid geometry was used. A rectangular volume of fine grid cells (8 sites deep in the third dimension), was enclosed in a larger rectangle of coarse cells with twice the spacing between sites.

[11] In fact extra viscosity in the outer regions is helpful in damping transients there and allowing the system to come to steady state much quicker

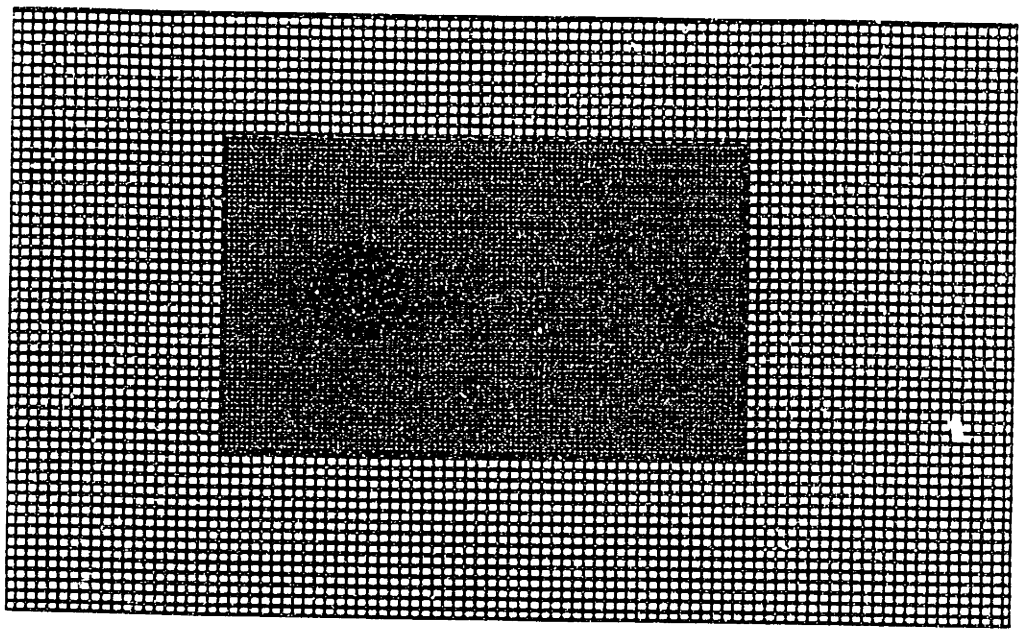

Figure 7.12: Geometry of the variable resolution lattice for the cylinder runs, showing cylinder placement in the fine grid. One fine grid surrounded by one coarse grid was used in these runs.

Some cases were run without multigridding and had no coarse region at all. The geometry is depicted in Figure 7.12.

By using the multigrid lattice. the blockage at higher Reynolds number flows was reduced significantly. Still. standard corrections for blockage had to be applied to reduce our values to the zero blockage results.

7.4.1 Attached Eddies, $Re < 45$: Run Conditions

Simulations were first run on a uniform grid lattice of height 256 sites and length 384 sites with a cylinder of radius 20 situated one-third of the way downstream. The depth of the simulation along the cylinder axis is 8 sites although the flow is constant in this direction. This direction was used to accumulate statistics of the flow and served to reduce the amount of time steps we had to average over to obtain a clean flow property profile. Once a simulation reached steady-state, the final averaged density and temperature were used to calculate the viscosity of the fluid from the shear wave results. Since the flow velocity far from the cylinder is an input parameter as well, the Reynolds number for the flow can then be calculated. The system could be started either from rest with significant injected mass, or from initially moving flow filling the tunnel everywhere except in the wake region. The final state was found to be independent of the startup scenario, even though the 'at-rest' start typically caused the mean fluid density to increase by about a factor of two. The 'initially-flowing' startup saved substantially on runtime and was used predominantly in the data presented below.

The main flow property that was varied to get different Reynolds numbers was the initial flow velocity although the cylinder diameter was sometimes alterred slightly. A list of the simulations we performed, outlining the Reynolds number, Mach number and system geometry for each case, is given in Table 7.6. The system geometry is given in units of lattice sites. The y- direction is the length of the simulation volume (the direction in which the flow is travelling), the z-direction is the height and the x- direction is the width (length of cylinder). The single grid system was used for Re= 9.6, 11.8, 28.8 where there are about 8×10^5 lattice sites in total. The Re=23.6 case illustrates an early multi-gridding geometry where the

Re	Mach No.	Lattice Size			Radius	Block.
		y	z	x	R	$\frac{2R}{z}$
9.6	0.12	384	256	8	20	15.6%
11.8	0.15	384	256	8	20	15.6%
23.6	0.25	384	344	8	20	11.6%
26.0	0.25	1280	512	8	22	8.6%
28.8	0.30	384	256	8	20	15.6%
36.7	0.38	1280	512	8	21	8.2%
42.6	0.38	1280	512	8	24	9.4%

Table 7.6: Summary of flow parameters for cylinder runs with $Re < 45$. Distances are measured in lattice spacings where the y-direction is down the length of the volume (the direction of flow), z- is the height and x- the width or length of the cylinder.

height and length of the volume were about the same with about 1×10^6 total sites. The final multi-gridded lattice was used for runs Re=26.0, 36.7, 42.6 where about 5×10^6 total sites were simulated. We compare the results for these three different lattice structures in order to show that the results are correct independent of the lattice size used. Of course, with a larger system, the blockage ratio is smaller and so the reliability of the relation that corrects for this factor is higher.

When steady-state had been reached[12], statistices were accumulated for a further 1000 time steps so that a time and space (x-direction) average produced clean flow results. The streamlines for steady-state flow past a cylinder for the

[12]Steady-state flow exists for $Re < 45$

$Re = 28.8$ case are shown in Figure (7.13) and Figure (7.14).

Recirculating eddies of equal size are clearly visible behind the cylinder. The drag on the cylinder was calculated by simply summing the force individual particles imparted to the cylinder upon colliding with it (this was twice the momentum in one time step), the same calculation we used for the force on the walls in Poiseuille flow. The ratio of the eddy length to cylinder diameter was also measured. This was also an easy measurement as we simply found the number of lattice sites directly behind the cylinder that had a negative (recirculating) velocity. To verify that the force measured on the solid was equal to the force lost by the fluid when passing the cylinder, the normal element of the stress tensor was measured down the length of the simulation, see Figure (7.15).

If we measure the drop in pressure across the cylinder integrated over the cross-section, which in the $Re = 28.8$ case is $256 \times 8 = 2048$ sites^2, we find essentially the same force as measured on the cylinder (225.2 for stress drop while drag force on cylinder is 225.3). This further illustrates what we had validated from the pipe flow experiments — the system is correctly transmitting stress. The "bump" in the stress around the cylinder is due to the Venturi effect in a constrained system. This is a result of blockage that must be corrected for in the data as discussed below.

Correct hydrodynamic behaviour is possible only when the flow does not allow the lattice to become manifest macroscopically. In Section 5.1 we showed how the three-speed lattice gas model can be made Galilean invariant through a chemistry trick which maintained the factor $g(\rho, T)$ at unity by alterring the energy exchange collision rate. As the flow develops around the cylinder, the properties of the fluid readjust themselves from the initial values to satisy the constraints

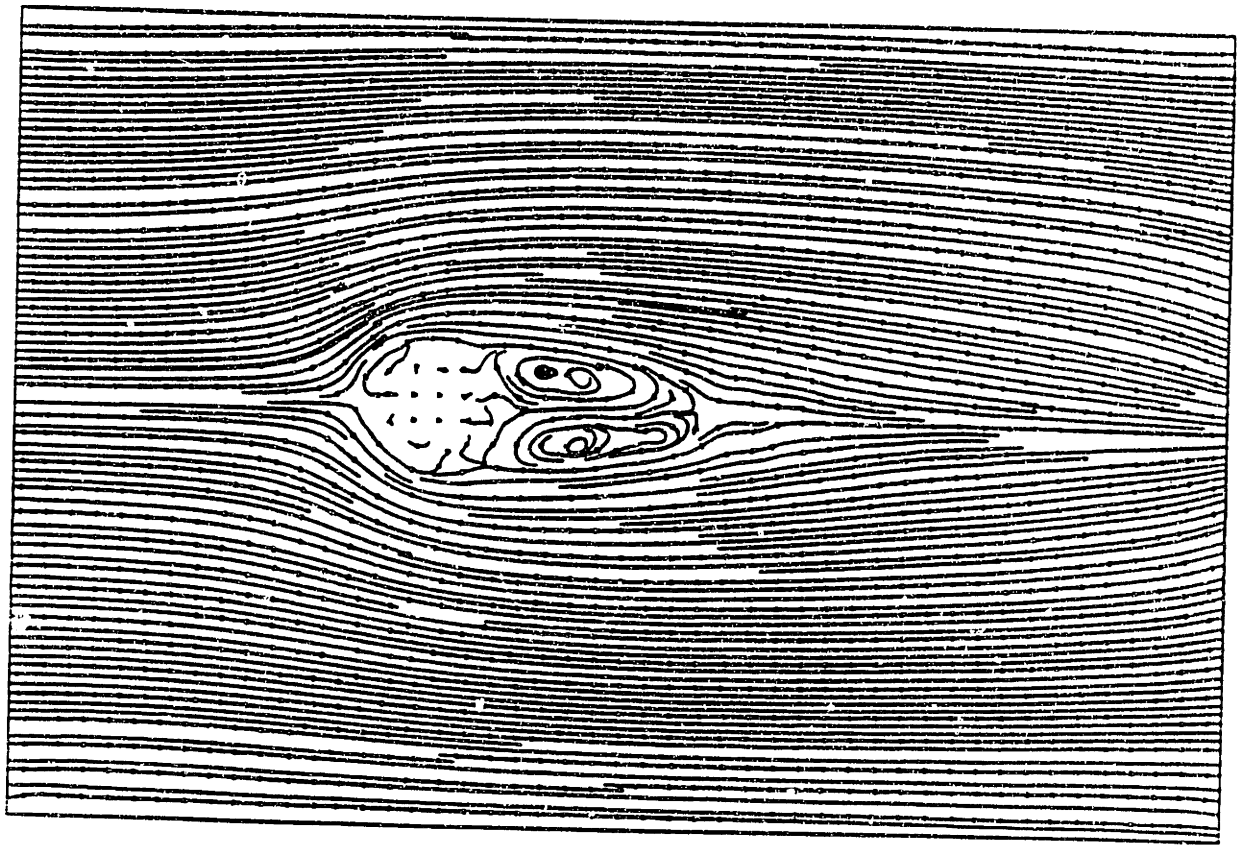

Figure 7.13: Streamlines in steady state at $Re = 28.8$. The entire lattice is shown. Streamlines originating from inside the cylinder are artifacts of the graphics program.

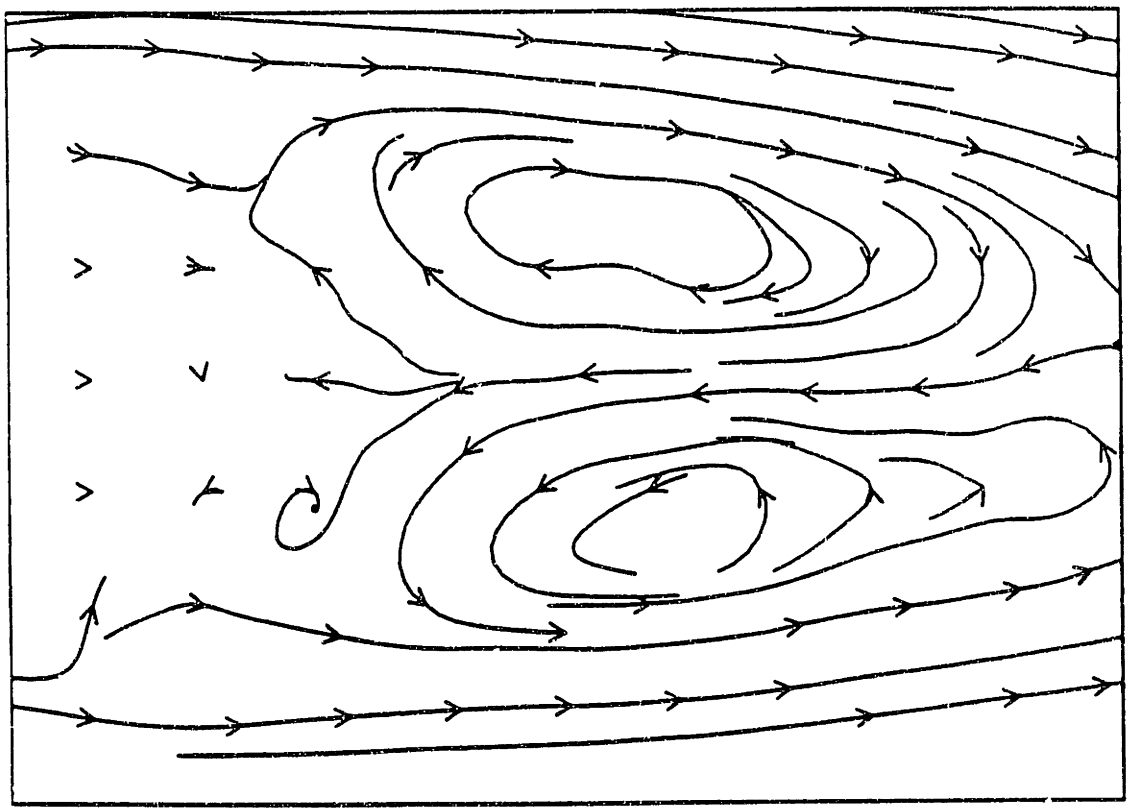

Figure 7.14: Close-up of streamlines in trailing wake behind cylinder at $Re = 28.8$ illustrating the steady, closed structure of the attached eddies. Streamlines originating from inside the cylinder are artifacts of the graphics program.

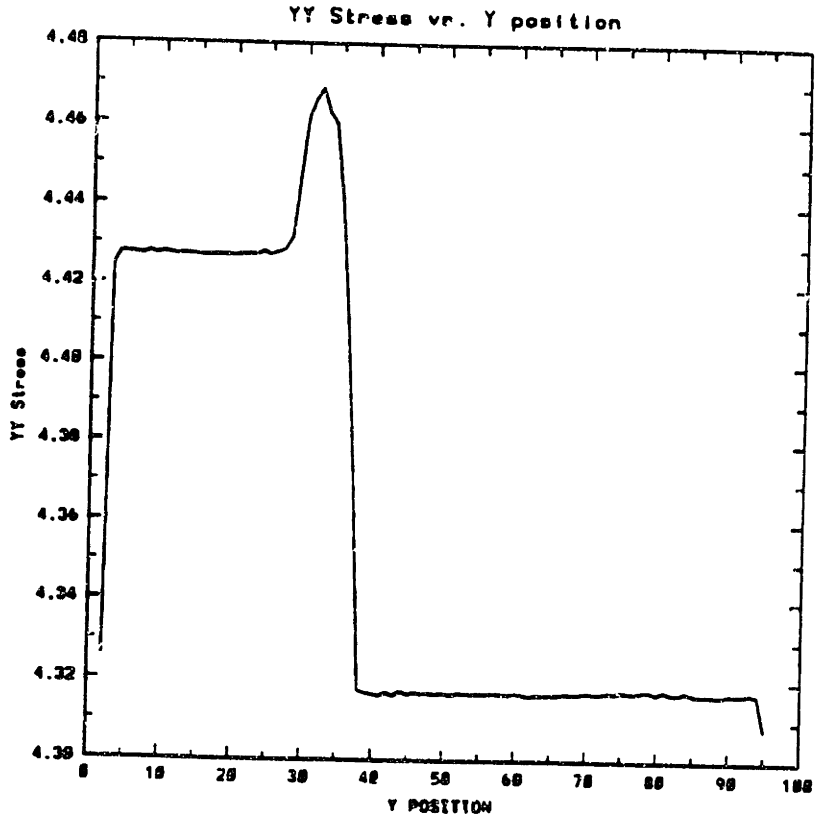

Figure 7.15: The drop in S_{yy} stress across the cylinder at Re=28.8 $\Delta S_{yy} = 0.11$. Units of position down the volume are in lattice sites divided by four, actual length is 384 sites. Cylinder is located between sites 108 and 148. When multiplied by the cross-sectional area of the model ($256 \times 8 = 2048$), this gives a force loss of 225.3. The measured force on the cylinder was 225.2. *Note*: The 'bump' in stress around the cylinder is due to the Venturi effect.

of hydrodynamics. Since g can depend on these parameters[13], a feedback system was incorporated into the model that senses the fluid properties and then alters the collision mask in order to maintain g at 1. We do this by measuring the temperature and density of the system and then recalculating the rate coefficient. The technique for accomplishig this was developed in Section 5.1 and the equation that allows us to calculate the system temperature from measured flow properties is given in eqn. (5.16). This allowed us to inject mass at high rates into a tunnel configuration with the fluid initially at rest and build up the density by a factor of two or more while still maintaining $g = 1$.

The results of Section 7.2.4 demonstrated that the model is able to maintain $g = 1$ to within an acceptable level so that anomalies in the pressure were not observable up to a value of Mach number, $M \sim .3$. In Figure 7.16, we show the measured value of g averaged over the lattice cross-section at steady-state where the values of density and temperature have changed by about 25% from their intially seeded values for the $Re = 28.8$ simulation. In this case, we are near the limit of acceptable Mach number since $M = .3$ here. Still we see that Galilean invariance has been maintained to good accuracy. Note that the jaggedness in the value of g occurs around the cylinder and it is attributable to the cylinder extent not filling up an entire subvolume height (of 4 lattice sities)[14] on the surface. Since we have averaged over the height in total subvolumes, there is a slight error in our normalization in the cylinder region. Furthermore, the measured value of g has a second-order Mach number dependence that should not be present in the actual g calculation. This is the same effect that we corrected for in the feedback

[13]although insensitively for the range of density and temperatures we used, see Figure 5.3

[14]Section 7.1 describes the 4 x 4 x 4 subvolume data structure

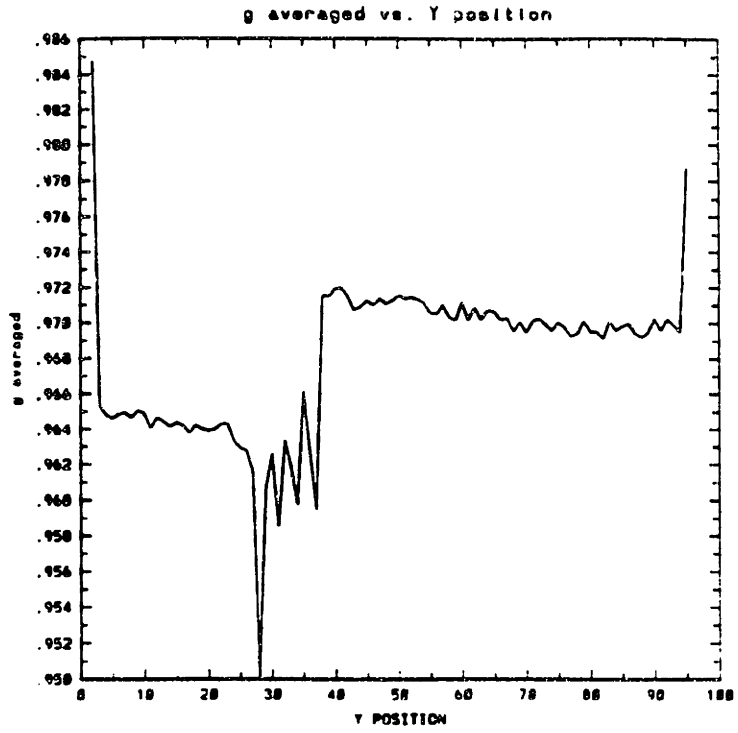

Figure 7.16: Feedback maintained cross-section-averaged Galilean invariance factor, $g \simeq 1$, as a function of distance downstream for the steady-state $Re = 28.8$ case. Jaggedness around the cylinder is due to a slight error in the cross-section normalization there and is not physical.

system. This correction for the g calculation is not shown in Figure 7.16.

Note the jumps in g observed at the ends of the tunnel. They are quite small in absolute terms, of course. These are characteristic of the boundary layers that form at the ends of the tunnel to bring the user specified incoming particle distributions into equilibrium with the system determined fluid response.

7.4.2 Attached Eddies, $Re < 45$: Results

For Reynolds numbers much smaller than five. the flow around a cylinder appears symmetric as the dominant viscosity effect diffuses the vorticity generated at the cylinder surface symmetrically away from the surface. At $Re \sim 5$, fore-aft symmetry becomes discernible as the vorticity at the surface is preferentially advected behind the cylinder. For $Re > 5$, closed streamlines appear at the rear of the cylinder. The length of these recirculating eddies grow with Re in a way that has been determined experimentally (Taneda[63] in 1956 whose results are reported in the classic fluid dynamics text by Batchelor[65], further examinations of the phenomenology of the attached circulating eddy have been carried out more recently by Acrivos *et al.*[66] in 1968 for many objects and by Coutanceau *et al.*[67] in 1977 specifically for the circular cylinder, which confirmed Taneda's results) up to a value of $Re \simeq 45$ where the eddies then become unstable.

Simulations were carried out for the several Reynolds numbers indicated in Table 7.6 spanning the range of attached eddies. As described in Section 7.4, blockage was reduced by utilizing multigridding. Eddy lengths were measured from both the streamlines and the centerline axial velocity. The drag force was measured along with the fluid properties in steady state to determine the drag coefficient,

$$C_d \equiv \frac{F_{cyl}}{A_{CS} \cdot \frac{1}{2}\rho u^2} \tag{7.34}$$

where F_{cyl} is the total force on the cylinder and A_{CS} is the frontal cross-section of the cylinder, equal to twice the radius multiplied by the cylinder length. The free stream dynamic pressure is measured at the entrance channel of the tunnel.

The measured wake lengths are displayed and compared to the careful observa-

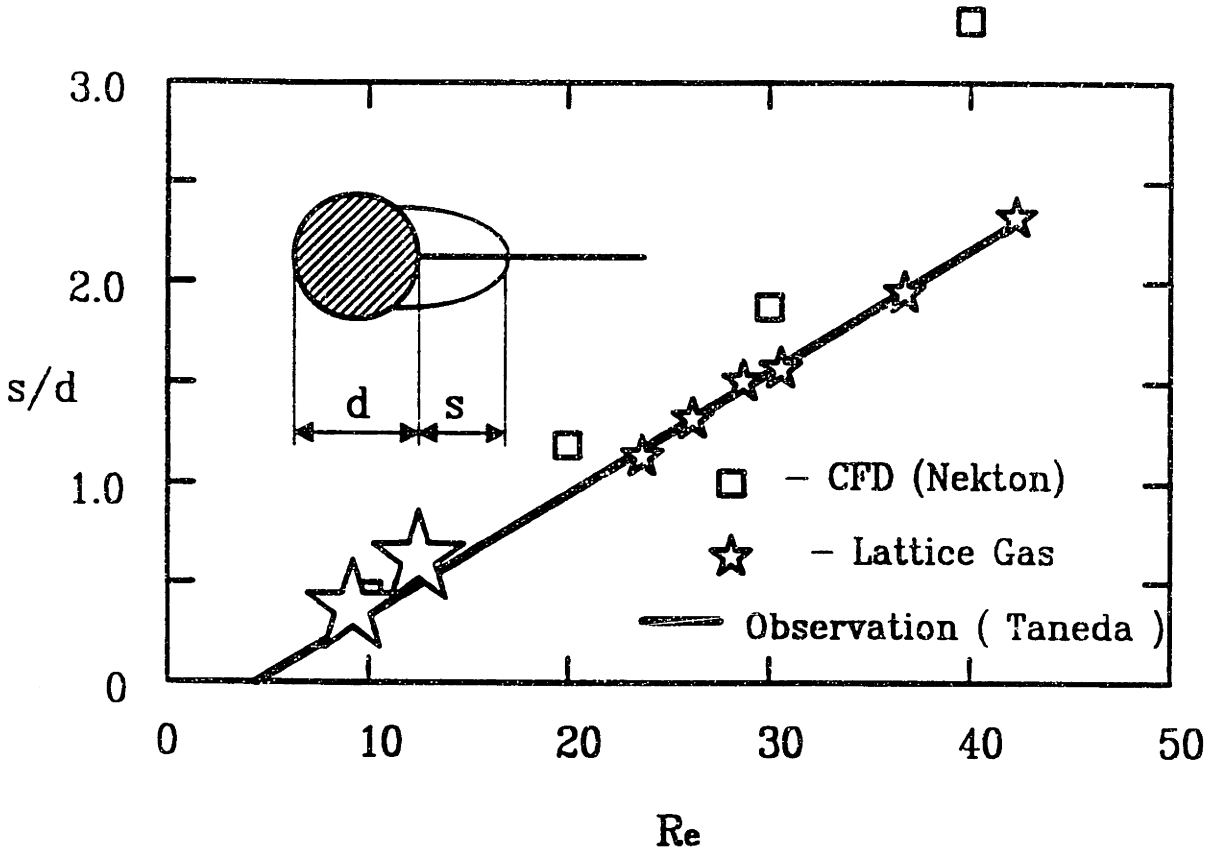

Figure 7.17: Wake length (s/d) as a function of Reynolds number (Re) for our results compared to observation and recent CFD results. The size of the data points represents the measurement error.

tions of Taneda [63] and recent results from a CFD spectral code simulation [56] in Figure 7.17. This figure is essentially a reproduction of the presentation of Taneda's data in Batchelor's book. Batchelor's figure displayed the data explicitly, which we have not done here since it fits the straight line so well and would clutter the figure unneccessarily.

Note that no discrepancies can be found between the lattice gas observations and those for a real fluid in the laboratory. The measurement errors at the two

smallest Reynolds numbers are large, owing to the poor sampling statisics over the small volumes occupied by the eddies[15]. At the other Reynolds numbers the lattice gas and laboratory measurement errors are comparable ($\sim$ 6 %).

Substantial discrepancies are apparent for the state-of-the-art CFD code, NEKTON, however, as evident from the published data of Karniadakis [56]. We attribute this discrepancy to remaining discretization errors that persist in the CFD approximation. Karniadakis seemed to believe that a subsequent set of experiments by Honji and Taneda [64] involving the transient formation of vortices under impulsive starting conditions might be more appropriate to his simulations. The Karniadakis paper [56] made no reference to the original Taneda work, and gave no explanation for why the nonsteady state results from the second Taneda paper (which showed significantly higher wake lengths for a given Re compared to his earlier steady results) should apply to his case, even though Taneda [64] never claimed that the second expermiments should supercede the first for the steady state case.

An examination of Coutanceau *et al.*'s [68] work on the unsteady development of eddies behind cylinders resolves this discrepancy and clearly shows that the Karniadakis results are in error. In Coutanceau's work we find that as the flow past a cylinder increases, the eddy length increases until steady-state is reached where the final eddy length ratio is equal to the results of the first steady flow Taneda results, as reported in Batchelor, as we would expect. They also show experimentally that as the eddy length is increasing in the unsteady portion of the flow that in certain cases it is possible for the measured eddy length ratio

[15]These measurement errors could easily be reduced by accumulating better statistics and resolving finer spatial scales in the near wake region.

to *exceed the steady-state value for awhile before decreasing to the final value.* Coutanceau explicitly demonstrates, by comparing the unsteady Taneda results to their own, that in Taneda's work on unsteady flows, they did not continue their experiments long enough to observe the decline to the steady-state result. Their work quotes the maximum, higher than steady-state, value. It is this value that Karniadakis compares his CFD results to, finding his results to be even higher than Taneda's already anomalously high results.

Drag measurements obtained from this set of runs are summarized in Table 7.7.

Notice that the blockage corrected drag coefficients agree quite well with the experimental observations of Tritton [62], who reported an uncertainity in his results of ±6%. With 8% blockage, these corrections are right at the boundary of where they would be considered trustworthy in wind tunnel measurements. The blockage correction was performed using a relation that is used in industry for low-speed wind tunnel testing as reported in Rae & Pope[61]. The relation, which calculates a zero-blockage drag coefficient[16] from the measured drag coefficient for a known blockage is given by

$$C_d = C_{du}\left[1 - 3\epsilon_{sb} - 2\epsilon_{wb}\right] \tag{7.35}$$

where

$$\begin{aligned} \epsilon_{sb} &= \pi^2 \frac{r^2}{h^2} \\ \epsilon_{wb} &= C_{du} \frac{2r}{4h}. \end{aligned}$$

[16]Tritton's results were obtained with cylindrical fibres with diameters in the micrometer range while the walls were about a meter distant so that the effective blockage is zero

Re	Mach #	Lattice Gas C_D Raw	Lattice Gas C_D Adj	Exp C_D ±6%	Drag Diff.	Force Shot Noise	s/n Macro	s/d LG	s/d OBS
9.6	0.12	4.08	2.77	3.00	7.7%	10%	0.45	0.4 ±.2	0.3
11.8	0.12	3.72	2.59	2.64	1.9%	7.5%	0.60	0.7 ±.2	0.5
23.6	0.25	2.41	2.06	2.00	2.9%	2.5%	1.79	1.1 ±.1	1.1
26.3	0.25	2.23	1.98	1.91	3.7%	2.8%	1.57	1.2 ±.1	1.3
28.8	0.30	2.52	1.90	1.85	2.7%	2.1%	2.16	1.5 ±.1	1.5
36.7	0.38	1.91	1.73	1.72	0.6%	1.1%	3.14	1.9 ±.1	1.9
42.6	0.38	1.88	1.67	1.58	5.7%	1.1%	3.26	2.3 ±.1	2.3

Table 7.7: Summary of Lattice Gas Data for the steady eddy cylinder runs showing that our blockage corrected drag coefficient data, column 4 (using Rae & Pope[61]), agrees with the experimental data, column 5 (from Tritton[62] 1959), to within the experimental error of 6%. Also shows the agreement of wake length to diameter ratio measurements for the lattice gas, column 9, and the observed results, column 10 (Batchelor[65]).

C_{du} is the measured drag while C_d is the corrected drag, r is the cylinder radius and h is the volume height so that $2r/h$ is the blockage.

A more direct indication of the reliability of the lattice drag results may be inferred from two sets of observations at $Re = 26.0$, and $Re = 28.8$, which are comparable except for the blockages used. Although the corrections were significantly bigger for the high blockage run, the net corrected drag coefficients were very close to the observed zero-blockage drag coefficient for both runs, and well within the measurement errors of the experimental observations. Future refinements in the multigridding configuration will reduce the blockage even further to make the blockage correction superfluous.

Also displayed in the table are several measurements of the noise levels. The observed difference between experimental and lattice gas results are within the shot noise level — or statistical error — in the measured force in the simulations. This force shot noise could be further reduced by collecting better statistics, but is already within the experimental errors for the most part. Perhaps more significant, in connection with the effects of shot noise on the mean dynamics, is the column in the table labeled "s/n Macro". This is the instantaneous signal to noise ratio of the *macroscopic force*. For the low Reynolds number cases this was actually less than 1. This means the instantaneous force was fluctuating wildly, time step to time step, with a *s/n ratio* of at most 3.26 for the $Re = 42.6$ run. There was hardly any evidence of hydrodynamic behavior on the individual time steps. Nonetheless, upon accumulating good statistics (in the present case this was done by time averaging and spatial averaging over the 8-site deep third dimension), the correct hydrodynamic behavior was observed to very high accuracy both in the force and the shape of the streamlines.

As a final point, we compare our drag data with CFD results. Karniadakis reports only one measured drag value for the steady eddy range of $Re < 45$. At $Re = 26$, he gets the result $C_d = 2.2$. The experimental result from Tritton is $C_d = 1.9$ at this Reynolds number indicating that the CFD result is 16 % in error, beyond the experimental error in the actual measurements.

7.4.3 Vortex Shedding, $Re > 45$

At Reynolds numbers above about 45. it is known that the two recirculating eddies do not remain steady, but alternately oscillate in size, shedding vortices that form a regular *vortex street* which propagates downstream. The frequency at which this happens is known as the Strouhal frequency and is dependent on the Reynolds number of the flow. What is not known precisely is the cause of this instability. Gresho *et al.*[69] reports that some researchers believe this phenomena to be a result of an instability in the wake, independent of the cylinder while others argue that the separation point on the trailing edge of the cylinder itself (upper and lower point behind the cylinder where the eddy is still attached) becomes unstable and its oscillatory motion causes the trailing waves.

By further increasing the cylinder diameter and number of lattice sites, the lattice gas code was run in a configuration that resulted in a Reynolds number of about 65 with a Mach number of $M = .3$. This also required elongating the inner, fine scale region, geometry in order to contain all the dynamics of shedding within a constant resolution (i.e. constant viscosity) region. The geometry of this simulation was a width of 8 sites, a height of 384 sites and a length of 2560 sites resulting in about 8 million sites total. The radius of the contained cylinder was

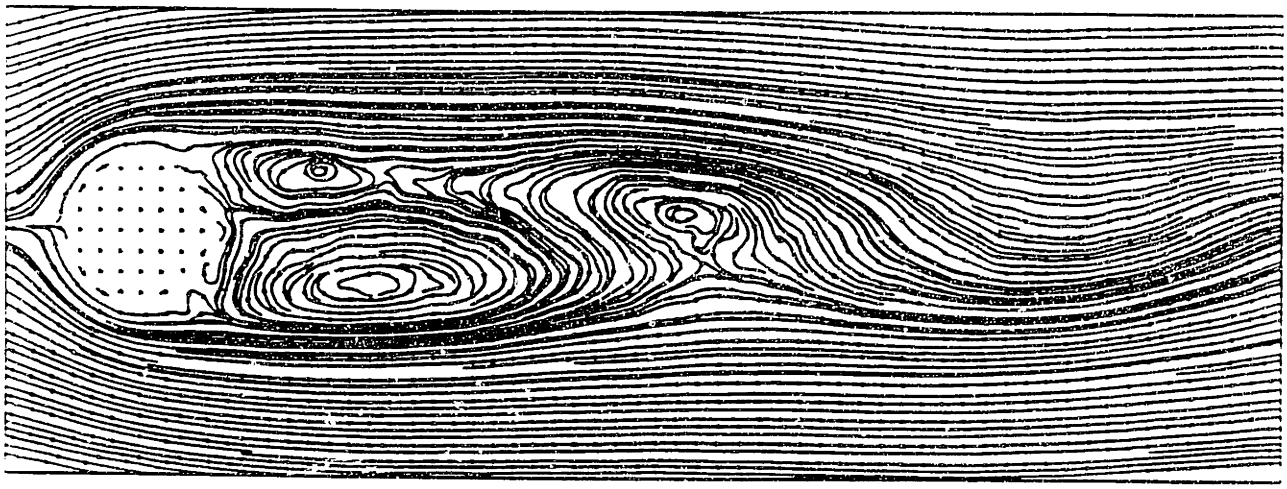

Figure 7.18: Streamline evolution during shedding at the beginning of a period. t=5600, for $Re = 65$. Two upper eddies. one shed and one still attached to the cylinder, are visible. The lower eddy is about to be shed and the remnant of the previously shed lower eddy is visible at the right.

34 lattice sites. This resulted in an 18% blockage situation[17].

Observation of the simulations showed the development of elongating eddies that became unstable and eventually set up an oscilliatory pattern with resulting shedding as would be expected for $Re > 45$. Once the simulation had reached the point of constant oscillatory period. 'snapshots' of the flow were taken at intervals throughout one period. Streamline evolution during a full period of the oscillation is displayed in figures (7.18) through (7.21). The period shown began at $t = 5600$ and ended at $t = 6800$ so that the time for one period of oscialltion was $\tau = 1200$.

[17]Essentially a limitation of software. not available memory, that can be improved in the future.

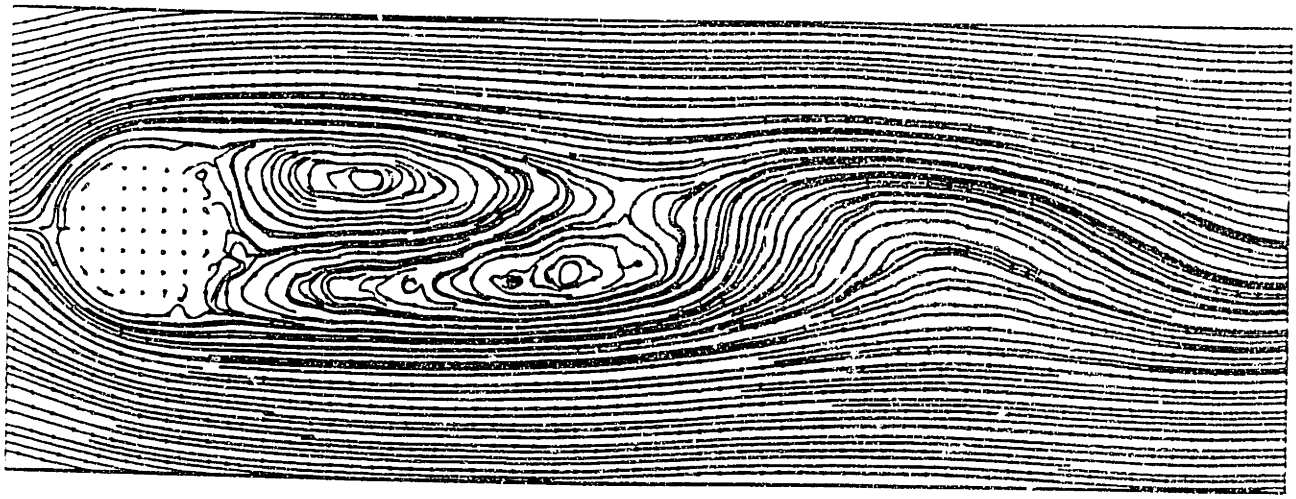

Figure 7.19: Streamline evolution during shedding one-third of the way through a period, t=6000. The lower eddy has been shed.

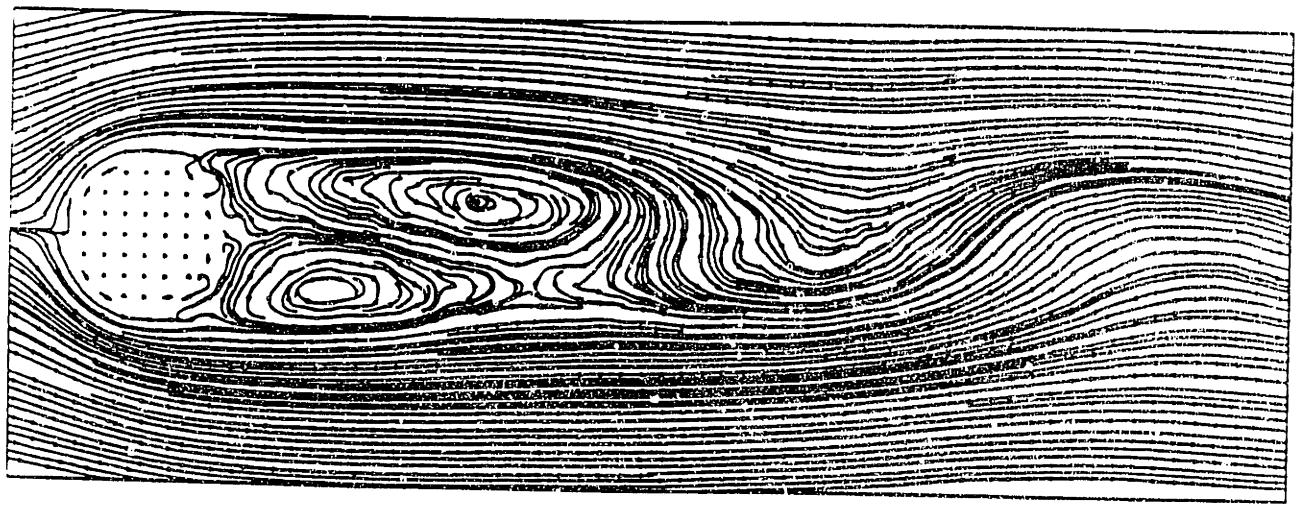

Figure 7.20: Streamline evolution during shedding two-thirds of the way through a period. t=6400. The upper eddy has been shed.

The dimensionless shedding frequency, or Strouhal number, is defined as

$$St = \frac{n\,d}{u} \tag{7.36}$$

where d is the cylinder diameter, u is the free stream velocity and n is the frequency at which the vortices are being shed. This is the inverse of the period of oscillation, $n \equiv \frac{1}{\tau}$. Thus for our case, the Strouhal number is $St \simeq .17$. The observed value at $Re = 65$ (with negligable blockage), due to Gerrard[70], is $St = .14$. Our observation of a Strouhal number about 20% higher than experimental observation is of the order of what would be expected from a blockage of 18%, since the Venturi acceleration of the flow past the cylinder would be expected to increase the frequency. Unlike the blockage correction for drag coefficient, there does not seem to be a standard technique for correcting for blockage in the Strouhal number calculation.

Simulations done with a single speed lattice gas[71] (using the hexagonal lattice in two dimensions), found that the frequency of shedding decreased by about 15% as the blockage was decreased from 30% to 20% at $Re = 108$. This qualitatively shows that the decrease in Strouhal number scales with blockage. However, the Strouhal number in the one-speed case was about a factor of 2 higher than observations at a comparable Reynolds number. This descrepancy is expected because of the lattice discreteness artifacts inherent in that model which prevents accurate hydrodynamic behaviour.

The reported values of the Strouhal number for $Re \sim 65$ from CFD simulations are in the range $St = .15 - .16$[56, 69, 72]. However, the resolution in the vortex street in these results are such that only two eddies may be observed at any instant, the eddy that is attached to the cylinder and the eddy that has just been shed [69, 72] whereas the lattice gas model results presented here enables us to see

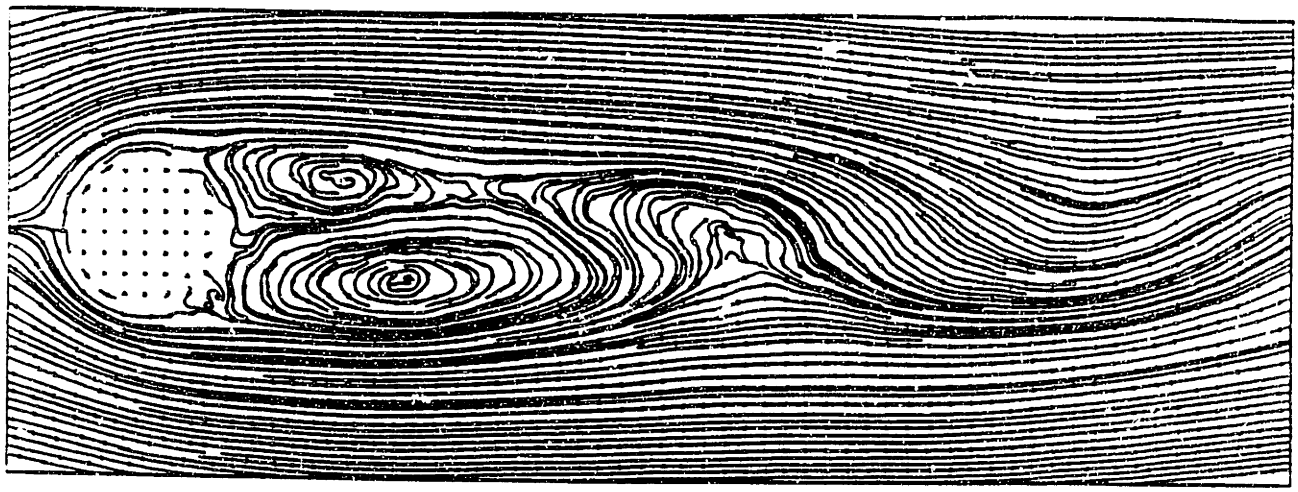

Figure 7.21: Streamline evolution during shedding after a completion of a period, t=6800. The flow here is identical to the flow at $t = 5600$, the beginning of the period.

three eddies at all times. Perhaps the most revealing statement of the inherently empirical nature of present CFD methods was given by Wang *et al.*[72] in his 1991 paper where he stated that their numerical solutions produced *symmetric wakes at Reynolds numbers greater than those for which vortex shedding is expected to occur.* It was necessary for them to perturb the flow numerically to stimulate wake asymmetry and vortex shedding when they expected that it should occur in order to produce their Strouhal number results. This is standard procedure in CFD simulation[51]. In striking contrast to this, all of the behaviour described here for the lattice gas cylinder experiment happened *naturally*, no artificial perturbation of the flow was needed to quantitatively reproduce the plethora of hydrodynamic behaviour observed in the cylinder experiment.

7.5 Summary of Lattice Simulations

We have demonstrated via computer simulation that the three-speed lattice gas model accurately describes hydrodynamic behaviour once the Galilean invariance artifact g has been removed in the way described in Section 5.1.

Shear wave decay experiments illustrated the removal of both the effect of the lattice on the advection of momentum and the anomalous dynamic pressure contribution when g=1. This is not possible in the single speed lattice case. Furthermore, accurate hydrodynamic behaviour was observed for Mach numbers up to .4 and for perturbations with half wavelengths as small as two lattice spacings, beyond the limits of what the theory would seem to allow. Simulation of flow between two flat plates illustrated that the momentum lost in the pressure drop down the tunnel was being accurately transferred to the walls in the form of shear

stresses. Finally the cylinder results demonstrated quantitative agreement with experimental results in measurements of the drag coefficient and wake length to diameter ratio for a wide array of Reynolds numbers.

The significance of these results is that they were obtained from an absolutely stable, exactly conserving algorithm with *no* adjustable parameters. It was not necessary to tailor the grid to the flow, modify the approximation scheme or adjust the boundary conditions to replicate actual flow results, and no discrepancies with experiment were observed. The system was simply driven by forcing mass through the configuration of an established size and shape, and it responded in accurate reproduction of fluid dynamic behavior, as the fundamental kinetic theory developed in Chapters 3 through 6 predicts that it must.

Although the cylinder experiment examined here was a very simple shape and we only examined low Reynolds number flow, the phenomena displayed, namely flow separation and vortex shedding, are among the most difficult to predict. Complex fluid dynamic design most often hinges on the ability to predict and control precisely these phenomena. Computational Fluid Dynamics codes either are substantially in error in comparison with experimental results in this range of Re, or must massage their simulations in the right way to get close to expected behaviour.

The accurate prediction of these features by the lattice gas method (an algorithm without adjustable convergence and smoothing parameters), is a compelling demonstration that the the lattice artifacts have been removed from the dynamics, and that the algorithm in fact behaves like a true continuum fluid.

Chapter 8

Comparison of Lattice Gas and CFD Computational Efficiency

The multiple-speed Boolean lattice gas algorithm is an inherently stable, precise physical system that can be used to directly and ideally model sub- and transonic fluid flow on a digital computer. Because the entire computational engine of the algorithm can be reduced to logic, the method is inherently stable; the primary units of computation in the lattice gas algorithm are bits which means that round-off error and other issues of numerical ill-conditioning are simply not an issue. The algorithm can be made precise because the discreteness artifacts associated with the underlying lattice can be erased from the system macrodynamics leaving the mean dynamics described exactly by the equations of hydrodynamics. Moreover, the lattice gas algorithm is comprised of two highly parallel suboperations: the collision operation which is site independent and the movement of particles along the lattice. This has resulted in the lattice gas algorithm becoming known as "embarrassingly parallel" [73] as only nearest-neighbour interprocessor communication

is required.

On the other hand, computational methods for description of fluid dynamics (CFD) approximate the elliptical (or sometimes hyperbolic for supersonic flow) partial differential equations that describe macroscopic fluid dynamics. This procedure is rife with potential pitfalls in the guise of stability concerns due to numerical round-off error and discretization step sizes, artificial or numerical viscosity and problems of uniqueness[51]. This has led to an inability of CFD to accurately predict complex fluid phenomena without having some prior knowledge of the flow being simulated. As a result. CFD has not been accepted as an alternative to actual fluid experimentation in wind tunnels nor does it seem it will ever become a general purpose substitute[1].

These properties alone point out the inherent superiority of the lattice gas algorithm over CFD as a method of fluid flow simulation. In this Chapter, we examine the computational requirements of the two methods. We will show that a lattice gas algorithm running on conventional computers actually is about as computationally efficient as current CFD methods. What makes the new algorithm truly revolutionary is the fact that it is possible to make the lattice gas algorithm execute about 1000 times faster than current CFD codes[73] by tailoring an arithmetic processing unit, of similar complexity to the floating point units found in most computers, to the needs of the Boolean lattice collision process.

The basic quantity that dictates the range of observed fluid behaviour is the Reynolds number, Re. The way that this is achieved in a simulation is through system resolution. In fact, Re and linear resolution are roughly equivalent numbers. The Reynolds number for a real gas can be written

$$Re = \frac{u L}{\nu} \sim M \frac{L}{\lambda}, \tag{8.1}$$

since $\nu \sim c_s\lambda$[16], where M is the Mach number. $M = \frac{u}{c_s}$, L is the macroscopic length scale of the flow, and λ is the molecular mean free path. The Reynolds numbers encountered in practical flows are of the order of thousands to billions. All these high Reynolds number fluids are characterized by the generation of large scale vortices or eddies spawned by the flow around objects and spatial inhomogeneities. These eddies in turn nonlinearly spawn a cascade of ever decreasing eddies until eventually being dissipated by viscosity into thermal heat energy at the so-called dissipation scale length. It has been argued by Orszag and Yakhot[49] that because of the discrete nature of the particle velocities in lattice gas algorithms, the noise that accompanies the average fluid velocity is large and an inordinate number of lattice sites must be used to resolve the fluid velocity at the dissipation scale. If true, this would make the computational work for the lattice algorithm scale very unfavourably with Reynolds number and inverse Mach number as compared to floating point methods. From the theory of Chapter 6 and the simulation results of Sections 7.2.3 and 7.2.4 we find that this conclusion is not valid for lattice gas algorithms.

In Chapter 6, we showed that the mean dynamics of the lattice gas algorithm is independent of noise so that it is not necessary to have enough lattice sites within the dissipation scale length to ensure correct behaviour at every time step. All that is needed is adequate time and spatial averaging to suppress the noise about the mean. Furthermore, the signal to noise ratio is almost independent of wavenumber so that one does *not* require an inordinate number of lattice sites per wavelength to resolve the large wavenumber fluctuations needed in the simulation of turbulence. This indicates that the resolution in a lattice gas is of order the lattice spacing, not some high Reynolds number-dependent multiple thereof, and, in fact, is about at the same level as is necessary in floating point methods. As

well, we have seen that the practical validity of the method is not limited to extremely small Mach numbers -Section 7.2.4-so that unfavourable Mach number scaling is not an issue.

The distance between two grid points, Δx, in the discretization of fluid dynamics will determine the effective mean free path in the simulated fluid. In Section 7.2.2 we found that the mean free path for the three-speed lattice gas model was actually less than 1 lattice spacing. Thus for the simulation, $\lambda \sim \Delta x$ and $Re \sim M\frac{L}{\Delta x}$. This applies for both the conventional finite element approximations of CFD and the lattice gas method we have described. Using $M = .3$. the limit of incompressibility, and $\lambda = .3\Delta x$, we have the rough relation that

$$Re \sim \frac{L}{\Delta x} \tag{8.2}$$

or that the Reynolds number scales like the number of resolved points in one direction. Therefore, in three dimensions, roughly Re^3 simulation cells are required. For example, accurate simulation of a car moving at a few kilometers an hour with $Re \sim 100\ 000$ requires 10^{15} cells. This is vastly beyond the limits of present day computer resolution, which has a current limit of about 1 million cells of resolution ($Re \sim 100$) [16, 3], nine orders of magnitude too small for accurate resolution of this problem.

Since both CFD and the lattice gas algorithm are bound by this resolution requirement, the dominant deciding factor between the two is the computational cost of evaluating a single fluid dynamical cell. There are two areas we must consider when attempting an efficiency comparison, the space requirements of either algorithm (the amount of storage required for each site) and the total time required to update each site, which includes the collision and translation processes. We will make these comparisons for the two algorithms running on a

CRAY supercomputer that has 64-bit words and supports word-oriented logical operations.

First of all, concerning space requirements, a typical CFD code must store all non-derivable thermodynamic quantities such as the velocity vector (three components), density and temperature as well as information about the local grid structure[51]. If one 64-bit word is used to store each of these variables plus a couple words for the grid structure we find that CFD requires on the order of 10 storage words per site. On the other hand, the lattice gas algorithm only needs to store the state vector for each site. In the three-speed model, this is a vector of length 54 bits to store the status of an entire site. If we say there is an additional bit required to indicate whether a site is solid or fluid and add a few bits as overhead we see that the lattice algorithm requires about 1 64-bit word to store all the necessary information for the method. From the microscopic distribution function, all macroscopic properties may be derived but this is done outside of the main engine of the method. We conclude that the lattice gas algorithm consumes about one-tenth the storage of the CFD code.

We now investigate time requirements, or equivalently, the work required to update a single cell completely. A standard rule of thumb for modern CFD algorithms is to allocate about 200 floating point operations to update a single grid point per time step[75]. For the lattice gas algorithm, we described in Section 7.1 that there are about 400 quadruplets of collisions we would like to test at each lattice site. This collision process may be performed entirely using CRAY supported logical operations in about 20 logical operations[57], ignoring register loads and stores. Since a single 64-bit word may be used to represent a three-dimensional subvolume of four lattice points on a side and we may perform logical operations

on the entire word with only one set of instructions. about 8000 instructions are required to perform the collision operations for all 64 sites. This works out to about 125 operations per site. Factoring in move operations, [1] statistics gathering and boundary reflections, about 200 instructions are required per site per timestep. We conclude that if the number of lattice sites in the two simulation methods are roughly the same, then the lattice gas and CFD codes should execute in similar amounts of time. A similar comparison of the computational work required for floating-point methods and lattice gas methods has been made by Zaleski[74].

The principle reason why a CFD code keeps up with a lattice gas code is the heavy hardware investment made in high performance processors for floating point operations. Because a lattice gas engine uses no floating point, the lattice code gains no advantage from hardware which one might view as highly specialized support for the numerical solution of partial differential equations. If we could run a CFD code on a processor with no hardware-supported floating point operations we would find that its performance would be a disaster. Since all the previously supported complex floating operations would now be reduced to their many step logical equivalents, each grid update would now take tens of thousands of instructions[76]. It would seem that an equally spectacular *speed-up* of the lattice gas update procedure could be accomplished if a specialized arithmetical processor could be discovered for the collsion update procedure that the lattice gas algorithm is repeatedly performing. In fact, it is trivial to specify a pipelined collision logic, with a design complexity equivalent to traditional pipelined floating point multiplier units, that achieves a throughput of about one lattice site updated per clock or operation[73]. This represents an improvement in computa-

[1] Which has computational requirements that scale like the ratio of surface area to the volume of the subvolume in comparison with the collisional requirements[57].

tional efficiency of over 100 times in comparison with the moderately parallelized word-per-state lattice gas formulation on a 64-bit processor!

We conclude that although the computational work required for current CFD codes and the lattice gas three-speed algorithm is about the same on the CRAY 64-bit processor, specialization resulting in a dedicated collision logic unit for the lattice gas algorithm, of comparable complexity to the floating point processor in conventional computers, would result in a storage $\times$ efficiency win for the lattice algorithm over the CFD code operating on the CRAY of about three orders of magnitude. If this 1000-fold increase in computational power was translated into lattice sites, this would allow the lattice algorithm to simulate flows with $Re = 2000 - 5000$. While this result is a huge improvent over present limitations for accurately resolved flow, $Re \sim 100$, these values are still well below the range of most practical flow phenomena. In order to get to large Reynolds numbers, a truly *BIG* machine would have to be designed. It is estimated[73] that a computer with 10 million chips, using a highly specialized collision update processor, with 1 million lattice sites per chip could attain a Reynolds number of about 1 million, which would allow adequate resolution of the atmosphere to a lattice spacing equivalent to 100 meters. Such a machine would consume about 100 MegaWatts of power and cost about the same as a large wind tunnel.

Alternatively, for large Reynolds number flows where the width of the boundary layer scales with the inverse square root of the Reynolds number[5] the relevant scaling is that the square root of the Reynolds number scales with the number of linear sites in the boundary layer. Consequently, in this regime the lattice gas algorithm could reach Reynolds numbers in the 100 000 to one million range which would allow for the simulation of many practical flows.

Chapter 9

Conclusions

Multiple speed lattice gas methods can be made to accurately and efficiently model a true continuum fluid. In this thesis, we have developed the general theory for multiple speed lattice gas algorithms employed on the 4D face-centred hypercube lattice, where previously only a theory for single speed models existed, and specifically have found a series of low-speed models that remove the artifacts inherent to the lattice gas method. For one of the methods, the three-speed model that removes the Galilean invariance factor from the momentum equation, we have demonstrated for the first time the ability of lattice gas algorithms[1] to reproduce quantitatively correct hydrodynamic behaviour through simulation and accurate reproduction of important flow properties of a few basic fluid experiments such as flow between flat plates and flow around a circular cylinder.

The two main advantages of using multiple speed lattice gas algorithms to simulate fluid flow are its algorithmic accuracy and its computational efficiency,

[1] an algorithm based entirely on logical operations

as we have demonstrated in this work.

Algorithmic accuracy is a result of having completely removed the discreteness artifacts from the macroscopic dynamics and maintaining mean dynamics that are unaffected by shot noise. In the limit of an infinite discrete continuum of speeds, the 4D FCHC lattice gas has the property that the artifacts converge naturally to their continuum values. The 4D FCHC lattice, the only regular lattice that permits this to happen, has the following characteristics: 1) It permits all integral energies to be represented, 2) The set of velocity vectors for each energy have sufficient symmetry to allow for an isotropic stress tensor at each energy *individually*, 3) All energies may interact via energy exchange collisions, and 4) Discrete microscopic Galilean invariance. All of these properties are required of the underlying lattice if we are to extend the LGA concept to infinite speeds. In finite multiple speed systems, the artifacts can be removed by adjusting an added degree of freedom which allows the rates of energy exchange collisions between particles to be alterred. Since each added rate coefficient adds enough freedom to the system to set one artifact equal to its correct continuum value, to remove all three artifacts we need a system with three rate coefficients or in the low-density limit where there are only two artifacts, two rate coefficients. Besides the three-speed model for accurately describing momentum transfer, the four-speed model derived here will allow accurate simulation of heat transfer problems at low to moderate Mach numbers ($M \leq .15$) while the low density five-speed model removes all lattice artifacts from the conservation equations. The mean dynamics remains true despite large fluctuations in instantaneous flow characteristics because the Boolean nature of the lattice advection term and collision operator results in a *Shot Noise Theorem* that states that the mean kinetic theory dynamics of a lattice gas are independent of the shot noise fluctuation level to all orders in the

fluctuations. All non-shot noise fluctuations were negligible in the simulations we performed due to the large number of lattice sites in the models simulated.

The computational efficiency of the algorithm stems from the inherent simplicity of the logical operations that fully describe the dynamics together with the very high collisional efficiency that comes from the discretization. In contrast with a real fluid that requires a large number of particles to overcome the short range nature of the intermolecular forces to ensure effective collisionality, the discrete property of the lattice algorithm coupled with the possibility of multiple residency of a site at a given time permits a very short mean free path for collisions. Thus, very efficient collisionality is possible in the lattice algorithm. This condition, plus the conservation of mass, momentum, and energy, are necessary ingredients for hydrodynamics. With reference to computational work requirements, this result ensures that there is no computational effort wasted on resolving cells where interaction does not occur.

The significance of our simulation results is that they were obtained from an absolutely stable, exactly conserving algorithm with *no* adjustable parameters. It was not necessary to tailor the grid to the flow, modify the approximation scheme or adjust the boundary conditions to replicate actual flow results, and no discrepancies with experiment were observed. The system was simply driven by forcing mass through the configuration of an established size and shape, and it responded in accurate reproduction of fluid dynamic behavior, as the fundamental kinetic theory developed in this work predicts that it must.

Clearly, the next step is to validate the ability of lattice gas models to replicate heat transfer in the continuum accurately. The four-speed model developed here removes the Galilean invariance artifact, g, and the ratio of specific heats

artifact, γ, which should result in accurate heat and momentum transfer in low Mach number fluids, $M \leq 0.15$. Thus this model is the ideal candidate for such tests. Essentially all that is needed is the extension of the state-space vector from fifty-four to 150 elements (there are ninety-six possible directions for energy=3 particles) and the extension of the current list of 276 collisions to include energy=3 particles in the collisions. Because the largest component in the energy=3 vector is the same as in the energy=2 vectors that are already present in the LGA code[2], no additional support is needed in the 'move-particle' portion of the code. This is also true of the low-density no-artifact five-speed model that requires a state-space of 169 elements (only one stopped particle).

Lattice Gas models are not constrained to simulate only the behaviour of single phase ideal gases. Gunstensen & Rothman[36] have demonstrated how attaching the notion of "colour" to lattice particles allows the simulation of different phases and immiscible fluids. These researchers also found that it was necessary to remove the Galilean invariance factor artifact to get even *qualitatively* accurate hydrodynamic behaviour. By introducing nearest-neighbour interaction potentials for particles on a two-dimensional FHP lattice, Chen *et al.*[77] have shown how a lattice gas can have a nonideal gas equation of state. Unfortunately, this model does not remove the Galilean invariance artifact and it does not seem that the multiple-speed theory developed here will allow easy removal of this artifact once potential energy has been added to the model[39]. New research is also continuing in the application of lattice gas models to simulate other diverse phenomena such as flow through porous media, chemical reactions, diffusion and even magnetohydrodynamics.

[2]Energy =2: (1,1,1,1) or (2,0,0,0) Energy =3: (2,1,1,0)

A necessary prerequisite for accurate simulation of any of these applications is the removal of the discretness artifacts from the basic conservation equations of lattice gas methods. It is only then that the promise of ~ 1000 times computational efficiency improvement over CFD becomes meaningful. With the models developed in this work, this step has been accomplished.

Appendix A

Equilibrium Solution for Lattice Gases

In this appendix, we prove that the following two statements are equivalent:

- The N_{jli} 's are a solution of the set of equations

$$C_{\mathrm{j}}(n_{\mathrm{j}}) = \sum_{s,s'}(s'_{\mathrm{j}} - s_{\mathrm{j}})A(s \rightarrow s')\prod_{\mathrm{j}'} N_{\mathrm{j}'}^{s_{\mathrm{j}'}}(1 - N_{\mathrm{j}'})^{(1-s_{\mathrm{j}'})} = 0 \quad \forall \mathrm{j} \qquad \text{(A.1)}$$

- The N_{jli} 's are given by a generalized Fermi-Dirac distribution

$$N_{jli} = \frac{r_j}{r_j + exp(\alpha m_j + \gamma m_j \mathbf{c}_{jli} \cdot \mathbf{u} + \beta \epsilon_j)} \qquad \text{(A.2)}$$

  where $r_j \equiv \langle I^j \rangle / \langle F^j \rangle$, is the rate coefficient factor, α, γ, β are arbitrary real numbers, and $\mathbf{u}$, is an arbitrary D-dimensional vector. The quantities, m_j, $\mathbf{c}_{jli}$, and $\epsilon_j = \frac{1}{2} m_j c_j^2$, are the microscopic mass velocity and energy, respectively.

In Section 2 we defined average hole and quasi-particle densities as follows:

$$\mathcal{N}_{jli} = \langle F^0 \rangle N_{jli} \tag{A.3}$$

and

$$\bar{\mathcal{N}}_{jli} = \langle I^0 \rangle \bar{N}_{jli} \tag{A.4}$$

We then have an equation identical to eqn. (A.1) for the quasi-particle densities except N_j is replaced with $\mathcal{N}_{\mathbf{j}}$,

$$C_{\mathbf{j}}(\mathcal{N}_{\mathbf{j}}) = \sum_{s,s'}(s'_{\mathbf{j}} - s_{\mathbf{j}})A(s \to s') \prod_{\mathbf{j}'} \mathcal{N}_{\mathbf{j}'}^{s_{\mathbf{j}'}}(1 - \mathcal{N}_{\mathbf{j}'})^{(1-s_{\mathbf{j}'})} \tag{A.5}$$

We define

$$\hat{\mathcal{N}}_{\mathbf{i}} = \frac{\mathcal{N}_{\mathbf{i}}}{1 - \mathcal{N}_{\mathbf{i}}} \tag{A.6}$$

and

$$\prod = \prod_{\mathbf{i}}(1 - \mathcal{N}_{\mathbf{i}}) \tag{A.7}$$

Equation (A.5) may now be written

$$C_{\mathbf{j}}(\mathcal{N}_{\mathbf{j}}) / \prod = \sum_{s,s'}(s_{\mathbf{j}'} - s_{\mathbf{j}})A(s \to s') \prod_{\mathbf{j}'} \hat{\mathcal{N}}_{\mathbf{j}'}^{s_{\mathbf{j}'}} = 0. \tag{A.8}$$

Break this into two sums

$$\sum_{s,s'} s_{\mathbf{j}'} A(s_{\mathbf{j}} \to s_{\mathbf{j}'}) \prod_{\mathbf{j}'} \hat{\mathcal{N}}_{\mathbf{j}'}^{s_{\mathbf{j}'}} - \sum_{s,s'} s_{\mathbf{j}} A(s_{\mathbf{j}} \to s_{\mathbf{j}'}) \prod_{\mathbf{j}'} \hat{\mathcal{N}}_{\mathbf{j}'}^{s_{\mathbf{j}'}} = 0. \tag{A.9}$$

In the first sum, interchange the primed variables ($s_{\mathbf{j}} \leftrightarrow s'_{\mathbf{j}}$)

$$\sum_{s,s'} s_j A(s'_j \to s_j) \prod_{j'} \hat{\mathcal{N}}_{j'}^{s'_{j'}} - \sum_{s,s'} s_j A(s_j \to s'_j \prod_{j'} \hat{\mathcal{N}}_{j'}^{s_{j'}} = 0. \tag{A.10}$$

The main reason for introducing these script variables was that the transition probability now obeys the detailed balance condition

$$A(s'_j \to s_j) = A(s_j \to s'_j) \tag{A.11}$$

Thus we may replace A in the first sum of eqn. (A.10) and combine the two terms into one,

$$\sum_{s,s'} s_j A(s'_j \to s_j) \prod_{j'} \left(\hat{\mathcal{N}}_{j'}^{s'_{j'}} - \hat{\mathcal{N}}_{j'}^{s_{j'}} \right) = 0. \tag{A.12}$$

For this to vanish, we must have

$$\prod_{j'} \hat{\mathcal{N}}_{j'}^{s'_{j'}} = \prod_{j'} \hat{\mathcal{N}}_{j'}^{s_{j'}}, \text{ whenever } A(s \to s') \neq 0 \tag{A.13}$$

If we take the logarithm of both sides we find that this is equivalent to

$$\sum_{j} \ln(\hat{\mathcal{N}}_{j'})(s'_{j'} - s_{j'}) = 0 \quad \forall s, s' \tag{A.14}$$

This equation indicates that $\ln(\hat{\mathcal{N}}_{j'})$ is a collision invariant. Because there are no spurious invariants, $\ln(\hat{\mathcal{N}}_{j'})$ must be a linear combination of the three known invariants – mass, momentum, and energy,

$$\ln(\hat{\mathcal{N}}_{j'}) = -(\alpha m_j + \gamma m_j \mathbf{c}_{jli} \cdot \mathbf{u} + \beta \epsilon_j) \tag{A.15}$$

Using the fact that eqn. (A.6) implies

$$\hat{\mathcal{N}}_j = \frac{\hat{\mathcal{N}}_j}{1-\hat{\mathcal{N}}_j} = \frac{\langle I^j \rangle N_j}{\langle I^j \rangle (1-N_j)} = \frac{N_j}{r_j(1-N_j)} \tag{A.16}$$

since $r_j = \langle I^j \rangle / \langle F^j \rangle$, we solve for N_j,

$$N_j = \frac{r_j \hat{\mathcal{N}}_j}{1 + r_j \hat{\mathcal{N}}_j} = \frac{r_j}{r_j + 1/\hat{\mathcal{N}}_j} \tag{A.17}$$

Plugging in for $\hat{\mathcal{N}}_j$ from eqn. (A.15) gives the final result

$$N_{jli} = \frac{r_j}{r_j + exp(\alpha m_j + \gamma m_j \mathbf{c}_{jli} \cdot \mathbf{u} + \beta \epsilon_j)}. \tag{A.18}$$

Thus we have an H-theorem that assures the Fermi-Dirac distribution function when thermal equilibrium is reached.

Appendix B

The Second Root that Makes $g' = 1$ in the Continuum

In Section 4.1 we calculated an expression for the third lattice artifact, g', in the continuum (eqn. (4.10))

$$g' = \frac{n+2}{(D+2)(n+1)^2}\left[n(DK(n,a)+2) + (\frac{D^2}{2} - D)(1 - K(n,a)) + 2\right] \quad \text{(B.1)}$$

where K(n,a) was a function with the following form

$$K(n,a) = \frac{n}{n+1}\frac{\langle E^{n+1}\rangle\langle E^{n-1}\rangle}{\langle E^n\rangle^2}. \quad \text{(B.2)}$$

The notation $\langle E^n\rangle$ stands for

$$\langle E^n\rangle \equiv \int_0^\infty cE^n N dE \quad \text{(B.3)}$$

where N is the distribution function and c is a constant, the value of which is not important for this analysis. Although we know that N has Fermi-Dirac form for a lattice gas,

$$N = \frac{1}{1 + a\exp(E/T)} \quad \text{(B.4)}$$

we begin by examining the result for N being Maxwellian

$$N = \frac{1}{a}\exp(-E/T) \tag{B.5}$$

which is the limit of the Fermi-Dirac expression for large values of a. It is possible to calculate K(n,a) since for N Maxwellian and $n > 0$

$$\langle E^{n+1}\rangle = n(n+1)T^2\langle E^{n-1}\rangle \tag{B.6}$$

$$\langle E^{n}\rangle = nT\langle E^{n-1}\rangle. \tag{B.7}$$

Plugging this into eqn.(B.2) we find that

$$K(n,a) = 1 \tag{B.8}$$

so that eqn.(B.1) reduces to

$$g' = \frac{n+2}{(D+2)(n+1)^2}\left[n(D+2)+2\right]. \tag{B.9}$$

When we require that $g' = 1$ in order to remove this artifact, there is only one solution for n

$$n = \frac{D-2}{2}, \tag{B.10}$$

the one we expect.

Returning to the Fermi-Dirac distribution, the expression for K(n,a) does not simplify and when we solve eqn.(B.1) with $g' = 1$ we get two solutions, the desired $n = \frac{D-2}{2}$ and the implicit equation

$$(n+2)(1-K(n,a)) - \frac{2}{D} = 0. \tag{B.11}$$

We expect that for large values of a, where Fermi-Dirac approaches Maxwellian, that K(n,a) $\rightarrow$ 1 and there is no solution to the above relation. When N is Fermi-Dirac, it is not possible to do the integration indicated in eqn. (B.3) in closed form

but for $a \geq 1$ we can represent this integral as an infinite sum

$$\langle E^n \rangle = \int_0^\infty \frac{E^n dE}{1 + a\exp(E/T)} = n! T^{n+1} \sum_{k=1}^{\infty} \left(\frac{1}{a}\right)^k \frac{(-1)^{k+1}}{k^{n+1}}. \tag{B.12}$$

The sum does not converge for $a < 1$. The expression for K(n,a) when $a \geq 1$ can then be written as

$$K(n,a) = \frac{\left[\sum_{k=1}^{\infty} (\frac{1}{a})^k \frac{(-1)^{k+1}}{k^n}\right] \left[\sum_{k=1}^{\infty} (\frac{1}{a})^k \frac{(-1)^{k+1}}{k^{n+2}}\right]}{\left[\sum_{k=1}^{\infty} (\frac{1}{a})^k \frac{(-1)^{k+1}}{k^{n+1}}\right]^2} \tag{B.13}$$

so that K(n,a) is independent of temperature. The expression K(n,a) was calculated numerically for the range $0 < n \leq 8.0$ and $0 < a \leq 10.$, see Figure B.1. For a given value of a, K(n,a) increases monotonically with n to asymptotically approach the value 1. This is because as n becomes large, the numerator and denominator of K(n,a) become equal as can be seen in eqn. (B.13). For fixed n, raising a causes N to approach a Maxwellian. Thus we would expect K(n,a) to approach the value 1., as observed.

With these values of K(n,a) we may investigate eqn.(B.11), with D=4 since our model is 4-dimensional, to see if there are any roots to this implicit equation. We split the analysis of this equation into two regions, $a > 1$ and $a << 1$ for convenience. We wish to find values of n that make eqn.(B.11) equal zero. Figure B.2 shows this equation plotted for values of a greater than one. We find that there are no roots because K(n,a) is close enough to 1.0 in this range that a solution is not possible. When we investigate values of a considerably less than one, however, we find that solutions *are* possible since for small a, K(n,a) may be appreciably less than the value one (see Figure B.3). There are values of n and a that make eqn.(B.11) equal zero in this range. Figure B.4 shows that for $a < .3$, there are values of n that will make $g' = 1$.

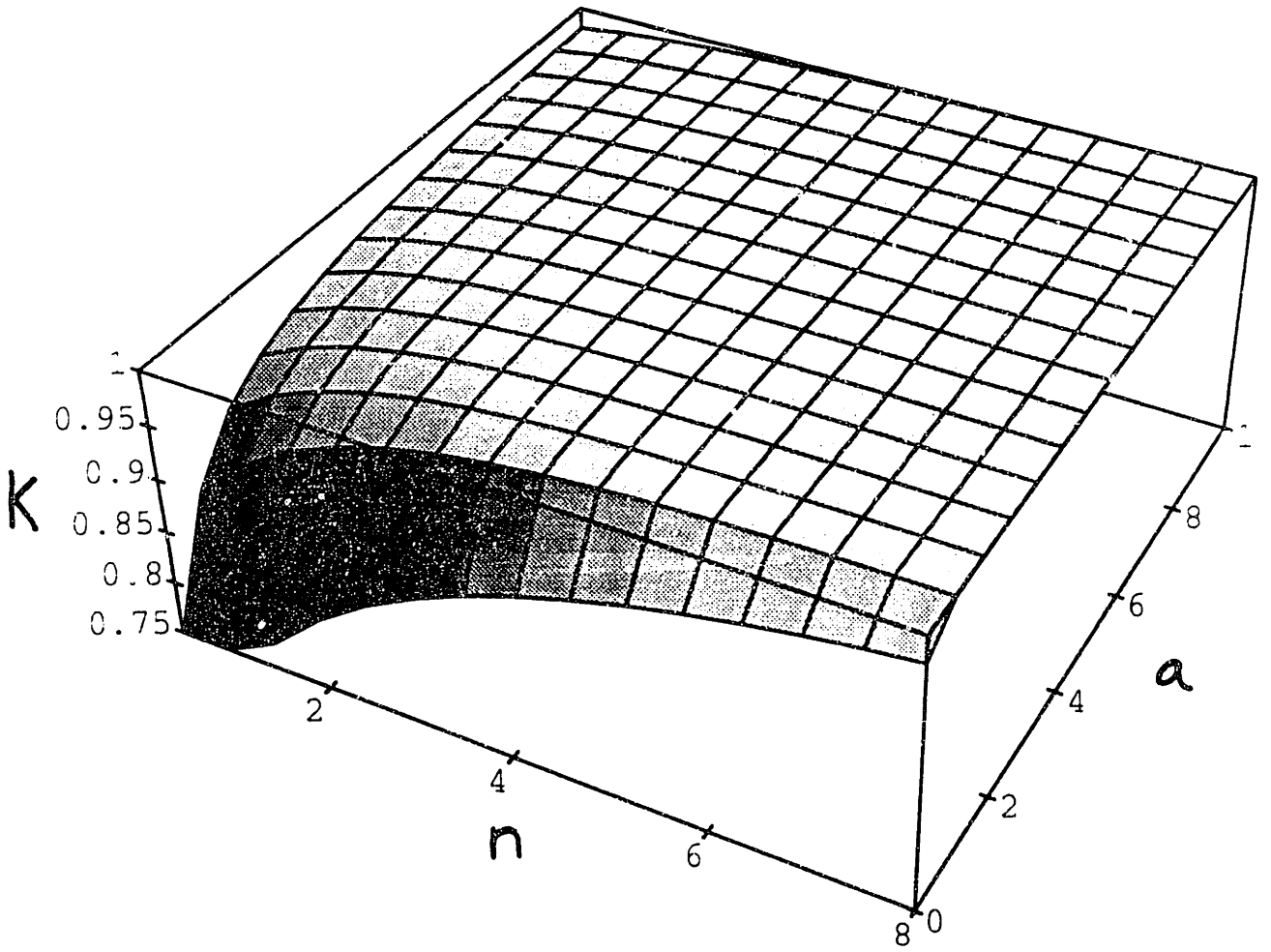

Figure B.1: The quantity K(n,a) used to calculate the second root for the $g' = 1$ equation for the range $0 < n \leq 8$ and $0 < a \leq 10$. This quantity approaches the Maxwellian value of 1 when either n or a becomes large.

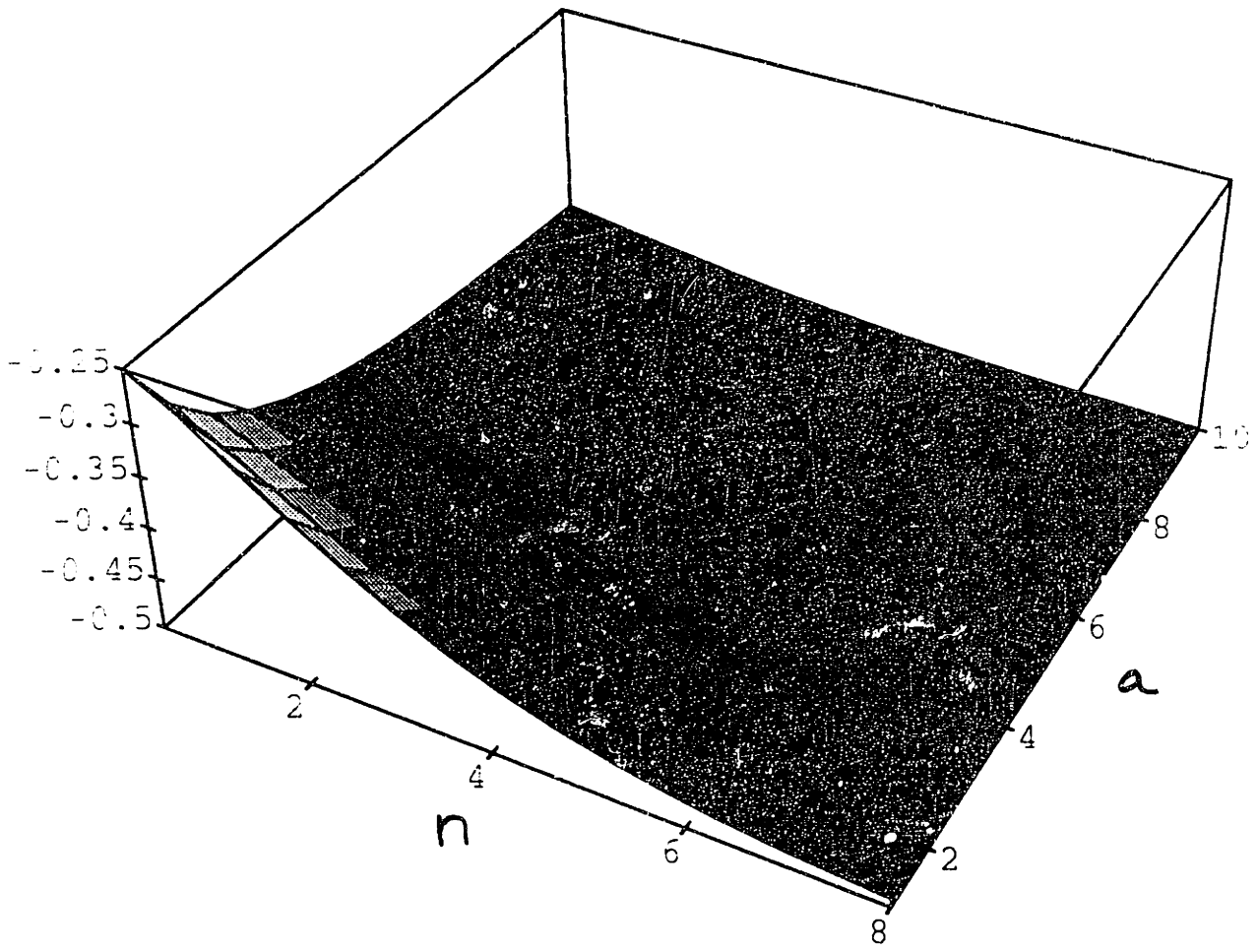

Figure B.2: Plot of the implicit second root for $g' = 1$ for the range $0 < n \leq 8$ and $1. \leq a \leq 10.$ For the inverse fugacity, $a > 1$, there is no solution as the root equation cannot be satisfied.

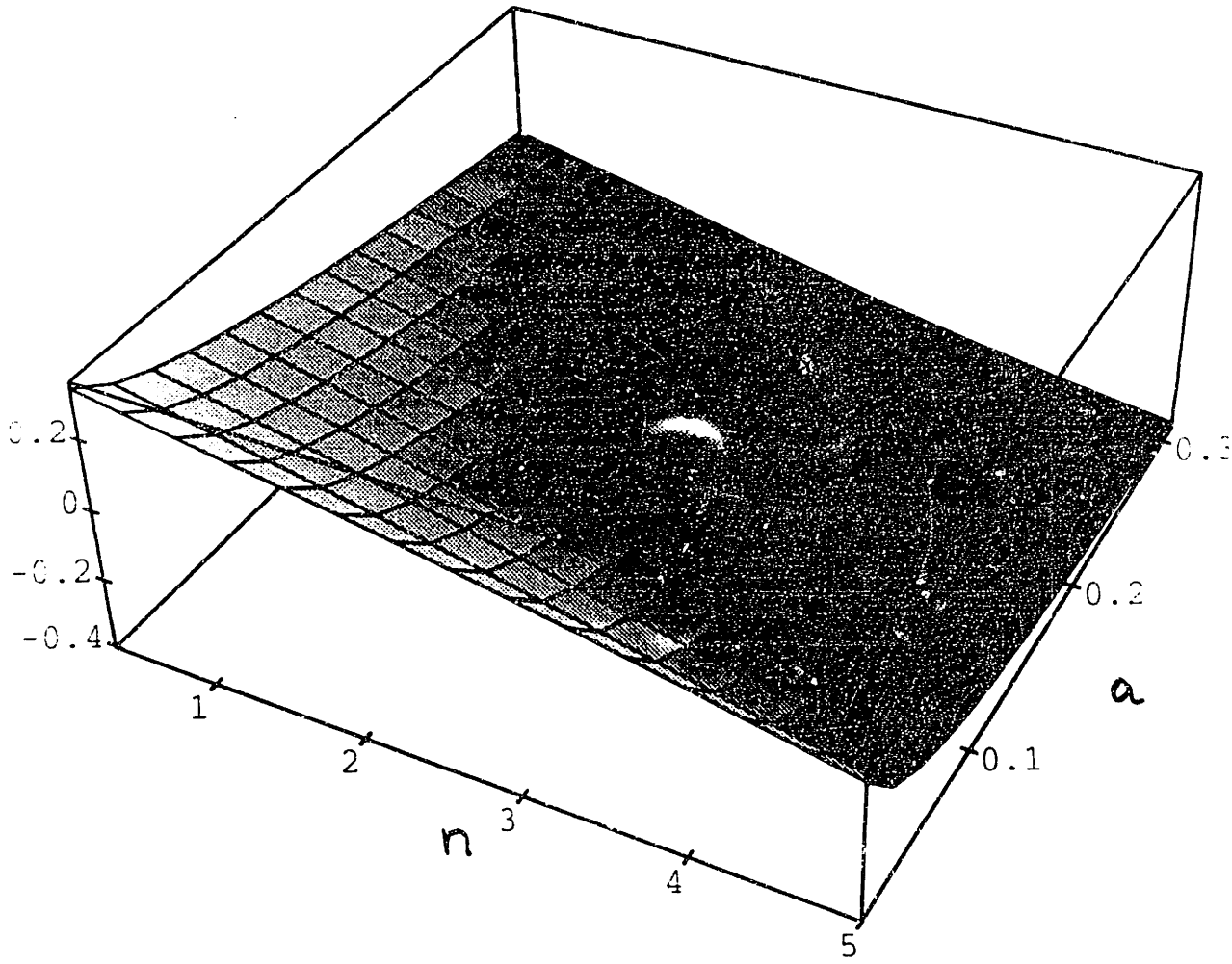

Figure B.3: Plot of the implicit second root for $g' = 1$ for the range $0 < n \leq 8$ and $0.0 \leq a \leq 0.3$. We see for a value of the inverse fugacity much less than 1, the equation may be satisifed. The solution is the locus of points that gives the value zero in the above graph.

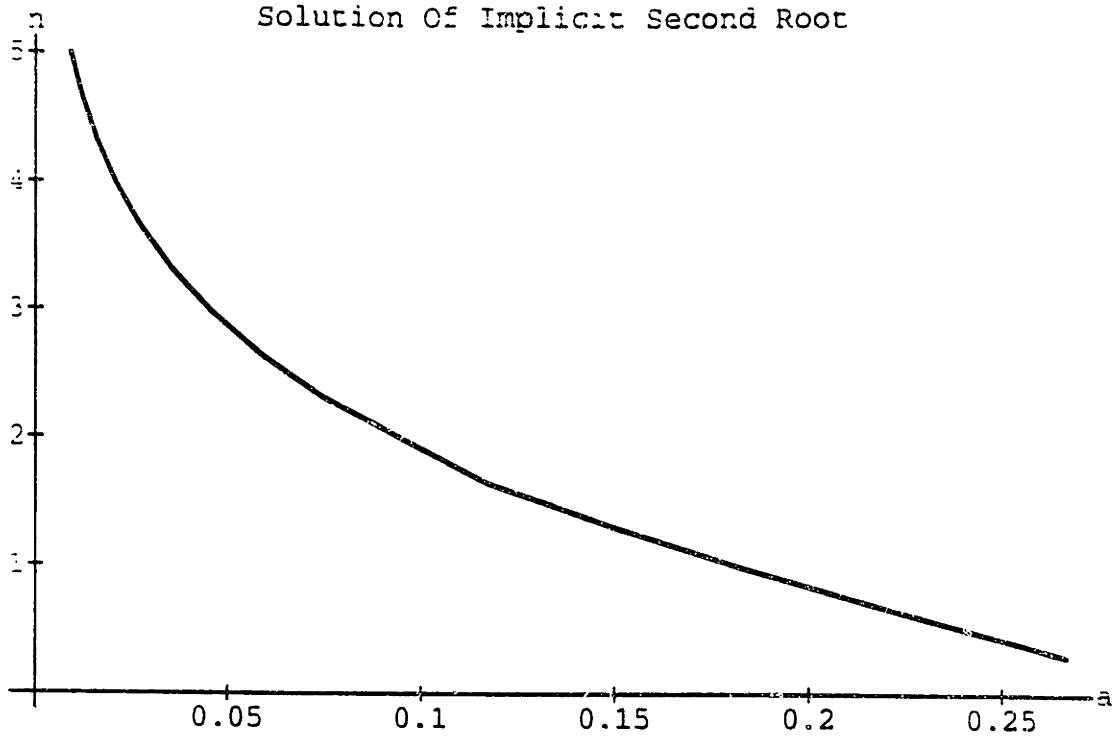

Figure B.4: The locus of points, n(a), that makes $g' = 1$. For a given value of a < .3, there is a value of n that will make $g' = 1$. Although a solution exists, it has no physical significance.

When interpreting this result, we must remember that this analysis was based on conjecturing a form of the lattice property, d_j - the number of directions for a specific species j - that was linearly related to energy raised to some power n. We have found two solutions, one that depends only on the dimensional space of the system and one that depends on the dimension as well as a property of the fluid, namely the inverse fugacity, a. Since it does not make physical sense that a lattice property should depend on the fluid it is trying to simulate, we are forced to conclude that the second solution is extraneous and should be ignored.

Appendix C

Proof of Fourth-Order Symmetry Relation

In Section 4.1.1 we proved that the 4D FCHC lattice has sufficient symmetry to ensure that both the second and fourth order stress tensor is symmetric for every energy individually. In fact, we found that this was the *only* regular lattice that had this remarkable property. The fact that the fourth-order tensor was symmetric hinged on a series of classical results from the theory of numbers that we will restate here.

First of all, let $R_4(n)$ be the number of ways the non-negative integer n can be represented as the sum of four squares; i.e. $R_4(n)$ is the number of different integral solutions (x_1, x_2, x_3, x_4) of the equation

$$x_1^2 + x_2^2 + x_3^2 + x_4^2 = n \tag{C.1}$$

where the sign and order of the x_i matter. The first result is that

$$R_4(n) > 0 \tag{C.2}$$

for all n. This was proved by Lagrange, with some help from Euler, in 1770[44]. Secondly, the value of $R_4(n)$ for all n is known and is given by

$$R_4(n) = 8\sigma(n) \qquad \text{if n is } odd \tag{C.3}$$

$$R_4(n) = 24\sigma^{\circ}(n) \qquad \text{if n is } even \tag{C.4}$$

which was discovered and proved by Jacobi in 1828[44]. The function $\sigma(n)$ is the sum of the divisors of n and $\sigma^{\circ}(n)$ is the sum of only the *odd* divisors of n. Note that in our notation $R_4(n) \equiv d_j$ and $n \equiv c_j^2$ where the latter is always even due to the nature of the FCHC lattice.

The third result, which we used for the fourth-order symmetry proof, is

$$\sum_{n}(x_1^4 + x_2^4 + x_3^4 + x_4^4) = \tfrac{1}{2}n^2 R_4(n) \tag{C.5}$$

where n is any *even* integer. The summation takes place over all $R_4(n)$ quadruples that satisfy eqn. (C.1). This result was stated by Liouville but first proved by Stern[45] in 1889. Unlike the first two results, which are found in most elementary textbooks on number theory, this third result seems to have remained obscure with only a paper by Rankin[47] in 1945 making reference to it. For this reason, a proof of eqn.(C.5) based on Stern's method is provided here.

Stern derived this result by observing that every representation

$$m = x_1^2 + x_2^2 + x_3^2 + x_4^2 \qquad \text{where } m \text{ is odd} \tag{C.6}$$

gives rise, in general, to three representations of the even number $n = 2^{2l+1}m$, where l is a non-negative integer, namely

$$\begin{aligned} n = 2^{2l+1}m &= 2^{2l}\left[(x_1+x_2)^2 + (x_1-x_2)^2 + (x_3+x_4)^2 + (x_3-x_4)^2\right] \\ &= 2^{2l}\left[(x_1+x_3)^2 + (x_1-x_3)^2 + (x_2+x_4)^2 + (x_2-x_4)^2\right] \\ &= 2^{2l}\left[(x_1+x_4)^2 + (x_1-x_4)^2 + (x_2+x_3)^2 + (x_2-x_3)^2\right] \end{aligned} \tag{C.7}$$

and also three representations of the even number $n = 2^{2(l+1)}m$ where l is again integral and non-negative. namely

$$\begin{aligned} n = 2^{2(l+1)}m &= 2^{2l}\left[(2x_1)^2 + (2x_2)^2 + (2x_3)^2 + (2x_4)^2\right] \\ &= 2^{2l}\left[(x_1 + x_2 + x_3 + x_4)^2 + (x_1 - x_2 + x_3 - x_4)^2\right. \\ &\quad \left. +(x_1 + x_2 - x_3 - x_4)^2 + (x_1 - x_2 - x_3 + x_4)^2\right] \qquad \text{(C.8)} \\ &= 2^{2l}\left[(x_1 + x_2 + x_3 - x_4)^2 + (x_1 - x_2 + x_3 + x_4)^2\right. \\ &\quad \left. +(x_1 + x_2 - x_3 + x_4)^2 + (x_1 - x_2 - x_3 - x_4)^2\right]. \end{aligned}$$

Even though these representations need not all be different (e.g. if $x_2 = x_3$) we know from eqn. (C.4) that the number of representations $R_4(n)$ for n even only depends on the *odd* divisors of n. Thus, factors of 2 in n do not affect the value of $R_4(n)$. Using eqn. (C.3) we may conclude that

$$R_4(2^{2l+1}m) = R_4(2^{2(l+1)}m) = 3R_4(m) \qquad \text{(C.9)}$$

where m is odd and l is a non-negative integer. Since there are three times as many representations of the even number n as the odd number m where $n = 2^k m$, k being integral and non-negative, and we have expressions for three representations of n using the components of the solutions for representing m, eqns. (C.7) and (C.8), we find that a sum over the solutions of

$$n = y_1^2 + y_2^2 + y_3^2 + y_4^2 \qquad \text{where } n \text{ is even} \qquad \text{(C.10)}$$

of some function of the quantities (y_1, y_2, y_3, y_4) is equal to a sum over the solutions of the ways of representing m, eqn. (C.6), of the same function of the x_i in the combinations represented on the right side of either eqn. (C.7) or (C.8), depending on whether n is an odd multiple of 2 or an even multiple of 2 multiplied by m.

In particular, the function may be the sum of the fourth powers of the components of the solutions. In this case, there are two identities that we use to aid us in the proof

$$\begin{aligned} 6(x_1^2+x_2^2+x_3^2+x_4^2)^2 &= (x_1+x_2)^4+(x_1-x_2)^4+(x_3+x_4)^4 \\ &+ (x_3-x_4)^4+(x_1+x_3)^4+(x_1-x_3)^4 \\ &+ (x_2+x_4)^4+(x_2-x_4)^4+(x_1+x_4)^4 \\ &+ (x_1-x_4)^4+(x_2+x_3)^4+(x_2-x_3)^4 \end{aligned} \tag{C.11}$$

and

$$\begin{aligned} 24(x_1^2+x_2^2+x_3^2+x_4^2)^2 &= (2x_1)^4+(2x_2)^4+(2x_3)^4+(2x_4)^4 \\ &+ (x_1+x_2+x_3+x_4)^4+(x_1-x_2+x_3-x_4)^4 \\ &+ (x_1+x_2-x_3-x_4)^4+(x_1-x_2-x_3+x_4)^4 \\ &+ (x_1+x_2+x_3-x_4)^4+(x_1-x_2+x_3+x_4)^4 \\ &+ (x_1+x_2-x_3+x_4)^4+(x_1-x_2-x_3-x_4)^4. \end{aligned} \tag{C.12}$$

Thus for $n = 2^{2l+1}m$,

$$\begin{aligned} \sum_n (y_1^4+y_2^4+y_3^4+y_4^4) &= \sum_m 2^{4l}\left\{(x_1+x_2)^4+(x_1-x_2)^4+\cdots+(x_2-x_3)^4\right\} \\ &= 6\times 2^{4l}\sum_m (x_1^2+x_2^2+x_3^2+x_4^2)^2 \\ &= 6\times 2^{4l}m^2R_4(m) = 6\times 2^{4l}\frac{n^2}{2^{4l+2}}\frac{R_4(n)}{3} \\ &= \tfrac{1}{2}n^2R_4(n) \end{aligned} \tag{C.13}$$

the final result. Similarly, for $n = 2^{2(l+1)}m$,

$$\sum_n (y_1^4+y_2^4+y_3^4+y_4^4) = \sum_m 2^{4l}\left\{(2x_1)^4+(2x_2)^4+\cdots+(x_1-x_2-x_3-x_4)^4\right\}$$

$$
\begin{aligned}
&= 24 \times 2^{4l} \sum_{m} (x_1^2 + x_2^2 + x_3^2 + x_4^2)^2 \\
&= 24 \times 2^{4l} m^2 R_4(m) = 24 \times 2^{4l} \frac{n^2}{2^{4l+4}} \frac{R_4(n)}{3} \\
&= \tfrac{1}{2} n^2 R_4(n). \qquad \text{(C.14)}
\end{aligned}
$$

We have now completed the proof of eqn. (C.5) for n even, a relation that allows us to prove that the fourth-order stress tensor is completely symmetric for all energies individually in the 4D FCHC lattice.

Bibliography

[1] "CFD: An Assessment Of Critical Technologies," Aerospace America Vol. 30, No.1, January 1992.

[2] C.E. Rhoades, ed. *Future Generation Computer Systems*, Special Issue on "Grand Challenges to Computational Science," Vol. 5, nos. 2-3, September 1989, pp.167.

[3] T. Toffoli and N.H. Margolus, "Programmable Matter: Concepts and Realization," in Lattice Gas Methods: Theory, Applications, and Hardware, ed. G.D. Doolen, Physica D **47**, 263 (1991).

[4] V.L. Petersen, "Computational Challenges in Aerospace," Future Generation Computer Systems **5**, 243 (1989).

[5] H. Schlicting, *Boundary-Layer Theory*, McGraw-Hill, New York, Seventh Edition 1979.

[6] E.Fredkin and T. Toffoli, "Conservative Logic," Int. J. Theor. Phys. **21**, 219 (1982).

[7] G.Y. Vichniac, "Simulating Physics With Cellular Automata," Physica **10D**, 96 (1984).

[8] T. Toffoli, "Cellular Automata as an alternative to (rather than an approximation of) Differential Equations in Modeling Physics," Physica **10D**, 117 (1984).

[9] L.P. Kadanoff, "On Two Levels," Physics Today **39**, 7 (1986).

[10] T. Toffoli, N. Margolus, and G. Vichniac, "Cellular Automata Supercomputers for Fluid-Dynamics Modeling," Phys. Rev. Lett. **56**, 1694 (1986).

[11] O. de Pazzis, J. Hardy and Y. Pomeau, "Molecular Dynamics of a classical lattice gas: Transport properties and time correlation functions," Phys. Rev. A **13**, 1949 (1976).

[12] J. Salem and S. Wolfram, in *Theory and Applications of Cellular Automata*, S. Wolfram ed., 382 (World Scientific, 1986).

[13] B. Hasslacher, U. Frisch and Y. Pomeau, "Lattice Gas Automata for the Navier-Stokes Equation," Phys. Rev. Lett. **56**, 1505 (1986).

[14] U. Frisch, B. Hasslacher, P. Lallemand, Y. Pomeau, D. d'Humières and J.P. Rivet, "Lattice Gas Hydrodynamics in Two and Three Dimensions," Complex Systems **1**, 649 (1987).

[15] J.P. Boon and S. Yip, *Molecular Hydrodynamics*, McGraw-Hil, New York, 1980.

[16] J.P. Boon, "Statistical Mechanics and Hydrodynamics of Lattice Gas Automata: An Overview," in Lattice Gas Methods: Theory, Applications, and Hardware, ed. G.D. Doolen, Physica D **47**, 3 (1991).

[17] H.A. Lim, "Lattice-Gas Automaton Simulations Of Simple Fluid Dynamical Problems," Mathl. Comput. Modelling **14**, 720 (1990).

[18] D. d'Humiéres, P. Lallemand, and Y.H. Qian, "Review Of Flow Simulations Using Lattice Gases," in *Proceedings of the International Seminar on Hyperbolic Problems* Bordeaux, France, June 13-17, 1988 (Springer-Verlag, 1988) pp.57.

[19] D. d'Humiéres and P. Lallemand, C.R. Acad. Sci. Paris II **302**, 983 (1986).

[20] D. d'Humiéres and P. Lallemand, Physica **140A**, 326 (1986).

[21] D. d'Humiéres and P. Lallemand, "Numerical simulations of hydrodynamics with lattice gas automata in two dimensions," Complex Systems **1**, 598 (1987).

[22] S. Wolfram, "Cellular Automaton Fluids 1: Basic Theory," J. Stat. Phys. **45**, 471 (1986).

[23] H.S.M. Coxeter, *Regular Polytopes*, Macmillan, New York, 1963.

[24] F. Hayot, "The Effect of Galilean Non-Invariance in Lattice Gas Automaton One-Dimensional Flow," Complex Systems **1**, 753 (1987).

[25] B. Hasslacher, "Discrete Fluids," *Los Alamos Science*, Special Issue No. 15, 175 (1987).

[26] M. Hénon, "Viscosity Of A Lattice Gas," Complex Systems **1**, 763 (1987).

[27] M. Hénon, "Isometric Collision Rules for the Four- Dimensional FCHC Lattice Gas," Complex Systems **1**, 475 (1987).

[28] G.Y. Vichniac, in *Instabilities and Nonequilibrium Structures II*, edited by E. Tirapegui and D. Villarroel (D. Reidel, 1989).

[29] P. Lallemand, D. d'Humières and U. Frisch, "Lattice Gas Models for 3D Hydrodynamics," Europhysics Letters **2**, 291 (1986).

[30] D. d'Humiéres and P. Lallemand, "2-D and 3-D Hydrodynamics on lattice gases," Helvetica Physica Acta **59**, 1231 (1986).

[31] K. Huang, *Statistical Mechanics*, John Wiley & Sons, Inc., New York, 1963.

[32] L.D. Landau and E.M. Lifshitz, *Fluid Mechanics*, Pergamon Press, Oxford, Second Edition 1987.

[33] B. Chopard and M. Droz, "Cellular Automata model for heat conduction in a fluid," Phys. Lett. A **126**, 476 (1988).

[34] C. Burges and S. Zaleski, "Buoyant Mixtures of Cellular Automaton Gases," Complex Systems **1**, 31 (1987).

[35] K. Molvig, P. Donis, J. Myczkowski and G. Vichniac, "Removing the Discreteness Artifacts in 3D Lattice-Gas Fluids," in Discrete Kinetic Theory, Lattice Gas Dynamics and Foundations of Hydrodynamics, edited by R. Monaco, World Scientific 1988.

[36] A.K. Gunstensen and D.H. Rothman, "A Galilean-Invariant Immiscible Lattice Gas," in Lattice Gas Methods: Theory, Applications, and Hardware, ed. G.D. Doolen, Physica D **47**, 53 (1991).

[37] D. d'Humiéres, P. Lallemand and G. Searby, "Numerical Experiments on Lattice Gases: Mixtures and Galilean Invariance," Complex Systems **1**, 633 (1987).

[38] B. Dubrulle, U. Frisch, M .Hénon, and J.P. Rivet, "Low-Viscosity Lattice Gases," J. Stat. Phys. **59**, 1187 (1990).

[39] K. Molvig, P. Donis, and C. Teixeira, "Lattice Gas Aerodynamics," submitted to Physics Of Fluids A, 1992.

[40] M. Hénon, "Isometric Collision Rules for the Four-Dimensional FCHC Lattice Gas," Complex Systems **1**, 475 (1987).

[41] J.P. Rivet, "Turbulence et systèmes dynamiques," Status Report of D.E.A., University of Nice, June 1986.

[42] S. Chen, H. Chen and G. Doolen, "How the Lattice Gas Model for the Navier-Stokes Equation Improves When a New Speed Is Added," Complex Systems **3**, 243 (1989).

[43] C. Teixeira, R.P. Bosch, Jr., and K. Molvig,"Flow Simulation Validations of Lattice Gas Aerodynamics," submitted to Physics of Fluids A, 1992.

[44] G.H. Hardy and E.M. Wright, *An Introduction to the Theory of Numbers*, Fifth Edition, Clarendon Press, Oxford, 1979.

[45] M. Stern, "Beweis eines Liouvilleschen Satzes," *J. reine angew. Math.* **105**, 357 (1889).

[46] G. Dahlquist and Å. Björck, *Numerical Methods*, Prentice-Hall, Englewood Cliffs, New Jersey, 1974.

[47] R.A. Rankin, "On The Representations Of A Number As A Sum Of Squares and Certain Related Identities," Proceedings Of The Cambridge Philosophical Society **41**, 1 (1945).

[48] F. Reif, *Fundamentals of Statistical and Thermal Physics*, McGraw-Hill, New York, 1965.

[49] S.A. Orszag and V. Yakhot, "Reynolds Number Scaling of Cellular-Automaton Hydrodynamics," Phys. Rev. Lett. **56**, 1691 (1986).

[50] C.K. Birdsall and A.B. Langdon. *Plasma Physics via Computer Simulation*. McGraw-Hill, New York, 1985.

[51] P.J. Roache, *Computational Fluid Dynamics*, Hermosa Publishers, Albuquerque, New Mexico, 1976.

[52] B. Chopard, "Nonequilibrium Static Correlation Functions for Thermo-Hydrodynamics," Ph.D. Thesis No. 2306, University of Geneva, 1988.

[53] N.A. Krall and A.W. Trivelpiece, *Principles Of Plasma Physics*. San Fransico Press Inc., San Fransico, 1986.

[54] F. Mujica, *Lattice Gas Wind Tunnel*, M.S. Thesis, Massachusetts Institute Of Technology, Cambridge, M.A., February 1991.

[55] R. P. Bosch, Jr., K. Molvig, and C. Teixeira, "A Multigrid Algorithm for Lattice Gases," submitted to Physics of Fluids A, 1992.

[56] G. Karniadakis, "Numerical Simulation of forced convection heat transfer from a cylinder in crossflow," Int. J. Heat Mass Transfer **31**, 107 (1988).

[57] G.M. Papadopoulos (private communication - 1991).

[58] S. Younis (private communication - 1991).

[59] R. Cornubert, D. d'Humiéres. and D. Levermore, "A Knudsen Layer Theory For Lattice Gases," Physica D **47**, 241 (1991).

[60] M. Hénon, "Optimization of collision rules in the FCHC lattice gas, and addition of rest particles," in Discrete Kinetic Theory, Lattice Gas Dynamics and Foundations of Hydrodynamics, R. Monaco, ed. (World Scientific, 1989), pp. 146.

[61] W. H. Rae, Jr., A. Pope, *Low-Speed Wind Tunnel Testing*, John Wiley & Sons, New York, 1984.

[62] D. J. Tritton, "Experiments on the flow past a circular cylinder at low Reynolds numbers," *Journal of Fluid Mechanics* **6**, 547, (1959).

[63] S. Taneda, "Experimental Investigation of the Wakes behind Cylinders and Plates at Low Reynolds Numbers, " *Journal of the Physical Society of Japan*, **11**, 302, (1956).

[64] H. Honji and S. Taneda, "Unsteady flow past a circular cylinder," *J. Phys. Soc. Japan*, **27**, 1688, (1969).

[65] G.K. Batchelor, " An Introduction to Fluid Dynamics," Cambridge University Press, Cambridge, 1967.

[66] A. Acrivos, L.G. Leal, D.D. Snowden and F. Pan, "Further experiments on steady separated flows past bluff objects," J. Fluid Mech. **34**, 25 (1968).

[67] M. Coutanceau and R. Bouard. "Experimental determination of the main features of the viscous flow in the wake of a circular cylinder in uniform translation. Part 1: Steady Flow," J. Fluid Mech. **79**, 231 (1977).

[68] M. Coutanceau and R. Bouard, "Experimental determination of the main features of the viscous flow in the wake of a circular cylinder in uniform translation. Part 2: Unsteady Flow," J. Fluid Mech. **79**, 257 (1977).

[69] P.M. Gresho, S.T. Chan, R.L.Lee and C.D. Upson, "A Modified Finite Element Method for solving the time-dependent incompressible Navier- Stokes equations. Part 2: applications," Int. J. Numer. Meth. Fluids **4**, 619 (1984).

[70] J.H. Gerrard, "The wakes of cylindrical bluff bodies at low Reynolds number," Proc. R. Soc. Lond. **A289**, 351 (1978).

[71] F. Hayot, and M. R. Lakshmi, " Cylinder wake in lattice gas hydrodynamics," Physics D **40**, 415 (1989).

[72] X. Wang and C. Dalton, "Numerical Solutions For Impulsively Started and Decelerated Viscous Flow Past a Circular Cylinder," Int. J. Numer. Meth. Fluids **12**, 383 (1991).

[73] K. Molvig and G.M. Papadopoulos (private communication - 1992).

[74] S. Zaleski, "Weakly compressible fluid simulations at high Reynolds numbers," in Discrete Kinetic Theory, Lattice Gas Dynamics and Foundations of Hydrodynamics, R. Monaco, ed. (World Scientific, 1989), pp. 384.

[75] A. Despain, C.E. Max, G.D. Doolen and B. Hasslacher, *Prospects for a lattice-gas computer* in Lattice Gas Methods for Partial Differential Equations, ed. G. Doolen (Addison-Wesley, Reading, MA., 1989) pp. 211.

[76] S. Remondi (private communication - 1992).

[77] S. Chen, H. Chen, G.D. Doolen, Y.C. Lee, H. Rose and H. Brand, "Lattice Gas Models For NonIdeal Gas Fluids," in Lattice Gas Methods: Theory, Applications, and Hardware, ed. G.D. Doolen, Physica D **47**, 97 (1991).